Workshop Digest

European Workshop on Optical Fibre Sensors

8-10 JULY 1998

PEEBLES

SCOTLAND

THE UNIVERSITY OF STRATHCLYDE

Volume 3483

REPORT DOCUMENTATION PAGE

Form Approved OMB No. 0704-0188

1. AGENCY USE ONLY (Leave blank)	2. REPORT DATE	3. REPORT TYPE AND DATES COVERED
	4 November 1999	Conference Proceedings

4. TITLE AND SUBTITLE

European Workshop on Optical Fibre Sensors

5. FUNDING NUMBERS

F61775-98-WE046

6. AUTHOR(S)

BRIAN CULSHAW AND JULIAN D C JONES

7. PERFORMING ORGANIZATION NAME(S) AND ADDRESS(ES)

University of Strathclyde
204 George St.
Glasgow G1 1XW
United Kingdom

8. PERFORMING ORGANIZATION REPORT NUMBER

SPIE VOL 3483

9. SPONSORING/MONITORING AGENCY NAME(S) AND ADDRESS(ES)

EOARD
PSC 802 BOX 14
FPO 09499-0200

10. SPONSORING/MONITORING AGENCY REPORT NUMBER

CSP 98-1062

11. SUPPLEMENTARY NOTES

12a. DISTRIBUTION/AVAILABILITY STATEMENT

Approved for public release; distribution is unlimited.

12b. DISTRIBUTION CODE

A

13. ABSTRACT (Maximum 200 words)

The Final Proceedings for European Workshop on Optical Fibre Sensors, 8 July 1998 - 10 July 1998

This is an interdisciplinary conference. Topics include physical, mechanical, electromagnetic, chemical, environmental, biochemical, and medical sensors; optical fiber gyroscopes; sensor networks; in-fiber gratings and special fibers; and components for sensors, both active and passive.

14. SUBJECT TERMS

EOARD, Metrology & Calibration, sensors, Optical Sensors, passive sensors, Optoelectronic components, Distributed sensors, Optical fiber sensors

15. NUMBER OF PAGES: 315

16. PRICE CODE: N/A

17. SECURITY CLASSIFICATION OF REPORT	18. SECURITY CLASSIFICATION OF THIS PAGE	19. SECURITY CLASSIFICATION OF ABSTRACT	20. LIMITATION OF ABSTRACT
UNCLASSIFIED	UNCLASSIFIED	UNCLASSIFIED	UL

NSN 7540-01-280-5500

Standard Form 298 (Rev. 2-89)
Prescribed by ANSI Std. 239-18
298-102

European Workshop on Optical Fibre Sensors

Brian Culshaw
Julian D. C. Jones
Chairs/Editors

8–10 July 1998
Peebles, Scotland

Sponsored by
University of Strathclyde
Heriot-Watt University
U.S. Air Force European Office of Aerospace Research and Development
European Commission Brite-EuRam Programme

Cosponsored by
Institution of Electrical Engineers
Institute of Physics
Institute of Measurement and Control
SPIE—The International Society for Optical Engineering
IEEE/LEOS

Published by
SPIE—The International Society for Optical Engineering

Volume 3483

SPIE is an international technical society dedicated to advancing engineering and scientific applications of optical, photonic, imaging, electronic, and optoelectronic technologies.

Please use the following format to cite material from this book:
Author(s), "Title of paper," in *European Workshop on Optical Fibre Sensors*, Brian Culshaw, Julian D. C. Jones, Editors, Proceedings of SPIE Vol. 3483, page numbers (1998).

ISSN 0277-786X
ISBN 0-8194-2938-4

Published by
SPIE—The International Society for Optical Engineering
P.O. Box 10, Bellingham, Washington 98227-0010 USA
Telephone 360/676-3290 (Pacific Time) • Fax 360/647-1445

Printed in the United States of America.

Contents

Thursday, 9 July 1998

CHEMICAL, ENVIRONMENTAL, AND MEDICAL SENSORS — **Chair: Anna G. Mignani**

INTERFEROMETRY AND DISTRIBUTED SENSORS

Chair: Julian D. C. Jones

Thursday–Friday, 9–10 July 1998

SYSTEMS APPLICATIONS AND FIELD TRIALS — **Chair: Robert A. Lieberman**

Friday, 10 July 1998

IN-FIBRE GRATINGS — **Chair: Michel Lequime**

Technical Organising Committee

Dr A G Mignani, Italy
Professor K Blotkejaer, Norway
Dr T Bosselmaan, Germany
Dr M Breidne, Sweden
Dr J P Dakin, UK
Professor R Dewhurst, UK
Professor J P Goure, France
Professor K T V Grattan, UK
Professor J M Lopez-Higuera, Spain
Dr H C Lefèvre, France
Dr M Lequime, France
Dr B D McCraith, Ireland
Professor A Rogers, UK
Professor J L Santos, Portugal
Professor M Tur, Israel
Mr M R-H Voet, Belgium
Dr R Willsch, Germany
Professor O Wolfbeis, Germany

International Advisory Committee

Dr J Berthold III, US
Dr R O Claus, US
Dr A D Kersey, US
Professor B Y Kim, Korea
Dr R A Lieberman, US
Dr W B Spillman, US
Professor Y Ohtsuka, Japan
Professor T Yoshino, Japan
Professor G Woolsey, Australia

Local Organising Committee

Professor B Culshaw, Strathclyde University, Glasgow
Professor J D C Jones, Heriot-Watt University, Edinburgh
Dr D Uttamchandani, Strathclyde University, Glasgow
Dr J S Barton, Heriot-Watt University, Edinburgh
Mrs A M Mitchell, Strathclyde University, Glasgow

European Workshop on Optical Fibre Sensors

Welcome to our workshop and to Peebles in the heart of the Scottish Border country.

Julian Jones and I have organised this workshop as a relatively informal get together and we hope to give everyone who attends the opportunity to exchange ideas and formulate a view on where we are going, why and possibly even when.

It is now well over thirty years since the first patents on the "Fotonic" sensor were filed and like all good inventions this particular sensor has been much reinvented. The fibre optic gyroscope came of age a year or so ago and is now a routine production item. However the gyroscope is perhaps the only really mass produced sensor to evolve from optical fibre sensor technology. All the other candidates for production - some of which have already emerged - may well appear as the hand crafted items more typical of the sensor industry in general. Or will they? One of our aims in the workshop is to find out.

This digest contains the papers which will be presented at the workshop. All the papers in this volume - with the exception of the five invited presentations - will appear as posters grouped together by topic as the basis for discussion sessions. It is however interesting to reflect that now most of the work reported herein and in OFS technology overall takes place in an applications oriented context. It is now very rare that the research community investigates sensor technology for its own sake. Perhaps then much of the work reported here is really embryonic product - we can hope so.

Even the fibre Bragg grating has now been with us for well over a decade - but it remains a source of great excitement in the OFS community. For strain and temperature sensing there is no doubt that the FBG will find a niche. The concepts have certainly served the research community very well since typically a quarter or more of current OFS publications involve some aspect or other of grating technology. In the communications sector, the FBG is now a volume item which can be precisely defined and which can have very stable temperature and ageing characteristics. These components must find their way into sensor technologies.

Julian Jones and I have greatly enjoyed bringing this workshop together and hope that all the attendees will find our programme stimulating and enjoyable. We should also like to thank all those who helped bring the meeting together, the Technical Organising Committee who reviewed the contributions with speed and skill, Deepak Uttamchandani who maintained the website and last, but by no means least, Aileen Mitchell who, as conference secretary, brought everything together and having brought it together held everything firmly in position thereafter.

And as for Peebles - here we are in a small town of a few thousand souls taking advantage of a well established retreat originally conceived as an escape route for the industrial and commercial magnates of central Scotland. We hope that our guests at the workshop will also take some time to explore what this quiet corner has to offer.

Brian Culshaw, Glasgow

Julian Jones, Edinburgh

Invited Presentations

Optical fibre sensors : has their time come ?

Hervé C. Lefèvre

Photonetics
52 avenue de l'Europe, BP 39
78160 Marly-le-Roi (France)
Phone : +33-(0)1-39-16-33-77
Fax : +33-(0)1-39-16-56-06
E-mail : hc-lefevre@photonetics.com

As pointed out by our chairman, this workshop aims at being prospective, but for this introductory talk, its seems important to see where we are and where we come from. Optical fibre sensors started in the late seventies with a strong worldwide growth of R & D activity in the eighties. It was also the time of enthusiastic marketing analysis : you know, the ones with nice exponential curves with an automatic shift of 11 months each year !

Following these early forecasts, today market should be more than 10 times bigger than what it is actually. Does that mean that we have to be pessimistic ? Not at all, pessimism does not apply to the past, and the ones who are here are stronger, more experienced, more patient. They know that clear signs are showing that things are changing and that optimism should apply to the future, even if growth was much slower than expected (or dreamt !).

There is a wide variety of optical fibre sensors which are difficult to discuss all in a single presentation, but let us take some significant examples. The fibre-optic gyroscope is clearly seen by the inertial guidance and navigation community as the important new technology. It is starting to fly on commercial aircrafts, and is finding a lot of various applications. An impressive accomplishment has been realized by Hitachi producing 2000 gyros per month for automobiles with a cumulated number of more than 50,000. Distributed temperature sensors based on sophisticated non-linear phenomena are now deployed, in particular for petroleum applications. Compact micro-cavities placed at the tip of fibres provide accurate measurement of various parameters (pressure, temperature, index of refraction...) using white light

SPIE Vol. 3483 • 0277-786X/98/$10.00

interferometry for remote sensing in harsh environment. Acoustic arrays, developped by NRL, are used at sea, as well as current sensors for very high voltage power lines in the field. Biological and chemical sensors are also finding their first applications after a complex interdisciplinary development.

Finally in-fibre Bragg gratings, which came later in the field, are may be the hottest R & D subject today. This technological breakthrough is bringing reality to smart structures and array sensing.

All these facts show that the answer to the title question is clearly yes ; and that reminds me a dinner with friends where I met a specialist of sensing at Schlumberger. We casually discussed about our work and potential use of optical fibre sensors in the petroleum industry. Smiling, he told me : "You are kidding ! Nothing for the next ten years". It was in 1988 !

Fibre-optic interferometric sensors for measurement of physical quantities

Wolfgang Ecke
IPHT Institut fuer Physikalische Hochtechnologie, Helmholtzweg 4, D-07743 Jena, FRG
Tel. +49-3641-302 808; Fax +49-3641-302 850; e-mail ecke@ipht-jena.de

ABSTRACT

Fibre-optic monochromatic interferometers have the significant advantage to measure displacements, fibre strain, and other physical parameters using secondary transducers, with extreme resolution and large dynamic range. In order to maintain their performance in hostile environment, they can be constructed as remote, electrically passive sensors. In a critical survey of components, architecture, and applications of fibre-optic interferometric sensors and sensor networks, their practical results and specific problems are discussed.

Advances in Distributed Optical-fibre Sensing

A. J. Rogers, V. A. Handerek, M. Farhadiroushan, R. Feced,* T. R. Parker, F. Parvaneh

Department of Electronic Engineering,
King's College London,
Strand,
London WC2R 2LS

1. *Introduction*

The ability to make distributed measurements on extended structures is of increasing importance. For example, the measurement of strain distribution on aircraft operating close to their performance limits, the distribution of temperature in boilers, pressure vessels, high voltage transformers etc., are all examples of application areas where the distributed measurement of critical performance parameters offers an additional dimension for purposes of monitoring, control or the improved understanding which can lead to significant enhancements in design.

Optical fibres, via the linear and non-linear effects which they sustain, offer unique advantages for distributed sensing. However, in order to achieve optimum performance appropriate to a given measurand and measurement environment, careful matching of system to environment, and detailed system design are necessary.

This paper highlights some of the system optimisation methods which we have studied recently, with a view to providing improved system performance and thus greater application flexibility.

2 *Forward-Scatter and Backscatter Methods*

Most distributed optical-fibre methods employ non-linear optical effects. The fundamental reason for this is that these effects exhibit varied and distinctive responses to external measurands, thus providing for a range of applications-specific sensors.

Backscatter methods, employing the OTDR technique for spatial resolution, have the advantages of high sensitivity and single-ended operation. Their disadvantage is that of a low-level signal and thus a long response time, resulting from the necessity to integrate over many pulses.

The forward-scatter techniques, usually employing counter-propagating pulse-wave interactions, generally are of lower sensitivity and (normally) need access to both ends of the fibre, but they often provide sufficiently powerful signals to operate in a single-shot mode, thus leading to a response time not greater than that of the go-and-return light passage along the fibre.

Clearly, the choice of system must depend on the required system performance.

In this paper we describe three systems, two backscatter systems and one forward-scatter system, which have been optimised with a view to extending their applications potential.

3. *Advances in System Design*

The advances in system design, using three established techniques will now be described, in illustration of the approaches which are necessary in order to provide increased applications flexibility.

(i) Raman Distributed Temperature Sensing Using Time-correlated Single Photon Counting in Backscatter

In the standard Distributed anti-Stokes Raman Thermometry (DART) [1] an intense laser pulse is launched into the sensing fibre. As a result of spontaneous Raman scattering, some anti-Stokes and Stokes photons are generated along the fibre. A fraction of these scattered photons is captured in

* Now at ORC, Southampton

guided modes of the fibre and then propagated back towards the launching end where they are detected by a fast photodetector.
As we try to increase the spatial resolution of the DART sensor, the backscattered photon flux becomes very weak. Ideally, to optimise the signal-to-noise ratio we should use a detection technique in which the circuit noise would be negligible and the excess noise factor would be equal to 1. Then, the only source of noise would be that associated with the photon statistics. A digital time-correlated single photon counting technique which satisfies these two conditions has been proposed [2] to improve the spatial resolution of DART sensors. The technique consists of the repetitive measurement of the delay time between the first detected Raman backscattered photon and the laser trigger signal.
The experimental arrangement is shown in Fig. 1. Laser pulses from a semiconductor gain-switched laser are launched into a multimode graded-index fibre through a fibre coupler. The laser pulse width was adjusted to be 200 ps. Anti-Stokes and Stokes backscattered photon distributions were measured for different temperatures of the oil bath. The temperature was increased from room temperate (20°C) up to 115°C in steps of 10°C. The measurement time for each temperature was 1 minute. Fig. 2 shows the normalised traces which were obtained. The FWHM of the spatial response varied from 3.5 cm to about 5 cm. The temperature resolution was ~ 2°C for a 10 cm. spatial resolution [3]. This represents the best performance achieved for a DART system to date.

(ii) Simultaneous Measurement of Distributed Strain and Temperature Using Brillouin Backscatter

The frequency shift in Brillouin backscatter has been researched for purposes of measurement of distributed strain [4]. Since the Brillouin shift is sensitive to both temperature and strain, it is not possible to isolate changes due to temperature from those due to strain when the fibre is subject to both. However, the spontaneous Brillouin power is also temperature and/or strain dependent and it is possible to measure simultaneously the temperature and strain by measuring both the Brillouin frequency shift and the spontaneous Brillouin power level [5].
We may express the dependences of spontaneous Brillouin power P_B and frequency ν on strain and temperature by the following equations :-

$$\frac{\delta P_B}{P_B} = C_{P\varepsilon}\,\delta\varepsilon + C_{PT}\,\delta T$$

$$\delta\nu = C_{\nu\varepsilon}\delta\varepsilon + C_{\nu T}\,\delta T$$

where $\delta\varepsilon, \delta T$ are the changes in strain and temperature, respectively, to which the fibre is subjected.
We obtain the following values for the Brillouin strain and temperature coefficients:

$$C_{\nu\varepsilon} = 0.0483 \pm 0.0004\ MHz / \mu\varepsilon,$$

$$C_{\nu T} = 1.10 \pm 0.02\ MHz / K,$$

$$C_{P\varepsilon} = -(7.7 \pm 1.4)\text{x}\,10^{-6} / \mu\varepsilon,$$

$$C_{PT} = (3{\cdot}6 \pm 0{\cdot}6)\text{x}10^{-3} / K$$

where the power coefficients are given in terms of a percentage relative to the power at 300K, $0\mu\varepsilon$.
Fig. 3 shows Brillouin spectra recorded for various points in a fibre (smoothed with a 50-point running average) interrogated by a special OTDR instrument designed to analyze Brillouin scattering. The movement in the peaks with strain and temperature can be seen clearly. Double peaks are seen when the temperature and/or strain distribution(s) vary appreciably over distances less than the spatial resolution (see Fig. 3). Fig. 4 shows the Brillouin power and shift versus distance, with the Brillouin power compensated for losses. Here the cross-sensitivity experienced

by a shift-only measurement system is seen in the form of a pronounced peak in the Brillouin shift profile at the section of the fibre at 70°C. Fig 5 shows the calculated strain and temperature distributions.
A further development has shown [6,7] that it is feasible to work with increased laser power, in the non-linear backscatter regime, by using a linearized Brillouin power which is defined in terms of the measured Stokes and anti-Stokes powers.

(iii) Single-Shot Distributed Optical-fibre Temperature Sensing Using the Frequency-derived Technique.

The technique now to be described is a distributed temperature sensor system with a SNR sufficient to permit distributed temperature measurement in a single shot. Such a system would be useful in industrial environments that requires rapid hot-spot detection, for example. The experimental arrangement and the principle used here have been reported previously [8]. In this technique a high-power, circularly polarized pulse of light launched into a high-birefringence fibre induces a transient birefringence grating by means of the optical Kerr effect; the grating spacing will be equal to the birefringence beat length. This results in power transfer between the linear polarization eigenmodes occupied by a propagating probe wave of similar wavelength to the pump. If the cw probe beam is at a slightly different wavelength and is counterpropagating with respect to the pump, the resulting spatial variation of probe wave coupling gives rise to a periodic exchange of power between the polarization eigenmodes occupied by the probe wave.
The local fluctuation of power at any point occurs at a rate (the derived frequency) that depends on the value of the local birefringence at the point; thus a measurement of this derived frequency provides the value of the birefringence at each location which is effectively scanned by the pump pulse as it propagates along the length of the fibre. Hence the technique permits the distributed measurement of any physical parameter, such as temperature, that is capable of modifying the fibre's birefringence.
The experimental setup is shown in Fig 6. The fibre used (supplied by Andrew Corporation) had an elliptical core and was operating in a single mode at 633 nm, at which wavelength it had a birefringence beat length of 4 mm.
Curves (a), (b), (c), and (d) of Fig 7 show the frequencies of the base-band signals for temperatures of 150, 120, 90, and 60°C, respectively. The normalized frequency shift in the base-band signal can be represented as the percentage change compared with the frequency generated at room temperature. This normalized frequency variation as a function of temperature is shown in Fig. 8, which shows the expected linear relationship between the frequency shift in the base-band signal and the temperature.
This technique could be a valuable asset for measurement of either temperature or strain when the allowable measurement time is very limited.
Temperature accuracy was ± 1.2°C and spatial resolution, although temperature dependent, was good (0·56 m at 150°C).

4. *Conclusions*

We have shown that careful attention to optimisation of system design can lead to significant enhancement in performance for distributed optical-fibre sensing. This enhancement can make a crucial difference in regard to competing technologies in specific applications areas.

5. *References*

(1) Dakin J. P., Pratt D. J., Bibby G. W. and Ross J. N., 'Distributed Optical-fibre Raman Temperature Sensor Using a Semiconductor Light Source and a Detector', Electron Lett, June 1985, Vol. 21, No 13, pp 569-570.

(2) Stierlin R., Ricka. J., Zysset B., Battig R., Weber H. P., Binkert T., and Borer W. J. 'Distributed Fibre Optic Temperature Sensor using Single Photon Counting Detection', Appl. Opt. 1987, Vol. 26, No. 8, pp 1368-1370.

(3) R. Feced, M Farhadiroushan, V. A. Handerek and A. J. Rogers, 'Advances in High Resolution Distributed Temperature Sensing using the Time Correlated Single Photon Counting Technique', Proc. IEE Optoelectronics, Vol. 144, No. 3, June 1997, pp 183-188.

(4) D. Culverhouse, F. Farahi, C. N. Pannell, and D. A. Jackson, 'Potential of Stimulated Brillouin Scattering as a Sensing Mechanism for Distributed Temperature Sensors', Electron Lett., Vol 25, No. 14, pp 913-915, 1989.

(5) T. R. Parker, M. Farhadiroushan, V. A. Handerek, and A. J. Rogers, 'Temperature and Strain Dependence of the Power level and Frequency of Spontaneous Brillouin Scattering in Optical Fibers'. Opt. Lett., Vol. 22, No. 11, pp 787-789, 1997.

(6) T. R. Parker, M. Farhadiroushan, R. Feced, V. A. Handerek and A. J. Rogers, 'Simultaneous Distributed Measurement of Strain and Temperature from Noise-initiated Brillouin Scattering in Optical Fibres' IEEE JQE (to be published, 1998).

(7) R Feced, T. R. Parker, M. M. Farhadiroushan, V. A. Handerek and A. J. Rogers, 'Power Measurement of Noise Initiated Brillouin Scattering in Optical Fibres for Sensing Applications', Opt. Lett., January 1998, Vol. 23, No. 1, pp 79-81.

(8) F. Parvaneh, V. A. Handerek and A. J. Rogers, 'Frequency-derived Remote Measurement of Birefringence in Polarization Maintaining Fibre by Using the Optical Kerr Effect', Opt. Lett, Vol. 17, No. 19, Oct., 1992, pp 1346-1348.

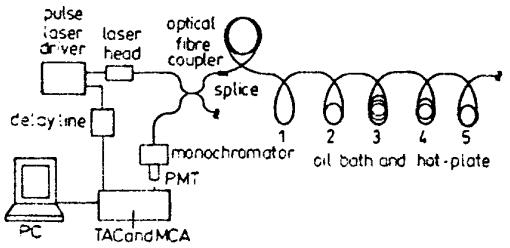

Fig. 1. Experimental set-up for high spatial resolution distributed optical fibre sensor.

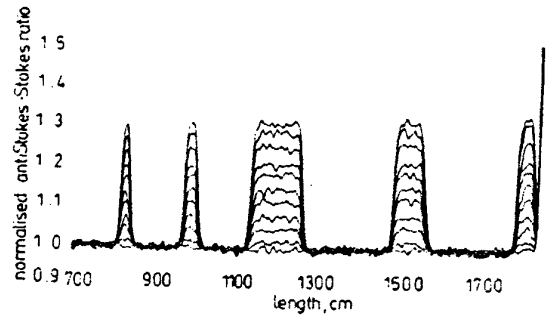

Fig. 2. Normalised and Processed Anti-Stokes/ Stokes Ratio for Several Temperatures:(20°C, 35°C, 45°C, 55°C, 65°C, 75°C, 85°C, 95°C, 105°C, and 115°C)

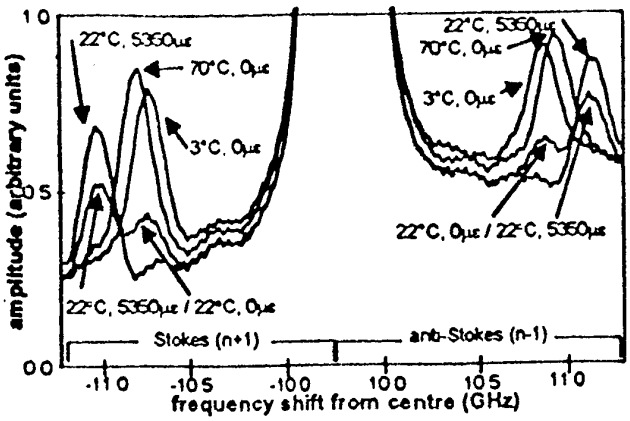

Fig. 3. Brillouin spectra recorded for various locations in the fibre.

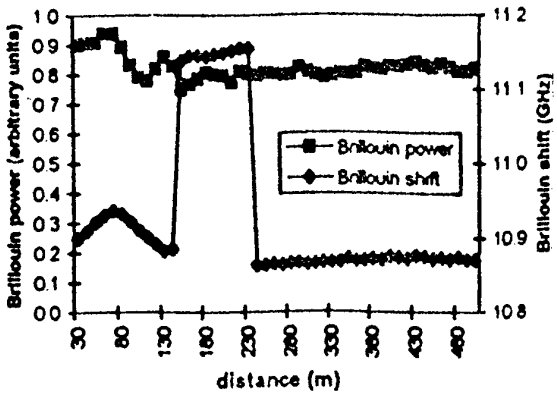

Fig . 4. Brillouin power and Brillouin frequency shift versus position

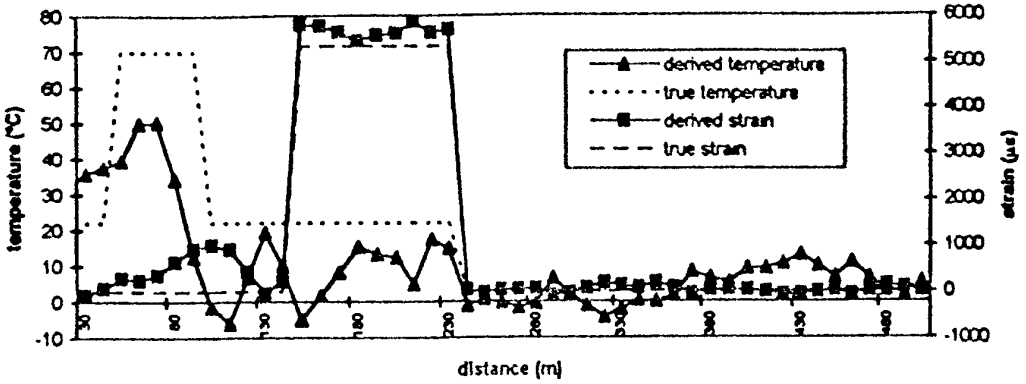

Fig. 5. Derived and true temperature and strain versus position.

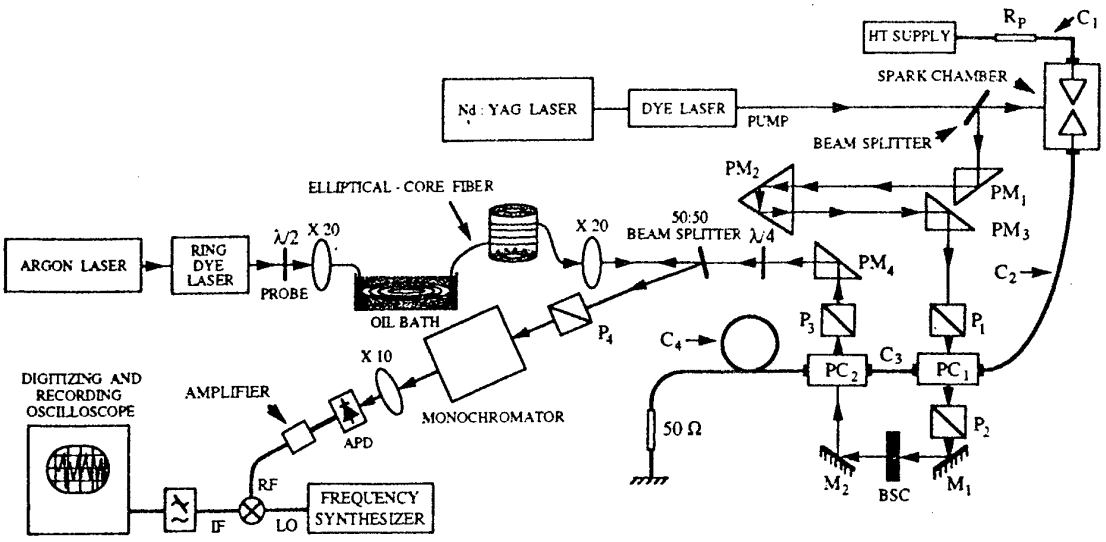

Fig. 6. Experimental setup for single-shot temperature sensing measurement: C_4, attenuating cable, M_1, M_2, mirrors; P_1, P_2, P_3, P_4, polarizers; Rp, limiting resistor; APD, avalanche photodiode; HT, high tension; IF, intermediate frequency; RF, radio frequency.

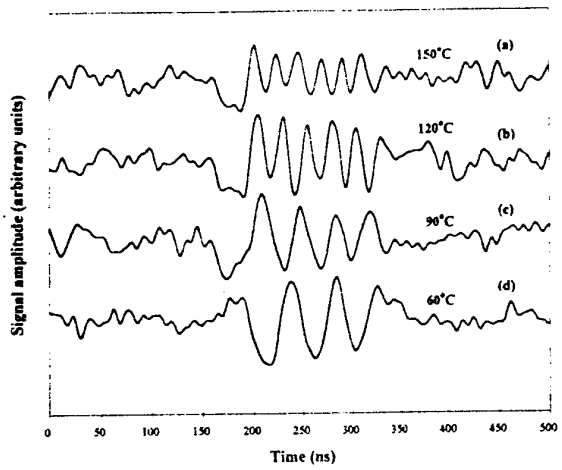

Fig. 7. Variation of the frequency of the base-band signal with temperature.

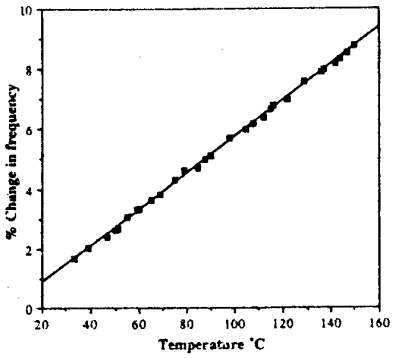

Fig. 8. Temperature dependence of the normalized derived frequency.

Optical Current and Voltage Sensors for Power Industry – A Long Way to the Market

T. Bosselmann
Siemens AG, Corp. Techn. ZT EN 5, POB 3220, D-91050 Erlangen, Germany
Phone: +49 9131 7-31745, Fax: -32164, e-mail: thomas.bosselmann@erls.siemens.de

ABSTRACT

Optical fibre current and voltage sensors for power industry have needed about 20 years of devleopment time to gradually emerge at the market. The advantageous potential separation is confronted with an expectation of high reliability and low costs.

FIBER LASERS FOR SENSING

Byoung Yoon Kim

Department of Physics, Korea Advanced Institute of Science and Technology
373-1, Kusong-dong, Yusong-gu, Taejon, 305-701 Korea
Fax: 82-42-869-5527, E-mail: yoonkim@sorak.kaist.ac.kr

INTRODUCTION

Optical fiber sensors have been developed for more than two decades and are now in practical use for many different applications. Their advantageous characteristics, such as high sensitivity, immunity to electromagnetic interference, small size, environmental stability, and multiplexing capability, make it possible to measure new physical parameters and to place the sensors in new environment. We have witnessed many different forms of fiber sensors optimized for the individual applications, but new sensor ideas are still being introduced. It is important to take advantage of new fiber component technologies originally developed for telecommunications applications, such as fiber gratings and rare-earth doped fiber amplifiers. Since high quality components are becoming available at a reduced cost with increasing use in communication market, high performance fiber sensors can be readily designed and manufactured. Even at this stage of fiber sensor development, new sensor concepts are often needed to overcome the limitations of existing fiber sensors that cannot be dealt with based on straightforward engineering.

In this paper, as an attempt to stimulate some new thoughts, fiber sensors using Er-doped fiber (EDF) lasers as a sensing medium and/or a light source will be described. The fiber laser sensors are different from the conventional sensors with external optical sources in that the fiber laser cavity is used also as the sensing element. Optical parameters of the laser output, such as laser frequency and intensity distribution responds to the external perturbations, and provide unique forms of output that can lead to better performances with simpler sensor configurations compared to conventional passive fiber sensors. Some of the novel functions obtainable from fiber lasers can also be utilized to probe sensors.

FIBER LASER GYROSCOPES

Fiber-optic gyroscopes have been used in the field for quite a few years and the performance has been improving with the use of a polarization maintaining fiber, broadband optical source and proton exchanged $LiNbO_3$ waveguide for a polarizer and a phase modulator. Efforts have been devoted to reduce the cost without sacrificing the performance. In recent years, high

performance fiber gyroscopes have been pursued for undersea and space applications. Although the traditional fiber gyroscope technologies may provide adequate solutions for current problems, alternative technologies with radically different approaches have to be explored for their unique potential. When an active laser cavity is used as the rotation sensing element of a gyroscope, the reciprocity is automatically satisfied regardless of the birefringence in the fiber circuit. In the absence of spurious back scattering, it should be easier to achieve stable bias, and the stringent requirements imposed on the polarization maintaining fiber and the polarizer can be removed. Another potential importance of the fiber laser gyroscopes is that the electronic signal processing may be simplified.

One such example is a fiber ring laser gyroscope based on stimulated Brillouin scattering [1], that had difficulties with complicated optical and electronic configuration. A similar device with an EDF as the gain medium [2] had to be modified [3] to yield clean signal to work with. In the latter fiber ring laser gyroscope shown in figure 1, the basic cavity configuration is a linear cavity formed by a fiber grating and a Sagnac loop mirror that also acts as a rotation sensing element. At any given time, there are two mode-locked pulses in the cavity, and a 1x2 electro-optic switch directs the two pulses in the opposite directions when they enter the loop mirror. In this way, the laser can be operated as a ring laser gyroscope with spectral stability (owing to a fiber grating) and minimum backscattering effect (owing to short pulse operation). The two pulses that traverse the Sagnac loop in opposite directions will experience different cavity length when the laser is rotating, which can be monitored by measuring the beat frequency between them. Figure 2 shows a typical beat note. There are undesirable effects that have to be dealt with; gain competition between the pulses, optical Kerr effect, and the differential phase shift from the electro-optic modulator. Although the solutions for these problems are yet to be discovered, this is the first fiber ring laser gyroscope based on an EDF that produces clean beat frequency output.

Another form of a fiber laser gyroscope that has been studied is also a mode-locked fiber laser and is shown in figure 3. The laser cavity is formed by a Sagnac loop mirror and a planar mirror or a fiber grating. An EDF, a diode laser, or a semiconductor optical amplifier are used as the gain medium [4-7]. The mode locking is provided by the modulation of reflectivity of the loop mirror generated by a phase modulator, as depicted in figure 4. As in the case of fiber ring laser described earlier, there are two pulses in the laser cavity, and the timing of pulses is determined by differential phase shift induced by rotation. Therefore, the rotation rate can be measured by using a time interval counter with simple digital electronics. It has been found that spurious back reflections cause deformation of the pulse shapes and also instability of the pulse intensity, that should be reduced for improved performance. Amplified spontaneous emission from the optical amplifier, especially for the cases of diode

amplifiers with fast gain recovery time, is another error source that should be eliminated. The use of fiber grating helps reduce the amplified spontaneous emission. The sensitivity of 4 deg/hr/$\sqrt{Hz}$ and bias stability of 100 deg/hr has been demonstrated with a fiber laser gyroscope using diode laser amplifier [7].

Despite the uncertainties in the achievable performance, the fiber laser gyroscopes open up new possibilities that may bring the rotation sensing beyond the limitations of current gyroscope technology.

POLARIMETRIC FIBER LASER CURRENT SENSOR

A more straightforward application of fiber lasers to sensing is a polarimetric beat detection. Here, the fiber laser cavity supports two orthogonal polarization laser modes whose frequency difference is determined by the fiber birefringence. When external perturbations modulate the fiber birefringence, the beat frequency between them changes that can be monitored as the sensor output [8-10]. The physical parameters that can easily alter the fiber birefringence include temperature, stress and strain, and longitudinal magnetic field. It should be noted that the two eigen polarization modes of a linear cavity fiber laser are always linearly polarized at the location of end mirrors regardless of the fiber birefringence as long as it does not contain any non-reciprocal element. If the laser operates in multiple longitudinal modes, the beat note tends to be noisy both in magnitude and frequency. A solution for this problem was found by reducing the number of longitudinal modes in each polarization modes to one or two [11,12]. The mode control technique involves the use of a saturable absorber and position control of the gain medium in the fiber laser cavity. The discovery of unique polarization properties of a fiber laser with a Faraday rotating mirror made it possible to introduce the fiber laser current sensor with a direct frequency read out [11,12]. It turns out that the eigen polarization states of the laser output at the opposite end from the Faraday rotating mirror are always circular polarizations making it ideal for current sensing. An example of a current sensor is shown in figure 5 along with the measured beat frequency shift as a function of applied current to the solenoid. The particular sensor demonstrated a reasonable sensitivity with direct frequency readout. The fiber laser current sensor does not have the troubling lead sensitivity that is another attractive property.

WAVELENGTH SWEPT FIBER LASER FOR FIBER GRATING SENSOR ARRAYS

A novel fiber laser whose output wavelength can be swept in time is applied to the interrogation of fiber grating sensor arrays [13]. With a broad wavelength span of 28 nm, high output power of a few mW, and narrow spectral resolution, the fiber laser translates the change in reflection wavelength of the fiber grating to timing shift of the reflected pulses that

can easily be measured without the help of complicated wavelength dispersive optical elements. When applied to a sensor array, the individual sensors with different reflection wavelengths are registered at different times within a wavelength sweep cycle. The arrangement is shown in figure 6. Strain measurements can be done as shown in figure 7. Resolution of 0.47 microstrain at a sampling rate of 250 Hz has been demonstrated [13]. This approach may lead to very simple fiber grating sensor arrays with high sensitivity.

REFERENCES

[1] S. Huang, L. Theveve, K. Toyama, B. Y. Kim and H. J. Shaw, Optical Kerr-Effect in Fiber-Optic Brillouin Ring Laser Gyrosscopes,, IEEE Photon. Technol. Lett. 5, 365 (1993).

[2] S. K. Kim, H. K. Kim, and B. Y. Kim, Er^{3+}-Doped Fiber Ring Laser for Gyroscope Applications", Opt. Lett. 19, 1810 (1994).

[3] S. H. Chang, S. J. Ahn, S. K. Kim, B. Y. Kim, "Direction Swithched Mode-Locked Er-Doped Fiber Laser for Gyroscope Applications", OFS-12, Williamsburg, Virginia, USA, 130 (1997).

[4] M. Y. Jeon, H. J. Jeong and B. Y. Kim, "Mode Locked Fiber Laser Gyroscope," Opt. Lett. 18, 320 (1993).

[5] H. J. Jeong, Y. W. Koh, B. W. Lee, M. Y. Jeon, and B. Y. Kim, "Analysis of Polarization Properties of Mode-Locked Fiber Laser Gyroscope", Appl. Opt. 35, 2206 (1996).

[6] K. H. Park, , B. W. Lee, and B. Y. Kim, "Mode-locked Fiber Laser Gyroscope based on a Distributed-Feedback Semiconductor Laser Amplifier", Opt. Lett. 21, 92 (1996).

[7] B. W. Lee, H. J. Jeong, B. Y. Kim, "High-Sensitivity Mode-Locked Fiber Laser Gyroscope", Opt. Lett. 22, 129 (1997).

[8] H. K. Kim, S. K. Kim, H. G. Park and B. Y. Kim, "Polarimetric Fiber Laser Sensors,, Opt. Lett. 18, 317 (1993).

[9] H. Y. Kim, S. K. Kim, H. J. Jeong, H. K. Kim, and B. Y. Kim, "Polarization Properties of a Twisted Fiber Laser", Opt. Lett. 20, 386 (1995).

[10] H. Y. Kim, B. K. Kim, S. H. Yun, and B. Y. Kim, "Response of Fiber Lasers to an Axial Magnetic Field", Opt. Lett. 20, 1713 (1995).

[11] J. S. Park, S. H. Yun, S. J. Ahn, and B. Y. Kim, "Polarization- and Frequency-Stable Fiber Laser for Magnetic-Field Sensing", Opt. Lett., 21, 1029 (1996).

[12] M. L. Lee, J. S. Park, W. J. Lee, S. H. Yun, Y. H. Lee, B. Y. Kim, "Polarimetric Current Sensor Using Orthogonally-Polarized Dual-Frequency Fiber Laser," Meas. Sci. and Technol. (1998) (in press).

[13] S. H. Yun, D. J. Richardson, B. Y. Kim, "Interrogation of fiber grating sensor arrays using a wavelength-swept fiber laser", Opt. Lett. 23, (1998) (in press).

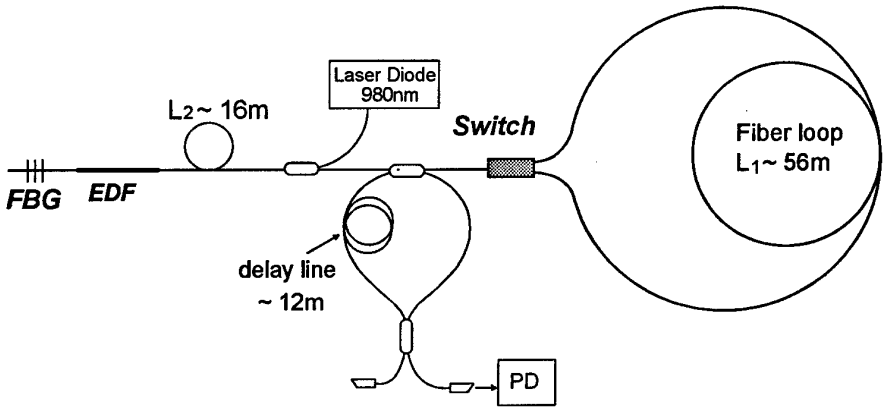

Figure 1: Schematic of the direction switched mode-locked fiber ring laser gyroscope. FBG, fiber Bragg grating; EDF, erbium doped fiber.

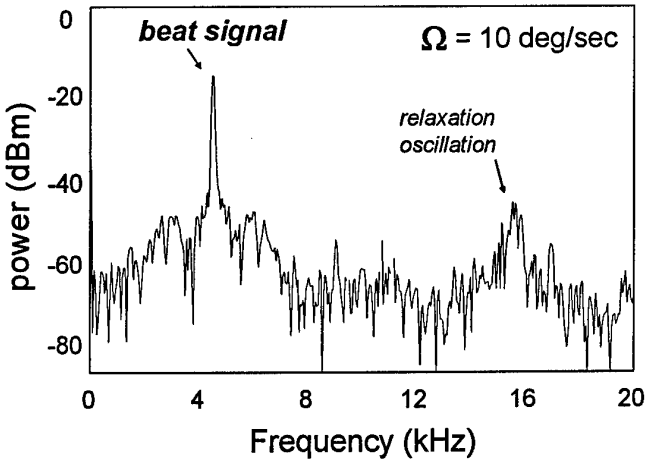

Figure 2: Gyroscope beat signal on rf spectrum analyzer.

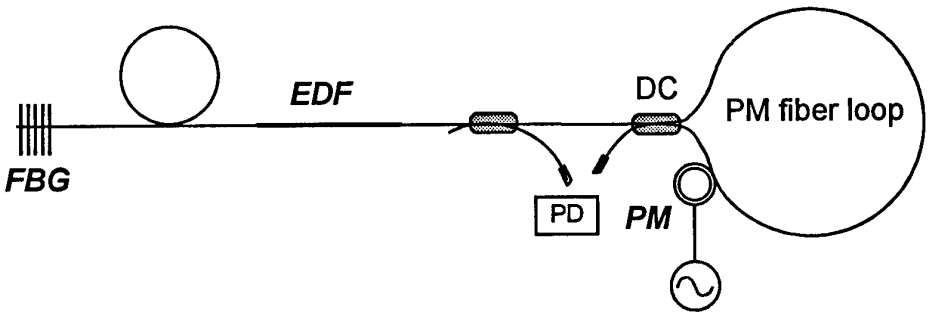

Figure 3: Schematic of the mode-locked fiber laser gyroscope. FBG, fiber Bragg grating; EDF, erbium doped fiber; PM, PZT phase modulator.

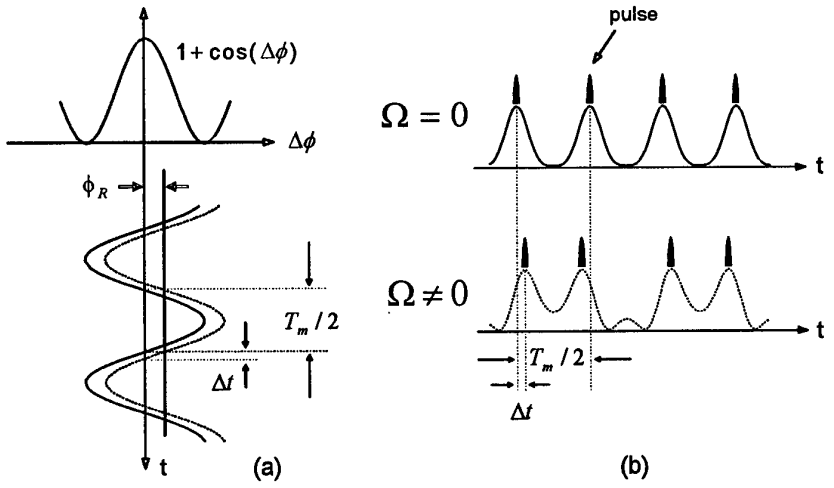

Figure 4: (a) Response of the loop reflectivity to sinusoidal phase-difference modulation. (b) Positions of the mode-locked pulses in the time domain

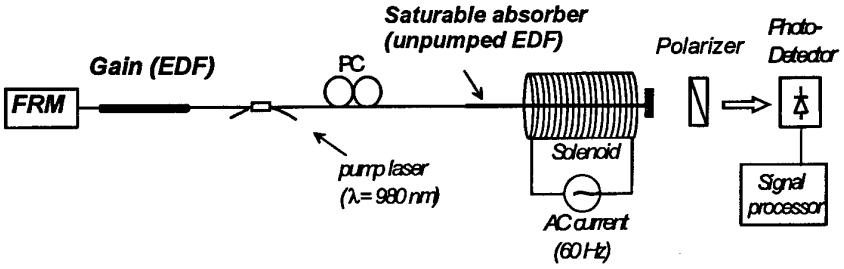

(a)

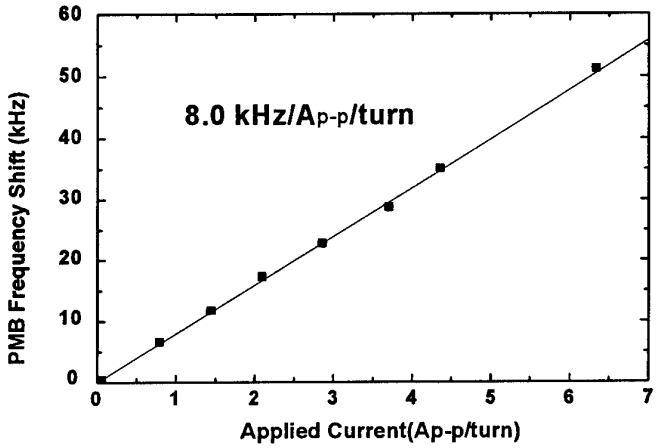

(b)

Figure 5: (a) Configuration for a fiber laser current sensor using a Faraday rotating mirror (FRM). (b) Scale factor.

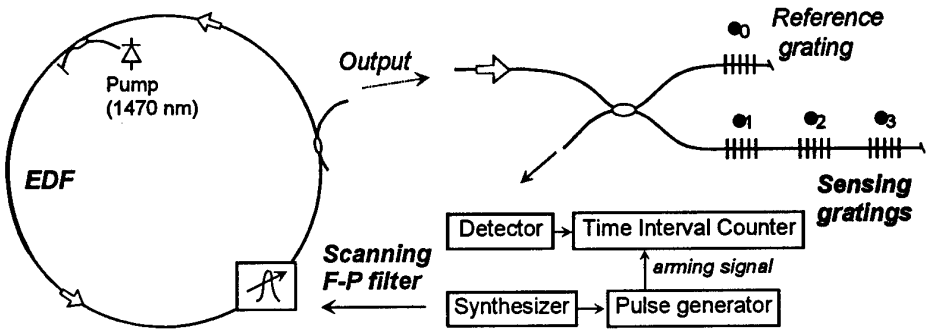

Figure 6: Arrangement for the fiber grating sensor interrogation using a wavelength-swept fiber laser. EDF, erbium-doped fiber; F-P, Fabry-Perot.

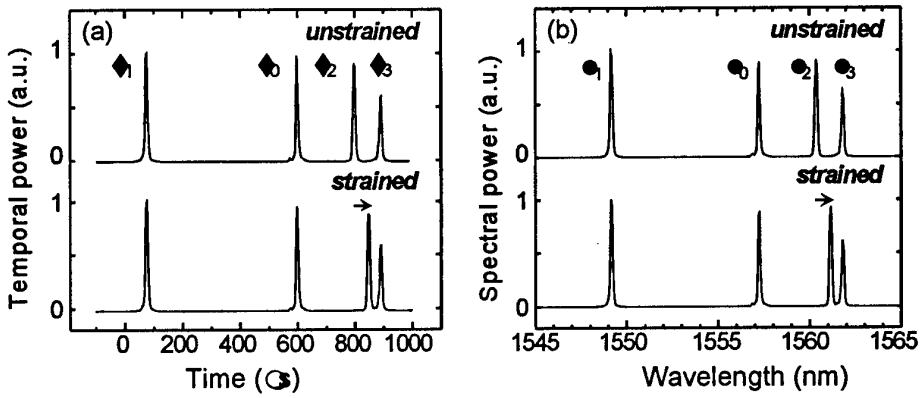

Figure 7: (a) Time-domain reflection signal of the wavelength-swept fiber laser output from the gratings. (b) Reflection spectrum of the gratings measured with an amplified spontaneous emission erbium fiber source.

Physical and Mechanical Sensors

Wednesday, 8 July 1998

Chair: Brian Culshaw, University of Strathclyde (UK)

Description of Polarization dispersion effects in embedded fiber optic sensors using the Principal states of polarization

Avishay Eyal, Michal Ben Artzi, Ofer Shapiro and Moshe Tur

Faculty of Engineering, Tel Aviv University, Tel-Aviv, ISRAEL 69978
Tel: 972-3-6408125, Fax: 972-3-6410189, E-mail: tur@eng.tau.ac.il

Introduction

The process of embedding an optical fiber into a host medium is often accompanied with high pressure and high temperature. It is expected, therefore, that during that process significant birefringence will be induced into the embedded fiber. In this paper we consider the effect of the induced birefringence on the behavior of a specific sensor: a fiber optic radio frequency (RF) interferometer strain sensor (Fig. 1).

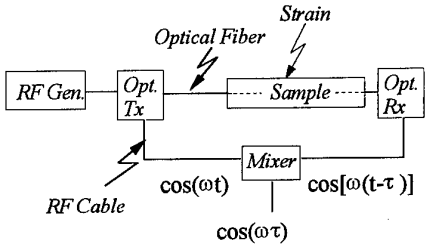

Fig 1: A fiber-optic RF interferometer strain sensor

This sensor utilizes an embedded optical fiber and RF interferometry [1] to measure the average strain in a composite structure, which was in our case a composite laminated plate. Instead of using the rather too sensitive optical interferometry, the light intensity through the embedded fiber was modulated at GHz frequencies and the detected signal was electronically mixed with a reference at the same RF frequency. The resulting signal is the cosine of the RF phase, which depends upon the optical length of the embedded fiber. Under longitudinal loading stress, the plate is strained and it is the purpose of the RF fiber-optic sensor to measure the longitudinally-average strain.

Since carrier modulation is involved, all delays are determined by the relevant *group* velocities and the corresponding analytical description of the propagation can only be formulated using the Principal States of Polarization (PSPs)[2], because, by definition, they do not depend on wavelength to first order. Assuming the input optical signal to be $\vec{E}(t, z=0) = e(t)e^{i\omega_o t}\hat{e}_i$, where $\hat{e}_i$ is a unit Jones vector representing the input state of polarization and $e(t)$ is a slowly varying function of time, describing the RF modulation, the output optical field at $z=L$ is expressed by:

$$\vec{E}(t,L) = c_+\hat{e}_{o+}e^{i\left[\omega_o t-\phi_+(\omega_o)\right]}e\left(t-\tau_{g+}\right)+c_-\hat{e}_{o-}e^{i\left[\omega_o t-\phi_-(\omega_o)\right]}e\left(t-\tau_{g-}\right) \qquad (1)$$

Here $c_{\pm}$ are the projections of the input state of polarization (SOP) onto the input PSPs, $\tau_{g\pm}$ and $\hat{e}_{o\pm}$ are, respectively, the corresponding group delays and output PSPs, and $\phi_{\pm}(\omega_o)$ are two phase delays (which are of no importance for RF interferometry). The group delay difference between the PSPs ($\tau_{g+} - \tau_{g-}$) is commonly termed the Differential Group Delay (DGD) and is widely used as a measure to the Polarization Mode Dispersion (PMD) in fiber-optic communication [3]. Clearly, in the presence of nonzero DGD, the measured RF delay will depend on the values of $c_{\pm}$, which may change during the plate loading.
In this paper we show that the embedding process increased the DGD of the embedded fiber by almost two orders of magnitude. Moreover, the measured PSPs and DGD considerably varied with the straining force. This phenomena led to variations of $c_{\pm}$, resulting in polarization-related fluctuations of the measured strain, also described below.

Theory
Under RF modulation, the envelope of the electric field, $e(t)$, is expressed by $e(t) \propto \sqrt{1+m\cos(\omega_{rf} t)}$ ($\omega_{rf} << \omega_o$), so that, following Eq. (1), the detected microwave signal at the receiver end is a weighted sum of two delayed versions of the original modulating signal, each with a different delay:

$$V(t) \propto |c_+|^2 \cos\left[\omega_{rf}\left(t-\tau_{g+}\right)\right] + |c_-|^2 \cos\left[\omega_{rf}\left(t-\tau_{g-}\right)\right] \qquad (2)$$
$$= A(strain)\cos\left[\omega_{rf}\left(t-\tau_{eff}(strain)\right)\right]$$

The strain dependent amplitude, A, and the strain dependent delay time, τ_{eff}, are given by (defining $\bar{\tau}_g \equiv \frac{1}{2}\left(\tau_{g+}+\tau_{g-}\right)$ and $DGD \equiv \tau_{g+} - \tau_{g-}$):

$$A = \sqrt{1+2|c_+|^2|c_-|^2\left(\cos(\omega_{rf} DGD)-1\right)} \approx 1 \qquad (3)$$
$$\tau_{eff} = \bar{\tau}_g + \tfrac{1}{2} DGD\left(|c_+|^2 - |c_-|^2\right)$$

Here we used: $|c_+|^2 + |c_-|^2 = 1$ and $\omega_{rf} DGD << 1$. The latter assumption was confirmed by our measurements as will be described in the following section. Finally, $V(t)$ is mixed with a reference at the same RF frequency ω_{rf} and at the mixer output around DC is:

$$U = M\cos\left(\omega_{rf}(\tau_{eff} - \tau_r)\right) \qquad (4)$$

Here τ_r is the delay along the reference arm. Expressing τ_{eff} as a sum of its unstrained value and a strain induced deviation: $\tau_{eff} \equiv \tau_{eff}^0 + \delta\tau_{eff}$, and assuming that ω_{rf} is properly adjusted so that $\cos\left(\omega_{rf}\left(\tau_{eff}^0 - \tau_\gamma\right)\right) = 0$ and $\sin\left(\omega_{rf}\left(\tau_{eff}^0 - \tau_\gamma\right)\right) = 1$, we obtain ($\tau_r$ does not change with the strain):

$$
\begin{aligned}
U &= M\sin\left(\omega_{rf}\delta\tau_{eff}\right) \\
&\approx M\omega_{rf}\delta\bar{\tau}_g + \tfrac{1}{2}M\omega_{rf}\delta\left[DGD\left(\left|c_+\right|^2 - \left|c_-\right|^2\right)\right] \\
&\equiv U_0 + \tfrac{1}{2}U_f
\end{aligned}
\tag{5}
$$

The last two lines state that the response of the sensor can be represented by two terms: the first, $U_0 \equiv M\omega_{rf}\delta\bar{\tau}_g$ is proportional to the average strain along the sample, while the second term, $U_f \equiv M\omega_{rf}\delta\left[DGD\left(\left|c_+\right|^2 - \left|c_-\right|^2\right)\right]$ fluctuates as the weights c_+, c_- and the DGD vary during the plate loading.

When the plate is loaded, $\bar{\tau}_g$ changes as a result of two major effects: the fiber length, l, is changed by δl and its refractive index, n, also changes due to the strain-optic effect by δn. Following [3] the total change in $\bar{\tau}_g$ is:

$$
\delta\bar{\tau}_g = \frac{1}{c}(n\delta l + l\delta n) = C\bar{\tau}_g\varepsilon \quad , \quad \varepsilon \equiv \frac{\delta l}{l}
\tag{6}
$$

Where c is the speed of light, ε is the average strain within the fiber, and C depends on the Pockels constants and the Poisson ratio of the fiber.

Experiment and Results

The average strain along a longitudinally loaded composite laminated plate was measured using the fiber optic RF interferometer (Fig. 1). An RF signal generator operating at 2.5GHz was used to modulate the intensity of a 1.3μ optical transmitter. The dependence of the longitudinally-average strain on the applied force, as measured by the RF interferometer appears in Fig. 2. The output of the RF interferometer does increase with the applied force but its value fluctuates around the expected linear dependence (A resistive-type electronic strain gauge, glued to the plate surface near its center, has indeed produced a smooth straight line).

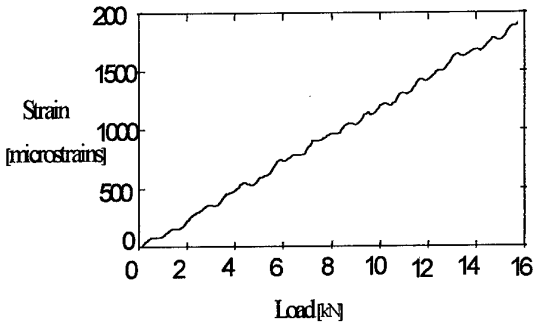

Fig. 2: Strain Vs. applied force

To confirm our explanation for the fluctuations we measured the PSPs and their DGD as functions of the applied strain, using the Jones Matrix Eigen Analysis method [3]. The variations of the PSPs are plotted in Fig. 3. The polarization characteristics of the down- and up-leads (regular SMF28 fibers about 10m in total) were separately evaluated using equivalent

fibers of the same lengths. The birefringence of these leads was found to be very small as attested by the low measured *DGD* ($<10^{-15}$ sec) and the fact that the PSPs barely changed with wavelength over a 30nm range. Once the *DGD* and PSPs are obtained for a particular stressed condition of the composite plate, the projections of the input SOP on the PSPs, $c_{\pm}$, can be evaluated, and the fluctuations in Fig. 2 can be directly calculated from Eq (5). Unfortunately, the setup under study did not allow for a measurement of the input SOP. Thus, we estimated the amplitude of the fluctuations by finding the mean of $\text{abs}\left(|c_+|^2 - |c_-|^2\right)$ over all possible input SOPs which was 0.4. Combining this estimate for $|c_+|^2 - |c_-|^2$ and the values of the *DGD*, which fluctuated between 0.1-0.4 psec, one can predict the fluctuations in Fig. 2 to be on the order of 65 microstrains. This is in general agreement with the measured data of Fig. 2.

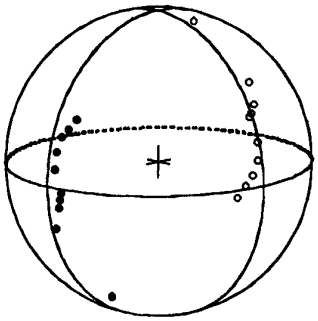

Fig. 3: Variation of the Principal States of Polarization during the loading of the plate

Conclusion

The effect of PMD on the behavior of a fiber-optic RF interferometer strain sensor was studied. The existence of PMD, induced into the embedded fiber by the embedding process, perturbed the linearity of the sensor, introducing sizable fluctuations in the measured strain vs. load curve. Since group velocities are involved, the PSPs were used to analytically describe these fluctuations. Moreover, it was also found that the PSPs of the embedded fiber depended considerably on the wavelength, indicating that the birefringence induced in it was not uniaxial. Thus, a simple analysis in which the embedded fiber is modeled by an high-birefringence fiber was inappropriate and a more general approach was needed. Using this approach a correct estimate to the size of the fluctuations was obtained. The observed phenomena may have important ramifications in other embedded fiber-optic sensors as well.

References

[1] B. Noharet, M. Turpin, J. Chazelas, P. Bonniau, D. Walsh, W.C. Miche, B. Culshaw Microwave subcarrier optical fiber strain sensor. *SPIE,* vol. 2361, pp. 236-239, 1994.

[2] C. D. Poole, N. S. Bergano, R. E. Wagner and H. J. Schulte. Polarization Dispersion and Principal States in a 147 km Undersea Lightwave Cable. *Journal of Lightwave Technology*, vol. 6 (no. 7): pp.1185-1988, 1988.

[3] B. L. Heffner. Automated Measurement of Polarization Mode Dispersion Using Jones Matrix Eigenanalysis. *IEEE Photonics Technology Letters,* vol. 4 (no. 9), pp. 1066-1069, 1992.

CHARACTERISTICS OF DOPED FIBRE INTRINSIC OPTICAL FIBRE SENSOR PROBES FOR WIDE RANGE AND HIGH TEMPERATURE OPERATION

Z. Y. Zhang, K. T. V. Grattan, A. W. Palmer, B.T. Meggitt and T. Sun
Department of Electrical, Electronic & Information Engineering, City University, Northampton Square, London EC1V 0HB

1. Introduction

Rare earth doped fibres have made a significant impact upon the development of effective optical communications systems. The authors[1] and others[2] have extensively explored the use of these rare-earth doped materials in fibre optic high temperature probes, to enable measurements over a wide range. For high temperature measurement (>500°C) pyrometry and blackbody techniques have been favoured historically, but at lower temperatures, due to the long wave nature of the emission, such methods tend to be less accurate. There has been a need to develop techniques which cover both the upper and lower ends of the temperature spectrum, in a stable and reliable way, from temperatures as low as those of liquid nitrogen (77K) to the temperatures experienced in furnaces and engines. Fluorescence-based methods offer such possibilities but have been restricted historically by the materials aspects of the construction of an effective sensor probe. Using optical glasses doped with appropriate luminescent ions (Nd^{3+}) and conventional cements, in a tailored mechanical probe, temperatures as high as approximately 400°C were reached in early research[1-3]

To extend on this, the Nd-doped optical fibre probe, employing a fluorescence decay measurement method, has been shown to cover the range -190°C to +750°C (with a precision of ±3°C), making it suitable for use in the turbine high pressure compressor area of an engine under test[4]. Such doped fibre probes are compact, relatively inexpensive to fabricate and operate over a wide temperature range. Their intrinsic nature offers many advantages, but for a number of applications in testing and evaluation there is a need for even higher maximum temperatures. However, degradation in the sensor performance at higher temperatures which was associated with irreversible fluorescence quenching and chemical/material changes, has limited the application of the technology as a more general aero-engine temperature probe for use in the higher temperature regions, such as the high pressure turbine blade area, where temperatures can reach up to 1300°C.

In the search for alternative fluorescent doped optical fibre, suitable for a temperature sensor probe which would operate up to even higher temperatures and over a wider dynamic range than Nd, Er-doped optical fibres attracted early attention. Firstly, the dopant erbium has a melting point which is much higher than that of neodymium and its atomic weight is also much higher. These indicate that the erbium dopant would behave more stably at high temperatures, both chemically and physically, by being less reactive and mobile within silica (SiO_2, the host material of the optical fibre) than the smaller and lighter Nd dopant. Secondly, due to the rapid development of the optical fibre amplifier for telecommunications use, Er-doped fibres are commercially available with a wide range of doping concentrations. A further alternative is thulium (Tm) doped fibre. Tm is a rare earth ion, which is available doped into optical fibre, and such fibre has also been designed primarily for use in telecommunications applications.

In this paper, the characteristics of several rare earth doped fibres are tested, especially in terms of their capabilities for a wide measurement range and sustained exposure to high temperatures. This aims to extend the investigation of the basic characteristics of such fibres carried out previously, and to evaluate the comparative advantage of Nd, Er and Tm-doped materials.

2. Experimental arrangement

The opto-electronic arrangement used for the measurement of the fluorescence characteristics of the temperature sensitive fibres is illustrated in Figure 1. Following upon the earlier success of Nd doped fibre, several other doped fibres were examined to try to achieve better high temperature performance.

The doped fibre under test, initially Er-doped, is fusion-spliced to a plain 1550nm single mode fibre. The latter fibre is connected to the 980/1550nm arm of a 980/1550nm wavelength division multiplexer (WDM) which has an isolation of 23dB against 970-990nm and 26dB against 1540-1560nm in the 1550nm and 980nm arms respectively. The sensor head, along with part of the transmission fibre, is loosely placed inside a fused quartz sheath, to minimize any stress caused by mismatching between the fibre and the sheath. The resulting test probe is inserted into a thermostatically-controlled oven or freezing mixture to yield the required calibration temperature.

The excitation light (from, for example, a LD in Figure 1) is coupled into the 980nm arm of a 980/1550nm WDM. Preliminary tests of this experimental arrangement have been carried out, using 650nm, 800nm and 980nm laser diodes as well as an argon-ion laser operating at 514nm as excitation sources. Here, for light sources other than 980nm, the 980/1550 WDM works as an 1×2 fibre coupler. The setup demonstrated that Er fluorescence could be efficiently excited at these wavelengths. However, the argon-ion laser offers little prospect for practical applications due to its bulky size and inflexibility in operation. Thus, after this preliminary test, all subsequent experiments were carried out using the laser diode sources only.

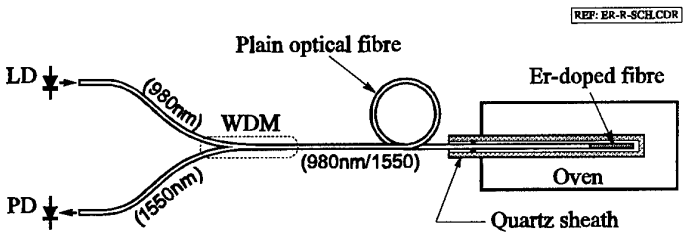

Figure 1: Opto-electronic arrangement for the measurement of the fluorescence characteristics of Er doped fibres.

More than 90% of the Er fluorescence passed to the 980/1550nm arm of the WDM, in the band 1540-1560nm, and was guided into the 1550nm arm. It was detected by an InGaAs photodiode with a spectral response from 1100nm to 1700nm, and the fluorescence decay signal was processed using the phase-locked detection technique or was recorded for waveform analysis by a desktop computer via an analog-to-digital converter (A/D).

3. Characterizing the Er-fibre sensor system

A number of tests were carried out on the Er-doped fibre probes, in order to investigate more fully and extensively their performance, extending from that reported in the preliminary work of the authors[5].

3.1 Initial Calibration

Temporal decay waveforms of the fluorescence in Er-doped fibres of three different ion concentrations were obtained. Before being subjected to high temperatures, the fluorescence decay of the three doped fibres of different concentrations was investigated and showed a near ideal single exponential feature. After being exposed to 950°C for ~24 hours, the single exponential feature in the temporal decay waveforms was still preserved for the fibres with low Er dopant levels. However, a small departure from the ideal single exponential feature was observed from the decay curve of the fibre with the Er dopant level of 4370ppm.

To compare the thermal characteristics of the fluorescence decay between Er doped fibres of different active dopant levels under similar conditions, probes were fabricated comprising the three doped fibre samples (Er: 200ppm, 960ppm and 4370ppm) in a quartz sheath. The results of the calibration, over the wide range from ~196°C to +950°C are shown in Figure 2 for fibres doped at 200, 960 and 4370ppm Er (all three show similar profiles displaced one from the other). Additionally, for comparison data for Nd and Tm doped fibres, obtained in a similar way, are shown.

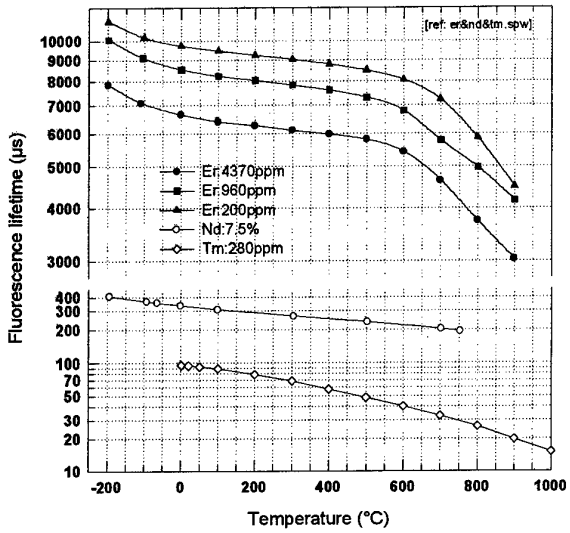

Figure 2: Thermal characteristics of Er-doped fibres which have been annealed at 950°C for ~24 hours (with other doped fibres for comparison).

3.2. Thermal cycle tests (0-1100°C)

These tests were designed to investigate the effect of annealing and thermal cycling, which had been seen to have had a profound effect upon the performance of the Nd-doped fibre and crystals or garnets in our previous work[3].

Prior to the calibration process, the Er doped fibre probe was annealed at 1100°C for ~140 hours. The change of the fluorescence lifetime during the annealing period was recorded

and depicted in Figure 3. This shows that upon reaching 1100°C, the fluorescence lifetime remains constant at ~3ms for ~30 minutes, but then it drops dramatically down to ~1.6ms. This was followed by a gradual increase in the value of the lifetime over period of ~50 hours. After that, the lifetime settled at a stabilized value of ~1.9ms and its fluctuation was within the limits equivalent to a ±5°C change in temperature, which correlated with the estimated temperature stability of the oven heater used.

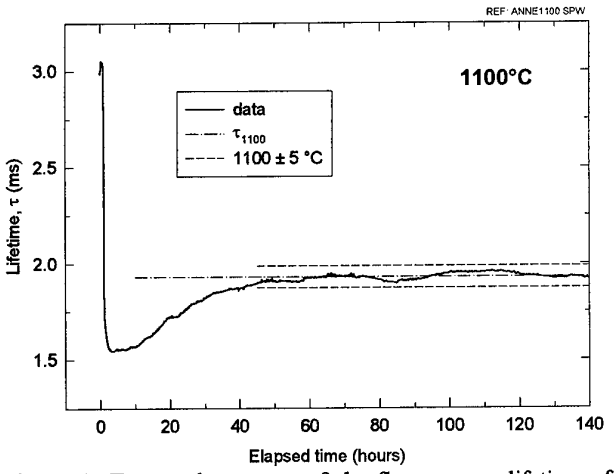

Figure 3: Temporal response of the fluorescence lifetime of the Er:200 ppm doped fibre during annealing at 1100°C.

The calibration graph of the lifetime during a series of thermal cycles from 0°C to 1100°C, taken after the annealing process, is presented in Figure 4. All lifetime data can be fitted closely to a 6th order regression curve as is shown in the figure. Deviations of these data from the regression fit are depicted in the upper graph of the figure. They are within the region equivalent to ±5°C changes in temperature and they show no indication of hysteresis in the lifetime measurements.

4. Discussion

In this research, the focus was upon the investigation of a stable region of operation of a doped fibre probe, over a wide range and extending to high temperatures (T>1000°C) While the Nd fibre probe showed a good response up to 750°C, attempts to use it at higher temperatures resulted in the Nd lifetime measurement becoming unstable[3] and the probe being of limited value for measurement beyond that. The results of this work confirm that the Er doped fibre can operate successfully over a wider range and at higher temperatures than the Nd-doped fibre (750°C) and consequently stable operation was observed for temperatures up to 1100°C, beyond which some drifting occurs in the measured lifetime of the fluorescence emission, setting an effective upper limit on performance. Further, stable performance in the region down to -196°C was observed, confirming the wide dynamic range of use for the probe.

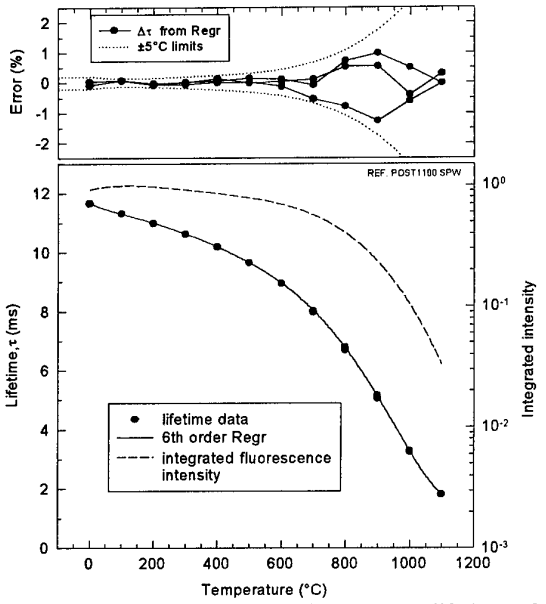

Figure 4: Thermal graph of fluorescence lifetime of the Er:200ppm doped fibre during annealing at 1100°C.

Acknowledgement

The authors are pleased to acknowledge that this work has been carried out with the support of DERA, Pyestock under Contract No. 2090/078 and valuable conversations with Graham Dadd and with Stuart Mortimer and Kevin McNicholas (Rolls Royce, Bristol).

References

1. K.T.V. Grattan, Z.Y. Zhang, *Fibre Optic Fluorescent Thermometry* (Chapman & Hall, London, 1995).
2. E. Maurice, G. Monnom, B. Dussardier, A. Saissy, D.B. Ostrowsky and G.W. Baxter, Erbium doped silica fibres for intrinsic fibre optic temperature sensors, Applied Optics 34, 8019, (1995).
3. Z.Y. Zhang, K.T.V. Grattan, A.W. Palmer and B.T. Meggitt, Potential for temperature sensor applications of highly neodymium-doped crystals and fibre at up to approximately 1000°C, Rev. Sci. Instrum. 68, 2759, (1997).
4. Z.Y. Zhang, K.T.V. Grattan, A.W. Palmer and B.T. Meggitt, Spectral characteristics and effects of heat treatment on intrinsic Nd-doped fiber thermometer probe, Rev. Sci. Instrum., accepted for publication, (1998).
5. Z.Y. Zhang, K.T.V. Grattan, A.W. Palmer, B.T. Meggitt and T. Sun, Fluorescence decay-time characteristics of erbium-doped optical fiber at elevated temperatures, 68(7), 2764, (1997).

FO Hydrophone with Hydrostatic Pressure Compensation: comparative experiment with a conventional piezo hydrophone

L.K. Cheng and D. de Bruijn

TNO Institute of Applied Physics (TNO/TPD)
PO Box 155, 2600 AD Delft, The Netherlands
Tel: +31 15 2692000, Fax: +31 15 2692111
E-mail: cheng@tpd.tno.nl

1. Introduction

This paper presents the performance of a TPD FO hydrophone with Hydrostatic Pressure Compensation. In particularly a comparison with a conventional piezo hydrophone system is discussed.

2. Sensor design

The TPD hydrophone is based on a flexural disc [1]. In the disc type of FO hydrophone, the sensing leg of a FO interferometer is coiled and fixed firmly on the disc. Pressure sensing by the disc type of FO hydrophone is based on the bending induced surface strains of the disc due to uniform pressure. This simple design can be easily extended to a push pull system and/or an acceleration canceling system [2].

Sensitivity of the disk type of FO hydrophone
In a FO hydrophone, the normalized sensitivity S_n is defined as the ratio of the strain ε in the sensing fiber and the applied pressure p:

$$S_n = 0.78\frac{\varepsilon}{p}, \qquad (1)$$

where the factor 0.78 is a result of the photoelastic effect of strain in the fiber. For the disc type of FO hydrophone, S_n depends on the flexibility of the disc while the absolute sensitivity S_a is proportional to the product of S_n and the length L_s of the sensing fiber. An higher absolute sensitivity can be achieved by either an higher normalized sensitivity or a longer sensing fiber.

The length L_s of the sensing fiber in a fiber coil with inner radius b, outer radius c and a fiber diameter D can be calculated as:

$$L_s = \frac{\pi}{D}(c^2 - b^2)\,. \qquad (2)$$

The fiber diameter D and the inner radius b are determined by the properties of the commercially available fiber. So, the length of the sensing fiber is determined by the outer radius c of the coil. In the disc type of FO hydrophone, the outer radius of the coil is restricted by the radius of the disc. Since a large size of the FO hydrophone is usually undesirable, the length of the sensing fiber is limited. (For example, for c = 15 mm, b = 5 mm and D = 135 μm, L_s is calculated to be about 4.6 m)

Provided the length of the sensing fiber is limited, the absolute sensitivity in a disc type of FO hydrophone can only be increased by an higher normalized sensitivity. However, an higher normalized sensitivity will limit the operation pressure.

Limited operation pressure
In the conventional FO hydrophone designs, the sensor is not able to distinguish the acoustic pressure from the hydrostatic pressure which is caused by the operation depth. The problem of a limited operation pressure is caused by the fact that optical fiber has a limited maximum strain of about 1%. Regarding Eq. (1), the maximum operation pressure of the FO hydrophone has to be lower than the pressure $P_{1\%}$ which corresponds to a strain of 1% in the sensing fiber ($P_{1\%} = 0.0078/S_n$). Consequently, a FO hydrophone with an higher S_n will reach the 1% strain at a lower pressure. In Fig. 1 the relation between $P_{1\%}$ and S_n is shown. For a certain level of maximum operation pressure, the normalized sensitivity is limited.

3. FO hydrophone with Hydrostatic Pressure Compensation

To solve the problem of a limited sensitivity due to a desired maximum operation pressure, we invented an Hydrostatic Pressure Compensation (HPC) mechanism. This mechanism is implemented in among others our M8c FO hydrophone. The M8c has an high normalized sensitivity of about -280 dB re 1/μPa [3]. The HPC is found to have no noticeable influence on the normalized sensitivity while the maximum operation pressure is increased from 0.7 MPa to more than 3.5 MPa. The normalized sensitivity of M8c is measured as a function of the hydrostatic pressure and shown in Fig. 2.

4. Comparative experiment between a FO hydrophone with HPC and a conventional piezo hydrophone system

In 1997 we performed a comparative experiment between one of our FO hydrophones with HPC and a conventional piezo hydrophone. The response the two systems for a pressure change with an high amplitude is recorded. During the measurement both hydrophones are put in a pressure tank and a 200 Hz acoustic signal is applied to the hydrophones (Fig. 3). The output signal of both systems are displayed in Fig. 4.

At the beginning of the experiment, the pressure in the tank is set at 2.5 MPa. The 200 Hz acoustic signal is detected by both systems. At t=T0, we opened the valve of the pressure tank, water flowed out of the pressure tank and the pressure in the tank declined. At t=T1, when the pressure is dropped to about 0.8 MPa, the valve is closed. Between T0 and T1 the pressure is assumed to be decreasing gradually while at T0 and T1 there was a sudden change in the pressure.

Regarding the piezo hydrophone system, the sudden change in the pressure at T0 and T1 results in an abrupt change in the output signal. During the pressure change from 2.5 MPa to 0.8 MPa between T0 and T1 (about 5 seconds), the piezo hydrophone system was not able to detect the 200 Hz acoustic signal. More important is that even a few seconds after the sudden pressure change at T1, the piezo hydrophone system was still not capable to detect the 200 Hz acoustic signal. It took up to t=T2 (T2-T1 = about 7 seconds) before the piezo system was fully recovered.

The pressure change from 2.5 MPa to 0.8 MPa between T1 and T0 has no visible influence on the 200 Hz output signal of the TPD FO hydrophone system. Even the sudden change in the pressure at T0 and T1 did not have any noticeable effect. The 200 Hz acoustic signal is found to be detected during the whole experiment. This advantage of the TPD FO hydrophone in comparison to the conventional piezo hydrophone system could be of overriding importance in critical situations. Detailed investigation of this effect is planned in early 1998.

5. Acknowledgement

The authors would like to acknowledge the Royal Netherlands Navy who funded the FO hydrophone research.

References

1. Brown D.A., et al., "Fiber Optic Flexural Disk Microphone", Proceedings of SPIE, Vol. 985, pp. 172, 1988.
2. Brown D.A., et al., "High-Sensitivity, Fiber-Optic, Flexural Disk Hydrophone with Reduced Acceleration Response", Fiber and Integrated Optics, Vol. 8, pp. 169, 1989.
3. Cheng L.K. and de Bruijn D., "Fieldtest of a Fiber Optic Hydrophone", 11th International Conference on Optical Fiber Sensors, pp. 184, 1996.

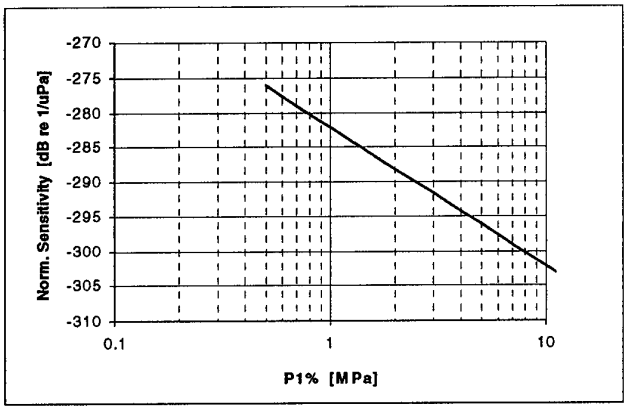

Figure 1 Relation between the norm. sensitivity and the pressure which corresponds to a strain of 1% in the optical fiber.

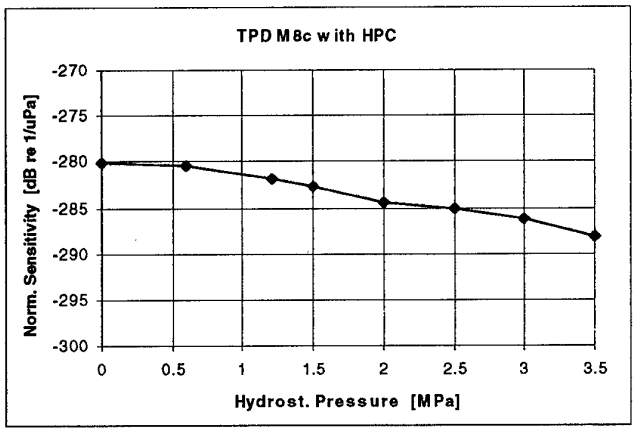

Figure 2 The norm. sensitivity of the M8c with HPC as a functie op the hydrostatic pressure.

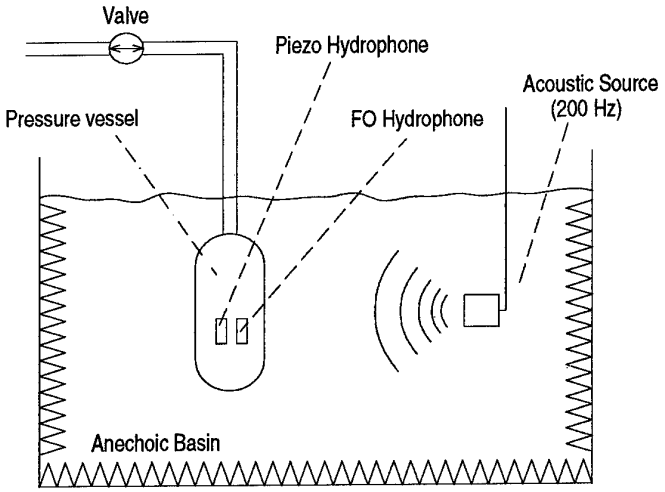

Figure 3 Experimental configuration.

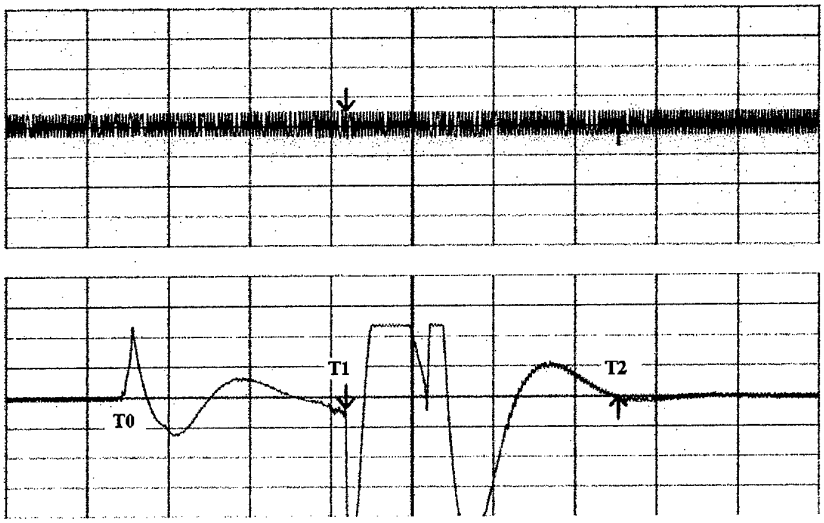

Figure 4 Influence of rapid change in pressure on the operation of the TPD FO hydrophone with HPC (upper figure) and a conventional piezo hydrophone (lower figure). During the experiment, a 200 Hz acoustic signal is applied to the two sensors The scale of the time-base is 2 seconds per division and the scale of the vertical axis is 1 Volt per division.

Accuracy-enhanced compensated optical fibre two-dimension microdisplacement transducer based on direct intensity modulation

M.A. Morante, A. Cobo, J.L. Arce-Diego, and J.M. López-Higuera
Photonic Engineering Group - University of Cantabria
Avda. Los Castros s/n, Santander 39005 Spain
Tel.: + 34 42 201539, Fax: + 34 42 201873
E-mail: morante@teisa.unican.es

Several industrial applications require precise microdisplacement measurements. Optical intensity modulated sensors are very suitable to meet these needs because they are simple and cost-effective. Many have been presented that monitor one-dimension displacement in the direction of the optical axis of the system [1]. Some lateral displacement sensing methods are based on quadrant or dual detectors [2], and others are based on reflective approaches that require microprocessing systems in order to obtain the two-dimension position [3, 4]. In this paper, we present a detection scheme for monitoring 2-D displacements that is based on direct intensity coupling between fibres. It can be used in industrial applications such as displacement, position, acceleration, or pressure sensors. Both the transducer head and the associated optoelectronics are very simple to construct and they employ inexpensive components. It is not sensitive to ageing and temperature effects, and its measurements have little error that can be improved by adequate selection of the coupling characteristics of the fibres. We prove the influence of the modulation function on the accuracy of the transducer, and show the way to minimise the output error.

The sensor head is composed of five optical fibres, that are depicted in Fig. 1 together with the X and Y axis. The in-plane movement to be detected changes the position of the illuminating fibre end with respect to the four-fibre collecting arrangement. The x and y position parameters are obtained from the light coupled from the former into the latter. As the operating displacement range is centred on the (0,0) position, the working zone in the coupling curve is the same for the four receiving fibres, so they all have the same modulation function. Besides, the collecting fibre bundle is easy to realise in practice by including the fibres in a tube with an inner diameter equal to $1+\sqrt{2}$ times the diameter of the fibres. The in-plane position of the emitting fibre, $P(x,y)$, is given by the following expressions:

$$x = \frac{1}{2\sqrt{2}}\left(d_3^{\,2} - d_1^{\,2}\right) \tag{1a}$$

$$y = \frac{1}{2\sqrt{2}}\left(d_4^{\,2} - d_2^{\,2}\right) \tag{1b}$$

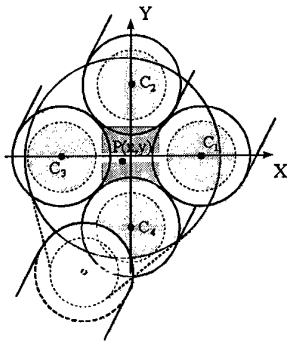

Figure 1. Optical transducer head for measuring the two-dimension position of the illuminating fibre end with respect to the fixed four-fibre arrangement.

where d_1, d_2, d_3, and d_4 are the transverse distances from the illuminating fibre to the four collecting ones, and can be approximated by a linear function of the four detected voltages:

$$d_i = mV_i + n, \qquad i = 1,2,3,4 \tag{2}$$

Eq. (2) is the modulation function of the transduction process, and it has been obtained by linearisation of the coupling curve within the working zone, which is limited by the minimum and maximum transverse distances that can be reached in the measuring range.

The transduction scheme presented in this work implements an approximation of Eqs. (1) that avoids the squaring of the detected signals and makes the output insensitive to environmental changes. The expression for the x parameter is:

$$x = \frac{1}{2\sqrt{2}}\rho\left(\frac{V_3 - V_1}{V_3 + V_1}\right) \tag{3}$$

where ρ is a weakly variable parameter that is substituted for a constant as follows:

$$\rho = (d_3 + d_1)(d_3 + d_1 - 2n) \cong 2d_0(2d_0 - 2n) \tag{4}$$

d_0 is the transverse distance from the (0,0) position to the receiving fibre centres, and has a value of $1/\sqrt{2}$ in length units normalised to the diameter of the collecting fibres. The maximum error of the approximation occurs at the corners of the two-dimension position range, $(\pm\Delta/2, \pm\Delta/2)$, Δ being the amplitude of the maximum displacement permitted on each axis. Such error can be expressed:

$$\begin{aligned}\delta\rho = &\left\{\left[\left(\frac{1}{\sqrt{2}} - \frac{\Delta}{2}\right)^2 + \left(\frac{\Delta}{2}\right)^2\right]^{1/2} + \left[\left(\frac{1}{\sqrt{2}} + \frac{\Delta}{2}\right)^2 + \left(\frac{\Delta}{2}\right)^2\right]^{1/2}\right\} \times \\ &\times\left\{\left[\left(\frac{1}{\sqrt{2}} - \frac{\Delta}{2}\right)^2 + \left(\frac{\Delta}{2}\right)^2\right]^{1/2} + \left[\left(\frac{1}{\sqrt{2}} + \frac{\Delta}{2}\right)^2 + \left(\frac{\Delta}{2}\right)^2\right]^{1/2} - 2n\right\} - \sqrt{2}\left(\sqrt{2} - 2n\right)\end{aligned} \tag{5}$$

The relative error in x is the same as the relative error in ρ, as they are linearly related by Eq. (3), and can be obtained by dividing (5) by $\sqrt{2}\left(\sqrt{2} - 2n\right)$. The main feature of this error is that it depends on the value of the n coefficient in the modulation function, and it can be considerably reduced by appropriate election of the optical coupling curve. Fig. 2 shows the magnitude of the approximation error as a function of the value of n, for three different

measuring ranges: 0.1, 0.2 and 0.3, in normalised length units. The error can be made negligible if the independent coefficient in Eq. (2) is about 1.4, and it can be significant if the value of n is far from this number. Therefore, the modulation function makes a great difference in the performance of a sensor using this detection scheme, and special attention must be paid on the direct coupling characteristics of the optical fibres employed.

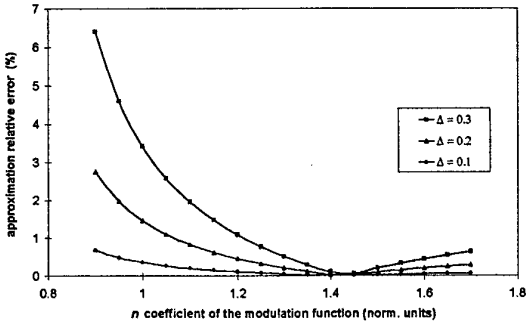

Figure 2. Approximation error as a function of the n coefficient in the modulation function for some measuring ranges.

The modulation functions for several multimode optical fibre pairs and different axial distances between them were measured, and practical conclusions were extracted. The coupling curves were taken by varying the transverse distance in 1-micron steps and averaging the measurements in 12 directions in the transverse plane. Relative power measurements were made by dividing the coupled light power by the emitted one. The position of the illuminating fibre was changed by means of a four-degree-of-freedom computer-controlled micropositioning system. The mode distribution was stabilised and uniformed both before and after the coupling procedure. The schematic of the complete laboratory set-up employed is shown in Fig. 3, and a picture is displayed in Fig. 4. Various types of fibres, both illuminating and collecting, were tested, and their modulation functions were obtained. Fig. 5 shows two of them, along with their mathematical expressions for a measuring range amplitude of 0.3. Taking into account their n coefficients, the approximation error for the first transducer is 3.5 %, while the error of the second one is 1.4 %. We also obtained that the longer the axial offset between fibres the larger the value of n, and that a larger illuminating fibre helps make the n coefficient closer to the ideal value. In order to minimise the approximation error the emitting fibre core should be large, and the longitudinal distance to the collecting bundle must be 6 or 7 times the receiving fibre size. The linearity error is 1.2 % and 0.6 %, respectively, for the two mentioned modulation functions.

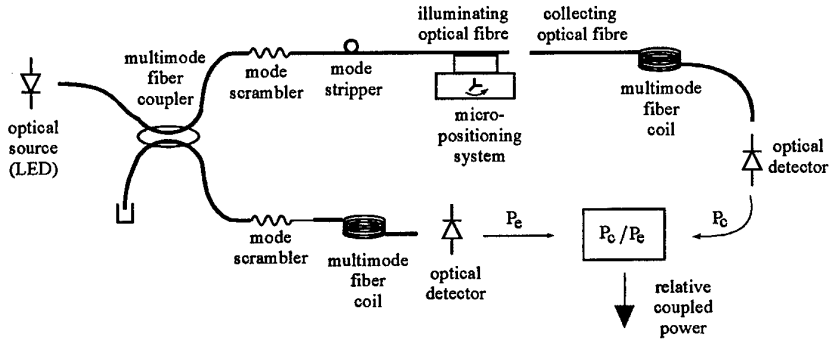

Figure 3. Schematic of the experimental set-up for the measurement of the optical intensity coupling between fibres.

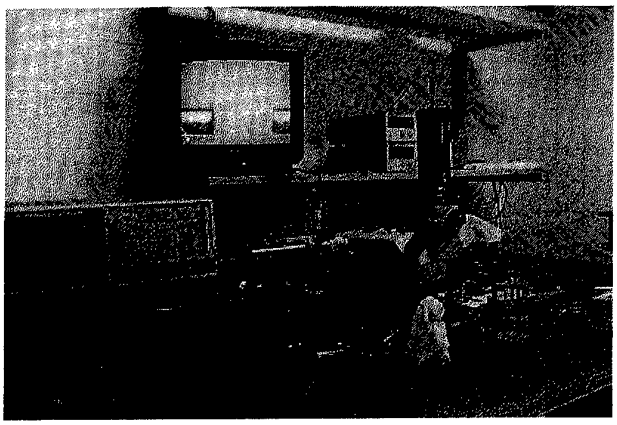

Figure 4. Laboratory set-up for measuring the direct coupling function between optical fibres.

Finally, the detection scheme is not sensitive to environmental and external factors, because they affect the two voltages in Eq. (3) equally. The proportionality factor in both electric signals derived from environmental effects, such as a change in the light emitted by the source or in the light lost due to fibre bending or in the gain of both photodetectors, is removed from the division and does not alter the value of x. Therefore, this transducer compensates for intensity variations that are not related to the transduction process implicitly, that is, without the need of a reference arm that monitors the intensity within the system. The y parameter has the same treatment than the x position.

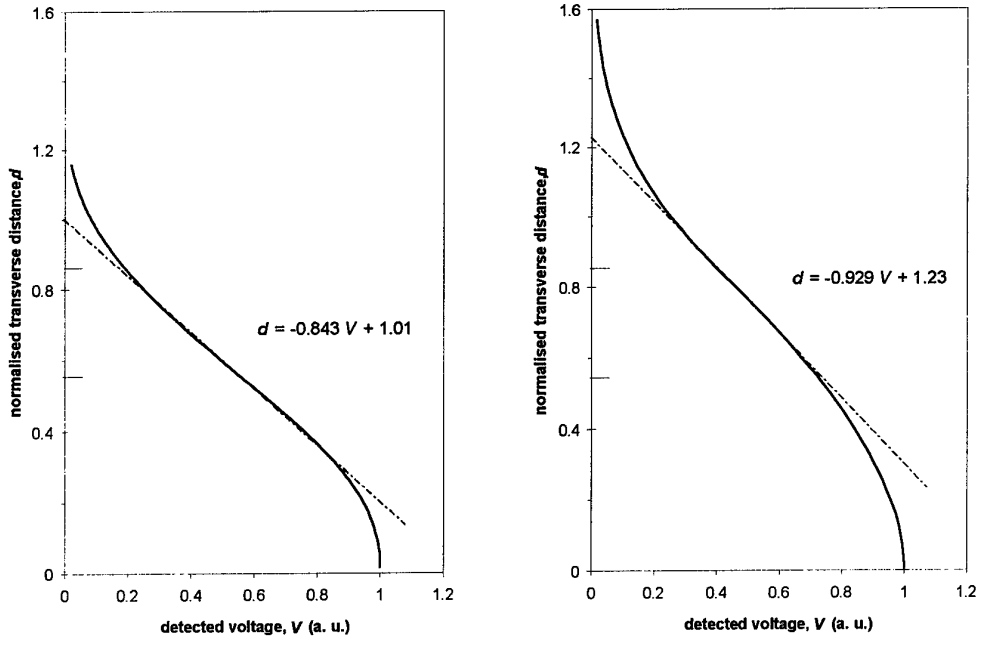

Figure 5. Experimentally obtained coupling curves and their associated modulation functions for a measuring range of 0.3. a) Coupling between two 100/140 fibres at an axial distance of 500 μm; b) Coupling from a 200/240 fibre into a 100/140 one separated 700 μm.

To sum up, a four-fibre collecting arrangement has been studied that can be used in a two-dimension position transducer with high accuracy and potential low cost. Although based on intensity modulation, it is not sensitive to temperature effects or fibre channel losses, due to its compensating detection scheme. A method of minimising the measurement error, consisting in the adequate selection of the optical fibres and their axial distance, has been developed. It allows to build a fibre sensor with very simple implementation and low error, that can be used either in static measurements, such as displacement or pressure, or in dynamic ones, such as velocity or acceleration.

The authors acknowledge support from the CICYT TIC95-0631-C04-01 project.

References

[1] Wang, D.X., Karim, M.A., and Li, Y., "Self-referenced fiber optic sensor performance for microdisplacement measurement". *Opt. Eng.*, Vol. 36, No. 3, pp. 838-842, 1997.

[2] Remo, J.L., "High-resolution optic displacement measurement using a dual-photodiode sensor". *Opt. Eng.*, Vol. 36, No. 8, pp. 2279-2286, 1997.

[3] Johnson, M., and Goodman, G., "One- and two-dimensional, differential, reflective fiber displacement sensors". *App. Opt.*, Vol. 24, No. 15, pp. 2369-2372, 1985.

[4] Braunschweiler, A., Llosas, P., Bertholds, A., and Baur, C., "Optical position sensor for automatic microassembling operations". *Opt. Eng.*, Vol. 34, No. 9, pp. 2660-2664, 1995.

ANALOG OPTICAL U-SHAPED FIBRE TRANSDUCER BASED ON INDEX MODULATION FOR QUASIDISTRIBUTED SENSING

J.L. Arce-Diego, J. Echevarría-Cuenca, M. A. Morante, A. Cobo, F. Madruga, M. Lomer, and J.M. López-Higuera
Grupo de Ingeniería Fotónica, Departamento de Tecnología Electrónica Ingeniería de Sistemas y Automática, Universidad de Cantabria, Avda. Los Castros s/n, 39005 Santander, Spain. Phone. +34-42-201498, Fax. +34-42-201873.

I.- INTRODUCTION

Optical time domain reflectometry (OTDR) is a very useful tool used in optical fibre communications and in sensor networks. The cost of an OTDR instrument prohibits sometimes its use in fibre optic sensor networks. Desforges et al[1] presented a scheme that allows the monitoring of 10 to 50 on/off microswitches along a fibre in industrial environments using retroreflected light. Detection of retroreflected rather than backscattered light improves the number of multiplexed sensors[2]. In this communication we present a retroreflecting analog optical fibre transducer for measuring physical parameters by OTDR. This transducer has a U-shaped single curve fibre optic. It is made of silica glass fibres in order to realise long distance measurement capability as well as to provide durable sensors. This transducer is all optical, it does not have any mechanical moving parts. It is analog, not on/off. It is low cost and easy to implement. First, the transducer structure, the principles of operation and preliminary experimental results in a transmissive scheme are presented. Then the transducer in a retroreflective scheme is evaluated. Finally, a prospective of use in quasidistributed measurements employing automated and optimised OTDR techniques is done.

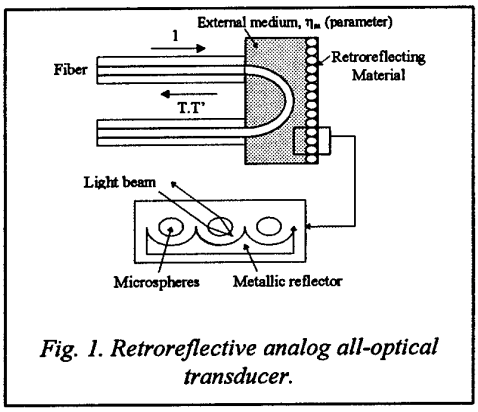

Fig. 1. Retroreflective analog all-optical transducer.

II.- TRANSDUCER DESCRIPTION. PRINCIPLES

Fig. 1 shows the transducer structure and principle of operation in which the fibre is stripped of its cladding along a certain length and the stripped section is further bent into a U shape. A retroreflecting material[3] is placed opposite to the bend. This material is composed of glass microspheres (3M) that reflect the incident optical radiation in a direction that goes parallel to the incident one. Therefore, by introducing between the bent fibre and the retroreflector an external optical medium with a refractive index n_m depending of the measurand, the light can be extracted from the core to the external medium, and then retroreflected into the fibre core, even if the retroreflector is not perpendicular to the incident light. The very low lateral offset between incident and retroreflected rays, due to the very small diameter of the glass microspheres, allows the light to be launched back into the fibre core. Since the critical angle is given by $\psi_c=\sin^{-1}(n_m/n_{co})$, assuming n_{co} and n_m are the refractive indices of the fibre core and the surrounding material, respectively, the light output from the fibre and after launched back into the fiber core is a function of n_m.

III.- TRANSMISSIVE TRANSDUCER: EXPERIMENTAL RESULTS

Transmissive transducer without retroreflection was previouly studied[4], and following that analysis the transmissive transducer was simulated, constructed and experimentaly evaluated. In order to verify its performance in the retroreflective scheme, a transducer using a material with temperature index dependence was made. A 350 μm radius transducer was fabricated with the aid of a conventional fusion

splicer, by means of controlling the stress applied to the fibre and the electric arc lapse time. The fiber cladding was removed and covered with silicone and its performance was verified in transmission. The experimental set-up is shown in Fig. 2. The Anritsu MG9002A laser diode launched the light at 820 nm into the transducer placed inside a climatic chamber HIGROS-15.

The output light was measured with a HP8153A power meter. The set up equipment was fully automatically controlled using the GPIB bus by a computer, which also worked as an automatic data acquisition unit. Several series of temperature cycles from 0 to 80 °C, and viceversa were done.

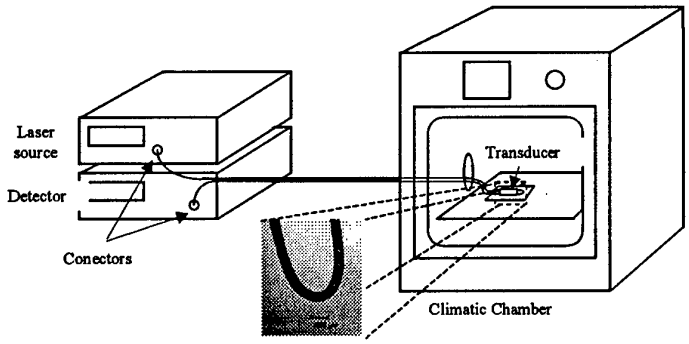

Fig 2. Set up to measure the temperature with the transmision transducer in which a detail of the developed transducer in the climatic chamber is shown.

The experimental results and their comparison with the theoretical ones, both normalised to 0 °C, are shown in the Fig. 3. In this figure the lack of hysteresis in the transducer can be seen. As the refractive index of the silicone decreases when temperature increases , n(T) = 1.4155-0.000475T (T is the temperature in °C), light loss decreases with temperature increments. The bending losses are inversely proportional to the relative increment of indices. Experimental results present a greater temperature dependence, giving a better sensitivity than the theoretical simulations.

IV.- TRANSDUCER THEORETICAL ANALYSIS IN RETROREFLECTIVE SCHEME.

Because multimode fibres are to be used for the transducer fabrication, we can analyse their characteristics using geometric optics methods. For simplicity, the transducer is assumed to have an ideal U shape, to consist of a fibre that is bent into a semicircle stripped of its cladding. The light retroreflected by the sensor head, i.e., the ratio of the retroreflected to the input light, can be obtained by tracing ray paths and calculating the reflectivities at reflection points in the transducer. It was assumed that most of the optical power of each ray is lost in the first point of intersection with the bend, P_1, the reflectivity of the retroreflector is considered to be unity, and the optical media are homogeneous and lossless. After being reflected on the retroreflector this power is launched into the fibre core going backwards to the optical input. By means of the Fresnel coefficients[5] the reflectivity and the optical power that comes out of the fibre in each point is calculated. Following the Snell law and after several complex

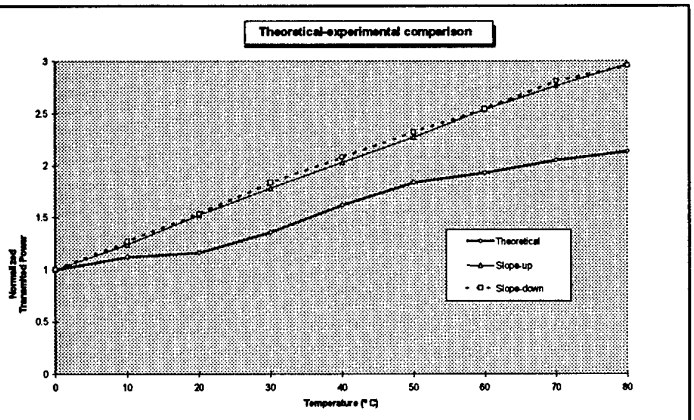

Fig. 3. Theoretical and experimental comparison for the temperature transmission sensor.

algebraic and trigonometric operations the direction vector $\mathbf{r}_i$ of the first refraction (see Fig. 4.a) is calculated as:

$$\mathbf{r}_i = \frac{n_{co}}{n_m} \cdot (\mathbf{s}_i - \mathbf{n}_i \cdot (\mathbf{n}_i \cdot \mathbf{s}_i)) + \mathbf{n}_i \cdot \sqrt{\left(1 - \left(\frac{n_{co}}{n_m}\right)^2 \cdot \left[1 - (\mathbf{n}_i \cdot \mathbf{s}_i)^2\right]\right)} \qquad (1)$$

Where $\mathbf{s}_i$ an $\mathbf{n}_i$ are the unitary vectors in the direction of the incident and the normal to the core material interface, respectively. Then, it is possible to calculate the amount of the optical power lost and it is given by the transmitance T. After been reflected by the retroreflector placed at the distance d_1 from the fibre bend the optical power that comes from the core in a direction $\mathbf{r}_i$ will be coupled again with an apposite direction $\mathbf{r}'_i = -\mathbf{r}_i$ to the exit one, see Fig. 4b. The reflected light will be incident into the optical fibre, in a point near to P_1. The percentage of optical power that is coupled in the fibre core and its direction after this reflection can be calculated. In a similar way to (1) an expression for the direction vector $\mathbf{s}'_i$ of the second refraction is obtained as

$$\mathbf{s}_i` = \frac{n_{co}}{n_m} \cdot (\mathbf{r}_i` - \mathbf{n}_i` \cdot (\mathbf{n}_i` \cdot \mathbf{r}_i`)) + \mathbf{n}_i` \cdot \sqrt{\left(1 - \left(\frac{n_{co}}{n_m}\right)^2 \cdot \left[1 - (\mathbf{n}_i` \cdot \mathbf{r}_i`)^2\right]\right)} \qquad (2)$$

Where $\mathbf{r}'_i$ and $\mathbf{n}'_i$ are the incident and the normal unitary vectors to the external medium-core interface, respectively. For this new refraction, the Fresnel coefficients are used again to calculate T', obtaining the retroreflected power for each ray as TT'. The scheme for ray tracing in the bend is illustrated in the Fig. 4.a. Assuming that, from a small area dS on one endface of the bend, a light pencil is emitted to the direction represented in spherical coordinates (θ,ϕ). The intensity of this ray is given by $dI = i_r(r) i_\theta(\theta) \cdot dS \cdot d\Omega$, where $dS = r \cdot dr \cdot d\alpha$, $d\Omega = \sin\theta \cdot d\theta \cdot d\phi$, and $i_r(r)$ and $i_\theta(\theta)$ are light intensities as functions of r and θ, respectively. Assuming the intensities of the ranges in relation to the spherical coordinates given by

$$i_r(r) = \text{constant}, \quad (0 < r < b) \qquad (3a)$$

$$i_\theta(\theta) = \cos(\pi\theta/2\chi_c), \quad (0 < \theta < \chi_c) \qquad (3b)$$

where $\cos \chi_c = n_{cl}/n_{co}$, and n_{cl} is the cladding refractive index. Thus, by summing up the light for all rays the expression for the total retroreflection coefficient of the transducer R_R becomes

$$R_R = \frac{\iint T \cdot T' \cdot i_r(r) i_\theta(\theta) dS d\Omega}{\iint i_r(r) i_\theta(\theta) dS d\Omega} \qquad (4)$$

This retroreflection coefficient R_R, has been obtained for a step-index 100/140 multimode optical fibre, with $n_{co} = 1.457$ and a numerical aperture 0.28 as a function of different curvature radius. As it is shown in Fig. 5, the retroreflected power increments as the refractive index of the external medium increases and approximates to the n_{co}. It is verified that for small curvature radius the losses also increase in the transducer. Therefore, an adequate selection of this external medium, this transducer can be applied in the measurement of physical parameters. Particularly, its application to temperature measurement was proved. Fig. 6 shows the variation of the retroreflected power with the temperature using silicone as external material. The same statement is applied to the changing of R_R with the bend radius.

The measurement of this retroreflected light instead of the backscattered by means an OTDR is more advantageous because it introduces a figure of merit M, inversely proportional to the pulse with τ and there is no trade-off between dynamic range and spatial resolution[1], but it presents the drawback of a worst resolution in commercial equipment. At present, we are working on the development of techniques that permit us, by means of getting and processing of the OTDR trace in a computer through the bus GPIB, automatise the measurements and improve the performance of these equipment in the monitoring of both reflective and retroreflective optical fibre sensors networks. Previous results have shown that up to 50 quasidistributed measurement points can be reached with a proper design.

V. CONCLUSION

A retroreflective intrinsic optical fibre probe with intensity modulation for the measurement of physical parameters has been designed. It is based in the bend losses of a multimode optical fibre immersed in a external medium with a refractive index dependent on the mesurand, and a retroreflector. The retroreflected optical power is index dependent and also dependent on the bending radius of the fibre. Its behaviour for the measurement of temperature with silicone as external medium, has been simulated and demonstrated. To increase the sensitivity of the transducer it is important to have an optical fibre without cladding and small bending radius. Experimental results obtained by the transmissive transducer are satisfactory and validate the theoretical model of the transducer.

AKNOWLEDGMENT: This work has been supported by the Spanish Ministry of Education and Science through the CICYT Project TIC95-0631-C04-01.

REFERENCES

1. Desforges F.X., Graindorge P., Jeunhomme L.B., Arditty H.J., "Progress in OTDR optical fibre sensors networks" in the Distributed Fibre Optic Sensing Handbook, J.P. Dakin Editor, Springer-Verlag, 1990.
2. J. Dakin and B. Culshaw, *Optical Fiber Sensors. Applications, analysis and future trends*, Vol. 4, (Artech House, 1997).
3. Will, S.R., " How retroreflectors really work, " Optics & Photonics News, pp. 6-7, December 1993.
Takeo T., and Hattori H., "Silica glass fiber photorefractometer," Applied Optics , Vol 31, No. 1, pp.44-50, January 1992.
4. Takeo T., and Hattori, H, "Silica glass fiber photorefractometer", Applied Optics, Vol 31, No 1, pp 44-50, January 1992.
5. A. Snyder and J.D. Love, *Optical Waveguide Theory*, (Chapman and Hall, London, 1996)

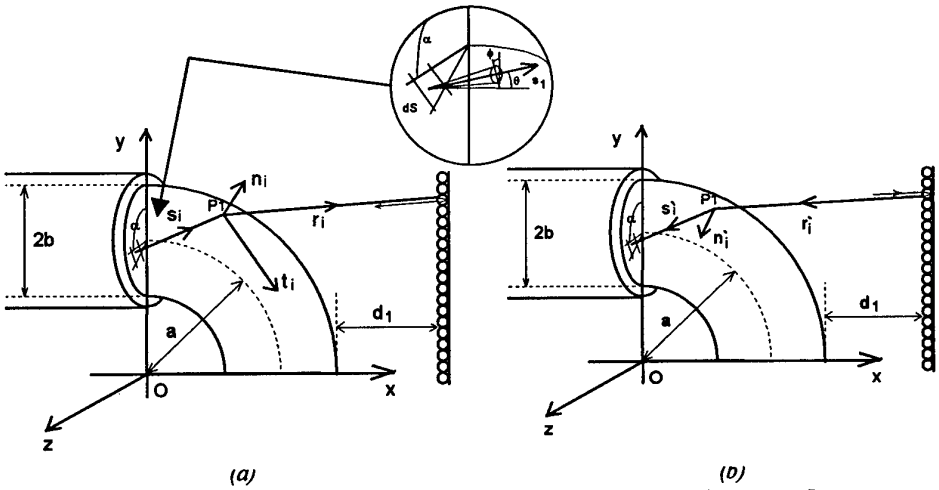

Fig. 4 a,b. Ray tracing in the (a) first and (b) second refraction in the retroreflective sensor.

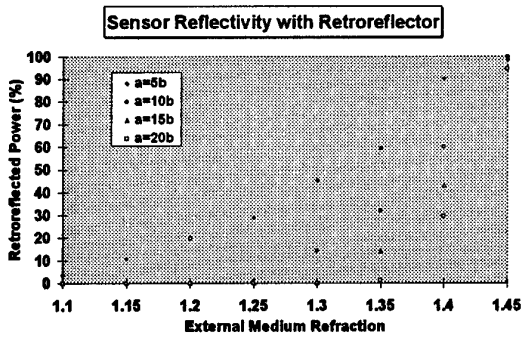

Fig. 5. Retroreflected power vs. refractive index of the external medium for several bending radius.

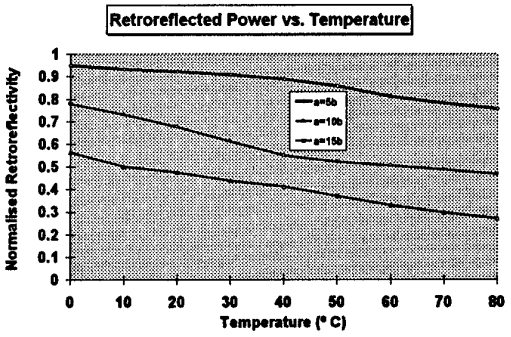

Fig.6. Retroreflected power vs. temperature for silicone.

Design aspects of alexandrite fluorescence lifetime fiberoptic thermometer

Andrej Kobe, Aleš Babnik, Janez Možina
University of Ljubljana , Faculty of Mechanical Engineering
Aškerčeva 6, 1000 Ljubljana, Slovenia
Tel. +386 61 1251161/47, Fax. +386 61 218 567, Email andrej.kobe@uni-lj.si

1. Introduction

Fluorescence lifetime based sensors have long since proven their advantages in several measurement fields, including thermometry[1]. Inherent stability to the source intensity fluctuations and possible reference-free design give them a unique position among optical sensors. However, certain issues, such as experimental design (measurement type, dynamic range) and signal processing to decode information from the fluorescence lifetime, still have to be addressed. Construction of the sensor influences response time, signal level and degree of reabsorption in the signal that introduces systematic error[2]. Detector with corresponding electronics inserts background noise, offset and discretization that all complicate an accurate determination of the fluorescence lifetime. Problems due to low signal levels have largely been solved with strong sources (lasers), new materials with high quantum efficiency and sensitive solid-state detectors.

2.Sensor probe design

All this issues have been challenged in our quest for a production of a simple yet effective and accurate temperature sensor. In a design phase, a numerical ray-tracing algorithm with Monte Carlo simulation techniques [3] has been developed in the laboratory to compare and optimise geometry of several different optical fibre sensors. Two configurations were chosen as candidates for the sensor. Two-fibre reflection type probe has been optimised for maximum SNR, with a theoretically predicted gap that closely matched our experimentally determined optimal gap. A one-fibre reflection type was the second choice, for which a modified experimental setup was arranged (see below).

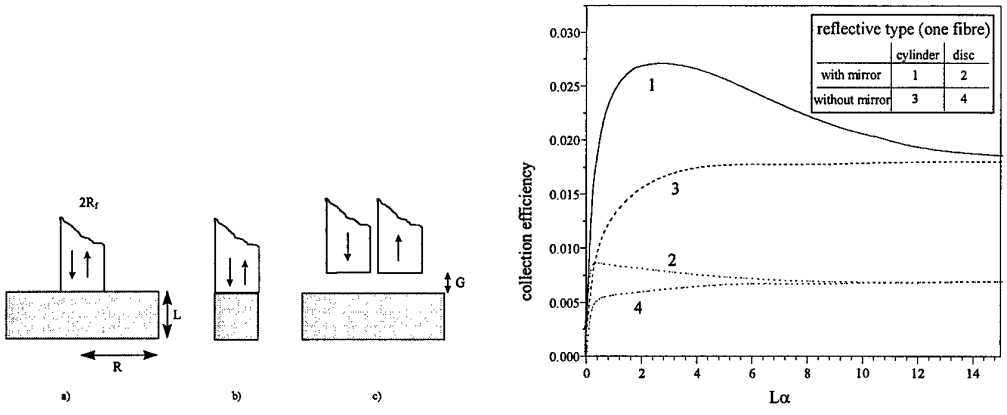

Figure 1. Two one-fibre reflection type probes and two-fibre reflection are presented. Two distinct options a) R>>Rf (disc) and b) R=Rf (cylinder) are considered with an additional option of mirror-like surface at the bottom. One-fibre probe collection efficiency is presented as a function of a dimensionless product of crystal height and extinction coefficient for excitation light.

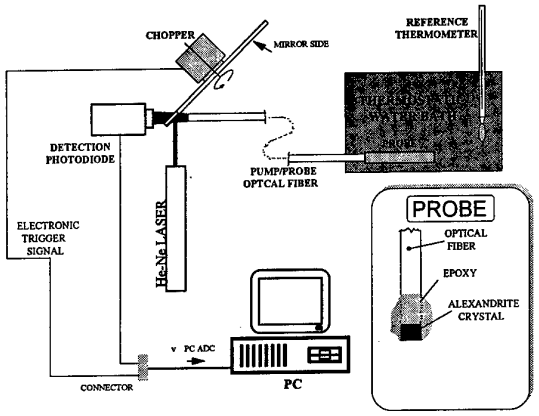

Figure 2. Experimental setup for a one-fibre reflection type sensor probe.

Thermometer has been calibrated with a Hg reference thermometer in a temperature range 20÷90°C in a thermostated water bath. In a wider range (-200°C÷220°C) K type thermocouple has been employed utilising a simultaneous dip in the dewar vessel half filled with liquid nitrogen for the cryogenic region and an oil bath for temperatures larger than 100°C. Signal from a photodiode was digitised with a PC-MIO-16E National instruments AD card (1MS/sec) and processed in a LabView environment.

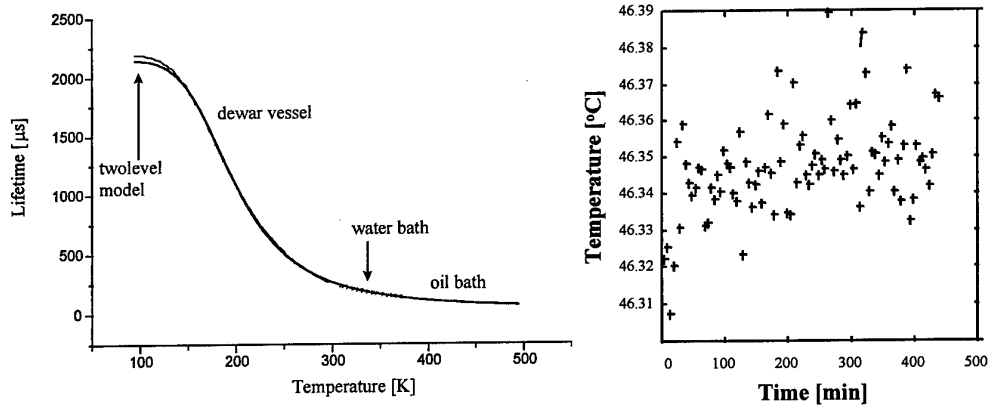

Figure 3. a) Calibration curve. Two-level model fit is superimposed on the calibration points. Discrepancy in the cryogenic region can be attributed to reabsorption effects. b) Stability representation taking measurements with sensor repeatedly dipped in thermostated water bath.

Calibration and stability are presented in Fig. 3. From the calibration curve a two-parameter model [6] coefficients were fitted. They are compared in Table 2. with the coefficients presented in literature. This device is capable of measuring around 10 measurements per second, with a response time of less than 3 sec. Reabsorption effects were confirmed only in part, changing the orientation of the crystal and observing up to 3% of lifetime change at constant room temperature. In the cryogenic region reabsorption effects play a much more important role, so additional low temperature experiments are currently on the way.

The reabsorption contribution in both types was again predicted using the modified ray tracing technique (Table 1). It can be seen that in two-fibre reflection type sensor the reabsorbed signal forms a significantly larger part of the total signal, introducing a non-exponential time dependence[2] that can severely influence the processed lifetime. The other advantage is a possible reduction of the sensing volume (observe last column) that results in a better dynamic response.

Sensor type (units in mm)	Primary rays (%)	Secondary rays (%)	Tertiary rays (%)	Collected signal (#emitted=3 10^6)
Disc $R = 3, R_f = 0.5, L=1$	89	9.7	1.2	76024
Cylinder $R=0.5, R_f=0.5, L=1$	86	12	1.8	83467
Reflection two-fibre $R=1, R_f=0.5, L=1$, Gap (around optimum) 1.2	59	23.5	10	10071

Table 1. Reabsorption data for different probe designs. Primary rays describe event when a excitation photon was absorbed and emitted fluorescence caught, whereas secondary rays describe events when emitted fluorescence was absorbed and reemitted...

3. Signal processing scheme

There are in general two ways to measure fluorescence lifetime. One is to excite sinusoidally and measure the phase lag between excitation and fluorescence[4]. Complex setup and errors due to nonlinearites and excitation leaking are disadvantages that founded our decision to use a direct method. A direct method is to excite the material for a short time, measuring the exponential decay signal when the source is shut off. Disadvantages are necessary high dynamic range and signal processing that has to take into account background offset contributions and noise. Several processing schemes have already been presented[1]. The digital integration scheme implemented in our experiment has also been thoroughly described elsewhere [5]. It is suited for on-line monitoring due to a feedback loop that is continuously locking the measurement interval width to a preset multiple of the measured lifetime. This technique, although in the present experiment completely implemented in software, has a very simple scheme that can be easily hardwired.

4.Experimental

Two sensor probe designs (Figure 1) have been verified experimentally using an alexandrite crystal (2x2x1mm). In a multiple fibre configuration a probe with a jacket, spacer and glued fibres (multiple receiving fibres to increase the signal) was constructed, whereas for one-fibre probe the crystal has been attached to the fibre with a Varian TorrSeal. To avoid using a beam splitter in a one-fibre configuration, a mechanical chopper with a silvered surface has been successfully applied (Figure 2).

Two-level model	Energy[cm^{-1}]	τ_s[μs]	τ_i[μs]
Experimental fit	842	2147±2	5.05±0.1
Grattan[6]	749	1540	6.6
Walling[7]	800	2520	7.86

Table 2. A two-parameter model coefficients.

5.Conclusions

The design of an accurate sensor has to take into account all aspects of measurement. Numerical results show us that with geometry optimisation up to threefold increase in SNR can be achieved. They also warn that though lifetime is an intrinsic quality of the material used, effects such us reabsorption can induce measured lifetime dependence on geometry, excitation wavelength etc. An alexandrite based optical thermometer is presented that gives accurate on-line measurements, with an experimental setup and the processing scheme than can be implemented cost effectively.

6. Bibliography

1. K.T.V.Grattan, Z.Y.Zhang, Fiber Optic Fluorescence Thermometry, pp. 1-19, Chapman&Hall, London (1995)

3. A.Kobe, A.Babnik, J.Možina, Reabsorption effects on calibration of fluorescence lifetime based sensors, Proc. SPIE 3099, pp. 369-375, 1997

3. A.Babnik, A.Kobe, D.Kuzman, I.Bajsič, J. Možina, "Improved probe geometry for fluorescence lifetime based temerature fiberoptic sensor", Sensors and Actuators A, 57 (3), pp.203-207, 1996

4. Z.Zhang, K.T.V.Grattan, A.W.Palmer,"Phase-locked detection of fluorescence lifetime", Rev.Sci.Instrum., Vol. 64 (9), pp. 2531-2540, 1993

5. A. Kobe, J. Možina, "Signal processing technique for proper on-line exponential decay monitoring in the presence of nonexponential and multiexponential contributions", Proc. SPIE 3100, pp. 2-8, 1997

6. Z.Zhang, K.T.V.Grattan, A.W.Palmer, "Temperature dependences of fluorescent lifetimes in Cr3+ doped insulating crystals", Phys.Rev.B, 48 (11), pp. 7772-7778, 1993

7. J.C.Walling,O.G.Peterson,H.P.Jenssen,R.C.Morris,W.W.O'Dell,"Tunable alexandrite Lasers", IEEE J. Quant. Electron., Vol. QE-16, No. 12, pp. 1302-1314, 1980

Simultaneous strain and temperature sensing using an interferometrically interrogated fibre Bragg grating written in bow-tie fibre

L A Ferreira[a], F M Araújo[a], J L Santos[b,a] and F Farahi[c]

a Unidade de Optoelectrónica, INESC - Porto
b Departamento de Física da Faculdade de Ciências da Universidade do Porto
Rua do Campo Alegre, 687, 4150 Porto, Portugal.
Tel. +351 2 6082601, Fax. +351 2 6082799, email lferreir@goe.fc.up.pt

c Physics Department, University of North Carolina at Charlotte
Charlotte, NC 28223, U.S.A.
Tel. +1 704 5472818, Fax. +1 704 5473160, email ffarahi@uncc.edu

1. Introduction

In recent years, fibre Bragg gratings (FBG) have shown an enormous potential for strain sensing in smart structures and composite materials [1]. However, temperature sensitivity of FBG can lead to significant limitations in their practical application. Besides, in most real situations, it is often desirable that both strain and temperature be measured simultaneously at pre-defined positions in the structure [2]. A few techniques have been demonstrated for temperature-strain discrimination, for example: reference FBG [3], dual wavelength FBG [4], non-sinusoidal FBG [5], FBG written in different diameter fibre [6], FBG and rocking filter [7], FBG and long period grating [8], FBG and Fabry-Perot [9], FBG and in-line fibre etalon [10]. More recently, Sudo et al. have demonstrated simultaneous measurement of temperature and strain using a FBG written in PANDA fibre by measuring the wavelength shifts corresponding to fast and slow axes [11].

In this paper, we present a demodulation scheme, based on interferometric interrogation [12], for a FBG written in bow-tie fibre. By selecting independently the polarisation corresponding to fast and slow axes, it is possible to measure the phase shifts associated with each of the Bragg wavelengths and determine the temperature and applied strain. A compact all-fibre interferometer was designed for this propose.

2. Principle of operation

In a highly birefringent fibre, two different FBG can be formed with the same spatial period Λ. This happens due to different refractive indices, n_f and n_s, corresponding to the fast and slow axes. Representing by λ_{Bf} and λ_{Bs} the Bragg wavelengths associated with each grating, the following set of equations can be written for temperature and strain dependencies:

$$\Delta\lambda_{Bf,s} = \frac{\partial\lambda_{Bf,s}}{\partial T}\cdot\Delta T + \frac{\partial\lambda_{Bf,s}}{\partial \varepsilon}\cdot\Delta\varepsilon \qquad (1)$$

This equation is only valid for limited variations of temperature and strain. For large measuring ranges, cross-sensitivity must be considered [13].

In general, similar temperature and strain sensitivities are expected for both fibre axes, since the dispersion effects are negligible for such a small difference in wavelengths. In this situation, the set of equations (1) can not be solved to obtain ΔT and $\Delta\varepsilon$. However, in bow-

tie fibre, the extra elements in the cladding introduce anisotropy stress which leads to different thermal sensitivities for fast and slow axes due to different coefficients of thermal expansion (typically a factor of three). Strain sensitivities are expected to be similar, since in this case the wavelength shifts result mainly from change in the grating period. It is therefore possible to interrogate independently both wavelength changes by using an unbalanced interferometer. The corresponding phase shifts are given by:

$$\Delta\phi_{f,s} = \frac{\partial\phi_{f,s}}{\partial T}\cdot\Delta T + \frac{\partial\phi_{f,s}}{\partial \varepsilon}\cdot\Delta\varepsilon = K_{f,sT}\cdot\Delta T + K_{f,s\varepsilon}\cdot\Delta\varepsilon \qquad (2)$$

where $\phi_{f,s} = 2\pi\cdot OPD/\lambda_{Bf,s}$ are the interferometric phases. Since a non zero matrix determinant is expected ($\Delta = K_{fT}\cdot K_{s\varepsilon} - K_{sT}\cdot K_{f\varepsilon} \neq 0$), the above equation can be inverted allowing ΔT and $\Delta\varepsilon$ to be derived.

3. Experiment, results and discussion

The experimental arrangement used to simultaneously measure strain and temperature using a FBG written in bow-tie fibre is shown in figure 1.

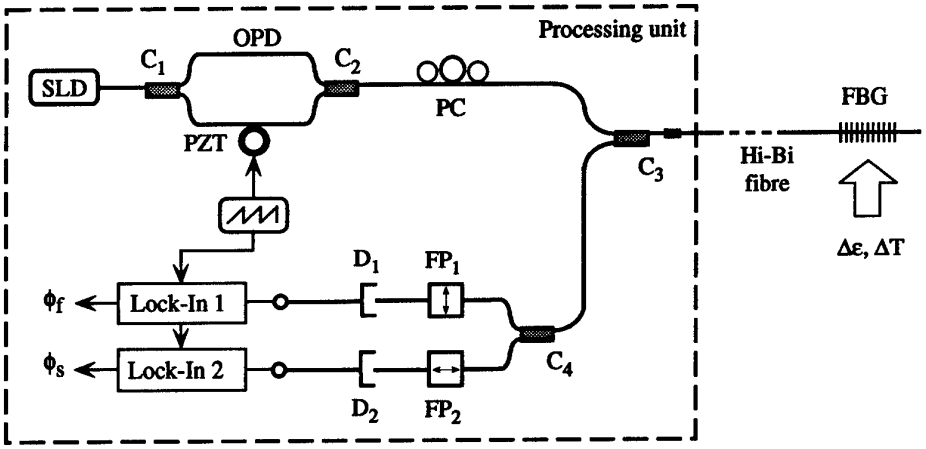

Fig.1 Experimental arrangement.

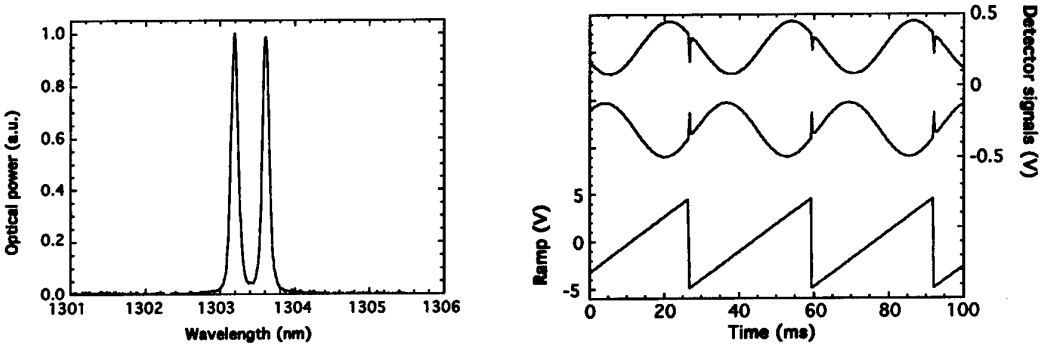

Fig.2 Light spectrum reflected by the fibre Bragg grating (a) and corresponding output carriers (b).

Light from a pigtailed superluminescent diode (Superlum SLD 561) was used to illuminate an all-fibre Mach-Zehnder interferometer with 30 cm arms and an OPD of 3.3 mm. In order to generate electrical carriers, a suitable voltage ramp signal with frequency of 30 Hz was applied to a PZT stretcher in one of the arms. Light coming from the interferometer was sent to the FBG. Because the SLD light was partially polarised, a polarisation controller was used to ensure proper illumination of both hi-bi fibre axes. The grating was written using the phase mask method in a York bow-tie fibre with $B = 5.5 \times 10^{-4}$. The obtained Bragg reflection peaks are shown in figure 2a. Light reflected from both Bragg gratings is recovered through coupler C_3 and conveniently separated in each individual polarisation state by using two in-line fibre polarisers (although C_3 and C_4 are standard 3 dB couplers, only residual polarisation crosstalk was observed). To improve the configuration, coupler C_4 and polarisers FP_1 and FP_2 could be replaced by a single polarisation fibre splitter. The two polarisation signals were then detected and their corresponding phase values were obtained using two lock-in amplifiers. Figure 2b shows both carriers together with the ramp signal used as reference for phase measurements.

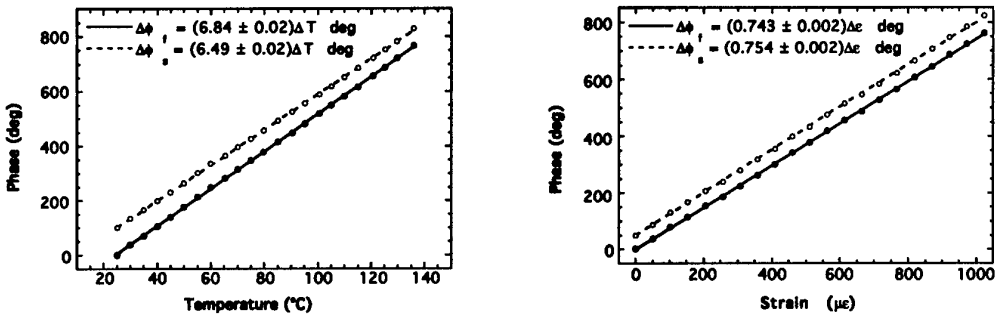

Fig.3 Sensor response to applied temperature (a) and strain (b).

To determine K_{fT} and K_{sT} in equation (2), a temperature change was applied to the FBG while keeping it unstrained. In a similar way, $K_{f\varepsilon}$ and $K_{s\varepsilon}$ were determined by keeping the temperature constant and stretching the fibre. The results are shown in figure 3. Good linearity is observable, and the obtained sensitivities are:

$$\begin{aligned} K_{fT} &= 6.84 \pm 0.02 \ \text{deg}\cdot°\text{C}^{-1} & K_{f\varepsilon} &= 0.743 \pm 0.002 \ \text{deg}\cdot\mu\varepsilon^{-1} \\ K_{sT} &= 6.49 \pm 0.02 \ \text{deg}\cdot°\text{C}^{-1} & K_{s\varepsilon} &= 0.754 \pm 0.002 \ \text{deg}\cdot\mu\varepsilon^{-1} \end{aligned} \qquad (3)$$

As expected from above considerations, the difference in the thermal sensitivities is the main responsible factor for the non zero matrix determinant: $\Delta = 0.34 \pm 0.03 \ \text{deg}^2\cdot°\text{C}^{-1}\cdot\mu\varepsilon^{-1}$. Using the values given by (3) in equation 2, we can solve for ΔT and $\Delta\varepsilon$ and write:

$$\begin{bmatrix} \Delta T \\ \Delta\varepsilon \end{bmatrix} = \begin{bmatrix} 2.22 & -2.19 \\ -19.1 & 20.1 \end{bmatrix} \cdot \begin{bmatrix} \Delta\phi_f \\ \Delta\phi_s \end{bmatrix} \qquad (4)$$

To evaluate the resolution of our system when it is simultaneously subject to strain and temperature change, the following experiment was performed. For $\Delta\varepsilon = 511 \ \mu\varepsilon$, ΔT was varied in a 100 °C range. The resulting values of $\Delta\phi_f$ and $\Delta\phi_s$ were then used in equation 4 to obtain the sensor output. Analogous procedure was followed in maintaining $\Delta T = 55$ °C and

varying $\Delta\varepsilon$ in a 1 mε range. The results are shown in figure 4a. Data in this figure indicates a maximum error of $\pm$ 1.3 °C and $\pm$ 13.5 $\mu\varepsilon$ in the determination of temperature and strain, respectively, for a system bandwidth of 0.26 Hz. An example of simultaneous measurement of quasi-static temperature and strain is shown in figure 4b (for a straight line in the $\Delta T\ \Delta\varepsilon$ plane). Figure 5 illustrates the performance of the system in a practical situation. Figure 5a shows the changes in the carrier phases as strain steps were applied while temperature was continuously changing. These data were then inserted in equation 4 in order to discriminate the instantaneous levels of temperature and strain. The results are those in figure 5b.

The results presented in this paper demonstrate the feasibility of using a FBG written in bow-tie fibre for simultaneous measurement of strain and temperature. Although the interferometric method used in this experiment and data in figure 3 suggest better resolutions than those cited above, the system performance is primarily limited by the small value of the determinant, which propagates the relatively small errors in measuring coefficients K [14].

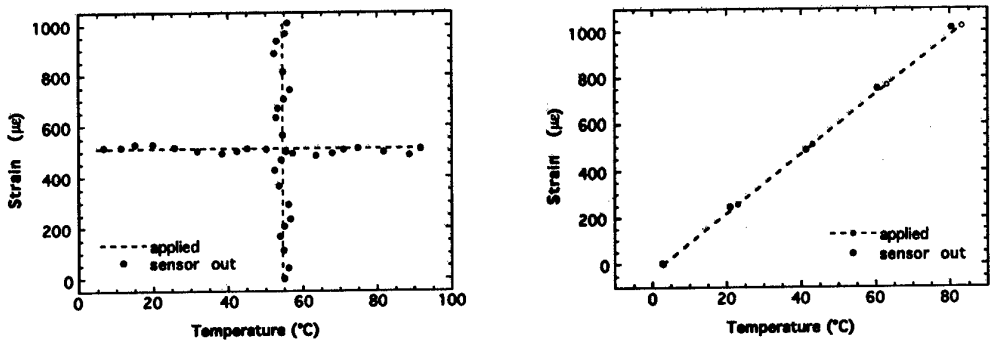

Fig.4 Sensor output as determined by equation 4 for: (a) applied strain at constant temperature and temperature changing at constant strain; (b) simultaneous change of strain and temperature.

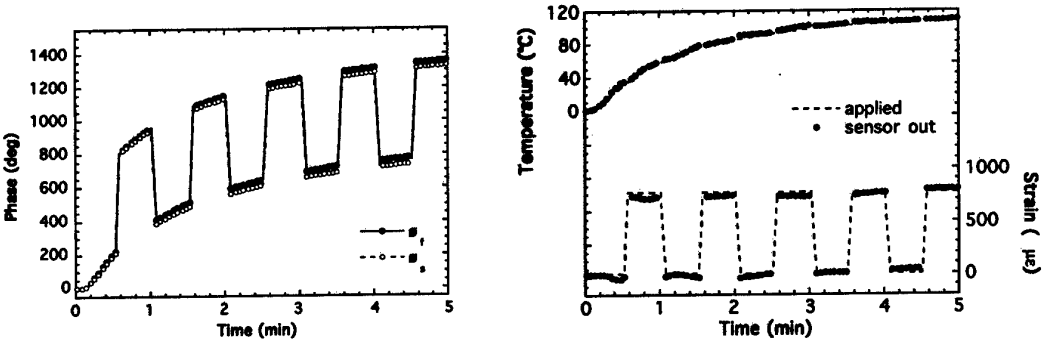

Fig.5 Sensor output for simultaneous change of strain and temperature: (a) carrier phases; (b) values of strain and temperature given by equation 4.

4. Conclusion

A demodulation scheme based on interferometric interrogation was presented for discrimination of strain and temperature simultaneously applied to a FBG written in bow-tie fibre.

Acknowledgements. L A Ferreira and F M Araújo acknowledge financial support from "Programa PRAXIS XXI". F Farahi acknowledge support from NSF grant DMI-9413966.

References

[1] Measures M R, Alavie A T, Maaskant R, Ohn M, Karr S and Huang S 1995 *Smart Mater. Struct.* **4** 20-30

[2] Jones J D C 1997 *OFS 12* 36-39

[3] Morey W W, Meltz G and Welss J M 1992 *OFS 8* **PD-4**

[4] Xu M G, Archambault J L, Reekie L and Dakin J P 1994 *Electron. Lett.* 30 1085-1087

[5] Brady G P, Kally K, Webb D J, Jackson D A, Zhang L and Bennion I 1994 *SPIE* **2839** 8-19

[6] James S W, Dockney M L and Tatam R P 1996 *Electron. Lett.* **32** 1133-1134

[7] Kanellopoulos S E, Handerek V A and Rogers A J 1995 *Opt. Lett.* **20** 333-335

[8] Patrick H, Williams G M, Kersey A D, Pedrazzani J R and Vengsarkar A M 1996 *Photon. Technol. Lett.* **8** 1223-1225

[9] Ferreira L A, Lobo Ribeiro A B, Santos J L and Farahi F 1996 *Photon. Technol. Lett.* **8** 1519-1521

[10] Singh H and Sirkis J 1996 *OFS 11* 108-111

[11] Sudo M, Nakai M, Himeno K, Suzaki S, Wada A and Yamauchi R 1997 *OFS 12* 170-173

[12] Kersey A D, Berkoff T A and Morey W W 1992 *Electron. Lett.* **28** 236-238

[13] Farahi F, Webb D J, Jones J D C and Jackson D A 1990 *J. Lightwave Tech.* **8** 138-141

[14] Jin W, Michie W C, Thursby G, Konstantaki M and Culshaw B 1997 *Opt. Eng* **36** 598-609

Two-Dimensional Bend Sensing with a Single, Multiple-Core Optical Fibre

P M Blanchard, A H Greenaway, J Burnett, P Harrison

Defence Evaluation & Research Agency, Electronics Sector,
St. Andrews Rd., Malvern, Worcs, WR14 3PS, U.K.

Tel. 01684 895080, Fax 01684 894498, email pmblanchard@dera.gov.uk

1. Introduction

The shape of a structure which is known to deform in one-dimension only can be measured using a single optical fibre with one or more sensing elements multiplexed down its length. However, to monitor the shape of a structure that can deform in three-dimensions the full vector strain, or strain field, is required. To achieve this a minimum of three fibres, embedded in a non-collinear geometry, is required. This approach is unattractive due to the difficulties and cost involved in embedding multiple fibres and because accurate knowledge of the fibre separation along their length is required for accurate shape reconstruction.

We have developed a novel vector strain sensing technique based on a single optical fibre containing multiple cores. Measurement of differential strain between the cores provides information about bend in two directions and an external reference fibre can be used to measure longitudinal strain and provide data on 3-dimensional shape. The ability to retrieve this information from a single embedded fibre will lead to a reduction of the costs associated with embedding the sensors, to a simpler and more-robust sensor design and thus an increased range of structural applications. Knowledge of the directional nature of structural strains will improve the diagnostics when monitoring the health and integrity of composite and smart structures. Use of broadband interferometric interrogation techniques[1] will allow the strain measurements to be temperature-independent, and also enable the measurement of temperature gradients within the structure.

2. Multi-Core Fibre

The interrogation of a multi-core fibre sensor is most straightforward if the cores are all single-mode and separated such that there is no significant coupling between adjacent cores. Our chosen procurement route involved a collaboration with the University of Bath to develop a technique for pulling multi-core fibres based on their, previously single-core, photonic crystal fibre structure. Photonic crystal fibre (PCF) is a novel fibre structure which is made entirely from undoped fused silica[2,3]. The fibre contains an array of holes running the entire length of the fibre, arranged in a hexagonal pattern, with a spacing of a couple of microns. This repeating refractive index structure with a period of order of an optical wavelength is called a photonic crystal. A solid silica defect is introduced into the crystal structure to act as the core of the fibre, and light is guided in this core by total internal reflection from the cladding, which effectively has a lower refractive index. Such a structure lends itself to the production of multi-core fibres, by introducing additional defects into the photonic crystal structure, and allows the core geometry and spacing to be easily varied.

PCF is fabricated in conventional drawing towers from silica preforms made by stacking identical circular silica capillary tubes into a hexagonal array. A number of capillary tubes are replaced by solid silica rods of the same diameter, to act as the multiple cores of the fibre. This structure is then processed twice through a drawing tower, resulting in a final fibre diameter of approximately 50μm. For the experiments described here a three-core PCF was fabricated. A scanning electron micrograph of the fibre end is shown in Fig. 1a, where the positions of the 3-cores can be identified by the absence of a hole. The hole pitch is ~2.5μm, the hole size ~0.38μm, the inter-core spacing ~17.5μm. Experimental characterisation of this fibre has shown the cores to be single mode and essentially uncoupled.

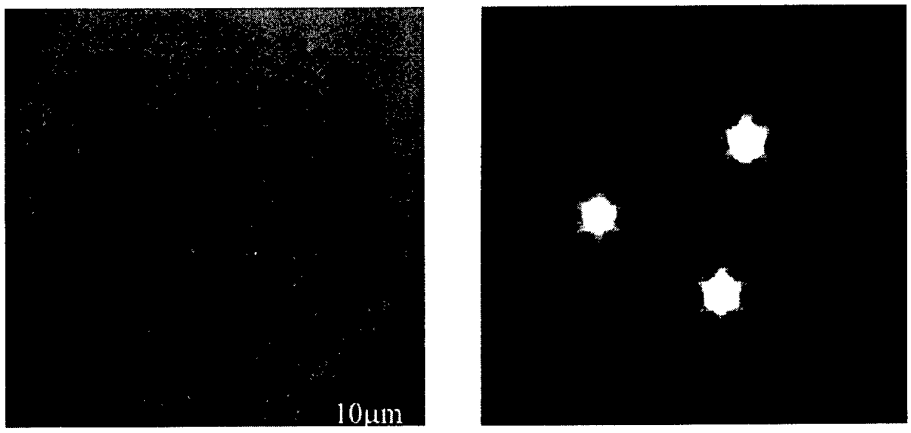

(a) (b)

Fig. 1. (a) Scanning electron microscope image of the end of a photonic crystal fibre showing three cores where a hole has been omitted. (b) Near-field pattern at the output of the 3-core fibre with all cores illuminated at 633nm.

3. Two-Dimensional Bend Measurements

When a multi-core fibre is deformed, a differential strain is introduced between cores in the plane of deformation, which in turn introduces a relative optical phase difference between light propagating in the two cores. If radiation from such a fibre is focussed by a lens and the resultant far-field interference pattern detected, the interference between each pair of cores can be uniquely identified by the period and orientation of the interference fringe produced. The relative phase between each pair of cores can be extracted by Fourier transforming the far-field fringe pattern. This interrogation approach has been used for the initial demonstration of bend sensing. Other interrogation techniques will be needed for practical implementation of multiple, well-defined sensor lengths in a single fibre. The experimental demonstration of two dimensional bend sensing described below is based on a similar experiment designed by our collaborators at Heriot Watt University.

For this experiment one end of a 30cm length of the fibre was coated with aluminium, allowing the interference fringes to be examined in reflection. The fibre was held loosely within a kevlar sleeve and placed inside a metal tube which acted as the bending element, with a bend length of 23cm. One end of the tube was fixed in a metal block and the other was attached to an x-y translation stage to allow controlled bending of the tube in two-dimensions

(see Figure 2). The end face of the fibre was illuminated with light from a laser at a wavelength of 633nm and light propagated down the fibre, reflected off the aluminium coating and back down the fibre where the far-field core-core interference pattern was imaged onto a CCD camera. The optical phase difference for each core spacing was extracted from the Fourier transform of this interference pattern.

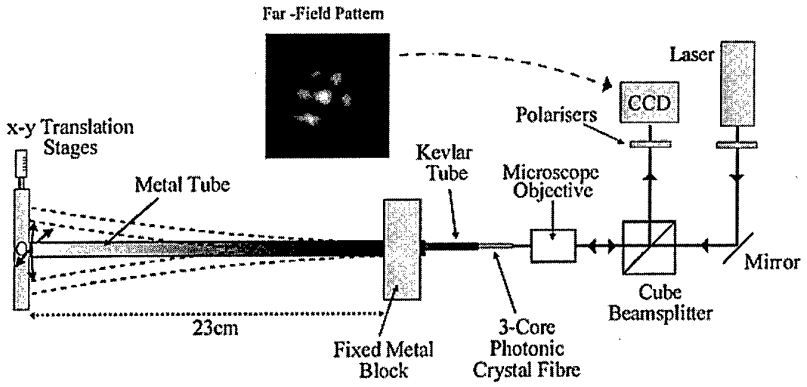

Figure 2 : Apparatus for demonstrating bend measurement with 3-core PCF

The first visual confirmation of the ability of multi-core fibre to measure 2-dimensional bend was observation of the fringes moving in different directions as the end of the tube was translated in x and y. Fringe patterns were recorded and analysed as the tube was translated in steps of 0.5mm in x and y independently. The extracted phase differences along each baseline are shown in Figure 3.

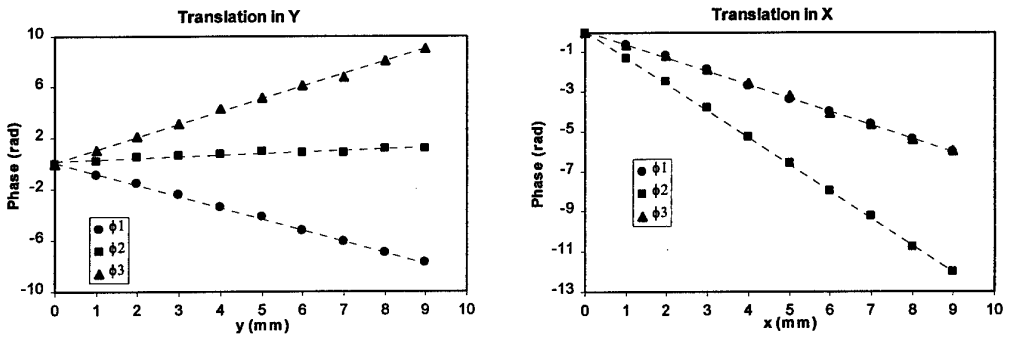

(a) (b)

Figure 3 : Variation of phase difference over each baseline, for translation of the fibre end in (a) y only and (b) x only.

In order to obtain a quantitative measure of bend sensitivity, it is convenient to convert the relative phase changes along the baselines into estimates of the orthogonal components, x and y, along which the fibre end was translated. Phase information from two baselines is needed in order to calculate x and y, and there are three possible combinations to choose from. Measurement of x and y can then be obtained by inverting three equations of the form

$$\begin{pmatrix}\phi_i\\ \phi_j\end{pmatrix} = A\begin{pmatrix}\cos\theta_i & \sin\theta_i\\ \cos\theta_j & \sin\theta_j\end{pmatrix}\begin{pmatrix}x\\ y\end{pmatrix}$$

with i,j = 1,2, i,j = 1,3 and i,j = 2,3. Figure 4 shows the results of the projection of the phase measurements onto the x and y-axes, demonstrating that x and y can be measured independently. The different combinations of baselines give very similar results and in practice the average of these three measurements could be used.

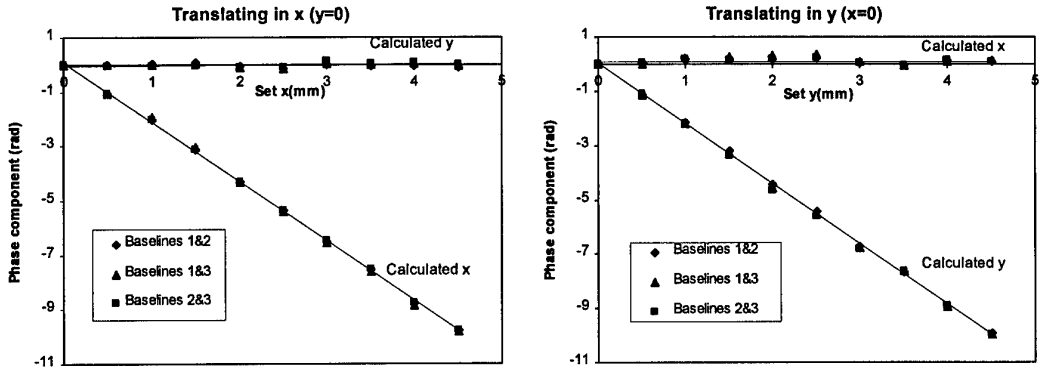

(a) (b)

Figure 4 : Projection of baseline phases onto x and y axes, for the three possible combinations of two baselines. a) Varying x only. b) Varying y only.

4. Sensitivity to Bend

Assuming that the tube and fibre bend as a cantilever, the relationship between displacement x and phase difference ($\Delta\phi$) between cores is

$$\Delta\phi = 6.84\frac{\pi x d}{\lambda L}$$

where d is the core-core separation (projected onto the x-axis) and L is the length of the sensing element. This equation predicts a phase change of 2.53 radians/mm compared to an experimental value of 2.33 radians/mm. The discrepancy between these values lies well within the tolerance range of the experimental parameters.

5. Conclusions

Two-dimensional bend sensing has been successfully demonstrated using a single 3-core optical fibre and the measured sensitivity of phase change to bend is in agreement with theoretical predictions. The technique has potential in a range of shape sensing and structural monitoring applications. Future work will include the study of multi-core fibres with different core geometries, the design of more practical interrogation approaches and means of defining sensor lengths within the fibre.

Acknowledgements

The authors acknowledge the work of P Russell, J Knight, B Mangan and T Birks at the University of Bath for the design and fabrication of the multi-core PCF, and R McBride, J D C Jones and M Gander of Heriot Watt University for extensive discussions

References

[1] D. A. Flavin, R. McBride, J. D. C. Jones, J. G. Burnett, A. H. Greenaway, Opt. Lett. **19**, 2167 (1994).
[2] J. C. Knight, T. A. Birks, P. St J. Russell, D. M. Atkin, Opt. Lett. **21**, 1547 (1996).
[3] T. A. Birks, J. C. Knight, P. St J. Russell, Opt. Lett. **22**, 961 (1997).

How to achieve the desired strain transfer for fibre-optic microdeformation measurements in cementitious building materials at early ages?

W. R. Habel* and B. Hillemeier
Institute for Rehabilitation and Modernisation of Buildings (IEMB) at the TU of Berlin

A. Bismarck and J. Springer
TU of Berlin, Institute for Technical Chemistry

Abstract
Compliant FPI-sensors were used to measure mortar deformation at very early ages with high strain resolution. An appropriate design of alternative coatings to achieve reliable bonding between fibre sensor and cement matrix is described.

Introduction and measurement task

The very high strain resolution of fibre-optic interferometer sensors can be used to detect acoustic emission events and to measure very low strain variations or deformation changes. Their small dimensions are one more reason that they are preferred as embedded sensors to measure microdeformations inside a material. In order to take full advantage, additional stress concentrations around such small sensors caused by mechanical elements, such as driving pins or lugs to achieve a better frictional joint must be avoided. A special non-reactive (non-rugged) design of the fibre Fabry-Pérot interferometer (FPI) sensor enables the investigation of the plastic shrinkage during the first few hours as well as of the drying shrinkage when the concrete has already attained its final set. Such highly resolvable strain measurements are required in laboratory research as well as on-site. They can help to prevent harmful damage in the structure's service life.

In order to substantiate such highly resolvable measurements, commonly used coatings of optical fibres must be replaced because of their instability under alkaline cement environment. As described [1], polyimide (PI)-coated fibres get cracks in their coating when they are embedded in cementitious materials. Fig. 1 confirms this behaviour. Different PI-coated fibres have been stored in aqueous concrete extract (pH = 12,4) for 35 months. The coatings seem to become embrittled in alkaline environment which will then lead to a disturbed strain transfer. And, the stressed optical fibre can break if coating pieces dig into it. From

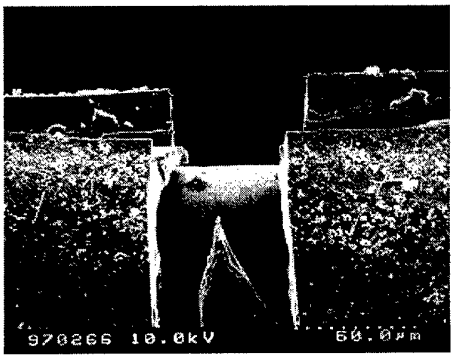

Fig. 1 Harmful influenced PI coating after storing 35 months in aqueous concrete extract.

* and Federal Institute for Materials Research and Testing (BAM) Berlin, Laboratory S. 12, D - 12200 Berlin (to whom correspondence should be addressed).

these considerations follows that, first, a fibre sensor intended for embedment needs a very thin coating which remains stable in alkaline cement environment for years. And second, this coating must ensure a good adhesion to the cement matrix. In the following is presented:

- one example of use of non-reactive FPI micro strain sensors embeddable in cementitious building materials to evaluate the initial deformation of a special grout,
- first results in manufacture of very thin alternative fibre sensor coatings for fibre-optic micro strain sensors, which guarantee the required strain transfer from the matrix to the sensor and which help, at the same time, to discourage the alkaline attack from the matrix to the surface of optical fibres and sensors.

Non-reactive measurement of initial deformation of cementitious mortars

The goal of our measurements was the optimisation of the deformation behaviour of special mortars which will take place during the early chemical hydration process in the cement gel. In order to not hinder these deformations of the plastic mortar matrix when it has not developed enough strength to deform stiff sensors, „sliding" fibre Fabry-Pérot micro interferometer sensors were embedded. The principle function of FPI sensors has been described elsewhere, e. g. in [2]. The end of the leading optical fibre (from the recording device) is able to slide very well inside the guiding tube. The leading fibre and the tube of the sensor are not additionally protected and therefore intimately washed by the mortar during embedment. The length of the tubular sensing element is about 10 mm, the outer diameter 0.5 mm. Only an axial force in the range from 0.15 mN to 0.2 mN is necessary to deform the sensor. Thus, the sensor is capable to measure displacements when the plastic cementitious material begins to deform immediately after placing. In order to achieve enough bonding between sensor and mortar, the cross-sectional area of the first sensors were slightly increased at its ends. However, this increase could influence the mortar behaviour in the interface zone to be evaluated. Therefore, alternative ways have been looked for to avoid such source of error (see below).

Fig. 2 shows the initial deformation of a special grout. It can be clearly seen that at the beginning of the hydration process the grout swells up (as expected). After about 5 hours ends the swelling process and a slight shrinkage can be observed. The degree of shrinkage after passing the maximum of expansion is an important response to characterise the grout's quality. This example demonstrates the high performance of this sensor design. The reproducibility of this method could be proved by several measurement with the same mortar sample. The sensitivity primarily depending on the wavelength of the laser source λ_S (here: λ_S = 850 nm) and the measuring device was 0.1 µm/m. Temperature changes modulates the sensing area because of the temperature-induced expansion/contraction of the glass components. The resulting faulty measurement is - 10 pm/K in terms of axial displacement and can be neglected.

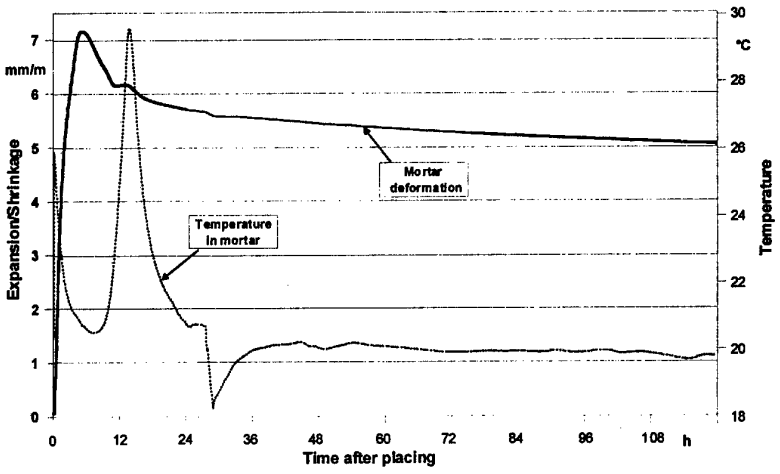

Fig. 2. Initial deformation of a special mortar for grouting of tendons in prestressed concrete structures [3]

In order to reduce further the disturbance of the mortar's microdeformation behaviour, sensors without any increasing elements should be embedded. In the following, first results in applying new methods for coating fibre-optic micro strain sensors are described.

Sensor treatment to achieve the desired strain transfer and to discourage harmful influence from the alkaline cement environment

Apart from the problem of instability of commonly used polymeric coatings of optical fibres under alkaline attacks, they show, generally, poor adhesion to the cement matrix. The e is a lack of interaction between untreated polymeric surfaces and the cement matrix. Therefore, we were looking for ways to achieve the desired strain transfer. Two ways have been gone to get satisfied bond between optical sensor element and cementitious matrix:

- Treatment of the decoated fibre surface with silane
- Coating the bare glass surface with a very thin plasma-polymer film, in a smooth as well as in a structured manner.

Silanized optical fibre surface

In order to discourage alkaline attacks from the surface of optical fibres, two special silane solutions [4] chosen of the group of hydrophobic agents commonly used for building protection have been used. The remaining rest activity of non-reacted silanol functionalities of silane bonded onto the surface may ensure chemical bonds between the modified fibres and the surrounding concrete matrix. The used silanization procedure and the characterisation of those fibres with respect to the bonding willingness of the treated fibre surface is described elsewhere [5]. It was necessary to improve the amount of silanol groups present at the fibre surface in order to guarantee a silane film onto the fibre surface as tight as possible. For this purpose, we used an oxygen plasma pre-treatment. The influence of the silane concentration to the resulting surface properties was investigated. An embedment of such modified glass fibres in a concrete matrix leads to a remarkable increase in measurable adhesive bond strength compared to polyimide-coated and chemically decoated glass fibres.

Plasma-polymerised coatings for optical fibres

An other way to create a protective coating which is suitable for embedment into concrete matrices is the deposition of a thin chemically bonded polymer film onto the surface of optical fibres. The advantages of such deposited very thin but tight fluoro-polymer network systems are that they nearly do not swell in almost all environments, and that they can partly recover the fibre strength when the usual coating had to be removed for application (e. g. when re-coated Bragg grating sensors are to be applied). It seems to be very probable that plasma polymerisation leads to bonding between the surfaces of existing cracks.

We have been created a thin polymer film onto the surface of optical fibres by using a well-known plasma polymerisation process with different freon gases/hydrogen mixtures [6]. It has been confirmed by other authors [7] that plasma films are highly adherent to glass and metal surfaces. The physico-chemical properties of such surfaces can be adjusted by controlling the chemical composition of the polymer (via the gas mixture). The thickness (100 Å to 1 µm) and the morphology of the polymer films is controllable by variation of the polymerisation time: Short polymerisation times lead to thin films, longer times to thick and rather roughly structured polymer films. Fig. 3 shows an example of a structured coating.

In order to improve the adhesion behaviour of the obtained hydrophobic surfaces resulting from the polymerisation process, an after-treatment, e.g. in oxygen plasma, can be applied to produce oxygen-containing functional groups on the polymeric surface. These improve the wetting behaviour by increasing the surface polarity. The polymer deposited onto the surface of our optical fibres contains aliphatic as well as fluoro-polymeric parts. Contact angles vs. water ranging from 60° to 120° have been controlled.

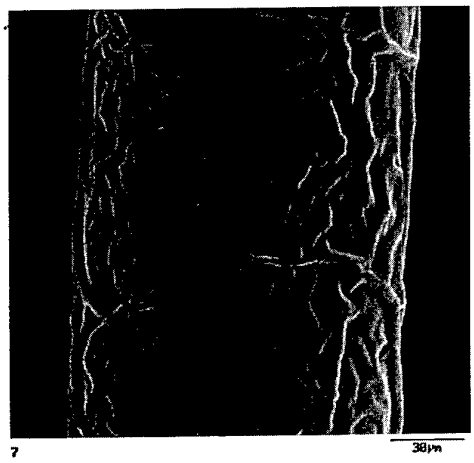

Fig. 3 Thin coatings (thickness < 1 µm) applied by plasma polymerisation

Conclusions

A compliant and embeddable fibre Fabry-Pérot interferometer sensor developed on the basis of the known EFPI sensor type enabled us to measure the initial expansion and shrinkage during the first few hours and days after placing cementitious building materials as well as over a time range of several weeks. Such sensors help to evaluate the deformation behaviour of cement mortars and other materials, especially as long as the material develops not enough strength to deform rugged sensors. An important detail to be considered is the use of an appropriate coating. Since usual polymer coating materials of optical fibres fail, alternative coatings have been manufactured and tested with regard to their physical and micromechanical properties. It could be demonstrated that silanized optical fibres ensure a better bond to the cement matrix than untreated polymer-coated fibres. An interesting method will be the use of plasma-polarised films deposited onto the surface of fibre-optical sensors. Such coatings can be designed very thin (< 1µm) and structured roughly.

By this technique one will be able to control the level of adhesion of fibre sensor coatings either to detect cracks in cementitious matrices or to measure strain profiles in large concrete components.

Acknowledgement

The investigations were partially supported by the BMFT of the Federal Republic of Germany, the Berlin Senate Administration for Science and Research, the Technologiestiftung Innovationszentrum Berlin (TSB) and by several companies: Lafarge Zement, Bilfinger+Berger Bau AG, Tricosal GmbH Illertissen and Heidelberger Zement AG. All supports are greatly appreciated. The authors would also like to thank Mrs. Dipl.-Ing. Egia Ajuriagojeaskoa (TU Berlin) for her skill in the preparation of the fibre samples and the test arrangements.

References

1. Habel, W. R.; Polster, H.: *The Influence of Cementitious Building Materials on Polymeric Surfaces of Embedded Optical Fibers for Sensors.* Journal of Ligthwave Technology. IEEE Piscataway, N. J. USA, 13(1995)7, 1324-1330.
2. deVries, M.; et al.: *Applications of Absolute EFPI Fiber Optic Sensing System for Measurement of Strain in Pre-Tensioned Tendons for Prestrained Concrete.* Smart Structures and Materials, SPIE-vol. 2446, 9-15.
3. Habel, W. R., B. Hillemeier, M. Jung; J. Plöhn and F. Basedau, 1998. "*Non-Reactive Measurement of Mortar Deformation at Very Early Ages by Means of Embedded compliant Fiber-optic Micro Strain Sensors*". will be published at the ASCE '98 Engg. Mechanics Conf., San Diego. May 1998
4. Brochure 1993. *Application of organofunctional silanes.* HÜLS AG.
5. Habel, W. R.; Schulz, E.; Kalinka, G.; Bismarck, A.: *Evaluation of Adhesion Behavior of Optical Fibers for Sensors Embedded in Cementitious Materials.* to be published at the Int. workshop on Fiber Optic Sensors for Construction Materials and Bridges, 3-6 May, 1998 NJIT, Newark, N.J.
6. Egia Ajuriagojeaskoa, E., A. Bismarck, J. Springer and W. R. Habel. 1998 "Surface-energetic investigation of modified and silanized glass fibers". (Original in French) to be published in Le Journal de Chemie physique.
7. N. Dilsiz, N. K. Erinc, E. Bayramli, G. Akovali, *Carbon*, **33** (1995) 853.

Measurement of Bending in Two Dimensions Using Multicore Optical Fibre

M. J. Gander, D. Macrae, E. A. C. Galliot, R. McBride, J. D. C. Jones
Department of Physics, Heriot-Watt University, Riccarton, Edinburgh EH14 4AS
Tel. +44 (0) 131 451 3038 Fax +44 (00) 131 451 3136 email M.J.Gander@hw.ac.uk

P. Blanchard, J. G. Burnett, A. H. Greenaway
DERA, St. Andrews Road, Great Malvern, Worcs WR14 3PS, UK

M. N. Inci, Department of Physics, Bogazici University, 80815 Bebek, Istanbul, Turkey

1. Introduction

We describe the use of a four-core optical fibre as the basis of a sensor capable of measuring the angle through which the fibre is bent in two dimensions. The intended application of the sensor is in measuring the shape of flexible structures. For example, in coherent imaging systems based on lightweight antennae, such as in towed hydrophone arrays [1], it is essential to know the shape of the structure in order to be able to reconstruct an accurate image [2].

Bending can be measured from the strain gradients in a structure. For example, the bending of a tube, i.e. magnitude and plane of curvature, could be measured from the differential strains in its walls. A minimum of three strain gauges would be required in general, as the tube can bend about two axes. The overall bend angle of a length of the tube can be measured using long gauges that integrate strain over their length. In principle, many of the reported designs of optical fibre strain sensors would be appropriate for bending measurements, although because of their unwanted temperature sensitivity it would be necessary for all of the gauges to have the same axial temperature distribution in order to yield an accurate result. Given that it is the transverse strain gradient that is required to measure bending, the gauges must maintain a constant separation along the whole length of the structure.

In this paper, we argue that multicore fibre offers a near-ideal optical sensing element for two-axis bend measurement. The fibre that we used has four single-mode cores with an accurately uniform separation of 42 μm and ensures that these cores are isothermal. We were able to make high-resolution measurements of the differential core-strains from the far-field interference pattern of light emerging from the fibre.

We previously showed[3] in principle that bend angle can be measured using a multicore fibre. Here, for the first time, we report two dimensional measurements using a practical arrangement in which the sensing element is addressed in reflection, requiring access to only one end of the fibre. Using a purpose-built bending rig, we were able to make bend angle measurements with a resolution of 100 μrad over a range of 40 mrad.

2. Bend measurement using multicore fibres

Coherent light transmitted by two cores of a multicore fibre, such as the four core design used in our experiments, will interfere in the far field to produce an interferogram whose phase will change with bending. The whole of the fibre acts as the sensor and so the phase change is

integrated over its entire length. As a result, phase change depends only on the difference in angle between the start and end of the fibre, and is independent of fibre or bend length. When the fibre is bent through an angle of $\Delta\theta$ in the plane of the two cores, the phase change $\Delta\Phi$ is proportional to bend angle, and is given by:

$$\Delta\Phi = \frac{4\pi d}{\lambda}\Delta\theta \; 1.16 \qquad (1)$$

where λ is the wavelength of light used, d is the core separation, the coefficient 1.16 is due to stress-optic effects[4] at wavelength 633 nm, and a factor of 2 is included as the sensor is double pass. When the plane of bending makes an angle of ψ with the plane containing the two cores, $\Delta\Phi$ is reduced by the factor $\cos\psi$.

Measurement of bending in two planes requires a multicore fibre with at least three cores. CNET have developed a four-core fibre for use in telecommunications, where the cores are arranged in a square[5] (fig 1). This arrangement is particularly convenient for bend measurement as the two diagonal core pairs provide independent interferograms relating to bending about two orthogonal axes.

CNET provided us with a sample of this fibre to investigate its use in bend measurement. We measured the separation of adjacent cores both using an optical microscope and by far field diffraction, obtaining a value of approximately 42 ±1 μm. Each core acts as an independent waveguide with a single-mode cut-off wavelength of around 1250nm.

3. Experiment

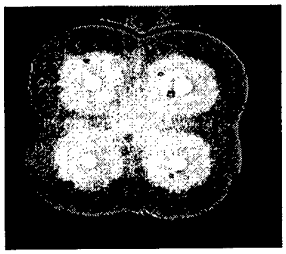

Figure 1 Cleaved face of CNET four core fibre

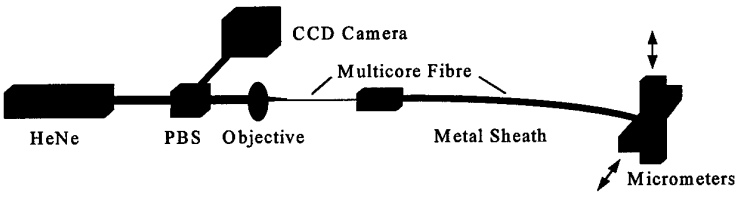

Figure 2 Schematic of the 2D bend measurement apparatus

The experimental arrangement is shown in fig 2. We deposited a semi-reflective (R~ 80%) silver coating on the end of the fibre. This allowed us to make measurements in reflection, while providing some transmission for rotational alignment. Horizontally-polarised light from a HeNe laser was coupled into all four cores. Due to birefringence in the multicore fibre, the return from the end face had a substantial vertically-polarised component. We used a polarising beamsplitter (PBS) to pick off the return signal from the distal face, while rejecting the near-face reflection.

We recorded the far-field interferogram using a digital CCD camera. The disadvantage of using the fibre at wavelengths within the silicon window, where it is overmoded, was tolerated for the convenience of obtaining a two-dimensional interferogram.

The fibre, in PTFE sleeving with an internal diameter close to the fibre's buffer coating, was housed inside a steel tube. One end of the tube was held fixed, while the other was displaced by two orthogonal micrometers, acting on the steel tube via an interface plate. The stiffness of

the steel tube ensured a smooth and repeatable bend geometry that could be calculated from the displacement of the end by simple beam theory[6] . We rotated the fibre inside the PTFE tubing so that the diagonal core pairs were horizontal and vertical, judged by viewing the far-field pattern.

We set the bend angle using the micrometers, verifying our beam theory calculation of this angle using an optical lever, a laser beam reflected off a mirror mounted near the end of the steel tube. The angles measured by the optical lever agreed with the calculated values, confirming that the steel tube was behaving as an elastic beam. We captured far-field interferograms for a range of bend angles about the horizontal and vertical axes.

4. Signal processing

We investigated two approaches to signal processing. In the first, we took a two-dimensional FFT of the entire far-field interferogram. This FFT contained a pair of peaks corresponding to each diagonal core pair. The phase of each peak gave the phase of the interferogram for that core pair. Unfortunately, the two dimensional FFT was time consuming, and this approach proved sensitive to the effects of overmoding. Our second approach, which is the one we subsequently adopted, involves reducing the two-dimensional interferogram to a pair of one-dimensional interferograms by summing along rows and columns of the CCD array. With the correct orientation of the fibre, each of these interferograms corresponds to one of the diagonal core pairs. We derived the phase of each interferogram from its analytic signal, which we calculated by FFT[7] .

5. Results and discussion

We first made measurements of phase change due to bending in a plane. Figure 3 shows how the phases ϕ_a and ϕ_b of the two interferograms varied with bend angle, where the suffixes *a* and *b* refer to the alternate pairs of fibre cores. These graphs show that the core pairs were almost, but not completely, aligned with the horizontal and vertical axes. Figure 4 shows the effects of bending over a larger range in the vertical plane. The response remains linear, with the same slope.

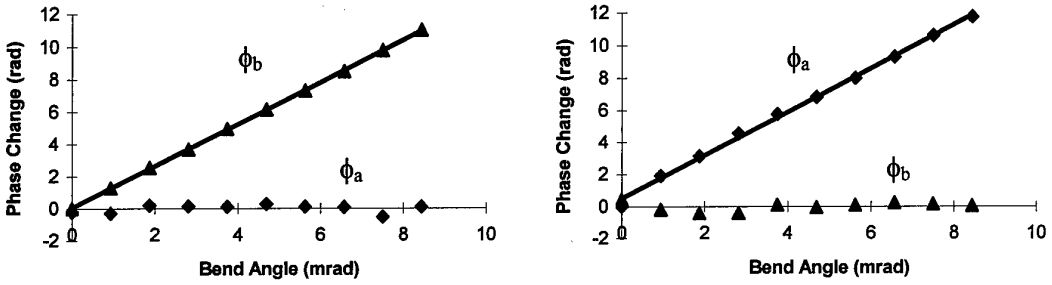

Figures 3: Phase change due to bending in vertical and horizontal planes.

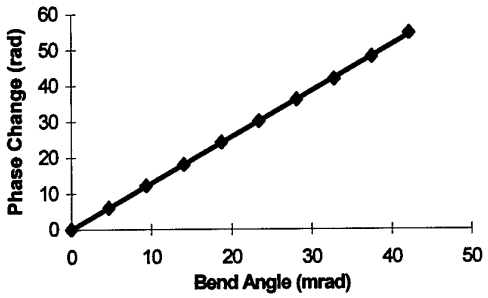

Figure 4: Phase change for vertical bending: extended range

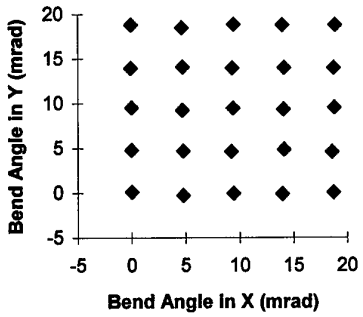

Figure 5: Measured bend angles for set values on a grid of pitch 4.69 mrad

If the core pairs were oriented perfectly horizontally and vertically, then ϕ_a would depend linearly on θ_x and ϕ_b on θ_y. The above graphs show that the cores are slightly misaligned, so instead these values are related by linear transformations involving both θ_x and θ_y. We determined the coefficients in this relationship by least squares fitting to a large number of measurements made for various settings of θ_x and θ_y. We could then invert the relationship, allowing us to derive values of θ_x and θ_y from measurements of ϕ_a and ϕ_b. Figure 5 shows the results obtained by setting bend angle at a number of points on a grid of pitch 4.69 mrad recovering bend angle by transforming the measured values of ϕ_a and ϕ_b.

The gradients of the graphs in figures 3 and 4, and the coefficients of the linear transformation, were within 5% of the theoretical sensitivity predicted from equation 1. A static test on the sensor gave an RMS noise of 0.036 rad in phase which translates to 0.026 mrad RMS bend angle resolution. . A least-squares fit to the grid gave an RMS deviation between the set and optically measured bend angles of 0.07 mrad in x and 0.12 mrad in y. We believe that the measurement resolution was limited either by mechanical effects—it corresponds to an error of 10 μm in setting the end position of the fibre—or by the effects of overmoding. The systematic error apparent in the right-hand plot of figure 3 may be due to the same cause.

6. Conclusion

We have successfully demonstrated the use of a four-core optical fibre to measure bend angle in two axes, with resolution in the 100 μrad range, and with a sensitivity within 5% of that predicted by theory. This performance was achieved even though the fibre was operated overmoded. Longer wavelength single mode operation and improved phase measurement resolution could be achieved by using either InGaAs array detectors or by interrogating the cores using tandem interferometry.

The enabling technologies being developed for communications, such as connectorisation[8-9], fusion and mechanical splicing, are making multicore fibres a practical choice for sensor applications.

7. Acknowledgements

This work has been carried out with the support of DERA, the EU Erasmus scheme (E. Galliot) and a NATO travel grant (N. Inci). We thank CNET for their generosity in supplying the fibre, making this work possible.

[1] B. G. Ferguson, "Sharpness applied to the adaptive beamforming of acoustic data from a towed array of unknown shape," J. Acoust. Soc. Am **88** 2695-2701 Dec 1990.

[2] E. C. van Ballegooijen et al. "Measurement of Towed Array Position, Shape, and Attitude Journal of Oceanic Engineering" **14** (1989) 375-383

[3] M. J. Gander et al. "Bend measurement using multicore optical fiber" OFS12 (1997)

[4] A. Bertholds and R Dändliker "Determination of the Individual Strain-Optic Coefficients in Single-Mode Optical Fibers" J. Lightwave Technol. **6** (1988) 17–20

[5] G. Le Noane et al. "Ultra high density cables using a new concept of bunched multicore monomode fibres: a key for the future FTTH networks" IWCS 1994 203–210

[6] Benham, Crawford and Armstrong, *Mechanics of Engineering Materials* 1996

[7] Joseph W. Goodman, Statistical Optics Wiley (New York) 1985

[8] H .Aoustin et al. "Connection Techniques for Bunched Multicore Monomode Fibers" 13th Euro. Fibre Optic Communications and Networks Conference 1995

[9] R. L. M Le Marer et al. "Fan out Components for Bunched Multicore Monomode Fibers: "Fan Out" a Key Component" 13th Euro. Fibre Optic Communications and Networks Conference 1995

Contributions to Wavelength Shifts of DFB Fiber Lasers used as Acoustic Sensors in Air.

Sigurd Weidemann Løvseth*, Kjell Bløtekjær*,
and Jon Thomas Kringlebotn†

* Norwegian University of Science and Technology
Department of Physical Electronics, 7034 Trondheim, Norway
Phone: +47 7359 4400, Fax: +47 7359 1441, E-mail: Sigurd.W.Lovseth@fysel.ntnu.no

† Optoplan A/S, Bjørkhaugvegen 27, 7035 Trondheim, Norway
Phone: +47 7394 2007, Fax: +47 7394 3823, E-mail: Thomas.Kringlebotn@optoplan.no

1 Introduction

Our aim is to investigate the use of distributed feedback (DFB) fiber lasers [1] as acoustic sensors. In this paper we will discuss the various contributions to the frequency shifts that make such sensing possible, and compare the theoretical results with preliminary experimental results. In model used in this paper the fiber is spanned perpendicularly to the wave vector of an acoustic plane wave. The fiber laser used so far has no coating and a center wavelength of $\lambda = 1550$nm, but the model is easily extendable to coated fiber lasers.

2 Temperature and pressure variations in the fiber at the acoustic frequency

When the pressure of the air varies due to the acoustic wave, the work applied to compress and decompress the air leads to temporal temperature variations, following the first principle of thermodynamics, which may be expressed by [2]:

$$\begin{aligned} dq &= \rho c_V \, dT + (c_p - c_V)\, \rho \left(\frac{\partial T}{\partial V}\right)_p dV \\ &= \rho c_p \, dT - (c_p - c_V)\, \rho \frac{T}{p} \, dp \end{aligned} \tag{1}$$

Here q is heat per unit volume added to a differential amount of air, T is the temperature, p is the pressure, ρ is the density and c_p and c_V are the specific heat capacities at constant pressure and temperature, respectively. In the last line of equation (1) the ideal gas approximation is used. dq must equal heat conducted from the surroundings [3]:

$$dq = \kappa \nabla^2 T \, dt \tag{2}$$

Here κ is the thermal conductivity. Due to the relative smallness of acoustic pressure compared with the static pressure, we can usually set $T/p \approx T_{\text{static}}/p_{\text{static}}$. By combining equations (1)-(2) and assuming a harmonic acoustic field with frequency $\omega = 2\pi f$ we thus get:

$$\begin{aligned} j\omega\,\Delta T &= \frac{\kappa}{\rho c_p}\nabla^2 T + j\omega\frac{c_p - c_V}{c_p}\cdot\frac{T_{\text{static}}}{p_{\text{static}}}\Delta p = D_{T_{\text{air}}}\nabla^2 T + j\omega\,\Delta T_0 \\ T(\vec{r},t) &= T_{\text{static}} + \Delta T(\vec{r})\cdot e^{j\omega t}, \qquad p(\vec{r},t) = p_{\text{static}} + \Delta p(\vec{r})\cdot e^{j\omega t} \end{aligned} \tag{3}$$

Here $D_{T_{\text{air}}}$ is the thermal diffusivity of air. We may neglect the Laplacian term in equation (3) far away from the fiber, and assume that the process is adiabatic, if:

$$\frac{D_{T_{\text{air}}}\left(\frac{\omega}{c}\right)^2}{\omega} = \frac{D_{T_{\text{air}}}2\pi f}{c^2} = \frac{22.5\cdot 10^{-6}\frac{\text{m}^2}{\text{s}}\cdot 2\pi f}{\left(350\frac{\text{m}}{\text{s}}\right)^2} \approx 1.15\cdot 10^{-9}\text{s}\cdot f \ll 1 \tag{4}$$

Here c is the velocity of sound, and typical values [3] for air at 300K are inserted. Thus, for frequencies up to several MHz, the only significant contributions to the Laplacian term in equation (3) come from the inhomogeneities caused by the presence of the fiber. In this paper we are working with acoustic frequencies in the range 100-20kHz, and we may therefore also safely ignore the spatial dependence of the acoustic pressure in the vicinity of the fiber. Thus, the temperature field is spatially dependent only on the radius r in cylinder coordinates, and equation (3) simplifies to an inhomogeneous Bessel equation of the zeroth order with general solution:

$$\Delta T_{\text{air}}(r) = \Delta T_0 + C_1\cdot J_0\left(\sqrt{\frac{\omega}{jD_{T_{\text{air}}}}}\cdot r\right) + C_2\cdot Y_0\left(\sqrt{\frac{\omega}{jD_{T_{\text{air}}}}}\cdot r\right) \tag{5}$$

In silica there is no significant acoustic generation of heat, and thus the temperature in the fiber is determined from a homogenous Bessel equation with general solution:

$$\Delta T_{\text{fiber}}(r) = C_3\cdot J_0\left(\sqrt{\frac{\omega}{jD_{T_{\text{silica}}}}}\cdot r\right) + C_4\cdot Y_0\left(\sqrt{\frac{\omega}{jD_{T_{\text{silica}}}}}\cdot r\right) \tag{6}$$

The constants $C_{1,2,3,4}$ in equations (5)-(6) are found by using the boundary condition $\lim_{r\to\infty}\Delta T(r) = \Delta T_0$ and requiring that both $T(r)$ and its derivative are finite and continuous everywhere.

The total frequency shift of the laser at the acoustic frequency can now be found by adding the frequency shifts due to the temperature and pressure variations in the fiber. The temperature sensitivity of the Bragg wavelength is approximately $\Delta\lambda/\lambda = 8.85\cdot 10^{-6}\text{K}^{-1}\Delta T$ [4, 5] , and $\Delta T_0 \approx 0.85\text{mKPa}^{-1}\,\Delta p$ at 300 K and atmospheric pressure. The acoustic pressure sensitivity has a predicted value of $\Delta\lambda/\lambda = 4.5\cdot 10^{-12}\text{Pa}^{-1}\Delta p$ [6, 7]. Because of the large ratio between the wavelength of the acoustic wave and the diameter of the fiber, we assume that the pressure is uniform across the transverse area of the fiber. We assume a Gaussian optical mode [8], and by integrating over the fiber cross section the product between the intensity of the mode and the temperature trans-

fer function, the spatial variation of the latter may be accounted for. This correction was however found to have only negligible effect. The total frequency shift per rms Pa sound pressure at a temperature of 300K is shown in figure 1. At low frequencies the total shift is many orders of magnitude larger than the contribution from the pressure variations alone, and this is confirmed by our preliminary experiments. The thermal effect is negligible for frequencies above ~8kHz.

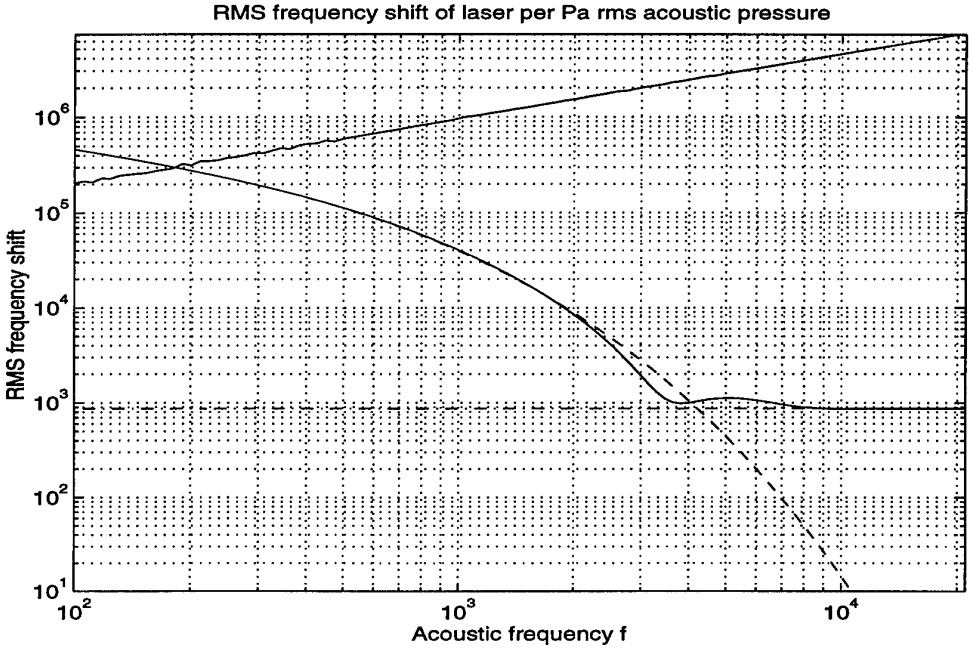

Figure 1: *The various contributions to frequency shifts per Pa rms acoustic pressure of a stripped fiber laser. The straight dash-dotted line is frequency shift of the laser due to pressure variations in the fiber. The dashed line is the contribution from the temperature variation, while the solid declining line is the sum of the two. The other solid line is the frequency shift due to longitudinal strain in a tightly spanned fiber laser as discussed in section 3.*

3 Longitudinal strain in fiber due to pressure gradients in the acoustic wave.

Although the pressure gradients of the acoustical field are small for the modest frequencies we have been working with here, the gradients will lead to a transverse force on the fiber. If the fiber is spanned tightly, this will lead to a longitudinal stress and strain in the fiber, and thus to a frequency shift of the laser. If the acoustic field propagates perpendicularly to the longitudinal axis of the fiber, it is straight forward to show that the rms transverse force F_{rms} per unit length of a fiber with radius R and rms acoustic pressure Δp_{rms} is:

$$F_{\text{rms}} = 4\sqrt{2}\,\Delta p_{\text{rms}} R \int_0^{\pi/2} \cos\theta \sin\left(\frac{\omega}{c} R \cos\theta\right) d\theta \tag{7}$$

It may also be shown that the longitudinal stress ϵ in the fiber can be found by numerical solution of the following set of equations:

$$\begin{aligned} \Delta l &= \frac{S_z^2}{KF}\left[\sqrt{1+\left(\frac{Fl_0}{2S_z}\right)^2}\cdot\frac{Fl_0}{2S_z} + \operatorname{arcsinh}\left(\frac{Fl_0}{2S_z}\right)\right] \\ \epsilon &= \frac{S_z}{K} = \frac{\Delta l}{l_0 + \Delta l} \end{aligned} \tag{8}$$

Here l_0 is the distance between the points of suspension of the fiber, Δl is the elongation of the fiber due to the transverse force, S_z is the longitudinal force along the fiber axis and $E = K/(\pi R^2)$ is Young's modulus. Note that due to the nonlinearity of equations (8), the wavelength shift will vary with an even multiplum of the acoustic frequency, and will therefore not interfere directly with the shifts discussed in section 2. Note also that this shift would be considerably reduced if the fiber is loosely spanned or is close to a maximum in a standing wave pattern. Using the same logic, we would suspect larger noise due to drifts in the air etc. when the fiber is tightly spanned, something that is confirmed in our preliminary experiments. Equation (8) also requires that F is constant along the span of the fiber, which is unlikely for very high frequencies. In order to give an idea of the magnitude of the effect, we solved equations (8) by inserting the rms value of F for 1Pa rms acoustic pressure, and using $l_0 = 10\text{cm}$, $E = 7.2 \cdot 10^{10}\text{Pa}$, and a strain sensitivity of $\Delta\lambda/\lambda = 0.78\epsilon$ [5] we get the result shown in figure 1.

4 Conclusions

We have found that adiabatic processes in the surrounding air are important when using fiber lasers as acoustic sensors for low frequencies. Likewise we have found that the way the fiber laser is spanned is important for its sensing capabilities. More experimental work will be done in order to confirm these theoretical results.

References

[1] J. T. Kringlebotn, J. Archambault, L. Reekie, and D. N. Payne, "Er^{+3}:Yb^{3+}-codoped fiber distributed feedback laser," *Optic Lett.*, vol. 19, no. 24, pp. 2101–2103, 1994.

[2] P. C. Riedi, *AN INTRODUCTION TO THERMODYNAMICS, STATISTICAL MECHANICS AND KINETIC THEORY*, ch. 2,3. London, UK: The MacMillan Press LTD, 1976.

[3] F. P. Incropera and D. P. DeWitt, *FUNDAMENTALS OF HEAT AND MASS TRANSFER*. New York, USA: John Wiley & Sons, third ed., 1990.

[4] S. Takahashi and S. Shibita, "Thermal variation of attenuiation for optical fibers," *J. Non-Crystalline Solids*, vol. 30, pp. 359–370, 1978.

[5] W. W. Morey, G. Meltz, and W. H. Glenn, "Fiber optic bragg grating sensors," in *Fiber Optic and Laser Sensors VII*, vol. 1169 of *Proc. SPIE*, pp. 98–107, 1989.

[6] M. G. Xu, L. Reekie, Y. T. Chow, and J. P. Dakin, "Optical in-fibre grating," *Elect. Lett.*, vol. 29, no. 4, pp. 398–399, 1993.

[7] S. Knudsen, *FIBER-OPTIC ACOUSTIC SENSORS BASED ON THE MICHELSON AND SAGNAC INTERFEROMETERS: RESPONSIVITY AND NOISE PROPERTIES.* PhD thesis, Department of Physical Electronics,University of Trondheim, Norway, 1996.

[8] D. Marcuse, "Loss analysis of single-mode fiber splices," *Bell Syst. Tech. J.*, vol. 56, pp. 703–718, 1977.

Large amplitude point-vibration measurement with optical-fibre moire based technique

J. D. R. Valera*, P. G. Sinha and T. Yoshino
Electrical Engineering, Gunma University, Kiryu 376, Gunma, JAPAN

O. J. Løkberg
Department of Physics, NTNU, N-7034 Trondheim, NORWAY

*Tel: ++47 73 59 34 14, fax: ++47 73 59 34 20
email: valera@phys.ntnu.no

Introduction

The real-time measurement of the vibration of a point in a large vibrating object is an application that is often encountered in industry. Many laser based point vibration measuring devices have been proposed. All have their advantages and disadvantages and which one is used is determined by the application conditions. For example, the optical fiber based vibrometer described in reference 1 has shown to be appropriate for many industrial applications. This instrument gives real time vibration information with submicron accuracy. However, if the vibration amplitude of the monitored point is larger than a few microns, or if the object has slight transverse displacements, then the device can not be used (because of speckle decorrelation). There are many applications where the points of interest are vibrating with amplitudes as large as several millimeters. This is typical of large vibrating objects.

The technique reported here can be used to measure the vibration of a point even if the amplitude is as large as a few millimeters and, in addition, the instrument is insensitive to small transverse movements of the object. In the following sections the principle of operation is described in detail. The experimental setup and results are given and finally the conclusion reviews the major points.

Theory

Assume that the object of interest is relatively large and essentially flat (e.g. hood of a car, wing of an airplane, a large ship etc). Then, the principle of operation can be understood by considering figure 1. The object point is illuminated by a small beam of light that is structured with a straight line interference pattern. This beam is incident at an angle with respect to the normal of the object surface (see fig 1). Lens L images this illuminated spot at plane P. It can easily be noted that as the object vibrates in the out-of-plane direction then the

image formed by lens L will move sideways in plane P. A Ronchi ruling (RR), with period equal to that of the spot image, is now placed at plane P and the total amount of transmitted light is monitored with a photodiode (det). This detected signal is then used, with the aid of servo electronics, to recover the vibration of the monitored object "point" in real time. In-plane object movement does not make this signal vary.

The sensitivity of the technique depends on the incidence angle and on the period of the illumination fringes (on the beam) and Ronchi ruling. However, if the Ronchi ruling period becomes very small then diffraction effects must be taken into account. For the experiments presented here the Ronchi period is relatively large and hence, diffraction effects can be safely ignored.

Experimental setup and results

The fiber projection system used to obtain the "structured" light beam that illuminates the probed point is included in figure 1. The light from a 10mW HeNe laser was coupled into an optical fiber directional coupler (DC) with 50/50 split ratio. The two output monomode fibers were placed next to each other as shown in figure 1 (with the protective coatings removed at the end). Hence, the cores of the fibers were separated by a distance of approximately 125μm (the fiber cladding diameter). The beams that exit the fibers expand and overlap to give rise to a straight line interference pattern. One of the fibers of the directional coupler had a fiber phase modulator that was constructed by wrapping approximately 4 meters of the fiber around a piezoelectric cylinder of 2.5cm diameter (PZT). A lens was used to "collimate" this beam and an aperture was used to limit its size. Hence, in this way, a collimated beam that is structured with a straight line interference pattern was obtained.

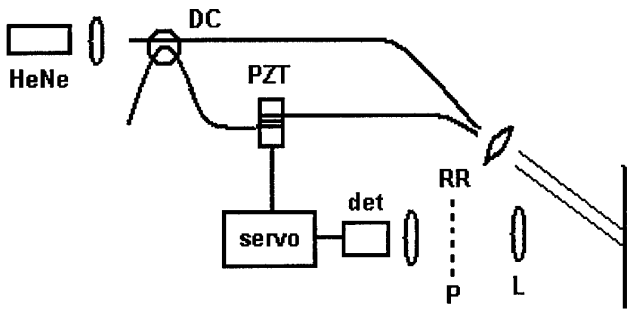

Figure 1. Experimental setup

In the experiments the beam was incident at an angle θ=17.6°. Lens L was used to image this "structured" spot onto plane P. A Ronchi ruling with 50 lines per inch and an aperture were also placed at plane P. The distance from the object to the lens (and hence from the lens to plane P) was varied until the period of the image at P was equal to the period of the Ronchi ruling used. A second lens was then used to image plane P onto the detector (Si photodide, area 4mm by 4mm).

The vibrating object was a flat piece of cardboard that was glued in front of a speaker (20cm diameter). By applying a sinusoidal voltage to the speaker the object would vibrate harmonically with amplitudes of several millimeters. The lower trace on figure 2 shows the signal detected when the object was made to vibrate at 100Hz.

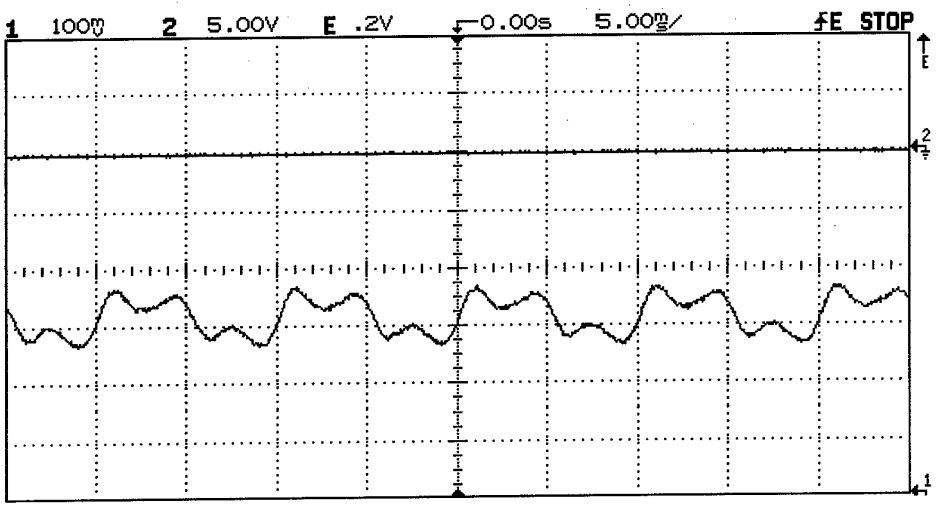

Figure 2. Object vibrating at 100Hz and servo off. Lower trace: total light transmitted through the Ronchi ruling.

The signal from the detector was used as input to a servo controller (with proportional and integral control) and the output was connected to the fiber phase modulator (PZT). The servo output applied a phase modulation to one of the fibers in the directional coupler that resulted in a shift of the fringes within the structured beam. Hence, the principle of operation is straightforward: as the structured image incident on the Ronchi grating moves sideways (due to the out-of-plane vibration of the object), the servo applies a voltage that shifts the fringes within the image in such a way the total light transmitted through the Ronchi ruling is a constant. Therefore, the voltage that is applied to the fiber phase modulator is proportional to the vibration of the point.

The object was made to vibrate at several frequencies and the vibration was recovered by this technique. Figure 3 shows the signal recovered (upper trace) when the object vibration was 100Hz. The lower trace represents the light transmitted through the Ronchi ruling and it is clear that the servo system tries to maintain this signal constant. Only low frequencies were used since only these provided the large amplitudes of interest.

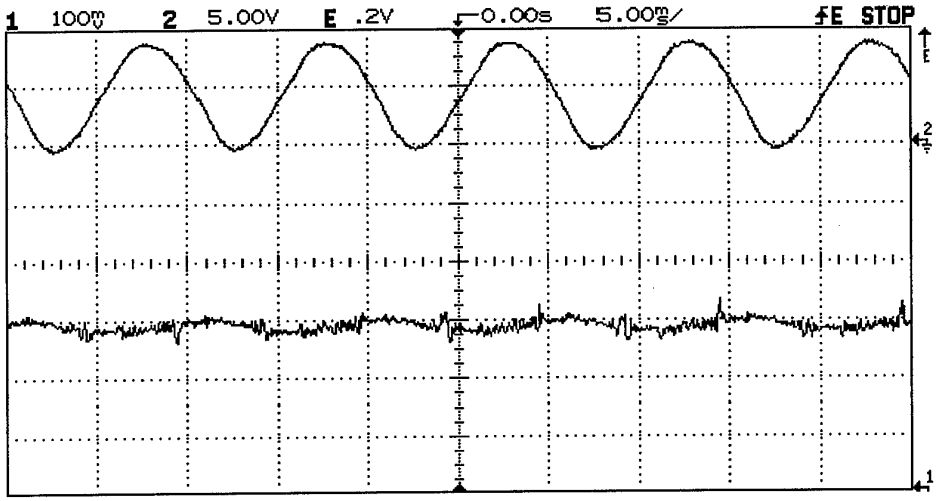

Figure 3. Object vibrating at 100Hz and servo on. Lower trace: total light transmitted thorugh the Ronchi ruling (maintained constant by servo). Upper trace: output from servo to the fibre phase modulator (PZT). This signal is proportional to the object vibration.

Conclusion

A simple technique has been described that allows the real-time measurement of displacement or vibration of a point. The technique offers the additional advantage that it does not require any special treatment for the surface of the monitored object. The technique can be used to monitor the vibration of points on objects that are relatively flat, large, and vibrate with amplitudes of several millimeters and the technique is also insensitive to small transverse movements of the object. The technique also allows the measurement of non-sinusoidal vibrations (assuming that the frequency components are within the bandwidth of the servo controller).

Acknowledgements

JDRV wishes to thank the Satellite Venture Business Lab of Gunma University for their kind invitation and for making this work possible.

References

1. JD Valera R, D Harvey and JDC Jones, Opt. Eng. **31**, 1646, 1992.

Transient Deformation Measurement with a Fibre-Optic Speckle Pattern Interferometer and a High Speed Camera

A. J. Moore, D. P. Hand, J. S. Barton and J. D. C. Jones
Department of Physics, Heriot-Watt University, Riccarton, Edinburgh, EH14 4AS, UK

Introduction

Speckle pattern interferometry allows full-field, quantitative measurements to be made on non-specular surfaces [1]. To measure the deformation of a test object, two phase-referenced speckle patterns are recorded by a camera, one before and one after deformation. Comparison of the two speckle patterns, typically by electronic subtraction, yields a fringe pattern denoting loci of constant phase change between the object and reference beams of the interferometer, which can be related to the object deformation. Measurement of harmonic vibrations and transient deformations is commonly performed with stroboscopic [2] or pulsed [3] laser illumination.

Fibre-optic illumination systems have been useful in making electronic speckle pattern interferometry (ESPI) more practical in engineering environments. High pulse repetition rates can be achieved (e.g. MHz with current modulation of a laser diode) but the object must be illuminated repeatedly during each camera frame period due to the low energy of the pulses. Single-mode fibres restrict the peak powers that can be used. Pulsed illumination (e.g. Q-switched, frequency-doubled Nd:YAG) is typically synchronized to give either one single pulse or a double pulse per camera frame, but at lower pulse repetition rates (e.g. 60 Hz) [4].

Whether or not single-mode fibre is used in the interferometer, choosing a pulsed laser to study transient deformations with ESPI is difficult: high temporal resolution of the dynamic event requires a high pulse repetition rate, but each pulse should also be sufficiently intense to expose a single camera frame. When a temporal resolution of more than a few ms is required, it is common to assume that the transient event is reproducible: a composite picture of the complete event can be built up from a series of successive experiments in which the delay between laser illumination and the start of the transient event is incremented [5].

We propose a simple solution to allow the measurement of non-reproducible transient deformations based on using a high-speed camera, with short exposure period and high framing rate, combined with a CW laser source. The solution allows transient deformations to be measured with a fibre-optic ESPI system. A deformation history with μs temporal resolution is obtained, restricted only by the camera framing rate and the laser power available. It is shown that the framing rate determines the maximum surface velocity that can be accommodated. We have applied the technique to measure harmonic vibration and transient deformations.

SPIE Vol. 3483 • 0277-786X/98/$10.00

Theory

For the arrangement shown in Figure 1, when the test object vibrates harmonically, the intensity recorded by the camera at pixel (x,y) during an exposure of duration t_s, centred at time t_n, due to interference between the object and reference beams may be approximated by:

$$I(x,y,t_n) = \frac{I_o}{t_s}\int_{t_n-t_s/2}^{t_n+t_s/2} 1 + V\cos\left(k\underline{s}\bullet\underline{a_i}\sin(\omega t+\phi_i)+\psi\right)dt$$

where $I_o(x,y)$, $V(x,y)$ and $\psi(x,y)$ are the background intensity, fringe visibility and random speckle phase for the rough test object respectively; $\underline{a_i}(x,y)$, $\phi_i(x,y)$ and ω are the amplitude, phase and circular frequency of object vibration respectively; $k=2\pi/\lambda$ where λ is the laser wavelength and $\underline{s}(x,y)$ is the sensitivity vector dependent on the angles of illumination and observation. For short exposure periods with respect to the vibration period, we can approximate the deformation by a linear expansion [6,7], yielding :

$$I(x,y,t_n) = I_o\left(1+V\,\mathrm{sinc}\left(ksa_i'(t_n)\frac{t_s}{2}\right)\cos\left(ksa_i\sin(\omega t_n+\phi_i)+\psi\right)\right)$$

where $a_i'(t_n)$ and $a_i(t_n)$ are the velocity and displacement at time t_n, respectively. Clearly, to maintain maximum fringe visibility, the argument of the sinc function should be zero, requiring low test surface velocity and a short exposure time. We can set the vibration amplitude at a given frequency (and hence velocity) to keep within a prescribed visibility variation. For example, to maintain $|\mathrm{sinc}(ksa_i'(t_n)t_s/2)| \geq 0.9$ requires $|ksa_i'(t_n)t_s/2|<0.8$. Substituting for the maximum velocity $a_i'(t_n) = |2\pi f a_i(t_n)|$ gives the maximum allowable framing frequency, f_s:

$$f_s \geq \frac{2\pi^2}{0.8}Nf$$

where $N = a_i(t_n)/(\lambda/s)$ is the object vibration amplitude in fringes and f the object vibration frequency. For transient deformations, the velocity limit can be set directly from $a_i'(t_n)$.

Experimental System

The schematic of the experimental system is shown in Figure 1. Light from a 10 mW HeNe laser (633 nm) was coupled into a single-mode optical fibre through a ×20 microscope objective (MO). The light was divided into object (90%) and reference (10%) fibres by a directional coupler (DC). The divergent beam emerging from the object fibre illuminated the test object. An image of the test object was formed by an SLR camera lens (focal length 50 mm, F/# 11) on to the detector of a high-speed camera (Kodak Ektapro 4540). Due to the low power of the laser used, the object was covered in retroreflective tape and the fibre output was placed on the lens optical axis. The optical path of the reference beam was matched to that of the object beam. The reference arm fibre was wound around a fibre polarization controller (PC) and a piezoelectric cylinder (PZT) (for phase-stepping). The divergent beam of the reference fibre passed through a neutral density filter and was reflected from a beam combiner (BC) on to the camera detector.

Experiments were performed at 4,500 frames per second (fps) (the highest camera frame rate for maximum resolution of 256 x 256 pixels) and at 40,500 fps (64 x 64 pixels). Eight-bit images are digitized directly to the camera memory (192 Mbytes). Once in memory, the images are played back at any desired speed. The CCIR signal during playback was digitized

by a PC-hosted frame grabber (Imaging Technology VFG). The camera must be calibrated against fixed pattern noise and shading errors, by recording to auxiliary memory a series of reference images with the lens cap on. These images are automatically subtracted from camera recordings to remove unwanted artefacts. We used this facility (AUX MEM) without the lens cap to record a reference speckle pattern with the test object stationary. This pattern, plus electronic artefacts, were automatically subtracted from a sequence of speckle patterns recorded when the object was deforming, to show ESPI subtraction fringes directly during playback,. The camera was operated at its highest gain (equivalent to ISO 3,000).

Results

Figure 2 shows a sequence of images recorded at 4,500 fps for a circular aluminium plate of 14 cm diameter vibrating harmonically at 198 Hz. The plate was excited by a piezoelectric crystal stuck to its rear surface, driven by an arbitrary waveform generator (AWFG). The camera was not synchronized to the object vibration frequency. A sequence of 12 images is shown, covering approximately one half period of vibration. An interesting asymmetry in the vibration behaviour can be seen. In order to obtain quantitative information about the object vibration amplitude and phase, it is necessary to synchronize the camera exposure to the object vibration. The AWFG was set to generate pulses at a given phase of the object vibration cycle, which served as an external trigger to acquire a single frame to the high-speed camera per cycle. Approximately $4{,}500/198 \approx 22.7$ s are needed to fill the camera memory, so there is sufficient time to apply a controlled voltage to the piezoelectric cylinder in the reference arm and record four optically phase-shifted fringe patterns. Figure 3(a) shows the first of four phase-stepped images recorded under the same conditions as Figure 2, for camera frame exposures at the object vibration maximum. Figure 3(b) shows the object vibrating with the same amplitude and frequency as the in Figure 3(a) but with the camera trigger pulse shifted by 90° with respect to the object vibration phase. Obviously the plate is passing through its equilibrium position and no deformation is seen. The fringes were lowpass filtered to remove speckle noise and the interference phase calculated using the well-known 4-bucket algorithm, Figure 3(c), where phase in the range $-\pi$ to π rads, has been linearly scaled between black (0) and white (255) for display. The continuous phase distribution, Figure 3(d), is obtained by removing phase discontinuities (phase unwrapping). A second phase map corresponding to Figure 3(b) can be calculated and the object vibration amplitude and phase determined [8]. For this real vibration mode, the amplitude is obviously identical to Figure 3(d) and the phase is constant across the image.

Figure 4 shows results obtained for a transient deformation. The camera was set to acquire frames continuously to memory at 40,500 fps until it received a trigger signal. The aluminium plate was struck impulsively from behind, approximately in the centre of the field of view, and a trigger signal generated to coincide with the impact. The trigger signal caused the camera to continue recording until a half-memory of images had been acquired. In this way, the images in camera memory straddle the moment of impact. Figure 4(a) shows the frame just before impact, and subsequent frames show the propagation of the mechanical wave.

Conclusions

We have demonstrated that the short exposure and high framing rate of a high speed camera can be used to record time-resolved deformation histories with a CW laser. This is particularly advantageous in single-mode fibre optic interferometers where the high peak powers of pulsed lasers cannot be tolerated. Despite the low optical power budget, we demonstrated vibration and transient deformation (including vibration amplitude and phase) measurements. The fibres are capable of carrying substantially greater power which would increase the size of objects that can be studied. Higher illumination power would also allow a shorter exposure (i.e. higher framing rate) to be used and extend the upper surface velocity limit.

References

[1] R.Jones and C.Wykes, "Holographic and speckle interferometry", Cambridge University Press, Cambridge, Second edition (1989)
[2] D.J.Anderson, J.D.Valera and J.D.C.Jones, Meas. Sci. Technol. 4 982-987 (1993)
[3] T.J.Cookson, J.N.Butters and H.C.Pollard, Opt. Las. Technol. 10(6) 119-124 (1978)
[4] A.J.Moore and C.Pérez-López, J. Mod. Opt. 43(9) 1829-1844 (1996)
[5] A.Fernández, A.J.Moore, C.Pérez-López, A.F.Doval and J.Blanco-García, Appl. Opt. 36 (10)2058-2065 (1997)
[6] G.O.Rosvold and O.J.Lokberg, Appl. Opt. 32(5) 684-691 (1993)
[7] G.M.Brown and G.H.Smith, Proc. SPIE 1162 36-45 (1989)
[8] J.D.Valera, A.F.Doval and J.D.C.Jones, Electron. Letts. 28(25) 2292-2294 (1992)

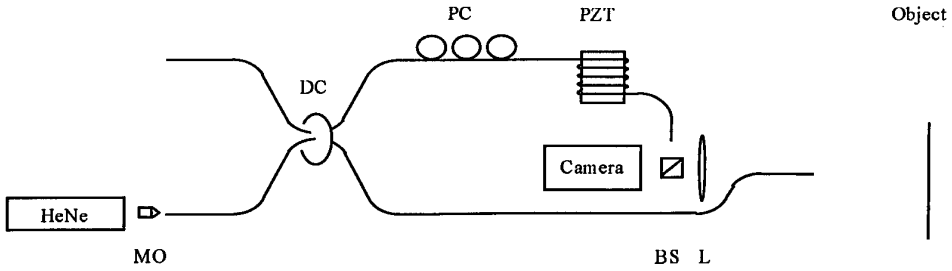

Figure 1: Schematic of experimental arrangement

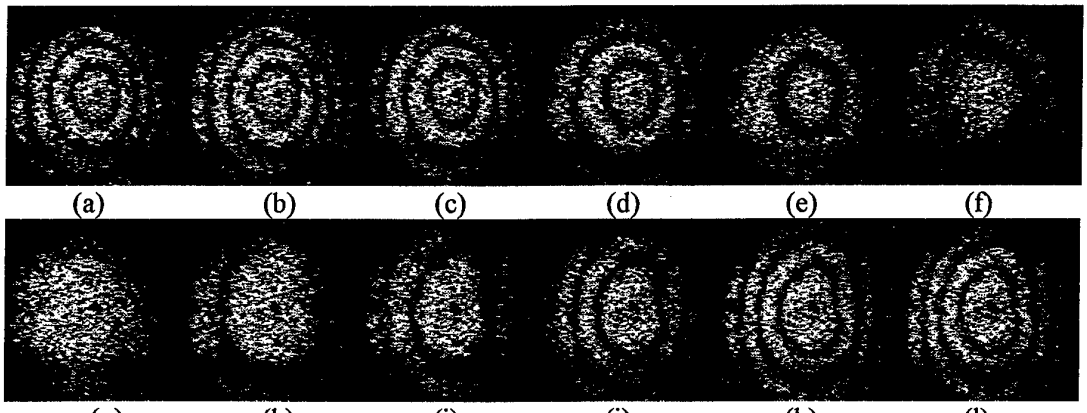

Figure 2: Consecutive frames at 4,500 fps, object vibration frequency 198 Hz.

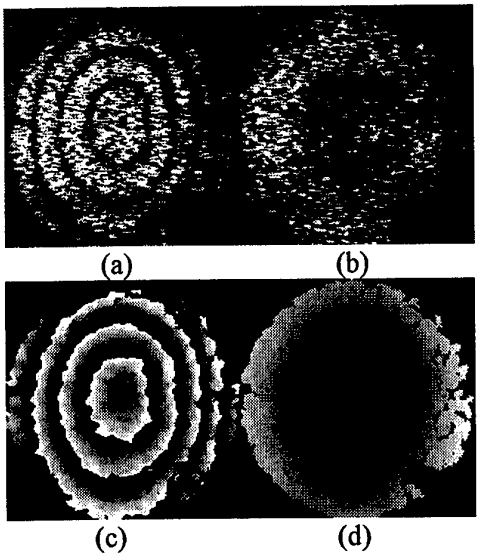

Figure 3: Vibration amplitude and phase; 198 Hz, 4,500 fps.

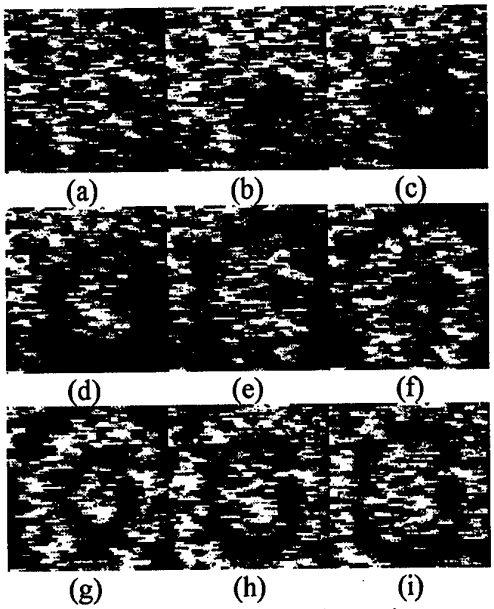

Figure 4: Transient deformation; 40,500 fps, 64 x 64 pixels

Chemical, Environmental, and Medical Sensors

Thursday, 9 July 1998

Chair: Anna G. Mignani, Istituto di Ricerca sulle Onde Elettromagnetiche (Italy)

DIRECT, REMOTE AND SIMULTANEOUS DETERMINATION OF URANIUM AND PLUTONIUM IN EIGHT DIFFERENT MEDIA, BY OPTICAL ABSORPTIOMETRY USING NON-IMMERSED OPTICAL FIBRE SENSORS

By L. COUSTON - J. DELAGE and D. POUYAT
Commissariat à l'Energie Atomique
C.E.A Valrhô - SEMP/LI - Bâtiment G1 - BP 171 - 30207 BAGNOLS/CEZE (France)
Tel : (33) 04 66 79 16 25 / Fax : (33) 04 66 79 16 22 / E-mail : laurent.couston@CEA.Fr

EXTENDED SUMMARY

Molecular absorptiometry is a fast, selective and sensitive method for the determination of the most part of lanthanides and actinides ions.

Separation steps of uranium, plutonium, and fission products on the nuclear fuel reprocessing are realised by a liquid-liquid extraction using pulsed columns. Kinetics are slow enough to allow the process to be controlled by liquid chromatography analyses. When centrifuge extractors are used, kinetics of extraction are very fast compared with pulsed columns and require an in-line analytical procedure such as direct molecular absorptiometry.

On a nuclearised laboratory prototype of the plutonium purification steps, equipped with small centrifuge extractors, new extracting scheme are testing, needing a real time determination of U, Pu, (valences and concentrations) to interpret the final extraction yield. The accuracy of the interpretations depends both on the sensitivity and the number of simultaneous measurements.

Classical spectrophotometers are not suitable for such a problem : Only one measurement channel, and a weak measurement range ($\Delta OD = 1$) when optical fibres are coupled to the apparatus.

SPIE Vol. 3483 • 0277-786X/98/$10.00

The chosen method is to expose a bundle of nine optical fibres entrance to an arc Xenon white light. The source is lead to nine identical sensors, using the same length of optical fibre. One of the nine sensor is used as a reference, and the others as measurement channels. After crossing the sensors, transmitting light is leading (by nine same length optical fibers) to the entrance of a flat field spectrophotometer equipped with a CCD matrix detector (256 lines x 1024 columns). The detector columns give the spectral information, and the lines distinguish the nine different channels. According to the Lambert-Beer law, the absorption spectra are calculated upon eight different lines with reference to a ninth.

Radioactive wastes associated with a short scale prototype process are very restricting for measurements : firstly, because sensors are manipulated with a remote manipulator ; Secondly because some chemical products are radiology or optic contaminators ; Thirdly, because the sensor size, compared with the tubing size and the solution flow is large enough to modify hydraulic behaviour of the process (air bubble, phase partition...).

Consequently, the studied technical consists in incorporated the process tubing inside the optic pathway of an optical fibre sensor. The commercial Teflon®-PFA tubing had been chosen on the process for its high chemical resistance and an exact diameter size. Although optical performances are not good enough in the ultraviolet wavelengths, some optical filters located between the light source and the optical fibre bundle modify the incident spectrum to get an approximate flat spectrum after the light had crossed the tubing. As a result, the measured spectrum covers the range 380-700 nm with about the same signal/noise ratio.

From a spectroscopic point of view Pu^{III} Pu^{IV} and the U^{IV} U^{VI} absorption spectra (aqueous or organic phase) present undesirable effects as spectral interference. In such a case, numerical methods applied to spectral treatments (such as Partial Least Square) are often used to separate the convoluted bands and give back the desired information ; 32 determinations are obtained every 3 seconds (Pu^{III}, Pu^{IV}, U^{IV} and U^{VI} on 8 measurement lines). This method gives good results in the case of linear interference, but is not very efficient when matrix effets are significant. As part of these matrix effects, uranium VI absorption spectrum is known to be amplified and its profile modified with an increasing nitric acid concentration. These matrix effects affect drastically uranium determination which depends both on uranyl and nitric acid concentrations.

To reduce matrix effects, an empirical relationship between absorbance, uranium and nitric acid concentrations is often used at the laboratory scale. Although results are given with a good accuracy, the use of such a model for an in-line U^{VI} determination is inadequate, due to the requirement of a simultaneous nitric acid determination.

Two others more complex models had been soon developed : one explains spectral distortion by the half band width and the wavelength position of each of the fourteen absorption bands of uranyle, and the other one uses a multivariate calibration after normalisation of the absorption spectra. Unfortunately, the first one is not appropriated to an on-line determination and the second one cannot bear spectral interference with others species.

For a better accuracy, a new chemical model has been developed in our laboratory, explaining spectral distortion as the superposition of elementary spectra arising from each complex uranyle formed with nitric acid (UO_2^{2+}, $UO_2(NO_3)^+$ and $UO_2(NO_3)_2$) : On the assumption that the UO_2^{2+} vibrational structure of the first excited state is more affected by the changes of the

dipolar moment than the strength of the bond with nitrate ions, spectral distortion is interpreted as the result of a bathochromic shift between uranyle ion and uranyle complexes. Only two elementary spectral shapes with a 18 nm shift have been measured which leads to explain one of the two profiles as the result of two identical spectral identities.

Fitting the experimental spectrum with the two elementary spectral shapes, total uranium is determinated apart from the nitric acid concentration with a 5% accuracy. From the two spectral shapes ratio, free nitrate concentration is deduced with a 8% accuracy.

Distributed Optochemical Sensor Network Using Evanescent Field Interaction in Fibre Bragg Gratings

K. Usbeck, W. Ecke, A. Andreev*, V. Hagemann, R. Mueller, and R. Willsch

Institut fuer Physikalische Hochtechnologie, Helmholtzweg 4, D-07743 Jena, Germany
Tel.: +49-3641-302 870; Fax: +49-3641-302 850; e-mail: usbeck@main.ipht-jena.de
*Institute of Solid State Physics, 72 Tsarigradsko Boulevard, 1784 Sofia, Bulgaria

Abstract
The optochemical sensor network uses side-polished optical fibre elements with wavelength multiplexed fibre-optic Bragg gratings. The refractive index of the overlay material near to the surface of the polished fibre influences the propagation constant of the guided fibre mode and, thereby, decides the spectral position of the Bragg reflection. The sensor network can be applied for on-line measurement of spatial material distributions and for process control in chemical and biochemical technology.

1. Introduction

Fibre Bragg gratings are very well known as sensor elements for detection of temperature and strain (e.g., [1]). The spectral encoding of the measurand into the peak wavelength of the Bragg reflection causes independence of the measuring result on variable transmission losses. Besides this direct influence of temperature and strain onto the optical length of the fibre grating period, there is the possibility to shift the effective refractive index of the guided fibre mode by changing the material properties within the evanescent field region. In previous reports, this effect has been demonstrated at the examples of etched D-fibre [2] and long-period grating [3]. In this report, side-polished fibre segments are arranged in a multi-point chemical sensor network.
This new optical fibre grating sensor is directed to perform fast on-line measurements of refractive indices, with small size of the individual measuring site and for potential applications in chemical and biochemical technology, in hazardous surroundings, as for monitoring fluids in very deep boreholes or in petrol industry. The planar structure of side-polished fibre allows deposition of microporous layers with particular sorption properties. In evanescent field contact to the Bragg gratings, measurement of, e.g., carbon hydride concentration in air is possible.
The sensor network uses wavelength multiplexing of Bragg gratings and high resolution detection of Bragg wavelength in a CCD based polychromator [4].
Additionally, the investigation of Bragg reflection can be used as an excellent tool for studying the modal properties of optical fibres and combined thin-film fibre structures in order to create and design new functional components based on modal effects.

2. Fibre optic configuration

Single-mode optical fibre with normal birefringence, step-index profile and depressed cladding, as well as high-birefringent fibre of Panda type, beatlength 1mm, both of cut-off wavelength 750nm, were cemented in grooved glass blocks 25x5x5mm³ with 25cm bent radius of fibre. The glass blocks with the embedded fibres are polished to residual cladding thickness of about 2...0μm. This geometry, shown in Fig. 1a, yields an interaction length L_i of the evanescent field region with deposited overlays of only $L_i \approx 1.5$mm. Bragg gratings have been written in the central part of polished fibre with the same length as L_i.

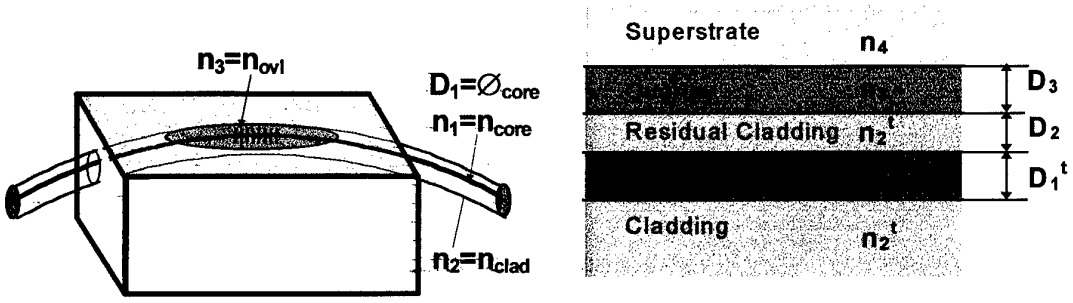

Fig. 1 Structure for evanescent field interaction between overlay and optical fibre Bragg grating

a) Sensor head basing on side-polished fibre **b)** Modal equivalent slab structure using transformed (^{t}) core and cladding parameter

A multipoint sensor array is addressed by wavelength multiplexing of sensor heads in series along one optical fibre with Bragg wavelengths between 820 and 850nm, and 6 nm apart from each other.

Shifts of the Bragg wavelengths of the gratings were measured in reflectance using a superluminescent diode as broadband light source, a spectral high-resolution polychromator with CCD line array as detector and a thermally compensated reference fibre grating for wavelength calibration. The resolution as well as the repeatability of Bragg wavelength measurement is obtained to <1pm using peak fitting algorithm [4].

3. Experimental results

The sensor heads can be used for measuring refractive indices n_{ovl} of either thin film overlays or thick layers of, e.g., liquids or other chemicals. In this report, the influence of n_{ovl} of thick liquid immersion layers onto the Bragg wavelength has been investigated. The experimental results in Fig. 2 show the tendency of increasing slope of $\lambda_B(n_{ovl})$ with decreasing residual cladding thickness D_{clad}. Also, this dependence of λ_B on the overlay material becomes slightly stronger for guided modes with smaller effective refractive index n_{eff}, i.e., for TM modes with weaker guiding conditions in the polished fibre configuration (example in Fig. 3).

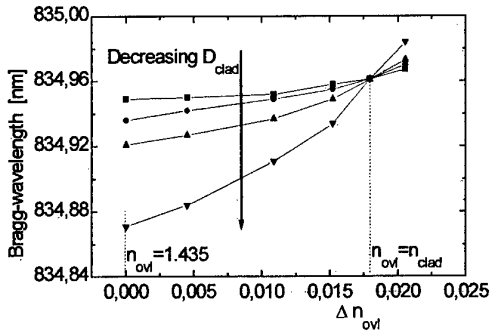

Fig. 2 Experimental dependence of $\lambda_B(n_{ovl})$ at decreasing residual cladding thickness (D_{clad}≈5...0.5µm)

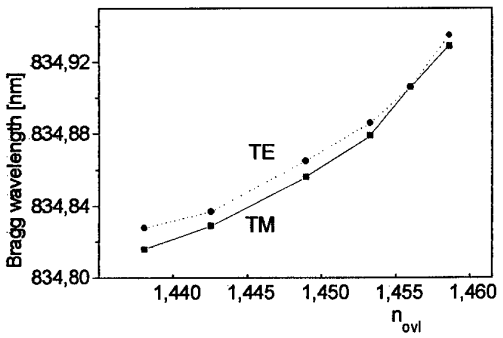

Fig. 3 Sensor efficiencies $\lambda_B(n_{ovl})$ for TE and TM modes in normal birefringent fibre D_{clad}≈0.5µm

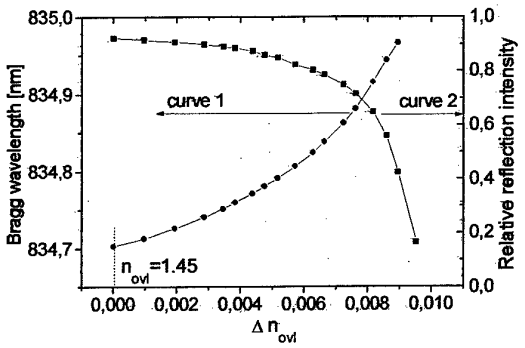

Fig. 4 Sensor characteristic at D_{clad}=0, D_{ovl}≈ 100µm, for TM mode in high-birefringent fibre, at n_{ovl}= 1.45..1.46: curve 1- $\lambda_B(n_{ovl})$; curve 2- $I_B(n_{ovl})$

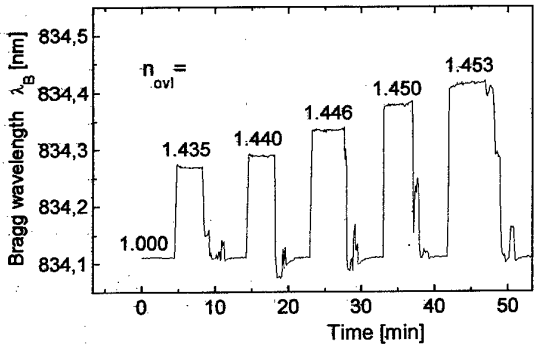

Fig. 5 Result of sensor test using various immersions as overlay material.
The test sample was manually cleaned and immersed during on-line measurement.

In further practical sensor tests, the shift of the Bragg wavelength has been measured in dependence on refractive index of the overlay material for the fast polarisation mode in high-birefringent fibre, at zero residual cladding thickness.

The sensor efficiency is characterised by the effect of overlay changes Δn_{ovl} on the effective refractive index n_{eff} of the guided mode ($\Delta n_{eff}/\Delta n_{ovl}$) or, more directly, by the Bragg wavelength shift per refractive index unit of the overlay ($\Delta\lambda_B$/riu). As the result is shown in Fig. 4, curve 1, the Bragg wavelength λ_B as well as its slope $\Delta\lambda_B/\Delta n_{ovl}$ increase with increasing n_{ovl}. In agreement with the theoretical model, the sensor efficiency becomes maximum near to the mode guiding limit, where losses of the Bragg reflection intensity I_B (curve 2 in Fig. 3) start to occur in the consequence of light modes radiating into the overlay. At lower values n_{ovl}=1.40..1.44, $\Delta\lambda_B$ amounts to 5nm/riu. The maximum sensor efficiency of 70nm/riu, or $\Delta n_{eff}/\Delta n_{ovl}$=0.11, was reached at maximum n_{ovl}≈1.46.

At a repeatability of Bragg wavelength measurement of 1pm, refractive index changes at the surface of side-polished fibre gratings of $\Delta n_{ovl}=2\cdot10^{-5}..10^{-4}$ are detected during on-line measurements (example in Fig. 5).

4. Theoretical model

In order to optimise the geometrical and optical parameters of the evanescent field Bragg grating sensor, i.e., to enhance its sensitivity to refractive index changes in the overlay, the modal properties of the polished fibre with overlay have been calculated in dependence on n_{ovl}. A multi-layered slab waveguide model with a layer structure according to Fig. 1b has been applied. In this model, the parameters of the fibre core, refractive index n_1 and diameter D_1, and the refractive index of the fibre cladding n_2 are transformed into the parameters of a modal equivalent slab waveguide n_1^t, D_1^t, and n_2^t [5]. This transformation is chosen in order to maintain the modal parameters - cut-off wavelength and effective refractive index n_{eff} - of the model slab waveguide equally to them of the single-mode fibre used in the experiments. The periodic Bragg grating structure of the refractive index in the fibre core is treated as a weak perturbation without influence on the mode calculation. The dependence of the Bragg wavelength λ_B on n_{ovl} of the fibre optic sensor is determined by:

$$\lambda_B(n_{ovl}) = 2\cdot\Lambda\cdot n_{eff}(n_{ovl}).$$

The intensity characteristic of the Bragg reflection is derived from the electric field distribution across the multi-layer structure. Some of the results are demonstrated in the example of Fig. 5. The sensitivity of the sensor is characterised by the slope of $n_{eff}(n_{ovl})$. At $n_{ovl}<n_{eff}$ and $n_{ovl}<n_{core}$, the overlay thickness is not limited. Already at $d_{ovl}\approx 5\mu m$, the sensor structure has its maximum sensitivity on changes in n_{ovl}. It increases with n_{ovl} approaching to n_{core}.
At very low d_{ovl}, also high-refracting overlays will not guide radiating modes, and the sensor efficiency is further increasing. The sensor efficiency can be optimised for lower n_{ovl} by choosing appropriate buffer layers below the sensing overlay, and by using single-mode fibre with higher working wavelength.

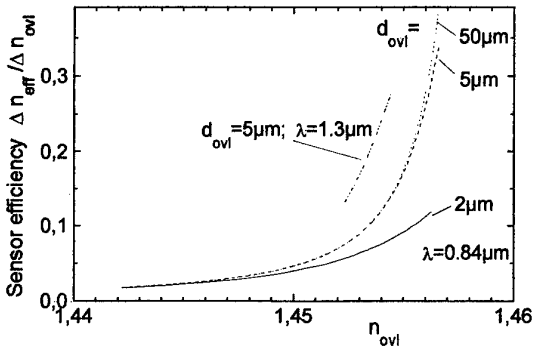

Fig. 5 Sensor efficiency $\Delta n_{eff}/\Delta n_{ovl}$ as derived from the modal equivalent slab model for various overlay thickness d_{ovl} (TE mode, n_4=1). Already at d_{ovl}=5μm (overall volume 40pl) the maximum sensitivity on overlay changes is achieved.
At longer wavelength, λ=1.3μm instead of 0.84μm, the sensor efficiency is increasing, too.

5. Conclusion

A spectrally encoded refractive index sensor structure using side-polished optical fibre elements with wavelength multiplexed Bragg gratings has been developed. Chemical sensor networks basing on Bragg gratings allow for fast on-line measurements of spatial distributions and process control in chemical and biochemical technology.
Practical sensor applications using microporous layers with specific sorption of carbon hydrides or humidity [6] are under preparation. According to the results from the theoretical model, highest sensitivity will be achieved using high refractive thin porous TiO_2/SiO_2 layers.
In the chemical multi-point sensor network, simultaneous measurement of refractive indices and of temperature will be performed. Temperature effects can be eliminated from the chemical sensor characteristics using the temperature-induced Bragg wavelength shifts in adjacent non-exposed parts of fibre gratings. For this reason, Bragg gratings will be written (i) with a length greater than the interaction length of the side-polished fibre, or (ii) separately, in the non-polished part of the embedded fibre.

6. References

[1] Yun-Jiang Rao, "In-fibre Bragg grating sensors", Meas. Sci. Technol. Vol. 8, pp. 355-375 (1997)

[2] G. Meltz, S.J. Hewlett, and J.D. Love, "Fiber grating evanescent-wave sensors", Proceedings of SPIE Vol. 2836 Chemical, Biochemical, and Environmental Fiber Sensors VIII, pp. 342-350 (1996)

[3] V. Bhatia and A.M. Vengsarkar, "Optical fiber long-period grating sensors", Optics Letters Vol. 21, pp. 692-694 (1996)

[4] W. Ecke, J. Schauer, K. Usbeck, R. Willsch, and J.P. Dakin, "Improvement of the stability of fiber grating interrogation systems using active and passive polarization scrambling devices", Proceedings of 12th Optical Fiber Sensor Conference, pp. 484-487 (1997)

[5] W. Haubenreisser, W. Ecke, S. Schröter, G. Schwotzer, and R. Willsch, "Matching of a bent step-index single-mode fiber by a modal equivalent slab waveguide structure", physica status solidi (b), Vol. 186, pp. 315-330 (1994)

[6] G. Schwotzer, K.-J. Reichelt, E. Sinn, T. Wieduwilt, and R. Willsch, "Potential low-cost spectral-encoded optical fiber sensor system: Technology and applications", Proc. of 12th Internat. Conf. on Optical Fiber Sensors, pp. 378-381 (1997)

Solution Concentration Measurements by means of Optical Fiber Long-Period Gratings

R. Falciai, A.G. Mignani, A. Vannini

IROE-CNR, Dept. Optoelectronics and Photonics, Via Panciatichi 64, I-50127 Firenze, Italy
ph. +39-55-42351, fax +39-55-4379569, email: falciai@iroe.fi.cnr.it

Introduction

The measurement of the concentration of stock solutions, dilutions, oils, and water-soluble industrial fluids is of interest in many quality control industrial processes in order to check the concentration stability and abnormal ageing effects. Off-line refractometers, such as the Abbe type, which offer a resolution of 0.2%, are commonly used.
This paper presents an optical fiber long-period grating which has been tested for the refractometry of sodium chloride and calcium chloride aqueous solutions for a range of density varying from that of distilled water to that of a nearly-saturated condition.

Working Principle

An optical fiber long-period grating (LPG) couples the fundamental mode to discrete forward-propagating cladding modes, which attenuate on propagation. Consequently, the transmission spectrum shows loss peaks at the resonant wavelengths [1-4]. When an un-jacked optical fiber LPG is immersed in a solution, the spectral position of the loss peaks is determined by the refractive index and temperature of the solution. If the solution is thermostatized, the measurement of the refractive index only is achieved, and, consequently, the solution concentration. Because measurements are recovered in the wavelength domain, they result intrinsically independent of any spurious intensity modulation of the electrooptic and fiber systems.

Experimental Setup

LPGs were provided by Bell Laboratories, Lucent Technologies. They are written in standard dispersion-shifted hydrogen-loaded fibers and have a periodicity of about 400 μm.
An ELED emitting at λ=1.55 μm and an Anritsu spectrum analyzer were used as source and detector. The spectrum analyzer resolution was set at $\Delta\lambda$=0.1 nm. The LPG was fixed to a rigid support and immersed in the liquid being tested, which was thermostatized at 20°C. Figure 1a shows the measured transmission spectra of the LPG in air and in distilled water. Because the width of the loss peaks was larger than 15 nm, a first derivative analysis gave more precise results, as shown in Figure 1b. For refractometric measurements, the spectral shift of the highest order loss-peak was taken into account.

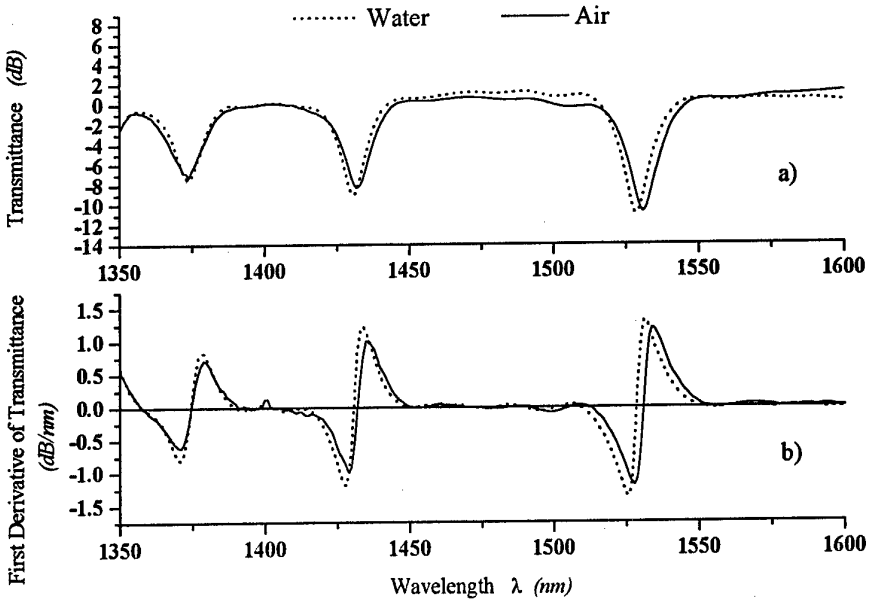

Figure 1 Measured transmission spectra and first derivative of LPG in air and distilled water

Solution Concentration Measurements

Aqueous solutions of sodium chloride (NaCl) and calcium chloride ($CaCl_2$) were tested in the concentration ranges of 40-260 g/l and 30-400 g/l, respectively. The refractive indices of the solutions were gauged by means of the minimum deviation method, using a hollow-prism spectrogoniometer with a $\Delta n=1.5\cdot10^{-3}$ resolution.

The spectral shift of the LPG highest-order loss-peak as a function of the solution refractive index and concentration for NaCl and $CaCl_2$ solutions is shown in Figures 2 and 3, respectively, while the superimposition of the fitting curves is shown in Figure 4.

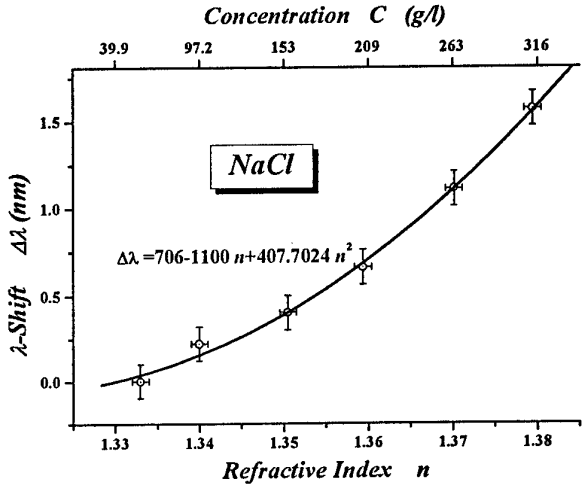

Figure 2 Spectral shift of the LPG highest-order loss-peak versus refractive index and concentration of NaCl solutions

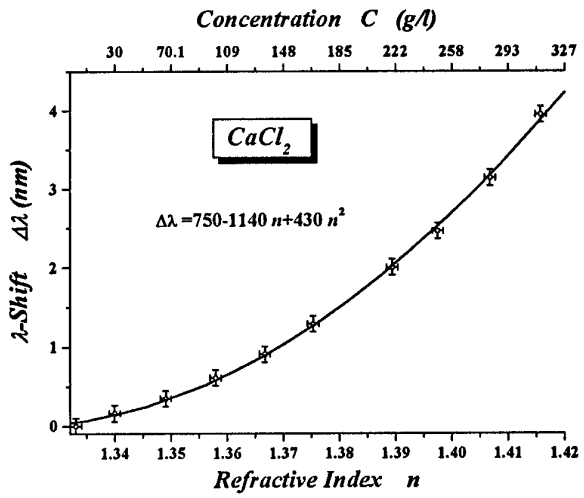

Figure 3 Spectral shift of the LPG highest-order loss-peak versus refractive index and concentration of $CaCl_2$ solutions

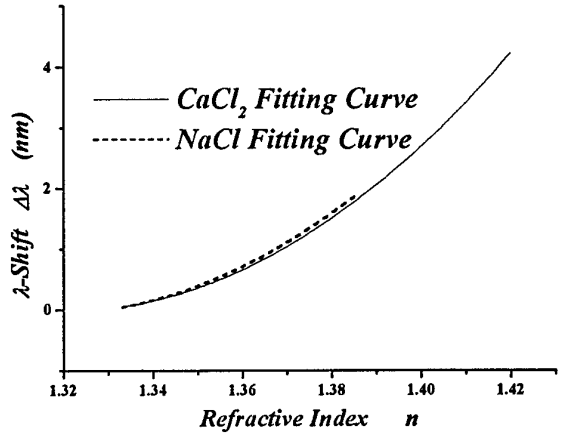

Figure 4 Superimposition of the fitting curves of Figures 2 and 3

The minimum concentration variations that can be resolved range between 40 g/l and 10 g/l for highly-diluted or nearly-saturated NaCl solutions, and between 30 g/l and 4 g/l for highly-diluted or nearly-saturated $CaCl_2$ solutions.

Conclusions

Optical fiber long-period gratings were tested for measuring the concentration of aqueous solutions having refractive indices in the 1.34-1.42 range. The resolutions achieved were comparable with those offered by conventional Abbe refractometers commonly used for concentration measurements. The optical fiber approach does not require any sample drawing,

and is indicated especially in the production of solutions the handling of which may be harmful. Harmful solutions under test are NaOH and H_2SO_4 solutions, the production of which has a significant industrial interest. In addition to concentration measurements, mixture analysis and emulsion characterization could also be performed.

Acknowledgements

The authors thank Ashish M. Vengsarkar of Bell Laboratories, Lucent Technologies for providing the optical fiber long-period gratings, and Giuseppe Molesini of National Institute of Optics for helping in the solution refractive index gauging.

References

1. V. Bhatia, A.M. Vengsarkar, "Optical fiber long-period grating sensors", Optics Letters vol. 21, n. 9, 1996, pp. 692-694.
2. V. Bhatia, T. D'Alberto, K.A. Murphy, R.O. Claus, A.M. Vengsarkar, "Optical fiber long-period grating sensors", Proc. 11th Optical Fiber Sensors Conference, AP961211, 1996, pp. 360-363.
3. V. Bhatia, K.A. Murphy, R.O. Claus, A. Vengsarkar, "Simultaneous measurement systems employing long-period grating sensors", Proc. 11th Optical Fiber Sensors Conference, AP961211, 1996, pp. 702-705.
4. Z. Zhang, J.S. Sirkis, "Temperature-compensated long period grating chemical sensor", Proc. 12th Optical Fiber Sensors Conference, 1996, pp. 294-297.

Radiation Dosimetry in Radiotherapy: a Model for an Extrinsic Optical Fiber Sensor

A.G. Mignani *, S. Romano **, F. Fusi **, A. Mencaglia §

* IROE-CNR, Dept. Optoelectronics and Photonics, Via Panciatichi 64, I-50127 Firenze, Italy
ph. +39-55-42351, fax +39-55-4379569, email: mignani@iroe.fi.cnr.it
** University of Florence, Dept. Clinical Physiopathology, Viale Morgagni 85,
I-50134 Firenze, Italy, ph. +39-55-434452, fax +39-55-414612, email: fusi@ieq.fi.cnr.it
§ PRODOTEC srl, Via Antognoli 28/30, I-50127 Firenze, Italy
ph. +39-55-416050, fax +39-55-435728, email: mencaglia@iroe.fi.cnr.it

Introduction

The success of radiotherapy relies on the on-line monitoring of the dose of radiation to which the tumour and its adjacent tissues are exposed. Conventional thermoluminescence dosimeters provide only off-line monitoring, since they determine the radiation dosage after completion of the exposure. In order to overcome this limitation, optical fiber sensors have been proposed, which allow for a minimally invasive, real time and continuous monitoring of the delivered dosage. These sensors make use of radio-transducers which are coupled at the end of a radiation-resistant fiber link, so as to obtain a radiation-induced intensity modulation. Typical radio-transducers are:

- *phosphors*, which are stimulated to produce a visible luminescence linearly related to the radiation exposure [1];
- *heavy-metal-doped fiber sections*, which undergo an intensity attenuation in the presence of radiation [2,3];
- *radiochromic dyes*, which exhibit radiation-modulated optical absorption spectra [4].

This paper presents preliminary tests of radiation dosimetry performed by means of an extrinsic optical fiber sensor which makes use of a radiochromic film as radio-transducer. The spectral behaviour of the transducer allows for two-wavelength differential measurements, so as to obtain a referenced intensity-based sensor output.

Working Principle

The sensing material is a Gafchromic™ film, model #37-041 [5]; the film consists of a thin sensitive layer (23μm) coated on a 100 μm polyester base. The sensitive layer is made of microcrystals of radio-sensitive monomer uniformly dispersed in a gelatin binder. When the microcrystals are irradiated, a polymerization occurs which produces an irreversible blue coloration.
Different samples of the same Gafchromic™ sheet were exposed to different doses of X-ray beam produced by a nominal 6 MV linac with doses in the 0-100 Gy range. Optical characterization of the Gafchromic™ films was performed by measuring the reflectance,

transmittance and absorption spectra of the radioexposed samples. Figure 1 shows the results obtained by means of absorption measurements [6]. For sensing purposes, the sensing and reference signals can be chosen in the radiation-modulated band around 660 nm and in the radiation-insensitive band for wavelengths longer than 750 nm, respectively,.

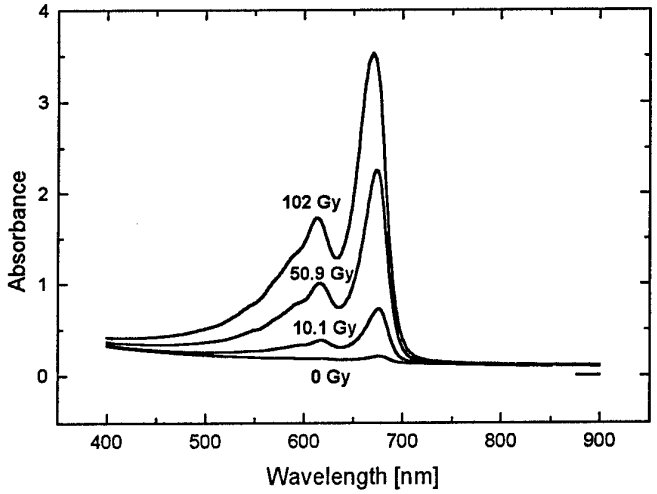

Figure 1 Absorption spectra of Gafchromic films irradiated at different dosages

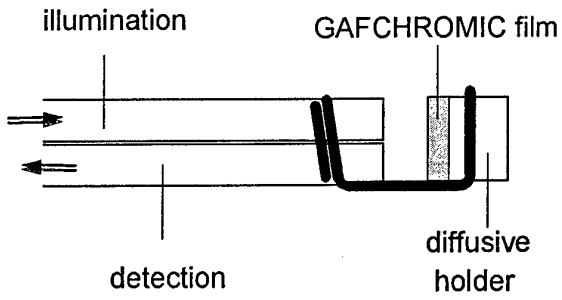

Figure 2 The optical fiber probe for radiation dosimetry

In order to demonstrate the possibility of implementing an optical fiber sensor, the radio-exposed films were examined by means of the probe sketched in Figure 2. The optical fiber link consisted of two identical fibers for illumination and detection, respectively. Plastic optical fibers 250 μm diameter were chosen on the basis of their near-water equivalent. The Gafchromic™ film was fixed on a small disc of PVC that acts as a diffusive layer, which was positioned in front of the fiber link by means of a spring. The coupling efficiency between the illumination and detection channels was better than 1%. The PVC holder was machined so as to allow reproducibility of film repositioning. Lastly, a transparent plastic cap was used for probe mechanical protection.

Experimental Results

The electrooptic module was a multiwavelength unit which was implemented for the interrogation of indicator-based optical fiber sensors. The module housed several LEDs to slice the 0.4-0.9 nm spectral range, and several PINs with different spectral sensitivities. LEDs and PINs were inserted in ST-compatible receptacles for easy connection to almost any fiber optic link. The unit was interfaced to a portable PC by means of an A/D board with input/output ports. LED driving and PIN outputs were software managed by means of a time division multiplexing procedure. This software made it possible to customize the measuring procedure according to the application requirements. For the experiment on radiation dosimetry, the module was programmed to perform two-wavelength differential measurements at 655 nm and 840 nm as sensing and reference signals, respectively.

The previously radio-exposed films were sequentially fixed to the PVC disc and analyzed by means of the afore-mentioned two-wavelength differential measuring unit. Practically, a combination of absorption, reflectance and scattering measurements was performed on the radio-sensitive film fixed to the PVC disc. The measurement performed on each radio-exposed film, M_{exp}, was compared with the measurement performed on a non-exposed film, M_{ref}. The model for the optical fiber sensor output was considered as $S=-10Log(M_{exp} / M_{ref})$.

Figure 3 and 4 show the results of this experimental trial, for low and high radiation dosages, respectively. The sensor output exhibited a dynamics of 9 dB for exposures to dosages in the 0-30 Gy range, with a dynamics of 2.5 dB and a nearly-linear behaviour in the 0-5 Gy range.

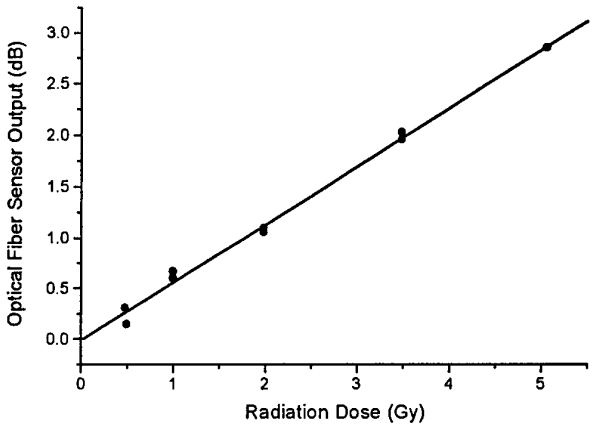

Figure 3 Optical fiber sensor output for low radiation dosage

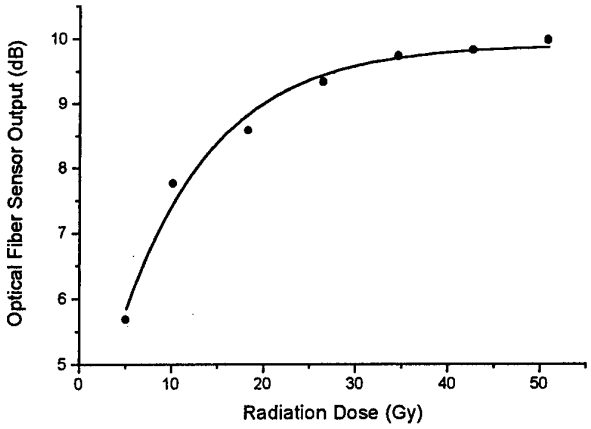

Figure 4 Optical fiber sensor output for medium-high radiation dosage

Conclusions

The use of a Gafchromic™ film for radiation dosimetry in combination with optical fibers has been demonstrated. Because of the non-reversible radiochromism of the film, potential applications involve only the implementation of disposable probes to be permanently inserted in a tumor or adjacent tissues, so as to dose the radiation during the whole cycle of exposures. Tests in phantoms are under investigation using the probe of Figure 2, together with studies of the Gafchromic™ film autodevelopment as well as the influence of temperature, humidity and ageing interfering effects.

References

1. Soltani, G. Pierce, "Novel fiber optic radiation sensor for in vivo dosimetry", Proc. SPIE vol. 1648 *Fiber Optic Medical and Fluorescent Sensors and Applications*, 1992, pp. 71-82.
2. H. Bueker, F.W. Haesing, E. Gerhard, "Physical properties and concepts for applications of attenuation-based fiber optic dosimeters for medical instrumentation", Proc. SPIE vol. 1648 *Fiber Optic Medical and Fluorescent Sensors and Applications*, 1992, pp. 63-70.
3. H. Bueker, F.W. Haesing, F. Pfeiffer, H.J. Schmitz, "A fiber-optic twin sensor for dose measurements in radiation therapy", Proc. 11th Optical Fiber Sensors Conference, AP961211, 1996, pp. 690-693.
4. P.B. Lyons, "Review of high bandwidth fiber optics radiation sensors", Proc. SPIE vol. 566 *Fiber Optic and Laser Sensors III*, 1985, pp. 166-171.
5. GAFChemical Corp., Wayne, NY.
6. S. Romano, F. Fusi, E. Bolla, A. Mencaglia, A.G. Mignani, "Optical fibers and radiochromic films for dosimetry in radiotherapy", Proc. SPIE vol. 2928 *Biomedical Systems and Technologies*, 1996, pp. 276-282.

MICROX II - A New Generation of Portable Measuring Systems for Microoptodes

Gerhard Holst, Michael Kühl and Oliver Kohls

Max-Planck-Institute for Marine Microbiology, Microsensor Research Group,
Celsiusstr. 1, D - 28359 Bremen, Germany
Tel: +49-(0)421-2028-834
Fax: +49-(0)421-2028-690
e-mail: gholst@mpi-bremen.de
mkuehl@mpi-bremen.de
okohls@mpi-bremen.de

Summary

Sediments, microbial mats, biofilms and other microbial communities are characterized by steep gradients of physical and chemical parameters. Fibre optical microsensors, microoptodes, that we developed over the last three years have become powerful tools to investigate and measure these parameters with a sufficient spatial resolution and with a minor disturbance of the micro-environment in natural systems.

Together with microoptodes for oxygen[1], pH, temperature we developed a sensitive measuring system[2,3] that enables the measurement of luminescence intensities and lifetimes of indicators that are immobilized at the tip of tapered fibers.

As light sources, we used light emitting diodes, that nowadays are available with a high optical power output even in the blue part of the spectrum, where many indicators can be excited. Furthermore, LEDs are easy to modulate and thus enable both, the measurement of luminescence intensities independent of ambient light and the measurement of luminescence lifetimes based on a phase modulation technique. The weak amount of light emitted at the tip of a dip-coated silica-silica fibre required, however, a photomultiplier tube (PMT) as detector[2,3]. Although the PMTs are very sensitive light detectors, the application in natural systems for measurement of concentration profiles with and without strong ambient light causes additional noise problems with the PMT[3]. Therefore, we improved the composition of the sensing layer

that covers the tapered fibre tip and the taper geometry, because both have a large impact on the signal (see abstract of Kohls et al.). Furthermore, we improved the optical setup to reduce inherent coupling losses and inherent noise signals like unwanted additional luminescence caused by epoxy, solvents etc..

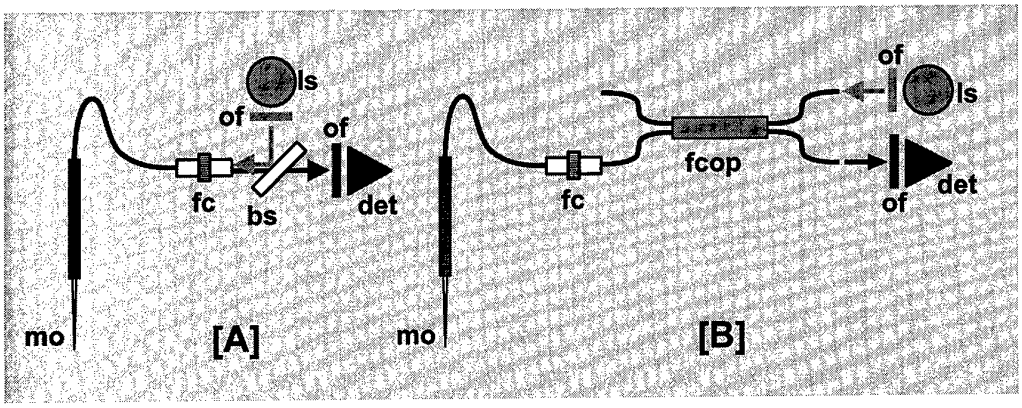

The figure above shows schematically the two principal optical setups that can be used for the application of microoptodes. Setup [A] consists of an excitation light source (ls), a LED, optical filters (of), a beamsplitter (bs), standard fibre connectors (fc) and the sensor, the microoptode (mo) and a PIN-photodiode detector (det). Setup [B] has a fibre coupler in place of the beamsplitter. To reduce the losses due to coupling, that usually amount to 50%, we applied wavelength selective coupling. In setup [A] the beamsplitter is a dichroic mirror and in setup [B] the coupler is a new device consisting of GRIN-lenses and a dichroic mirror. In case [B] we achieved a gain factor of 4 compared to the standard fibre coupler and in [A] the factor was between 8 and 10. This gain in optical signal together with the improved microoptode design enabled the use of photodiodes instead of PMTs.

We present the first all-solid-state instrument, MICROX II, that is based on the previously released portable instrument MICROX I, that uses a PMT as detector. Noise influences caused by additional luminescence in setup [A] and [B], and their possible reduction will be presented. Examples of first applications of the instrument will also be shown.

[1] „Fiber-Optic Oxygen Microsensors, a New Tool in Aquatic Biology", I. Klimant, V. Meyer and M. Kühl, Limnology and Oceanography, Vol. 40 (6), 1995, pp. 1159-1165.

[2] "A Novel Measuring System for Oxygen Microoptodes", G. Holst, M. Kühl and I. Klimant, Chemical, Biochemical and Environmental Fibre Sensors VII, SPIE EUROPTO, Munich, Germany, 19-23 June, Vol. 2508, 1995, pp. 387-398.

[3] "A Microoptode Array for Fine Scale Measurement of Oxygen Distribution", G. Holst, R.N. Glud, M. Kühl and I. Klimant, Sensors and Actuators B, Vol. 38, 1997, pp. 122-129.

Microoptodes: the role of fibre tip geometry for the sensor performance

Oliver Kohls, Gerhard Holst, and Michael Kühl

Max-Planck-Institut für Marine Mikrobiologie, Microsensor Research Group,
Celsiusstr. 1,
D-28359 Bremen, Germany; Tel.:+49-(0)421-2028-834, Fax: +49-(0)421-2028-690
e-mail: okohls@mpi-bremen.de

Key words: Microsensor, optode, fibre optics, taper, optical insulation, tip geometry

Summary

Established sensors for fine scale measurements in natural environments are based on electrochemical measuring principles for e. g. oxygen and pH. The preparation of such electrochemical sensors is, however, a time consuming process. Based on the technical progress in the field of fibre optical measuring techniques many well-known chemical principles can now be used for the preparation of optical sensors, e.g. the oxygen measurement by luminescence quenching, and the pH-measurement with absorption based dyes. The use of optical fibres offers a high potential for miniaturisation of sensors [1]. For high spatial resolution measurements, the sensor chemistry has to be immobilised on the fibre tip, and the excitation and emission light has to be guided via the same fibre.

Measurements in the gas phase or in a measuring cell with constant optical conditions are possible to do without additional manufacturing steps. For applications in natural environments optodes are however often overcoated by an additional layer – the optical insulation. This layer has to be highly permeable for the analyte in order to avoid a significant increase of the response time. In the past, the optical insulation was also necessary to enable measurements at ambient light. The modern lock-in technology is able to separate the modulated signal of the sensor from the background signal, which comes from ambient light. There are, however, additional influences on the signal in the same modulation frequency, which cannot be filtered out completely, e. g. back scattered light from gas bubbles or particles. Furthermore, there can be additional luminescence in the measuring medium. Chlorophyll, carotenoids, bioluminescence and many other substances exhibit changes of their optical properties in the same part of the light spectrum as optical chemosensors. In Figure 1 the luminescence spectrum of a microbial mat in approximately 2 mm depth is shown. The natural luminescence of the probe and back scattered light will also influences the life-time measurements, leading to a lower signal to noise ratio. Also, the light emitted from the sensor tip can influence

the natural conditions, in the probe. For example, the often used blue or bluegreen excitation light for oxygen optodes can stimulate photosynthesis and therefore a change of the oxygen concentration. Therefore, an optical insulation is still useful for many applications.

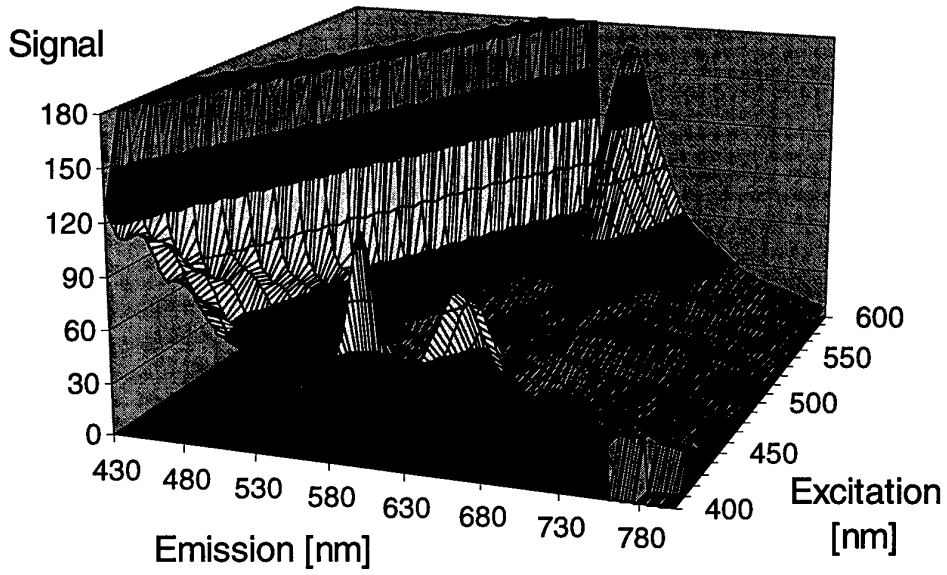

Figure 1: Luminescence spectrum of a microbial mat in a depth of 2 mm

In order to increase the spatial resolution of the measurement the optical fibre can be tapered. Microptodes with tip diameters of a few micrometers have been developed. The tapering process influences, however, the working principle of optical fibres. The needed thickness of the cladding material on the fibre core will be reduced also. In the taper, the thickness of the cladding layer can decrease down to a diameter where the light becomes able to pass it. The amount of guided light is, thereby, reduced and the signal decreases. Therefore the geometry of the taper becomes important for the construction of microoptodes especially for measurements in the aquatic phase, which has a refractive index closer to quartz glass.

We present investigations of the dependency of the signal intensity of microoptodes as function of the tip size and geometry. The manufacturing process is described in detail. The width of the heated part and the pulling force are the key parameters in this process. Measurements of the melting process and determinations of the final core to cladding ratio cannot be done in an easy way. Therefore, we looked for empirical correlation. We compared the macroscopic effects like the change in sensor signal from gas phase to aquatic phase. Finally, we give a suggestion for an optimal geometry of the taper, which leads to a high signal. All these investigations were based on a Ruthemium dye immobilised in polystyrene at the fibre tip.

For tapered microoptodes the optical insulation is much more complicated compared to untapered fibre sensors. Normally, black polymers like silicone are used for the optical insulation. The refractive index of these materials is in the most cases not useful to provide the needed difference for the light guiding. The amount of guided light is, therefore, reduced dramatically. Here we present microsensors, where a good compromise between insulation and signal intensity was obtained. In Figure 2 two different tapered microoptodes with tip diameters in the same range are shown, without (Fig. 2a and 2c) and with optical insulation (Fig.: 2b and 2d). Differences in the signals can be measured clearly.

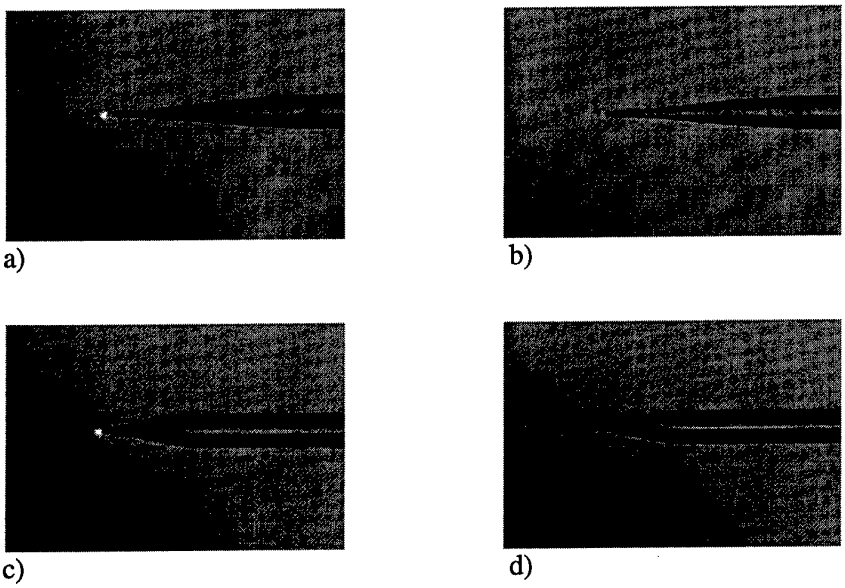

Figure 2: Oxygen microoptodes without (a and c) and with optical insulation (b and d). The tip diameter is approximately 10 to 15 µm

[1] Klimant, I.; Meyer, V.; Kühl, M.
Fiber-optic oxygen microsensors, a new tool in aquatic biology
Limnol. Oceanogr., 40, 6, 1159-1165, 1995

Optical fibre refractive index sensor using surface plasmon resonance and a TiO_2 coating obtained by sol-gel process.

A. Trouillet, C. Veillas, J.P. Goure and H. Gagnaire

Laboratoire Traitement du Signal et Instrumentation, CNRS UMR 5516
✍ : 23, rue du Docteur Paul Michelon - 42023 Saint-Etienne Cedex 2 - France
tel : +33 4 77 48 15 71 - fax : +33 4 77 48 51 20 - e-mail : ltsi@univ-st-etienne.fr

Abstract

A simple fibre sensor for continuous monitoring of refractive index variations of liquid mixtures is described. The principle of this sensor, based on the excitation of a surface plasmon at a metal/dielectric interface, has been descibed in previous articles. In this paper it is shown that this set-up, which uses monochromatic incident light, can work as a refractive index variation sensor either in a range between 1.36 and 1.40 when using a single silver layer or in a range shifted down to 1.33 when coating silver by a thin TiO_2 adaptative layer obtained by sol-gel process.

1. Introduction

Instrumentation development in new technologies for detecting chemical parameters is expected in various fields such as industrial processes, medical diagnoses and environmental control. Optical instruments, and, more precisely, optical fibres are promising because of their small size and their non destructive manner which offer considerable advantages compared to traditional sensors. The possiblity of performing remote detection measurements of chemical species in a hostile or explosive environment with continuous monitoring often makes optical fibre sensors very attractive for industrial applications.

Excitation of a surface plasmon resonance (SPR) was shown very interesting for measuring refractive index variations of a dielectric medium because it allows the realization of fast sensors with high accuracy. It can be shown from the electromagnetic theory that a p-polarized surface plasma (SP) wave may exist at the interface between a dielectric and a metal. The propagation constant (or the effective index n_{sp}) of this wave is very dependent on the dielectric constant of the metal and on the refractive index n_d of the dielectric. In actual situation, this SP wave can be excited by the evanescent wave from a high refractive index prism (n_p) as in the Kretschmann configuration. The angle of incidence on the prism basis θ_{sp} for which SPR occurs is greater than the critical angle $\sin^{-1}(n_d/n_p)$ and such that :

$$n_p.\sin\theta_{sp} = \text{Real Part}(n_{sp}) \qquad (1)$$

This angle gives the position of the dip in the reflectivity curves R(θ) where θ is the angle of incidence on the prism basis. As shown on figure 1, the value of θ_{sp} is very dependent on the refractive index n_d of the surrounding dielectric medium for a given metal (silver in our case). Therefore, Surface Plasmon Resonance (SPR) has been extensively studied for the detection of chemical and biochemical species. The Kretschmann configuration is very interesting and, therefore, has often been utilized because the refractive index and the angles of the prism may be chosen so that relation (1) is satisfied whatever the refractive index of the dielectric medium under test is. On the other hand, the incident beam must be properly polarized, either collimated or focused. So, the Kretschmann configuration cannot lead to a very simple arrangement. Therefore, it seemed necessary to replace the prism and the polarizer by another equipment.

Jorgenson and Yee described for the first time a SPR sensing configuration using a multimode optical fibre [1,2]. A white light source and a fiber optic spectrometer were needed. The refractive index of the dielectric medium to be sensed is determined from the value of the wavelength for which the SP resonance occurs. The dynamic range of their experimental set-up ranges from 1.25 to 1.40. More recently, we have developped a new system, simple and inexpensive, with an optical fibre eliminating both the traditional bulk prism and the spectrometer.

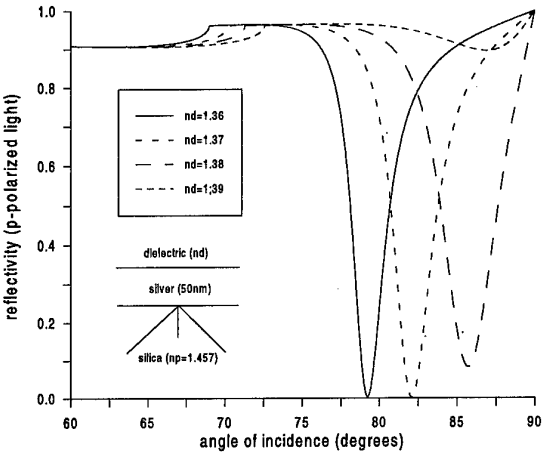

figure 1: Theoritical reflectivity R(θ)

2. Principle and experimental set-up

This sensor has been completely described previously [3,4]. It uses a multimode optical fibre which core replaces the high refractive index prism (figure 2) and a specific injection of a monochromatic light. The core is metallized on the sensing area (15 mm length). The collimated beam of a laser diode which emits in the visible range (670 nm) is injected into the fiber with the angle of incidence α that can be varied with high accurary between 0 and 30°. It is shown that some of the skew rays propagated in the fibre can undergo reflections at the core/metal interface with the specific SPR coupling angle θ_{sp}. Thus the light power P, transmitted through the entire fibre, is attenuated because an amount of the incident optical energy is transferred to the SP

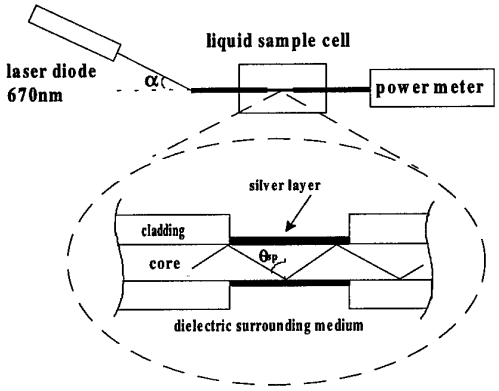

figure 2 : Experimental set-up

wave. The P(α) curves depend on the refractive index of the dielectric medium surrounding the fibre (figure 3). In other words small changes in the refractive index of the surrounding medium can be monitored by the variations of P measured for a fixed angle α (dashed vertical line in figure 3). The smallest change that can be detected with this device is about 5.10^{-5}.

The main differences between the P(α) curves (fiber configuration) and R(θ) curves (Kretschmann configuration) are the following :

- it can be shown that the SPR can occur in the fibre for different values of the angle α; therefore the dip in a P(α) curve is larger then that in the corresponding R(θ) curve,
- in the fiber, the s- and p-polarizations are mixed; so the minimal value of P(α) is different from zero despite the fact that each ray can undergo several reflections,
- due to the propagation of the light in the coated section of the fibre the coupling angle θ_{sp} lies roughly between 75 and 90°. Consequently, as shown on figure 1, the refractive index of the dielectric media under test ranges from 1.36 to 1.39 (silver layer).

It seems necessary to extend this range to values as low as 1.33 for detection in aqueous solutions. This can be done either by using another metallic compound (gold) or by coating the metallized part of the fibre with a thin dielectric layer whose refractive index is high.

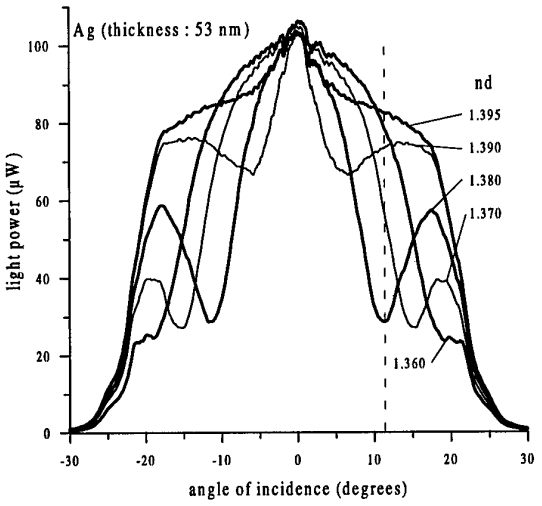

figure 3 : Experimental P(α) for silver layer

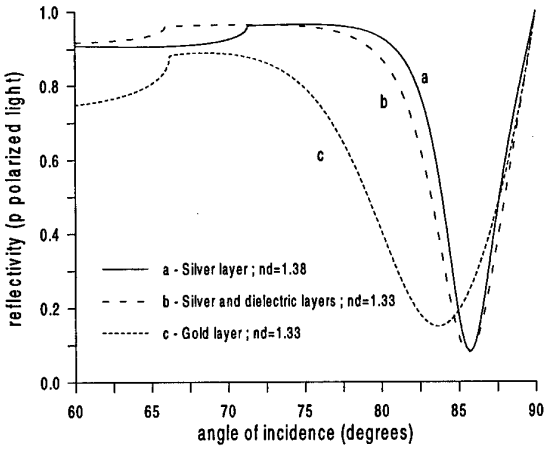

figure 4 : R(θ) for different sensing layers

3. Modification of the dynamic range

The amount of the light transmitted by the fibre mainly depends on the reflectivity of the p-polarized light. Figure 4 shows similar reflectivity curves a and b obtained respectively when the silver layer is surrounded by a 1.38 refractive index medium and when the silver layer coated by a thin dielectric layer is immersed in pure water. The layer's thickness t = 14 nm and its dielectric constant ε = 3.4 of the layer has been found by trial and error.

Such a layer allows detection of refractive index change of aqueous solutions. Nevertheless, the width of the dip in the R(θ) curve slightly increases when the thin layer is added and therefore the sensitivity of the sensor decreases a little. Curve c in figure 4 is the reflectivity

curve related to a gold layer immersed in water. The extension of the refractive index range could also be obtained by using gold as the metal ; but the width of the dip is too large and the sensitivity of the sensor would be poor.

4. Deposition of the adaptating layer by sol-gel process

The sol-gel technology is now well known. It enables the preparation at low temperature of amorphous inorganic oxide thin films through hydrolysis and condensation of liquid mixtures of metalalkoxides (the "sol"), which are homogeneous at the molecular scale, into a densely cross-linked network (the "gel"). This technology presents several advantages. The ability to modify the composition of the materials on a large scale (various metallo-organic precursors, various organic solvents,...) to monitor their optical properties (refractive index) and the easy shaping of the obtained materials (dip-coating) are of great interest for our purpose.

Several methods allow the preparation of "sols" of TiO_2, of SiO_2 or of a mixture of both of them. It is therefore possible to adapt the refractive index of optical thin films by the selection of the appropriated "sol". The precursor used for the synthesis of TiO_2 "sols" is titanium isopropoxide $Ti[OCH(CH_3)_2]_4$ or $Ti(OPr^i)_4$. The reactions of hydrolysis and condensation can be resumed as follows :

hydrolysis : $Ti(OPr^i)_4 + H_2O \rightarrow (OPr^i)_3Ti - OH + Pr^iOH$

condensation : $Ti - OH + HO - Ti \rightarrow Ti - O - Ti + H_2O$

$Ti - OPr^i + HO - Ti \rightarrow Ti - O - Ti + Pr^iOH$

The deposition of thin TiO_2 layers has been performed by dip-coating onto the metallized sensing area. The fibre is first dipped into the solution and then, to avoid vibrations, the solution is pulled down at uniform speed. The sample is then dried at controlled temperature (150°) for 15 minutes. The density (so the refractive index) and the thickness of the final layer depends on both the pulling velocity and the drying temperature.

5. Experimental results

Figure 5 presents the experimental P(α) curves obtained with a silver layer (thickness 50 nm, length 15 mm) coated by an adaptative layer of TiO_2. As expected the refractive index range for this sensor has been shifted down to 1.33. The dips in these P(α) curves are less sharp than those observed in figure 3 leading to a minor deterioration of the performances of the sensor. This may be due to a small absorption in the sol-sel layer not taken into account in the computed R(θ) curves (see figure 4).

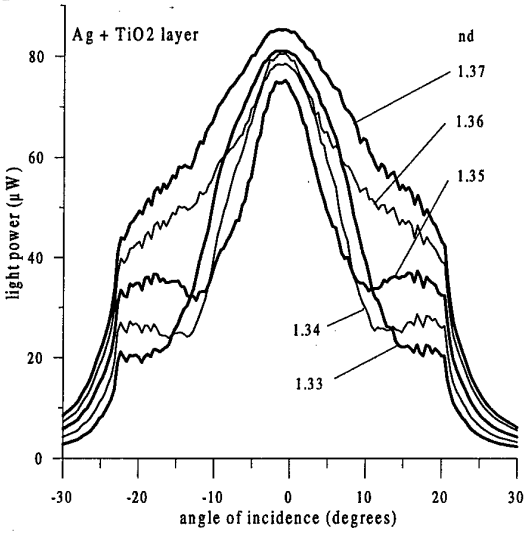

figure 5 : Experimental P(α) curves for silver layer coated by TiO_2

6. Conclusion

A simple fibre sensor for continuous monitoring of refractive index variations of liquid mixtures has been described. In this paper we have shown that the deposition of a thin dielectric adaptating layer on the sensing area allows a modification of the dynamic range of the sensor.

7. References

[1] R.C. Jorgenson and S.S. Yee, Sensors and Actuators B, 12 (1993), 213-220.
[2] R.C. Jorgenson and S.S. Yee, Sensors and Actuators A, 43 (1994), 44-48.
[3] A. Trouillet, C. Ronot-Trioli, C. Veillas and H. Gagnaire, Pure and Appl. Opt 5 (1996), 227-237.
[4] C. Ronot-Trioli, A. Trouillet, C. Veillas, A. El-Shaikh and H. Gagnaire, Analytica Chimica Acta 319 (1996), 121-127.

Non-invasive optical interrogation of the ocular anterior chamber

R. Blue, D. Uttamchandani*

Department of Electronic and Electrical Engineering

University of Strathclyde, 204 George Street, Glasgow, G1 1XW, Scotland (UK)

C. G. Wilson

Department of Pharmaceutical Science

University of Strathclyde, 204 George Street, Glasgow, G1 1XW, Scotland (UK)

*(corresponding author)

*Tel: + 44 141 548 2211, Fax: + 44 141 553 1955, E-mail: du@eee.strath.ac.uk

1. Introduction

Ophthalmic drug research and ocular diagnostics is hampered by an inability to perform continuous sampling of the aqueous humour contained within the anterior chamber of laboratory animal or human eyes. Direct sampling of the anterior chamber by paracentesis is technically problematic and is associated with the use of local or general anaesthesia. Moreover, sampling by direct injection exposes the eye to the risk of infection. We report results obtained from an optical instrumentation technique which is concerned with the direct and non-invasive measurement of optical scattering, absorbance and fluorescence produced in the aqueous humour by various compounds, thus avoiding the need for direct sampling.

Light scatter in the anterior chamber arises from particulate matter, such as cell debris and chemical precipitates following eye surgery (such as calcium hyaluronate). Absorbance is caused by the presence of materials such as haemoglobin, or results from the penetration of drugs such as hydroxyquinolines applied to the cornea. Fluorescence can be used to provide a sensitive measurement of fluoroquinolines in the anterior chamber.

2. Experimental

Our preliminary experiments began with a model eye. A (disposable) contact lens represented the cornea and various aqueous solutions could be introduced into the "eye". The refractive index of the human aqueous humour is 1.3374 which is close to that of water (1.333) and so our arrangement was a good physical model. The layout of the experimental apparatus is depicted in Figure 1, where fibre optics (terminated by GRIN lenses) were used to deliver light to and from the "cornea". To pass a beam across the "cornea" with minimal deviation required index matching and this was achieved by immersing the "cornea" within a small vessel of water. A monochromator was used to generate discrete wavelengths which were directed across the "cornea"

and a second GRIN lens captured the emerging light and carried it via the fibre optics to a detector. Fig. 2 shows the detection, by their characteristic absorbances, of the compounds nile blue, rose bengal [1] and fluorescein [2] (which are often applied to the anterior chamber in ophthalmic research) within the model eye.

This technique was then applied to real animal eyes. The useful lifetime of these animal eyes was extended by arterially perfusing them with a nutrient solution [3]. This also allowed for the addition of dyes to the circulating nutrient solution during which a small percentage (1 or 2%) of dye would eventually reach the aqueous humour. After perfusion the animal eyes were interrogated with the optical system. Three bovine eyes were perfused for one hour with different concentrations of fluorescein added to the nutrient solution. Figure 3 shows the absorption spectra recorded separately for each eye. The spectra indicate the presence of different concentrations of dye within the anterior chamber of these bovine eyes. Subsequent extraction of the aqueous humour by a hypodermic needle and analysis in a spectrophotometer confirmed the presence of different dye concentrations within the aqueous humour. We have also shown that this technique can be used to measure the absorption spectrum of tetracycline [4] (one of a wide range of drugs applied to the human corneal region) within sheeps eyes.

A further step towards a more practical optical system was taken with the construction of a special contact lens to avoid the need for immersing the front of the eye in an index matching water chamber. The special lens was machined from perspex into the shape of a traditional contact lens but surrounded by an angled mirrored perimeter, as seen in Fig. 4. This lens was then placed onto an excised rabbit eye and HeNe laser light was guided to the flat surface of the special lens using a fibre terminated by a GRIN lens. With this prototype lens the HeNe light could readily be seen to propagate across the anterior chamber of the eye in the desired manner. It is thus concluded that a compact optoelectronic system, as shown in the conceptual diagram of Fig 4, can be constructed to propagate and measure light travelling across the anterior chamber. Interaction length measurements may be conveniently undertaken using a small CCD array which, with appropriate external filters, could also measure any fluorescence and scattered light generated at right angles to the excitation light.

3. Summary

In summary, a method has been demonstrated to detect specific compounds introduced into model and real animal eyes by a non-invasive optical technique. We have also successfully made use of a specially constructed contact lens, incorporating fibre optics, for light delivery and collection from across the anterior chamber of a rabbit eye. These results indicate that the construction of a new, non-invasive optoelectronic instrument for ophthalmic drug studies is certainly very feasible.

4. References

[1] Y. C. Lee, C. K. Park, M. S. Kim and J. H. Kim, "In-vitro study for staining and toxicity of rose-bengal on cultured bovine corneal endothelial-cells", Cornea, **15**, 376 (1995).

[2] T. R. Neault, J. W. McLaren, J. H. Brubaker and R. F. Brubaker, "Spectral shift of fluorscein and carboxyfluorescein in the anterior chamber of rabbit eye following systematic administration",Current Eye Res., **5**, 337 (1986).
[3] W. S. Wilson, M. Shahidullah and C. Millar, "The bovine arterially-perfused eye: an *in vitro* method for study of drug mechanisms on IOP, aqueous humour formation and uveal vasculature",Current Eye Res., **12**, 609 (1993).
[4] T. Tilmouth and J. Briscoe, "Trachoma and oily tetracycline eye drops", Medical Journal of Australia, **140**, 119 (1984).

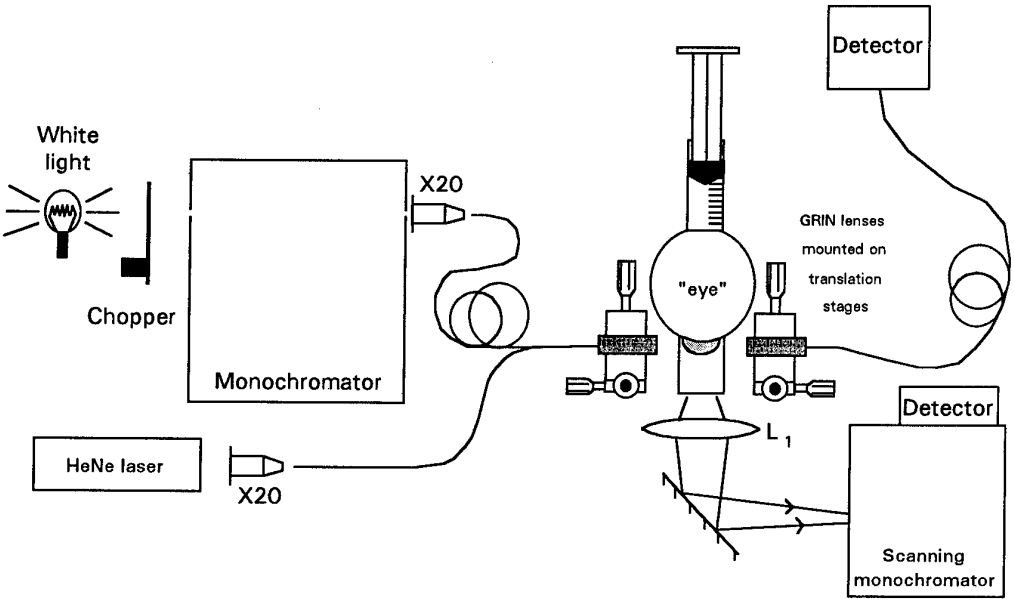

Fig. 1 Schematic representation of the experimental setup.

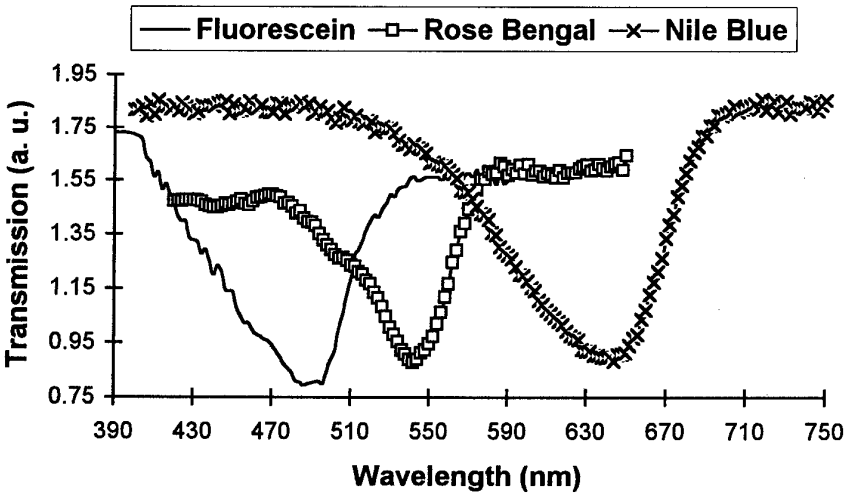

Fig. 2 Absorption spectra of three different compounds within the simulated anterior chamber.

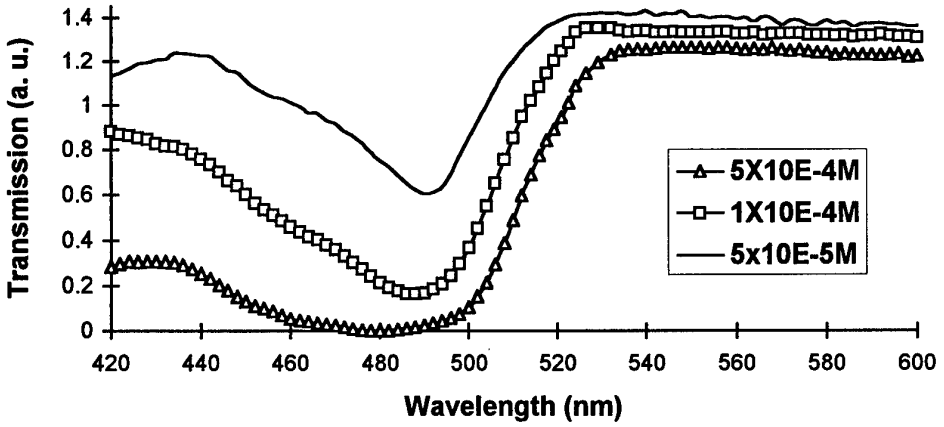

Fig. 3 Variation in optical transmission through of the anterior chamber of separate bovine eyes whose arterial network has been circulated with different concentrations of fluorescein.

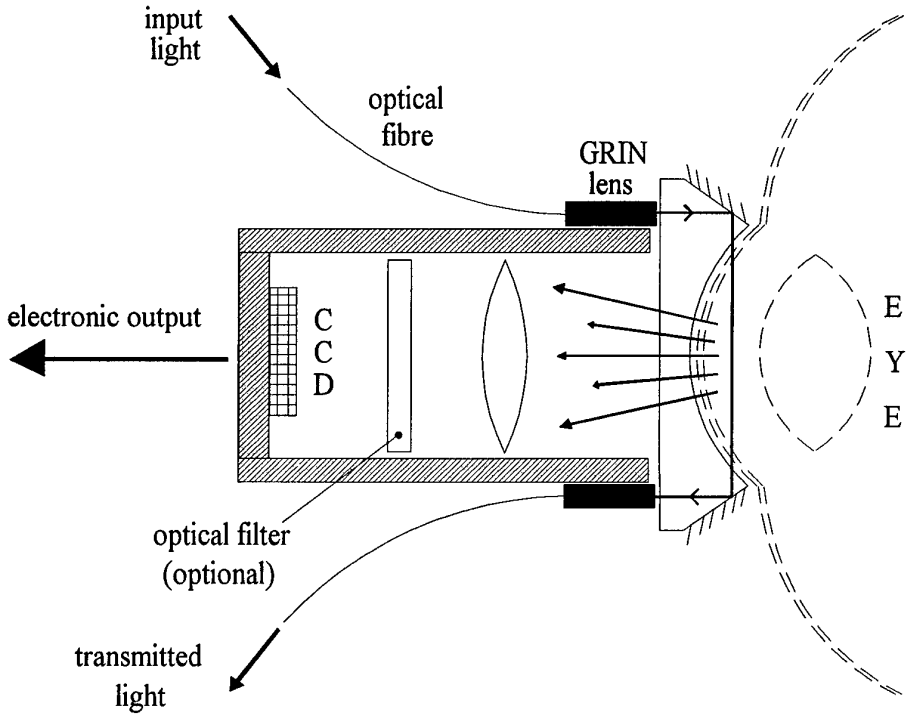

Fig. 4 Conceptual diagram of a future anterior chamber interrogation system.

Optoelectronic chemical sensing : from biological cells to power transformers

D Uttamchandani, R Blue, S McCulluch, U Noor
Department of Electronic and Electrical Engineering
University of Strathclyde
204 George Street
Glasgow G1 1XW, UK

Tel: + 44 141 548 2211, Fax: + 44 141 553 1955, E-mail: du@eee.strath.ac.uk

1. Introduction

Over the last four years, the authors have been involved in research in the broad area of optoelectronic and optical fibre chemical and biomedical sensing. The research projects have differed quite considerably in their applications and the technologies applied. Some, such as the micro-optrodes, have been based on the use of specially prepared fibre-optic micro-probes, whilst others have involved the use of sol-gel derived sensing materials and photopolymers. When fibre-optics have been involved, they have been used in the extrinsic sensing mode. The aim of this Workshop contribution is to demonstrate the wide, and sometimes surprising, range of applications for optoelectronic chemical sensors by citing some of the authors' recent results and experiences.

2. Micro-optrodes for pH and dissolved oxygen

Optrodes for pH [1] and dissolved oxygen [2] have been known for many years. Although many improvements in performance have been achieved on these devices regarding sensitivity, speed, reversibility and selectivity , there has been relatively little attention paid to size reduction. Our interest has been focused on the size reduction issue, and we have followed the pioneering work of Tan et al [3] who first reported optical fibre microsensors, produced using specially fabricated microtips. The work of Tan et al can be distinguished from the work undertaken at Strathclyde in two key ways. Our fibre microtips have been fabricated using a laboratory fusion splicer [4] in contrast to Tan who used a high power infrared laser. The conversion of the microtip into a microsensor in our laboratory has involved the attachment of reagent doped sol-gel derived coatings, in contrast to the use of photopolymers by Tan. It is appropriate to point out that we have also looked at the use of reagent doped photopolymers, but have settled on using sol-gels which were found to be generally more robust. The pH sensitive micro-optrodes have been tested in individual biological cells since the sharp micron sized tips can penetrate the cell membrane [5]. Dissolved oxygen sensors have also been constructed using a similar approach involving reagent (a ruthenium complex) doped sol-gel layers coated on the fibre tips. Figure 1 shows the layout of the apparatus used in our experiments, whilst a close-up of the micro-optrode is shown in Figure 2. Figure 3 shows the variation in sensor response (fluorescence intensity) at various concentrations of dissolved oxygen in water.

3. Optical sensing of H_2S using sol-gel derived films

Detection and monitoring of hydrogen sulfide, a gas that has been demonstrated to be highly toxic and can rapidly be fatal [6], is very important not only in the process and manufacturing sector but also from an environmental point of view. Environmental H_2S is generated from both natural and industrial sources. Naturally, it is released from a variety of sources such as decay of sulfur-containing organic material and from mines, gas wells, sewers etc. In the industrial sector, H_2S is one of the major by-product of many chemical processes including production of sythetic rubber, petroleum products, dyes, leather etc. Without proper monitoring of this gas there is risk of environmental pollution and a toxicity hazard.

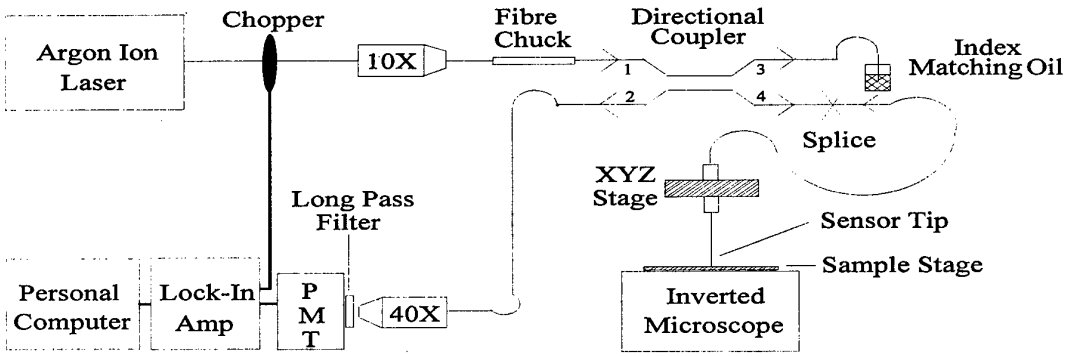

Figure 1. Schematic diagram of miniaturised oxygen sensing apparatus

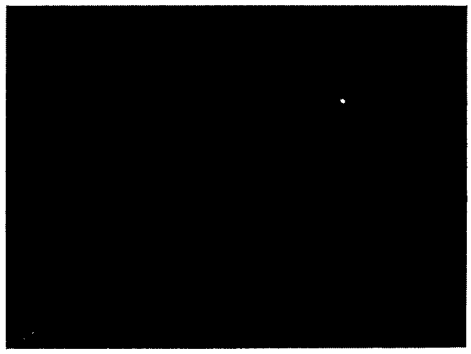

Figure 2. Photograph of aluminium coated fibre probe excited at 488 nm

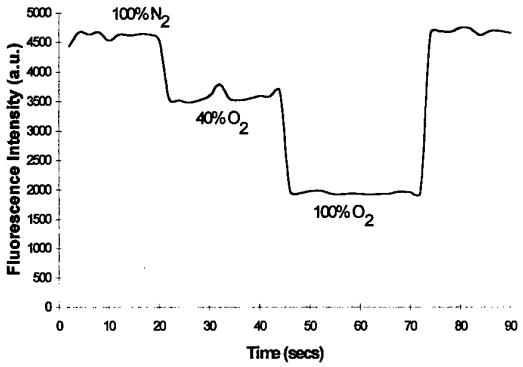

Figure 3. Sensor response to different dissolved oxygen levels

To date, most compact sensors for this gas involve the use of tin oxide and related compounds, whose electrical conductivity changes on exposure to the gas. Our interest is in devising an optoelectronic approach, which first requires the development and characterisation of a suitable sensing material. Accordingly, we have investigated reagent doped sol-gel materials [7]. Thionine dye immobilised in a porous ormosil matrix formed via

the sol-gel fabrication process using methyltrimethoxysilane (MTMS) as precursor was found to have a unique absorption spectrum which coincides with the emission wavelength of a red laser diode operating at 660 nm. The dye-doped matrix has been found to show a remarkable change in its absorption intensity in the presence of hydrogen sulfide (H_2S) gas in air at different concentrations when interrogated with the 660 nm laser diode. In our laboratories, a minimum level of detection of 100 ppm has been achieved with a simple optoelectronic sensor using fiber bundles to deliver and collect the laser light which interacted with the dye doped matrix exposed to the H_2S gas. This approach offers a simple and direct optical method for H_2S detection in environmental and industrial applications with a future view to on-line and continuous detection of the gas, as well as remote sensing. Figure 4 shows the variation in absorption spectrum of the thionine doped sol-gel derived film with the number of coatings whilst Figure 5 shows the change in transmitted intensity through the film upon exposure to the gas. These last measurements were conducted at 660 nm.

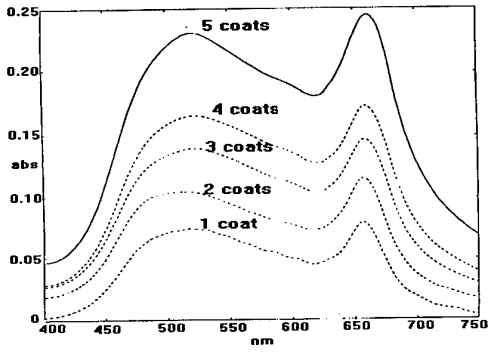

Figure 4. Absorption spectrum of thionine doped thin film

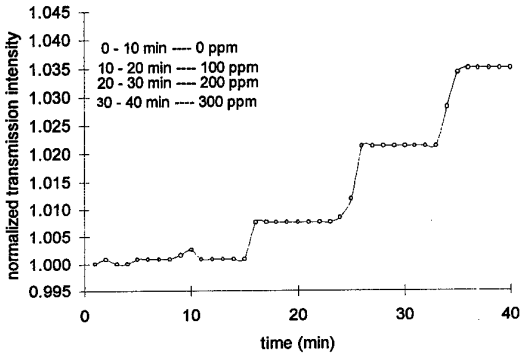

Figure 5. Change in transmitted intensity at 660nm with hydrogen sulphide conc.

4. Optoelectronic detection of transformer insulation degradation

High voltage transformers make use of paper-insulated windings immersed in transformer oil. During normal operation of the transformer the temperature of the windings will increase and over a period of time this causes the cellulose chains in the paper to cleave. As a result, the mechanical strength of the paper, measured through its degree of polymerization, degrades with time and this will have an adverse effect on the performance of the insulation. A feature of this paper insulation deterioration is the release, into the transformer oil, of the chemical product furfuraldehyde (FFA). This compound is a by-product specific to the paper degradation, and cannot be produced by the oil itself. Due to this thermally induced deterioration, regular monitoring of the paper insulation is necessary to guarantee the safe and reliable operation of the transformer. Unchecked degradation of the insulation can lead to the transformer being taken off-line for expensive repair, together with punitive financial penalties and loss of revenue. To circumvent direct sampling of the paper insulation of an operational transformer, electrical utilities periodically sample the oil and measure the concentration of FFA in a laboratory remote from the site of the transformer using either HPLC or a more recently developed colourimetric method involving the compound aniline acetate.

The reaction of the two compounds aniline acetate and FFA, which is key to the colourimetric method, results in the formation of a pink coloured complex whose optical characteristics can be measured on a spectrophotometer. We have developed a sol-gel derived material incorporating the reagent aniline acetate, and our experiments have shown that even in this form, the trapped aniline acetate will react with FFA producing the characteristic colour. The absorbance dip occurs at 530 nm, and we have shown that the absorbance of the sol-gel derived material increases with concentration of FFA in transformer oil when the material is immersed in the oil [8]. Availability of solid-discs of the aniline acetate doped sol-gel derived material allows the realisation of a compact optoelectronic instrument which could be used for transformer insulation monitoring. A further development of our work has involved fluorescence measurements on the same material, after reaction between the material and FFA doped oil samples. When optically excited at 514 nm, the material produces a fluorescence peak at 560 nm. The intensity of this peak has been shown to vary with FFA concentration in the transformer oil. Sub-ppm concentrations have been measured by both absorption (see Figure 6) and fluorescence (see Figure 7) techniques. In addition, we have developed a compact optoelectronic instrument based on optical absorption measurements for field use during transformer oil/insulation monitoring.

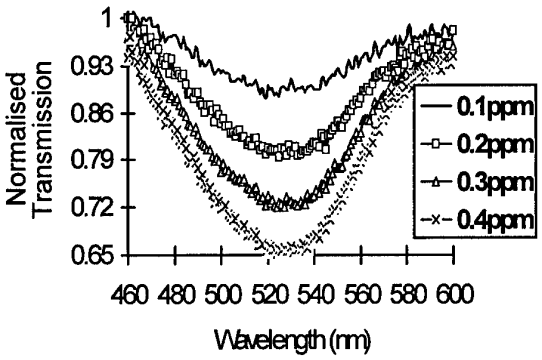

Figure 6. Change in absorption spectrum spectrum of sol-gel discs with FFA conc.

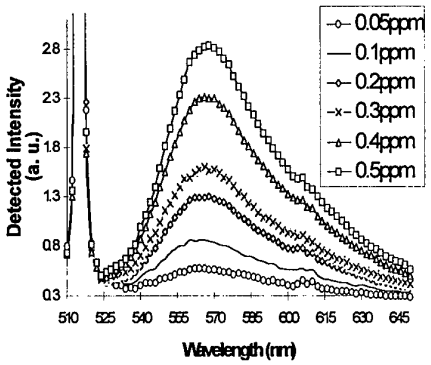

Figure 7. Change in fluorescence of sol-gel discs with FFA conc.

5. Summary

A range of applications for chemical sensing involving optoelectronic/fibre-optic sensing have been described and recent results presented. Although all the work has produced novel results, the need for interdisciplinary research has been found to be crucial, particularly in connection with the development of chemical reagents (dyes, indicators) for particular analytes.

6. References

[1] Y Kawabata, K Tsuchida, T Imasaka and N Ishibashi, "Fibre optic pH sensor with monolayer indicator",Anal. Sci., vol 3, pp7-9, 1987

[2] G O'Keeffe, B D MacCraith, A K McEvoy, C M McDonagh and J F McGlip, "Development of a LED based phase fluorimetric oxygen sensor using evanescent excitation of sol-gel immobilized dye", Sen. And Act. B, vol 29, pp226-230, 1995

[3] W Tan, Z Y shi and R Kopelman, "Development of sub-micron optical fibre sensors",Anal. Chem., vol 64, pp2985-2990, 1992
[4] S McCulloch and D Uttamchandani, "A simple reproducible technique for producing sub-micron fibre optic probes for near -field optical microscopy and chemical sensors", Meas. Sci. Tech., vol 6, pp1157-1162, 1995
[5] S McCulloch and D Uttamchandani, "Fibre optic micro-optrodes for intra-cellular chemical measurements", Proc BiOS '95, San Jose, California, 1995
[6] R O Beauchamp, B S James, P A James, B J Craig and A A Dragona, CRC Critical Review in Toxicology, vol 13, pp25-42, 1984
[7] U M Noor and D Uttamchandani, "Sol-gel derived thin films for hydrogen sulphide gas sensing", J. Sol-gel Sci. and Tech., (in press)
[8] R Blue, D Uttamchandani, O Farish, "A novel solid-state material for furfuraldehyde detection", IEEE Trans Dielect. and Elect. Ins.,vol 4,pp 341-343, 1997

A comparative study of sensitivity and detection limit for the protein bovine serum albumen using a new tensiograph assay against the standard UV-visible assay.

N.D.McMillan*, D.Dowling, M.O'Neill, T.Yeomans
Institute of Technology Carlow,
Kilkenny Road,
Carlow,
Ireland

Dr. habil. Reinhard Miller
Max-Planck-Institut für Kolloid- und Grenzflaechenforschung
Rudower Chaussee 5
D-12489 Berlin - Adlershof, Germany

* Telephone 353 503 70400
Fax 353 503 70500
E-mail McMillan@rtc-carlow.ie

1. Introduction

A new multianalyser tensiograph approach to concentration measurements of pure protein solutions has been devised. Much work has been done over a long period using tensiometers and other surface analysis methods on proteins, enzymes and complex surface active molecules. The principle of the new method is a development of the long established tensiometer technique and is here adapted for protein studies (BSA) but it might be noted that the method is applicable to enzymes as well. The paper briefly explains the basic method of operation of the tensiograph and the form of the multianalyser tensiotrace. Area D-values for the tensiotrace have shown to be the most appropriate for this comparative study against the standard UV-visible method. Very promising measurement criteria are reported for this first tensiograph analysis of BSA solutions and comparisons of the instrumental calibration sensitivity, analytical sensitivity and detection limits are reported against the standard UV-visible method. A short discussion of the potential advantages of the new method is given and some critically important limitations to the present work are pinpointed that will require to be clarified if the technique is to win general acceptance as a standard method in this field.

One of the standard methods for protein analysis and estimation is the Lowry method [1] which has a range of 20-200 $\mu g\ ml^{-1}$. The chemical procedure involved in this method takes approximately 45 minutes to complete. It is a two stage reaction which relies on a blue colour development. Several of the reagents required for this method need to be prepared freshly which can be a restraint in some cases. The extinction of the final coloured product must be read within a certain period of time and the timing of the reaction process is also critical, both these factors add further restraints to the procedures general applicability. There is also an amino acid concentration difference between proteins and due to this there is some protein-protein variation in assay results. Furthermore, there are six interfering agents regularly associated with the Lowry assay which are Tris buffer, sucrose, urea, sulphydryl compounds, mercaptoethanol and ammonia sulphate.

2. Theory

The science of tensiography can perhaps be simply stated as the extraction of physical, chemical and product information from the instrumental tensiotraces. The tensiotrace is a temporal optoelectronic trace that arises from the modulation of the light as it is coupled between the source and detector fiber in the drop. It is produced by the changes in the reflected light paths as the drop grows from the liquid added to the drop head by the stepper pump or other supply. The liquid drop on the fiber head develops gradually in size until it falls off to be replaced by a second growing drop and so forth repeatedly.

A typical water reference tensiograph is shown in Figure 1. The addition of proteins or enzymes to the water changes the tensiotrace radically and these traces can be used to fingerprint the liquid against those held in a reference library. These traces may be used to show the differences between this trace and the reference trace. The differentiation of one liquid from another can be done by defining discrimination functions which yield D-values. These values give a normalised standard measure of the differences in measurement features of the trace. The use of milli-differences has been found to be practical for the tensiograph discrimination functions. The area D-value is the only function required for the analysis of the proteins although many others have been defined by McMillan[2]

$$D_A = (A - A') * \frac{1000}{A} \qquad (1)$$

A is the area of the tensiotrace for the reference trace and A' is the area of the measurement trace.

The standard approach to quantifying sensitivity of instrumental methods of analysis for the *calibration sensitivity*, *analytical sensitivities* and *detection limits* proposed by Mandel and Stiehler [3], Kaiser [4] for the UV-visible have been adapted directly for the multianalyser.

3. Experimental

The basic principle of the method is best illustrated by Figure 1 which shows the tensiotraces for three solutions of BSA. It is visually quite obvious from inspection of the traces that there are drastic variations in the area of the tensiotrace. These variations in area translate directly into area D-value variations. Area D-values have been found to be the most appropriate for this present study with the range of concentration measurements chosen to coincide with those of the Lowry method. At concentrations above 300 $\mu g\ ml^{-1}$ the area D-value began to saturate at a value of 950. This saturation was produced by the signal decreasing to a level close to the noise. This problem could in practice be overcome either by changing the gain of the detector. This is however not a matter of much concern to the present study.

The calibration curves for both the UV-visible and multianalyser can be seen in Figures 2. The performance characteristics under which the two instruments can be compared are displayed in Table 1.

	UV-vis	Multianalyser
Average standard deviation of signals	0.0065	0.0093
Calibration sensitivity range:40-300μg/ml (Multianalyser) 20-400μg/ml (UV-vis)	0.0011	0.0027
Analytical sensitivity	0.1757	0.2944
Detection limits μg/ml	38.18	63.77
Standard deviation of blanks	0.014	0.057

Table 1. Results of the standard deviations, calibration sensitivity, analytical sensitivity and detection limits for both UV-vis and multianalyser measurements.

It can be seen from Table 1 that the standard deviations of the multianalyser are slightly inferior to those of the UV-visible spectrophotometer. However, both the calibration and analytical sensitivities are markedly superior. The slightly poorer detection limit of the multianalyser method with respect to the UV-visible method resulted solely from insufficient numbers of blank measurements. This experimental deficiency arose from some unforeseen problems with the acquisition package on the day of measurement which led to this artificially high standard deviation. Work is underway to improve these measurements reported here using point rather than area D-values. This approach will provide an order of magnitude better sensitivity than those reported here for the multianalyser. This approach will also give a correspondingly improved detection limit. The results were therefore considered to be sufficiently good for this preliminary study.

4. Concluding Comments

The present range of measurements 20 to 300 μg ml^{-1} is best handled by the use of area D-values. It is however very obvious that the most sensitive indicator of the variation in the tensiotrace is the point D-value which gave a value of 789 for the 20 μg ml^{-1} solution. For measurements below 40 μg ml^{-1} (in the range perhaps to 0.1 μg ml^{-1}) point D-values would be excellent measurement tools. Below this range the tensiograph has other measurement capabilities described by McMillan et al. [2] although these are not discussed in this present paper they will be the subject of a further communication. I-values therefore would probably allow measurements to concentration levels below 0.1 μg ml^{-1}. Further work is underway which will quantify the sensitivities of both the point and I-value measurement approaches for BSA, other proteins and for other important biomolecules such as DNA.

Despite the fact that the Lowry spectrophotometric assay has certain well known disadvantages with regard to other spectrophotometric protein assays, for the range of protein concentration 20-200μg/ml, it has long been considered the most applicable. Principally, because the Lowry assay is widely regarded as one of the most sensitive assays for proteins and since it provides both qualitative and quantitative results it was considered to be the best standard method against which to test the new multianalyser method. On some of the most obvious comparative measurements of instrumental performance of the two methods the new approach has performed very respectably.

The tensiometric approach to protein measurement removes the problems associated with both the two-step assays and also the colour development timed assays. The requirement for reagents is non-existent with the multianalyser method and although the Lowry assay only requires 0.5ml of sample (total sample volume), the tensiometric approach requires only half of this. Soon it is anticipated that the new instrument will be able to deliver measurements on 200 µl sample volumes.

In summary, this preliminary study has indicated the potential of this new technique. Some definite practical advantages for the multianalyser method with respect to the established Lowry method have been identified here, but the very much shorter analysis time is the most significant. This work is being extended because of the obvious improvements that can be made with the method but also because certain experimental limitations have been recognised and need to be resolved. If as anticipated the multianalyser method can be extended to the analysis of lower concentrations of BSA in the ongoing work to produce enhanced performance criteria over those presented here then this may prove to be a fundamental advantage for the method.

5. References

[1] O.H. Lowry, N.J. Rosebrough, A.L. Farr and R.J. Randall, J.Biol. Chem.193 (1951), 265-275.

[2] N.McMillan, V.Lawlor, M.Baker and S.Smith, From stalagmometry to multianalyser tensiography: The definition of the instrumental, software and analytical requirements for a new departure in drop analysis, in "Drop and Bubbles in Interfacial Research" Vol. 6, D. Möbius and R. Miller (Eds.), Elsevier, Amsterdam 1997.

[3] J. Mandel and R.D. Stiehler, J. Res. Natl. Bur. Std., 1964, A53, 155.

[4] H. Kaiser, Anal. Chem., 1987, 42, 53A.

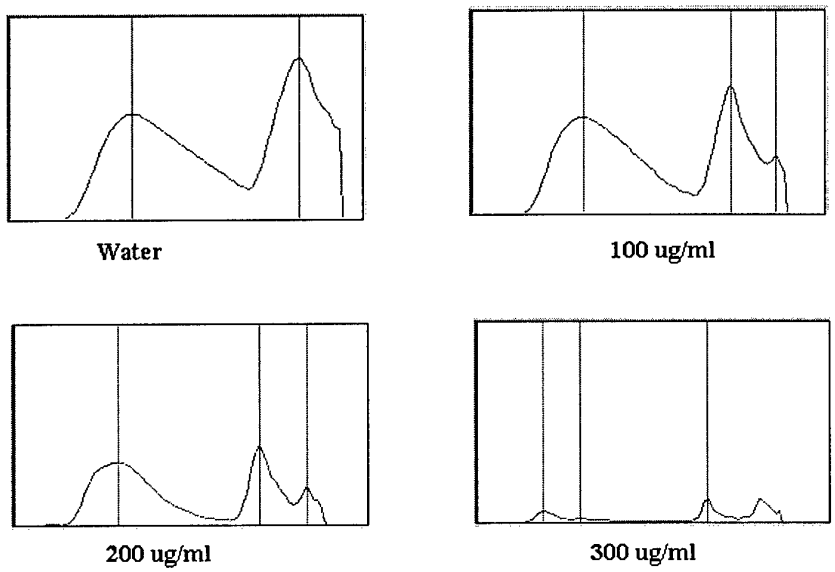

Figure 1. Tensiotraces for water and three BSA solutions of 100, 200 and 300 μg ml^{-1} measured at 30°C.

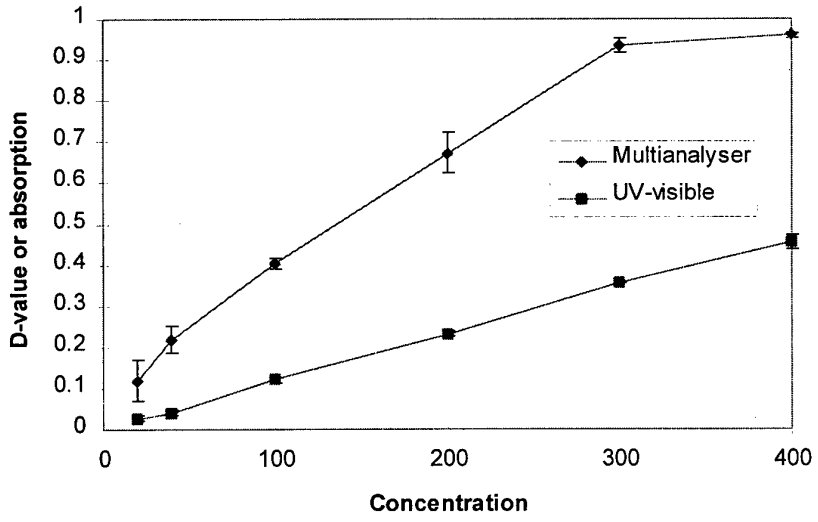

Figure 2. Graph of D-value or absorption against concentration for BSA.

Quasi-distributed optical fibre fluorosensor for pH measurement

P A Wallace, M Uttamlal, N Elliot, A S Holmes-Smith, M Campbell

Department of Physical Sciences, City Campus, Glasgow Caledonian University, Cowcaddens Road, Glasgow G4 0BA, United Kingdom

1. Introduction

Fibre optic sensors may be described as either 'intrinsic' or 'extrinsic' according to whether the fibre itself forms part of the sensing medium or merely acts as a waveguide [1]. One considerable attraction of the intrinsic type is the possibility of developing a spatially extended, position sensitive sensor system. Such a system is conventionally described as distributed if the position sensitivity extends over its entire active length and described as quasi-distributed if it consists of a series of sensitive regions spaced over the length of the fibre[1]. One method of deriving position information from the sensor is to analyse the temporally extended reflected light pulse originating from a short excitation pulse launched into the fibre. This technique is known as optical time domain reflectometry (OTDR) [1]. The advantage of using a fluorescence signal is that it is separated in wavelength from the excitation radiation. The concomitant drawback is that the time resolution of the system, upon which the positional information directly depends, is limited by the lifetime of the fluorescence de-excitation. Given a lower limit of 10 ns on the lifetime, and a propagation time of 5 ns per metre in the fibre, the lower limit for position resolution of the system would be ~ 1 metre. This would, however, be adequate for many environmental and hazard monitoring purposes.

The radiation guided within the core of an optical fibre is contained by the phenomenon of total internal reflection. The boundary conditions at the core-cladding interface require, however, that the electromagnetic field of the light wave should penetrate a short distance into the cladding. This is known as the evanescent wave effect. The evanescent wave decays exponentially with distance into the cladding and its effective extent is of the order of one wavelength.

The principle of operation of the sensor involves using the energy contained within the evanescent wave to excite fluorescence in dye molecules immobilised porous sections of fibre cladding. If the fluorescent emission is modulated by the presence of a chemical substance in the environment of the fibre, and if some of this emitted light couples back into the optical fibre core from the cladding, then a sensing mechanism will have been established.

The fluorescence emission from the indicator propagates in all directions, so that some of it will be at the angles which match the angles of the modes in the optical fibre, thereby coupling into the optical fibre. This light will propagate in both directions in the fibre and may therefore be detected at both ends. For a distributed system, the fluorescence is detected at the original launch end.

The authors have previously reported a prototype distributed system comprising a 100 metre quasi-distributed pH sensor based on the pH dependent fluorescence of sodium fluorescein [2]. The present work addresses some of the shortcomings of this system and, in particular, reports the development of improved sensor sites using a novel immobilisation method for the indicator.

2. Indicator Immobilisation

Current methods for the immobilisation of fluorophores on optical fibres (- including the above prototype system) usually involve entrapment in sol-gel matrices [3]. However, this preparation method suffers from the fact that leeching of the indicator occurs because there is no covalent link between the sol-gel, fluorophore and the fibre surface[2].

In this work we have developed new immobilisation procedures to covalently attach the fluorophore to the fibre surface using hydrogel films. Hydrogels are polymers having a large void space containing aqueous solution. The fluorophore is covalently bound to the hydrogel and the hydrogel is covalently bound to the fibre surface. The hydrogel/fluorophore films are prepared by means of photo-initiated polymerisation.

Several monomers have been investigated including hydroxyethylmethacrylate (HEMA), acrylamide, N-vinyl-2-pyrrolidone and co-polymers of these. The fibre surface was activated using several chemical steps to produce a surface with a free acrylate group suitable to facilitate adhesion of the photopolymer to the glass surface. For the preparation of a pH sensor acryloyl-fluorescein was prepared as shown in figure 1:

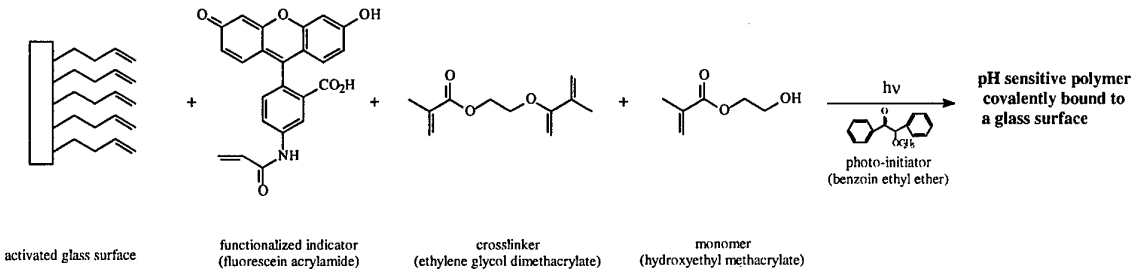

Figure 1: Photopolymer Preparation

This fluorophore is pH sensitive and contains a free acrylate group suitable for polymerisation. Fluorescein is one of the most commonly used pH indicators in use [4]. It has high molar absorbance at a wavelength of 488 nm, large fluorescence quantum yield

and good photostability making it a very useful and sensitive fluorescent label. Fluorescein in aqueous solution occurs in neutral and anionic (- and other) forms making its absorption and fluorescence properties strongly pH dependent:

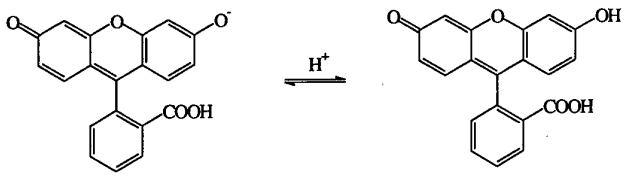

Figure 2: Anionic and neutral forms of fluorescein.

3. Sensor Fabrication

The sensor sites are fabricated using 200 μm core PCS fibre. The simplest method of construction involves stripping a short length of fibre and then coating it with a doped porous cladding as shown in figure 3 (a). This was the method used in [2]. The drawbacks of this method are the extent of the light loss due to the interruption of the waveguide geometry and the mechanical weakness introduced by the length of bare core. To ameliorate these problems we have developed a new sensor geometry whereby the fibre is embedded in a glass block and is then polished down to the core. This produces a flat glass surface upon which the polymer can be laid down.

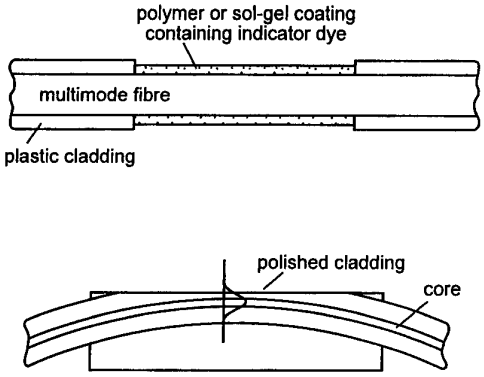

Figure 3: Preparation of sensor sites via (a) stripping, (b) polishing

4. Optical Instrumentation

The OTDR system consists of four main parts: (i) light source, (ii) launch unit and splice, (iii) sensing section and (iv) light detector and signal processing unit. Figure 4 is a schematic diagram of the system. The light source comprises a dye laser pumped by a N_2 laser which produces UV pulses of energy 100 μJ and duration 0.5 ns at 337.1 nm. The

dye laser produces short pulses at 490 nm which are launched into a 1×2 optical fibre coupler through a 40× microscope objective. Fibre, with several sensor sites, is spliced to the coupler. At the other arm of the coupler, a green band pass filter (525-535 nm) is placed between the coupler and an EMI 9125 photomultiplier whose output is displayed on a 500 MHz storage oscilloscope before being transferred to a computer.

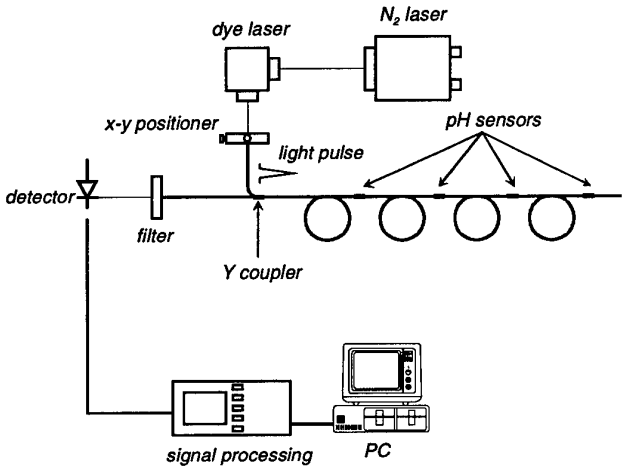

Figure 4: The experimental configuration for the distributed system

References

[1] B Culshaw, *Optical Fibre Sensing and Signal Processing*, 1984, Peter Peregrinus
[2] P A Wallace, M. Campbell, Y Yang, A S Holmes Smith, M Uttamlal, *J. Luminescence*, 1997, **72-74** ,1017
[3] C.Jeffrey Brinker, George W. Scherer, *Sol-Gel Science*, 1990, Academic Press
[4] R.Sjöback, J.Nygren, M.Kubista, *Spectrochimica Acta A*, 1995, **51**, L7-l21

Multi-Point Fibre Sensors for Trace Gas Monitoring Using Derivative Spectroscopy

G Stewart, B Culshaw, C Tandy*, D Moodie†, R Pride††

Department of Electronic & Electrical Engineering, University of Strathclyde, Glasgow UK, G1 1XW.
Tel: +44(0)141 552 4400, Fax: +44(0)141 553 1955, e-mail: g.stewart@eee.strath.ac.uk

*Gas Measurement Instruments Ltd, Inchinnan Estate, Renfrew, Scotland, UK, PA4 9RG.
Tel: +44(0)141 812 3211, Fax: +44(0)141 812 7820, e-mail: c.tandy@gmiuk.com

†OptoSci Ltd, Strathclyde University Incubator, 141 St James Road, Glasgow, UK, G4 0LT.
Tel: +44(0)141 552 7020, Fax: +44(0) 141 552 3886, e-mail: optosci@compuserve.com

††British Gas plc, Gas Research Centre, Ashby Road, Loughborough, UK, LE11 3QU.
Tel: +44(0)1509 282 761, Fax: +44(0)1509 283 118, e-mail russell.pride@bggrc.co.uk

Introduction

A number of important gases in the context of environmental and safety issues possess absorption lines in the near-IR region of the spectrum between 1 and 2μm. These include gases such as carbon monoxide, carbon dioxide, hydrogen sulphide and methane. The availability of low cost communications fibre and components such as connectors and couplers make this spectral region attractive for the development of fibre sensor networks for continuous monitoring of trace gases. However the absorption lines are weak and careful design of the modulation and signal processing schemes are required in order to obtain adequate sensitivities for commercial application. Furthermore the laser source must operate around the specific wavelength of the gas absorption line and the resulting high cost of manufacture needs to be mitigated by arranging for a large number of sensor locations within the fibre network. Here we illustrate how the above concerns can be met in the case of

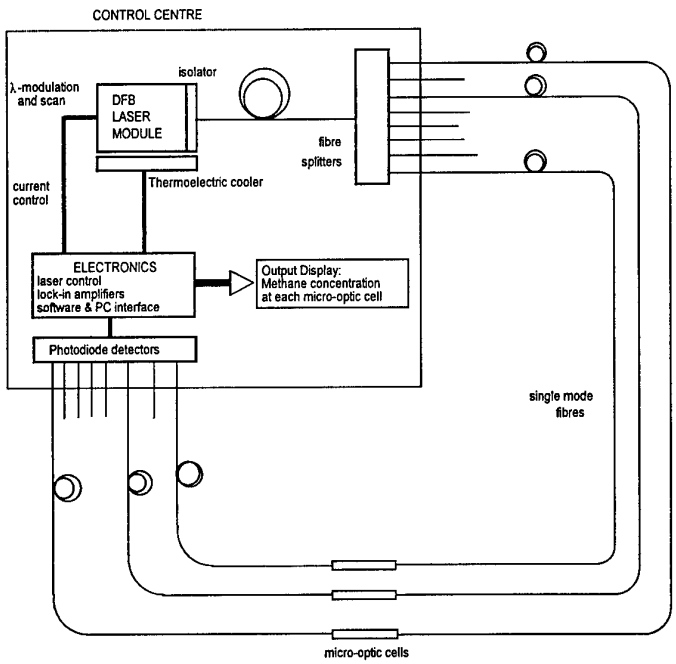

methane gas where we have developed a multi-point sensor network with adequate sensitivity for safety monitoring.

System description

The figure shows the basic layout of the fibre sensor system. The Anritsu DFB laser source was designed for operation at 1665nm corresponding to the Q6 rotational absorption line of methane. The thermo-electric cooler allows the wavelength to be adjusted to the centre of the absorption line (0.1nm/ ^{0}C) while wavelength modulation can be applied through the injection current (~0.0025nm/mA). The current modulation also produces amplitude modulation (AM) of ~0.04mW/mA. The laser output is connected through a fibre splitter arrangement to 64 (or more) micro-optic cells (l = 5cm) constructed from GRIN lenses. Each cell has its own photodetector and lock-in detection system.

Modulation format

The modulation scheme used with the DFB laser source is important for realising adequate sensitivity. Various methods have been classified in the literature as follows:

(i) wavelength modulation spectroscopy (WMS) where low frequencies (kHz range) are employed with large modulation depths[1]

(ii) frequency modulation spectroscopy (FMS) where rf frequencies are used with small modulation index[1]

(iii) two tone frequency modulation spectroscopy (TTFMS) where beat frequencies are detected[2]

(iii) combined wavelength and frequency modulation spectroscopy (CWFMS)[3]

In principle, high sensitivity can be obtained by locking the laser wavelength to the absorption line centre and detecting the second harmonic in a WMS scheme where the modulation amplitude set to ~2.2×γ, or ~0.93×γ if the ratio of second to first harmonic is used[4], where γ is the half linewidth of the absorption line. In practice, interference effects (etalon fringes) from the micro-optic cells also give rise to harmonics which are confused with the gas signal. Furthermore, locking to the line centre requires a reference cell and allowance must be made for the background AM of the laser source when using the first harmonic as an error signal in the lock loop.

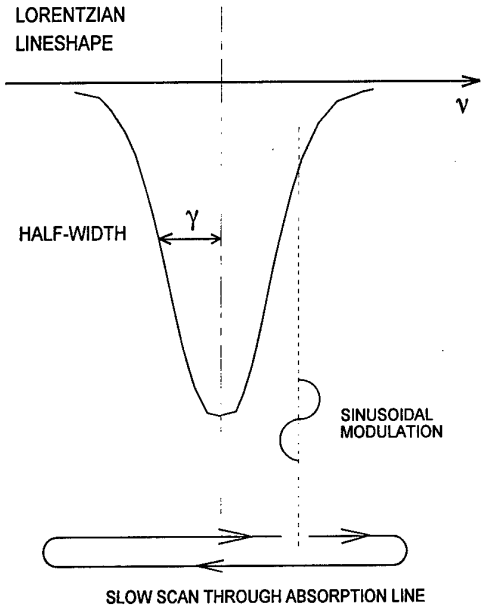

To overcome these difficulties we have used a combination of derivative spectroscopy with line scanning and first harmonic detection as illustrated. The amplitude of the sinusoidal modulation is chosen to minimise the etalon effects from the cells[5] while the scan through the absorption line generates a trace of the first derivative of the Lorentzian line-shape. This method has the advantages that (i) no reference cell is required since the line centre does not need to be exactly located at the centre of the scan and laser temperature control is sufficient (ii) the etalon fringes are separated from the methane signal (iii) the detection system is simple (low frequency kHz range for first harmonic signals) which is important for multiple cell systems (iv) the source AM level from each branch can be used as a reference to compensate for changes in system characteristics and (v) digital signal processing may be employed to analyse the retrieved signals and extract the gas concentration.

Network design

In the design of the multi-point system attention needs to be paid to the effect of the network on the system performance. The splitter arrangement is formed from standard telecoms (1550nm) fused fibre couplers but since the operation wavelength is 1665nm, split ratios are slightly modified and an exact 50/50% split ratio at 1665nm is not obtained from a standard 1:2 coupler. A theoretical analysis shows that, for a 64 point network formed from 1:2 splitters each with 52/48% ratio, the attenuation factor for the 64 cells can be specified as −18±1dB. Added to this figure are the excess coupler loss and the cell loss of ~1-2dB. These figures are quite acceptable for satisfactory operation of the multi-point sensor.

We can also estimate the signal to noise ratio of the system as follows. The (fibre coupled) power of the DFB laser source is ~1mW so the average power on the detectors from each branch of a 64 point network is I_b~0.01mW (–20dBm). Analysis, for a standard transimpedance type receiver circuit[6], shows that shot noise limited detection may easily be achieved since bandwidth requirements are very modest. The first harmonic signal level I_f in terms of the gas concentration in ppm.metre may be obtained from the first derivative of the Lorentzian function as:

$$\frac{I_f}{I_b} = \alpha_m \frac{\delta\nu}{\gamma} \frac{2\Delta}{\left(\Delta^2+1\right)^2} \left[\frac{ppm.metre}{10^6}\right]$$

where α_m is the absorption coefficient at the line centre ($\alpha_m \sim 0.2\text{cm}^{-1}\ \text{atm}^{-1}$ for the Q6 line of methane), γ is the half linewidth ($\gamma \sim 0.0865\text{cm}^{-1}$), $\delta\nu$ is the amplitude of

the sinusoidal wavelength modulation ($\delta\nu \sim 0.06\text{cm}^{-1}$ to minimise etalon fringes for a 5cm cell) and Δ is the deviation from the line centre, $\Delta = (\nu - \nu_0)/\gamma$ where ν is the wavenumber. Note that the signal peaks at $\Delta = \pm 1/\sqrt{3}$.

Hence under shot noise limited conditions and for $\Delta = \pm 1/\sqrt{3}$ the signal-to-noise ratio may be written as:

$$\frac{S}{N} = \alpha_m \frac{\delta\nu}{\gamma}\left(\frac{3\sqrt{3}}{8}\right)\left[\frac{ppm.metre}{10^6}\right]\sqrt{\frac{\Re I_b}{2eB}}$$

where $\Re$ is the photodiode responsivity ($\Re \sim 0.6$A/W), e is the electronic charge and B is the bandwidth (typically ~100kHz).

Hence with the typical values already given and for 1%LEL methane (500ppm or 25ppm.metre for our 5cm cell length) we have a signal-to-noise ratio at the photodiode receiver output of $\approx 10^{3/2}\sqrt{I_b}$ which becomes $\sqrt{10}$ for the 64 point system. The signal-to-noise ratio will be further enhanced after the lock-in amplifier stage.

In practice the system limitation comes from the level of etalon fringes remaining in the output signal, and from other sources of drift in the system. Interference effects may be minimised by choice of $\delta\nu$ as mentioned earlier, by anti-reflection coatings on the GRIN lenses and by use of a focusing cell design[7] but may not be totally eliminated from the signal.

Conclusion

We have realised a fibre optic multi-point system for methane gas detection with adequate sensitivity for commercial application (<1%LEL methane). The same principles may be applied to monitoring a range of other toxic or explosive gases with near-IR absorption lines. Furthermore development of multi-wavelength or switched sources would allow multiple gas sensing within the same fibre network.

Acknowledgement

This work was supported by the EPSRC/DTI LINK Photonics Programme in the UK (OMEGA Project)

References

[1] J M Supplee, E A Whittaker and W Lenth, "Theoretical description of frequency modulation and wavelength modulation spectroscopy," Appl. Opt., vol. 33, pp. 6295-6302, 1994.

[2] V G Avetisov and P Kauranen, "Two-tone frequency modulation spectroscopy for quantitative measurements of gaseous species," *Appl. Opt.*, vol. 35, pp. 4705-4723, 1996.

[3] H C Sun, E A Whittaker, Y W Bae, C K Ng, V Patel, W H Tam, S McGuire, B Singh and B Gallois, "Combined wavelength and frequency modulation spectroscopy: a novel diagnostic tool for materials processing," *Appl. Opt.*, vol. 32, pp. 885-893, 1993.

[4] W Jin, Y Z Xu, M S Demokan and G Stewart, Investigation of interferometric noise in fibre optic gas sensors with use of wavelength modulation spectroscopy, *Opt. Lett.*, 36 (1997), 7239-7246.

[5] G Stewart, A Mencaglia, W Philp and W Jin, Interferometric signals in fiber optic methane sensors with wavelength modulation of the DFB laser source, *J. Lightwave Technol.*, 16 (1998), 43-53.

[6] J Gowar, *Optical Communication Systems,* Prentice Hall, London, 1984.

[7] M A Morante, G Stewart, B Culshaw and J M Lopez-Higuera, New micro-optic cell for optical fibre gas sensors with interferometric noise reduction, *Electronics Letters,* 33 (1997) 1407-1409.

Interferometry and Distributed Sensors

Thursday, 9 July 1998

Chair: Julian D. C. Jones, Herriot-Watt University (UK)

Recent Developments in Fibre Optic Sensors for Point and Distributed Sensing in Large Structures

Y. J. Rao, N. Fisher, P. Henderson, V. Lecouche, C. N. Pannell, D. J. Webb and D. A. Jackson*

Applied Optics Group, School of Physical Sciences, University of Kent, Canterbury, Kent CT2 7NR, United Kingdom

*** Tele: +44(0)1227-764000 Ext: 3772 Fax: +44(0)1227 827558 E-mail: Y.Rao@ukc.ac.uk**

1. INTRODUCTION

The recent development of the in-fibre Bragg grating sensor (FBG) with its unique ability to detect temperature and strain and ease with which large numbers of such sensors, deployed remotely, can be multiplexed, has lead to the possibility of monitoring the structural integrity of major capitol items such as buildings and bridges. However, as Bridges are extremely large structures, the optimum strategy for sensor deployment and choice of sensor type is not straightforward. Given the wide range of measurement requirements, for example in monitoring the daily changes of static strain it is necessary to allow for thermally induced strains. Other questions such as how many measurement points and how to attach the fibre sensors to the Bridge are also crucial points which need to be addressed. Also valuable information about the 'state of health' of the Bridge can be obtained from dynamic measurements using ultrasonic techniques. Such sensors with flat frequency responses could have a dual sensory role; a) for monitoring traffic flow (low frequency response) and b) detecting the presence of 'cracks' or new 'defects' in the bridge.

The Applied Optics Group at the University of Kent at Canterbury has been developing a variety of optical fibre sensing techniques for diverse applications including monitoring large structures such as bridges.

In this paper, we discuss the following sensing techniques and their potential applications for monitoring the structural integrity of bridges:

(i) Fully distributed Brillouin sensor for temperature and strain sensing,
(ii) Quasi distributed FBG/Fabry-Perôt sensors array for strain, temperature and vibration sensing,
(iii) Point acoustic sensors for ultrasound sensing and possible impact detection.

2. BRILLOUIN DISTRIBUTED SENSOR FOR TEMPERATURE AND STRAIN SENSING

A truly distributed sensor seems the most reasonable means of addressing applications where a huge number of measurement points over a very large structure are required. Stimulated Brillouin Scattering is a unique parametric interaction which offers a simultaneous sensitivity to temperature and strain. The Brillouin process couples, through an acoustic wave, two counter-propagating light beams, which are frequency shifted by an amount dependent on the optical and elastic properties of the medium. A Brillouin based distributed sensor makes use of the temperature [1] or strain [2] dependence of the Brillouin shift. In practice two beams, namely the pump and the Stokes waves, are launched into both ends of the fibre. The measurement is derived from the acquisition of the transmitted pump or Stokes signal (referred to as the Brillouin loss or gain method respectively) as a function of the pump/Stokes frequency shift. This reveals a Lorentzian profile typical of the Brillouin interaction, the center frequency of which is a linear function of the temperature and strain parameters. Positional information, which requires that at least one of the beams be pulsed, is obtained through a standard time delay analysis. The spatial resolution of the sensor is fixed by the duration of the pulse, but is limited to about 1 meter by the finite response time of the Brillouin interaction.

Since it was first proposed in 1989, the method has been the subject of numerous improvements. We demonstrated an arrangement where the sensing fibre follows a double path in the structure to be monitored, attached to the structure one way, and thus subjected to both temperature and strain, and loose on the return path, measuring the temperature only [3]. A temperature resolutions of 1°C and a strain sensitivity of 25με with a spatial resolution of ~1m have been achieved. The method using a section of fibre as the reference sensor is highly reliable and simple to provide an efficient mean for monitoring temperature and strain in large structures, although the requirement of a double path may reduce the applicability of the system. Considerable efforts have been recently made in order to realize a cost effective and viable *in field* device.

One of the main problems which had to be addressed concerns the polarization sensitivity of the Brillouin gain. The polarization state changes randomly during the propagation along a standard communication fibre

link; furthermore, temperature or strain conditions influence this evolution which therefore drifts in time. Getting a maximum signal from every part of the sensing fibre requires at least two measurements with controlled polarization states for both the pump and Stokes waves. We demonstrated the use of a Faraday rotating mirror spliced at the far end of the sensor [4]. This ensures a strong returned signal and most importantly eliminates the need for active control of the state of polarization.

The major practical difficulty in realizing a Brillouin sensor is the requirement for two narrow linewidth laser sources with a 12 GHz frequency difference controlled to about 1 MHz. Several schemes have already been proposed in order to synthesize this dual frequency source from a single one. The solution that we proposed involves a Brillouin fibre ring laser [5], which has the advantage of having the required frequency shift with respect to the pump source, and can be designed to produce a highly stable train of pulses, as shown in Fig. 1.

3. QUASI-DISTRIBUTED FBG/FABRY-PERÔT SENSOR ARRAY FOR STRAIN, TEMPERATURE AND VIBRATION SENSING

A quasi-distributed sensing system for large engineering structures such as bridges requires many, perhaps hundreds, of sensing points. In monitoring the daily changes of static strain of bridges large temperature variations are common, hence compensation for the effect of ambient temperature fluctuation is required. By encoding temperature and strain as a variation in reflected Bragg wavelength, FBGs are an attractive choice of sensing element for such systems [6] - particularly as they may be written at arbitrary locations leaving the dimensions of the fibre unaltered, and offer the potential for low-cost mass production and easy wavelength-division multiplexing. Various techniques have been explored to solve this major problem [7]. However, few have been demonstrated for multiplexed sensor systems due to their relative complexity. In addition, the health of the bridge can be monitored by analysing the low-frequency vibration modes of the bridge. For this application, high sensitivity vibration measurement is required, but single FBG elements have a relatively low strain sensitivity (~1.2pm/με at 1.5μm) with limited options for enhancing the measurement sensitivity and sensing area.

To address these problems, we have explored new FBG-based sensors composed of in-Fibre Fabry-Perôt Interferometers (FFPIs) with mirrors of matched-wavelength FBGs [8]. The FFPI, formed by writing two FBGs with the same central wavelength and interrogated using low coherence interferometry [9] to minimise the interferometric phase noise, has much higher strain sensitivity than FBGs due to its long gauge length. The optical path difference change of the FFPI is used for high sensitivity vibration measurement whist the wavelength-shift of one of the two FBGs protected against strain is used for temperature measurement. Strain monitoring is simply obtained by directly measuring the wavelength-shift of another FBG sensor which is arranged in tandem nearby the FFPI and has a different central wavelength to the FFPI, as shown in Fig. 2. Pseudo-heterodyne signal processing was used for the measurement of the optical phase changes due to the optical path difference changes [10]. The scheme offers simultaneous monitoring of strain, temperature and vibration, together with multiplexing for these three sensors. An experimental system, including two 1m long FFPIs with central wavelengths of λ_1=1531nm and λ_2=1534nm and a FBG with a central wavelength of λ_1=1555nm, is demonstrated. A static strain resolution of better than 1με over a range of 5mε, a temperature sensitivity of 0.1^{0}C and a vibration amplitude sensitivity of better than 1nm/$\sqrt{Hz}$ for low-frequency vibrations (<20Hz) have been obtained. The system cross-talk measured is less than -50dB. For practical systems, a low-cost phase-locked loop would replace the electronic spectrum analyser, and some form of scanning filters would be used in place of the optical spectrum analyser.

4. POINT ACOUSTIC SENSORS FOR ULTRASOUND SENSING AND POSSIBLE IMPACT DETECTION

FBGs have also been demonstrated to detect and measure dynamic strain of up to MHz (ultrasound) frequencies. In structures, such high frequencies may for instance be due to impact damage. They can also be due to *acoustic emission* and it is the monitoring of this which may be of particular importance in evaluating the health of structures: many materials under stress release energy in the form of (surface) elastic waves. The occurrences of these transient frequency bursts gives an indication of potential catastrophic failure of the material or structure and the waveform of the bursts and their frequency spectra (0.1- to 1.0-MHz range) may be characteristic of the mechanism causing them e.g. twinning, dislocation motion or cracking [11]. Such sensors could also be used to determine the location of cracks etc., if the structure was excited by a transducer driven in either CW or pulse mode.

To demonstrate the feasibility of using FBGs to detect and measure these high frequency vibrations, an FBG was positioned at the focal spot of a focused continuous-wave ultrasound transducer (normal to the acoustic propagation direction), in water. The interrogation system is very similar to that shown in Fig. 1, in which a ramped integrated lithium niobate phase modulator (accurately set to produce a 2π peak-to-peak phase excursion) was used to frequency shift the light in one arm of an unbalanced Mach-Zehnder interferometer [12]. Strain induced changes in the central wavelength of the FBG induce a corresponding phase modulation of the electrical carrier produced by the phase modulator, which we measured by determining the amplitudes of the upper and lower side-band frequency components observed on a radio frequency spectrum analyser.

It is apparent that for the grating to operate correctly in response to the MHz acoustic field, the grating length should be made smaller than the acoustic wavelength in fused quartz that is ~3mm corresponding to compressional waves at ~2MHz. Hence, a 1mm FBG was used and exposed to the ultrasound field as other sections of the fibre need to be desensitised, which was done by jacketing the fibre with PVC sleeving (diameter < 1mm), to damp the compressional standing waves in the fibre induced by the ultrasound waves [13]. The preliminary results show that the system response is linear and (for this probe) we determined a noise limited pressure resolution of $\approx 1.8 \times 10^{-2}$ Atm $/\sqrt{Hz}$.

5. SUMMARY

The modes of operation and performances of two different optical fibre sensors - Brillouin distributed sensors and FBG-based sensors, for potential applications to structural monitoring have been discussed, their performances are summarized below:

1) A fully distributed sensor based on Brillouin scattering, this sensor offers extreme sensing range (in excess of 50 km) with resolutions of 1°C or 25με.
2) A quasi-distributed sensor based on the combination of FBGs and FBG-based Fabry-Perôt configuration offering simultaneous monitoring of strain, temperature and vibration, with a static strain resolution of better than 1με over a range of 5mε, a temperature sensitivity of 0.1^0C and a vibration amplitude sensitivity of better than 1nm/$\sqrt{Hz}$.
3) An acoustic point sensor based on a very short FBG with a linear frequency and amplitude response up to 2MHz.

The authors gratefully acknowledge the support of the UK Engineering and Physical Sciences Research Council and the Wellcome trust.

6. REFERENCES

[1] D. Culverhouse, F. Farahi, C.N. Pannell, and D.A. Jackson, "Potential of stimulated Brillouin scattering as sensing mechanism of distributed temperature sensor", *Electron. Lett.* **25**, 913 (1989).

[2] T. Horriguchi, T. Kurashima, and M. Tateda, "Tensile strain dependence of Brillouin frequency shift in silica optical fibers", *IEEE Photon. Technol. Lett.* **1**, 107 (1989).

[3] X. Bao, D.J. Webb, and D.A. Jackson, "Combined distributed temperature and strain sensor based on Brillouin loss in an optical fibre", *Opt. Lett.* **16**, 141 (1994).

[4] N. A. Heron, D.J. Webb, and D.A. Jackson, "Single ended Brillouin interaction based distributed temperature sensor using a Faraday rotating mirror", *Proc. SPIE* **2838**, 124-128 (1996).

[5] V. Lecoeuche, D.J. Webb, C.N. Pannell, and D.A. Jackson, "A simple and efficient technique for an offset frequency shifter for Brillouin based distributed fiber sensing", *Proc. OFS'12*, Williamsburg, Virginia, USA, p. 332 (1997).

[6] R.M.Measures, T.Alavie, R.Maaskant, M.Ohn, S.Karr, S.Huang, D.Glennie, C.Wade, A.Guha-Thakurta, G.Tadros and S.Rizkalla, *Proc SPIE*, **2071**, 21 (1993).

[7] Y. J. Rao, "Review Article: In-Fibre Bragg Grating Sensors", *Meas. Sci. & Technol.* **8**, 355-375 (1997).

[8] Y. J. Rao, P. J. Henderson, D. A. Jackson, L. Zhang, and I. Bennion, "Simultaneous strain, temperature and vibration measurement using a multiplexed in-fibre Bragg grating/fibre-Fabry-Perot sensor system", *Electro. Lett.* **33**, 2063-2064 (1997).

[9] Y. J. Rao, and D. A. Jackson, "Review Article: Recent progress in fibre optic low-coherence interferometry," *Meas. Sci. and Techn.* **7**, 981-999 (1996).

[10] D. A. Jackson, A. D. Kersey, M. Corke, and J. D. C. Jones, "Pseudo-heterodyne detection scheme for optical interferometer," *Electron. Lett.* **18,** 1081 (1982).
[11] J. Kaiser, "Investigation of Acoustic Emission in Tensile Testing," *Ph.D thesis* Technische Hochscule, Munich, Germany (1950).
[12] N. E. Fisher, D. J. Webb, D.A. Jackson, L. Zhang, and I. Bennion, 1996 "Response of in-fibre Bragg gratings to focused ultrasonic fields," *Proc. OFS'12*, Williamsburg, Virginia, USA (1997).
[13] N. Lagakos, et al, "Desensitization of the ultrasonic response of single-mode fibers," *J. Lightwave Techn.* **5** 1036-1039 (1985).

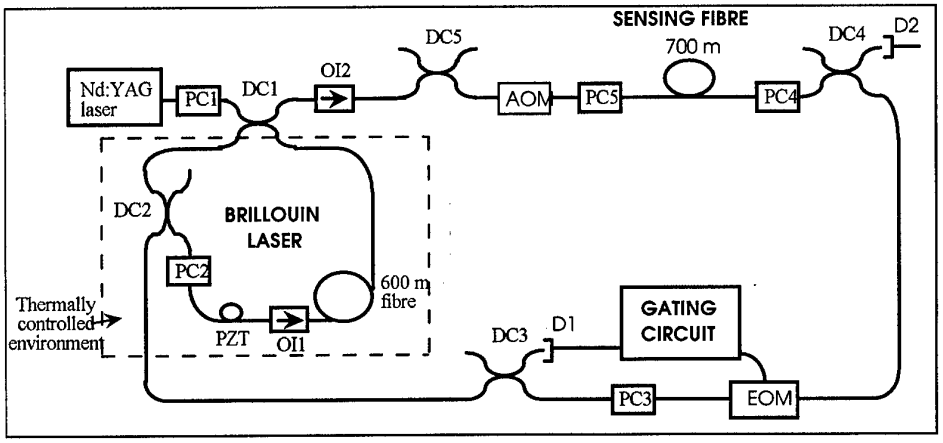

Figure 1: Experimental setup. PC: Polarization Controller, DC: Directional Coupler (1: 55/45%, 2-5: 87/13%), D: Detector, AOM: Acousto-Optic Modulator, EOM: Electro-Optic Modulator, OI: Optical Isolator, PZT: Piezoelectric.

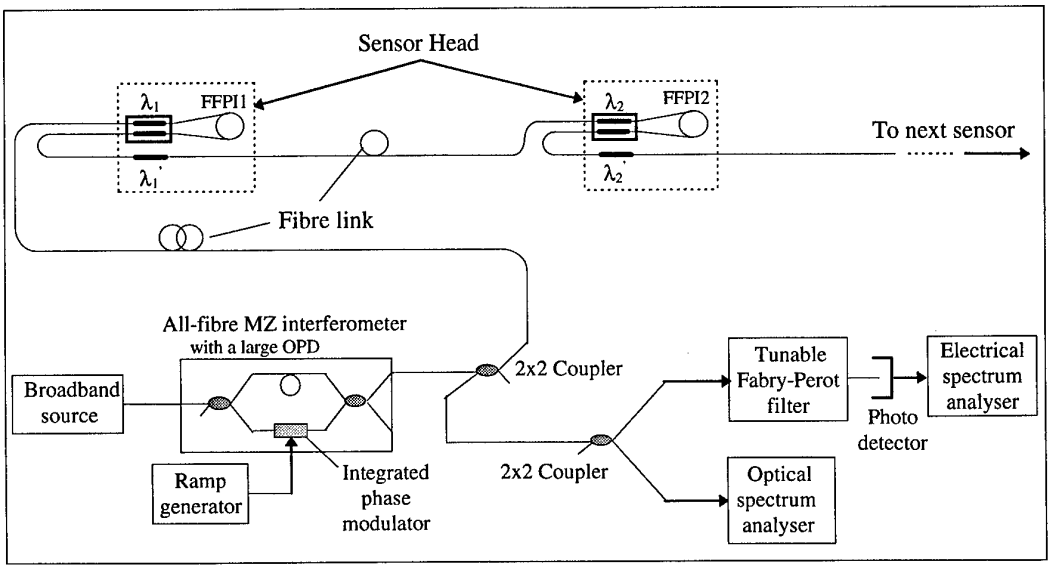

Figure. 2. Schematic diagram of the wavelength-multiplexed FBG/FFPI sensor system

The Distributed Temperature Sensor (DTS) Based on Correlation Technology

Author: Zhang Bo
Postgraduate Student, Electrical Engineering Department, University of Sydney,
NSW 2006, Australia,
Tel : 0061-2-93514895

Section 1. The principle of correlation DTS

The correlation DTS is based on correlation technology and Raman scattering concept. First let us know something about correlation and Raman scattering..

A. Correlation technique

A correlation DTS launches an optical direct Pseudonoise(PN) sequence to probe the fibre. By integrating a returning anti-stokes sequence from the fibre, we can get the temperature information. A PN sequence is a random binary code sequence, in which there are 50% logical 1 and 0 separately. A direct PN sequence can be calculated by PC and stored into EPROM.
The most attractive property of a PN sequence is its autocorrelation. The autocorrelation function of a maximum length PN sequence can be expressed as:

$$\frac{1}{NT}\int_0^{NT} f(t-pT)f(t-qt)dt = \begin{cases} -\frac{1}{N} & ,p \neq q \\ 1, & p = q \end{cases}$$

It means a particular sequence with a particular signal can be identified in a multi-signal system.

B.Raman Scattering

While light with frequency ν is propagating in an optical fibre, some molecules will absorb photons and rise to excited states. Molecules in new states are in new energy level. Two different frequencies of light will be emitted when molecules decay to a lower state. One is from Stokes scatter, referring to a new level higher than the original one. Another is from anti-Stokes scatter, referring to a new level lower than the original one. The energy difference is equal to one of vibration energy of molecules. Molecules radiating anti-Stokes photons have already been in an excited state. The number of excited molecules depends directly on the absolute temperature. The more excited molecules there are, the more anti-Stokes photons are radiated. This suggests a way to measure the temperature of optical fibre.

Section 2 : the System Design

Figure 1 is the block Diagram of the DTS system. It includes the following parts: PN generator, laser diode driver circuit, optical set-up, correlator, PC.

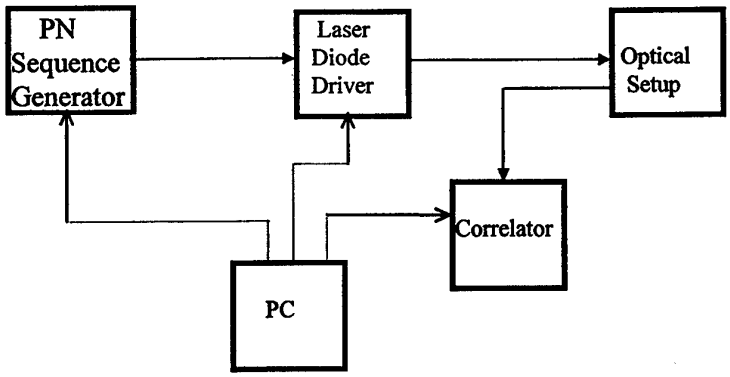

Figure 1

The operating principle is like this. The PN signal generator outputs PN codes to laser diode driver . The laser diodes driver amplifies the PN codes and uses them to drive laser diodes, so the PN codes are converted into optical signals and are probed into optical setup, which includes several kilometres long optical fibre. When the optical PN codes are propagating the fibre, Anti Stocks signal will be generated , and will travel to the side that PN signal input through. They go through a Raman filter, and reach the optical detector at last, then they are converted into electrical signal. The correlator will receive this signal and multiple it with the same PN codes which are certain clock period delayed. According the correlation principle, the anti-Stokes signal about a certain point can be gotten, so the temperature of a certain point can be calculated. repeat this process so that the temperature of every points along the optical fibre can be calculated.
In the following we discuss the every parts of DTS separately.

A. PN code generator

The structure of PN signal generator is as Figure 2. The PN codes are stored in EPROM. The logic circuit will make sure that one code is output in one clock period.

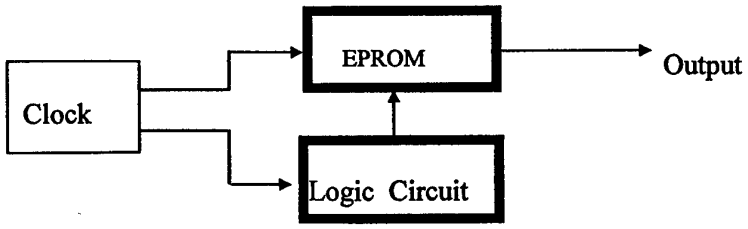

Figure 2

B. Laser driver circuit

The laser driver circuit is a high speed amplifier. It will amplify the input PN codes to drive a laser diode, and convert the PN code to a optical codes.

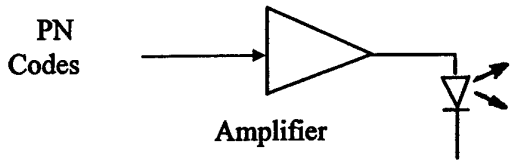

Figure 3

C. Optical set-up

The optical setup (figure 4) is mainly composed by laser diode, optical fibre, Raman filter, detector. The optical codes from the laser diode will be probed into optical fibre. When optical signal is travelling in the fibre, Anti stokes signal will be generated. Part of the signal will backscatter to the Raman filter. The Raman filter will remove all other optical signals except anti-Stokes signal, which will reach detector at last and be converted into electrical signal.

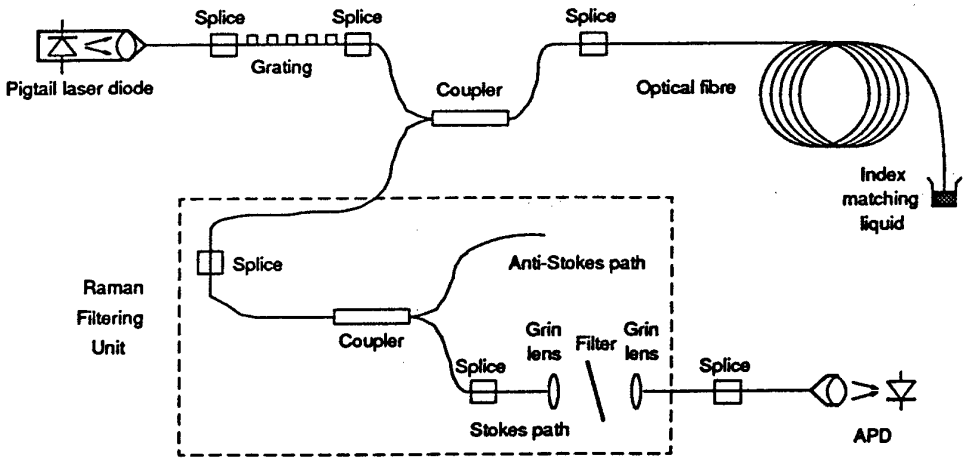

Figure 4

D. Correlator

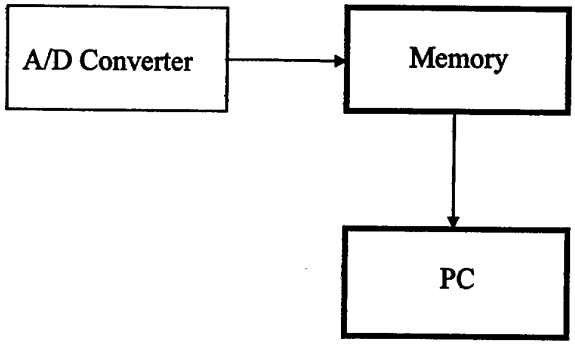

Figure 5

The correlator (figure 5) is a digital correlator. The analogue signal from detector will be converted into digital signal by A/D converter, and the data will be stored into memory. After the whole sequence of PN codes has been sampled, PC will read the data from memory and multiple them with the same PN sequence that is certain clock period delayed. According the autocorrelation function :

$$\frac{1}{NT}\int_0^{NT} f(t-pT)f(t-qt)dt = \begin{cases} -\frac{1}{N} & ,p \neq q \\ 1, & p = q \end{cases}$$

The Anti stokes signal of the point (p=q) can be distinguished, so we can calculate the temperature of that point.

Section 3 The advantage of correlation DTS

In a conventional DTS, only one pulse is launched into fibre, the backscatter is received at the launching end. The signal from different points arrive at the receiver at different time, so that the location of these points can be recognised with a timing circuit. A photo counter is used to count the anti-stokes signal and to measure the temperature at that point. However, as the anti-stokes signal is extremely weak, a high power laser source and long time average must be employed, the cost of the laser components and electrical components are very high, above fifteen thousand dollars. The correlation DTS can solve this problem . The correlation DTS outputs hundreds of thousands of PN codes instead of one pulse, so the mean launch power is greatly improved. Low power laser source and low sensitive laser detector can be used, so the cost of correlation DTS is much cheaper than conventional DTS, about several thousands dollar. The reliability of correlation DTS is also high, because we can use more reliable components.

The measure length of correlation DTS is several kilometres, and the accuracy of correlation DTS is supposed to be half an degree. Because of these characteristic, it has a wide range of application in practice.

A study of effects of phase modulator characteristics on interferometer system performance

Yicheng Lu, Ralf Pechstedt

Bookham Technology Ltd, 90 Milton Park, Abingdon OX14 4RY, UK
Telephone: ++44-1235-827200; E-mail: yicheng.lu@bookham.com

Optical interferometry is widely used for high accurate measurement and two-beam interferometry is one of the well-used techniques. Due to the nature of the Cosine response of an interferometer, a signal processing technique is necessary to obtain the measurand. A phase modulator is commonly used to demodulate the interferometer signal and to process the signal so as to recover the measurand. Naturally, interferometer performances depend on the response of the phase modulator, especially the linearity and the amplitude modulation. This paper investigates the effect of phase modulator characteristics on interferometer performances when the active homodyne technique is used to process the signal.

1. Measuring principle

The output of an two-beam interferometer has the general form:

$$I = I_0 [1 + \nu * COS(\Phi_s + \Phi_0)] \quad (1)$$

Where I_0 is the input light intensity to the interferometer, ν is the visibility, Φ_s is the signal produced by the measurand induced phase and Φ_0 is the phase equivalent of initial optical path difference (OPD). This equation indicates that the signal cannot be directly measured through measuring detector output (I) for the following reasons: a) the position may be at its least sensitivity position; b) the output intensity varies with any variation in the whole optical path such as source variation, intensity variation caused by micro-bending fibre or polarisation drifting; and c) non-linearity response. Signal processing techniques are necessary to solve the above problems. The active homodyne [1 – 4] (or active tracking through feedback) is one of the most widely used techniques. It offers the main advantages of simplicity, high accuracy, long term stability and large linear working range (only limited by the phase modulator). To realise the active feedback, a phase modulators is required to add a dithering signal and to feedback so that the system is always at the quadrature point. Common phase modulators are of the type of piezo fibre stretcher [1], $LiNbO_3$ Voltage controlled phase modulator [4] and SIMOX *PIN* diode phase modulator [5].

The active homodyne measuring principle is as follows. Adding a dithering signal (triangular or square wave) and a feedback signal into the interferometer through a phase modulator, equation 1 becomes:

$$I = I_0 [1+ \nu * COS(\Phi_s + \Phi_d + \Phi_f + \Phi_0)] \quad (2)$$

where Φ_f is the feedback signal and Φ_d the dithering signal.

If $$\Phi_s + \Phi_f + \Phi_0 = 0 \text{ or } 2m\pi \qquad m: \text{integer} \quad (3)$$

then the output from the detector at two dithering positions A & B (the same for triangular or square wave) will be equal ($V_a = V_b$ see figure 1(a)). This is the stable state or locking state. On the other hand, if condition (3) is not satisfied, the voltage at point A is not equal to the voltage at point B ($V_a \neq V_b$), which creates an error signal (see figure 1 (b)). This error signal can be used to feedback control the phase modulator until the voltages at these two positions

are equal. In other words, as long as the two voltages are kept same, the feedback phase is the measurement of the signal with a constant difference of initial phase Φ_0. For a relative measurement system or a calibrated system, the initial phase Φ_0 cancels itself out, and therefore the feedback phase (Φ_f) is the signal to be measured.

2. Effects of phase modulator non-linearity on interferometer system output

Feedback is realised by the phase modulator driver through voltage (for the $LiNbO_3$ phase modulator) or current (for the *PIN* diode phase modulator in silicon on insulator (SOI)) and the system output is the driving voltage/current. The output is an accurate measurement only when the phase modulator has a purely linear response. Unfortunately, this is not always true. In fact, the linearity only holds at a certain working range with certain conditions, especially for a PIN diode phase modulator. When the phase modulator response is not linear, the system output changes accordingly and is not exactly the same as the signal to be measured. Figure 2 illustrates this effect ($LiNbO_3$ is used as an example so the driving voltage is explicitly used). The discussion is also correct for a *PIN* diode phase modulator where driving current should be used instead. For a given signal Φ_s, the voltage required to generate a phase ($\Phi_f = -\Phi_s$) is V_f if the phase modulator is linear (see figure 2 a). Due to the non-linearity, now the voltage will be $V_{f'}$ to generate the same phase as $-\Phi_s$. The difference between positions f and f' is the system error that is equivalent to an phase error of $\Delta\Phi$. The system output (the feedback voltage) is uniquely decided by the phase modulator response. In fact, the system output response is the same as the phase modulator response but with X/Y axes reversed.

The above analysis does not include the effects caused by dithering signal when the non-linearity of the phase modulator exists. When dithering signal effect is taken into account, another error will be induced by the dithering signal. For the discussion of dithering signal influences, equation (2) is re-written as (Φ_0 is neglected):

$$V_a = \alpha I_0 [\, 1 + \nu * COS((\Phi_s + \Delta\Phi_a + \Phi_f)]$$
$$V_b = \alpha I_0 [\, 1 + \nu * COS((\Phi_s + \Delta\Phi_b + \Phi_f)] \qquad (4)$$

where α is current to voltage conversion factor, $\Delta\Phi_a = \Phi_f - \Phi_a$ and $\Delta\Phi_b = \Phi_f - \Phi_b$ are the phase differences relative to the phase Φ_f at positions A & B respectively (see figure 1 & 3) and Φ_f is the phase when the driving voltage is at its mid point. When $\Phi_f = -\Phi_s$, V_a should equal V_b if the dithering signal is not affected by the non-linearity. However, if the non-linearity effect is considered, V_a is no longer equal to V_b (see figure 3, the exaggerated condition). Now $\Delta\Phi_b$ is smaller than $\Delta\Phi_a$, which makes V_a smaller than V_b (depending on feedback direction). An extra feedback signal will be generated to shift the system into a new stable condition f' and the driving voltage now changes to V_f'. The voltage difference between position f and f' is the extra error created by the phase modulator non-linearity and the dithering signal together.

Error quantification is possible through more detailed analysis. At the new stable position we have, $\Delta\Phi_a' = \Phi_s - \Phi_a'$; $\Delta\Phi_b' = \Phi_s - \Phi_b'$ and $\Delta\Phi_a' = \Delta\Phi_b'$ (5)

Considering that positions A & B now are at quadrature points (if dithering range is π),

$$|COS(\Delta\Phi_a' - \Delta\Phi_a)| = |\Delta\Phi_a' - \Delta\Phi_a|$$
and $$|COS(\Delta\Phi_b' - \Delta\Phi_b)| = |\Delta\Phi_b' - \Delta\Phi_b| \qquad (6)$$

Note that Φ_b becomes larger while Φ_a becomes smaller and that the shift is much smaller compared with the dithering range, the phase shift for both positions are very close to each other. Thus,

$$\Delta\Phi_a - \Delta\Phi_a' \cong \Delta\Phi_b' - \Delta\Phi_b = \varepsilon \text{ (Error)} \quad (7)$$

making use of equation 5,

$$\varepsilon = (\Delta\Phi_a - \Delta\Phi_b)/2 \quad (8)$$

Equation 8 means that the extra error generated by dithering signal equals half of the phase difference between upper and lower half driving cycles. A specific response (parabolic) is taken as an example. The modulator response is:

$$\Phi = V + a*V^2 \quad (9)$$

If the dithering voltage amplitude is ΔV, the error introduced by the dithering signal can be proved to be: $\varepsilon = a*\Delta V^2$ (10)

It can be concluded (from equation 10) that a) the error equals the non-linearity error corresponding to the dithering amplitude and b) the error is constant if the phase modulator response is parabolic, which could be neglected like initial phase Φ_0.

The above conclusions were proved by numerical analysis.

3. Amplitude modulation effects.

For a two-beam interferometer with 50-50 splitter ratio with extra loss (amplitude modulation) caused by phase modulator in one arm, equation 2 can be written as

$$I = I_0/2\ [(1+\beta) + 2*\nu*\sqrt{\beta} * COS(\Phi_s + \Phi_f + \Phi_d + \Phi_0)] \quad (11)$$

where β amplitude modulation co-efficient which is a function of driving voltage and is always smaller than one. Using the similar way to non-linearity analysis and also note that the stable condition ($V_a = V_b$) is also at the quadrature positions for point A & B (see figure 4), we have:

$$V_a = I_0\ [(1 + \beta_a)/2 + \nu*\sqrt{\beta_a} * \varepsilon)] \quad \text{and} \quad V_b = I_0\ [(1 + \beta_b)/2 - \nu*\sqrt{\beta_b} * \varepsilon)] \quad (12)$$

Finally we get $\varepsilon = (\beta_b - \beta_a) / [(\sqrt{\beta_a} + \sqrt{\beta_b}) *\nu *2]$ (13)

This equation clearly demonstrates that

- The error is proportional to the difference between the two amplitude modulation co-efficients for two dithering positions.
- The error is inversely proportional to the visibility. Lower visibility causes larger error.

It should be noted also that the amplitude modulation causes detector intensity variation, which may affect the feedback speed/sensitivity. In the worst situation, this can cause instability of the feedback system (depending on the circuit).

4. Conclusions

The effects of phase modulator characteristics on performances of a two-beam interferometer with active homodyne processing technique are analysed. The following conclusions can be made from the analysis:

- The system output has the same response as the phase modulator but with reversed X/Y axes. This is the major error source to the system.

- Due to the existence of dithering signal, phase modulator non-linearity introduces an extra error to the system which equals the non-linearity in the dithering phase range. If the response of modulator is parabolic, the error will be constant and may be neglected.
- The dithering signal caused error is proportional to the dithering range by either non-linearity or amplitude modulation of the phase modulator.

5. References:

[1] Jackson, D.A. et al.; "Elimination of drift in a single mode optical fibre optical fibre interferometer using a piezo-electrically coiled fibre", *Appl. Optics*, Vol.9 pp2926

[2] Fritsch, K. & Adamasky, G.: "Simple circuit for feedback stabilisation of a single mode optical fibre interferometer", *Rev. Sci. Instrum.* Vol.52, pp996

[3] Cahill, R.F. & Udd, E.: "Phase-nulling fibre optic laser gyro", *Optics Letters*, Vol.4 pp93

[4] Porte, H. et al.: "Linear phase tracking in a coherence modulation electrical sensor system using integrated $LiNbO_3$ modulator/demodulator", *IEEE J. of Selected Topics in Quantum Electronics*, Vol. 2, 1996, pp319

[5] Tang, C.K. et al.: "Low-loss, single mode, optical phase modulator in SIMOX material", *J. of Lightwave Technology*, Vol. 12, Aug. 1994, pp1394

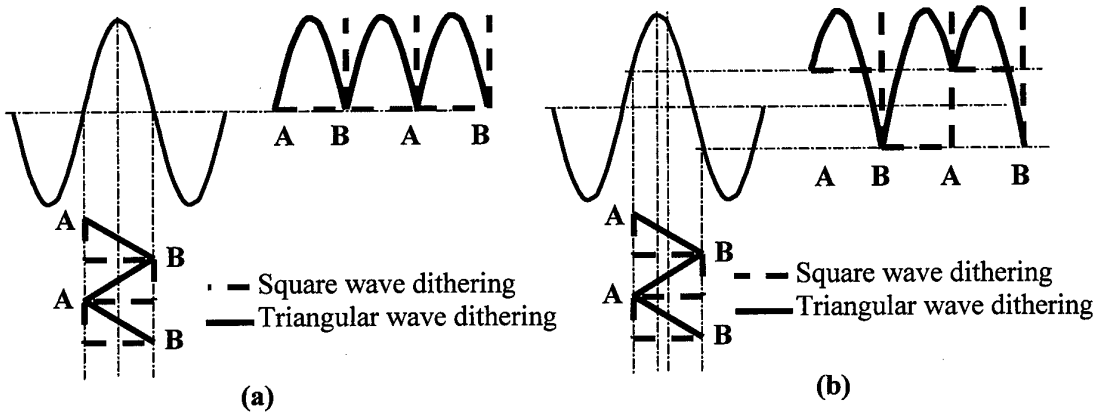

Figure 1 Principle of active homodyne processing technique. a) at locking state ($V_a = V_b$); b) not at locking position ($V_a \neq V_b$), feedback required.

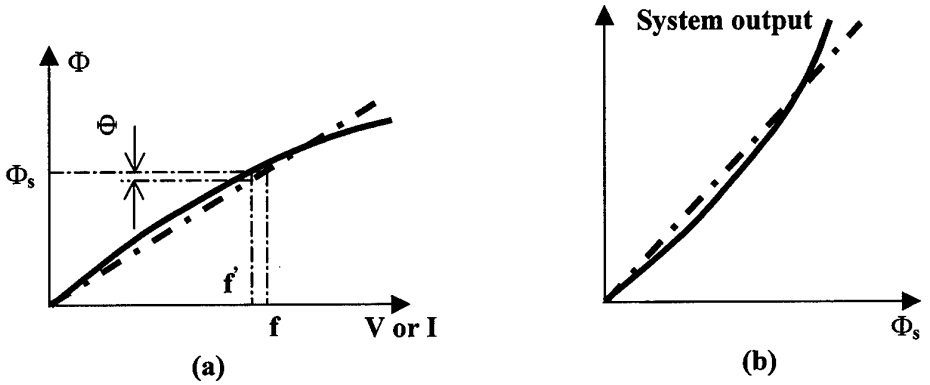

Figure 2 Non-linearity of phase modulator effects on system output. a) phase modulator response; b) system output

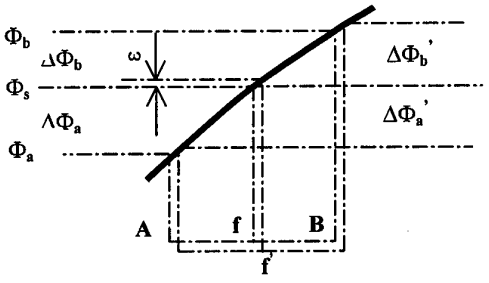

Figure 3 Error caused by dithering and non-linearity of modulator

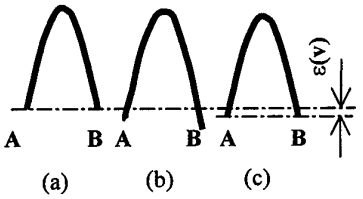

Figure 4 Error caused by amplitude modulation. (a) stable state without amplitude modulation; (b) with amplitude modulation; (c) new stable position

Active Silicon integrated Optical Circuits (ASOC™) for White-Light Sensing Applications

R. D. Pechstedt, Y. Lu and S.F. Knowles
Bookham Technology Ltd., 90 Milton Park, Abingdon, Oxon, OX14 4RY, UK
Tel: +44 1235 827203, Fax: +44 1235 827201

Introduction

Bookham Technology has developed a unique manufacturing technology called ASOC™ which employs low-loss silicon-on-insulator (SOI) rib waveguides combined with interfaces for waveguide-to-fibre coupling and hybridised optical sources and detectors [1]. Due to the inherent optical properties of silicon, low loss is achieved at wavelength above ~1.2μm, enabling us to cover the important telecommunication windows of 1.3μm and 1.5μm. The technology is based on standard wafer scale silicon processing techniques similar to those used in the microelectronic industry, and hence enables low-cost, high-volume manufacturing. It offers great flexibility leading to the possibility of exploitation in a number of different market areas.

Bookham is currently applying this technology to the access market ('fibre to the curb' and 'fibre to the home') [2]. The first products, bi-directional transceivers, were launched in February 1997 at the Optical Fibre Communication conference in Dallas, Texas. Fig.1a is a schematic of a bi-directional transceiver and Fig.1b shows an assembled ASOC™ transceiver. Recent additions to Bookham's product range include bi-directional DWM 1310/1550nm transceivers and transceivers incorporating a transimpedance amplifier.

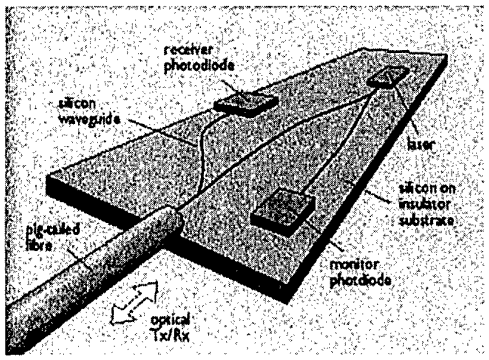

Fig.1a Schematic of ASOC™ transceiver

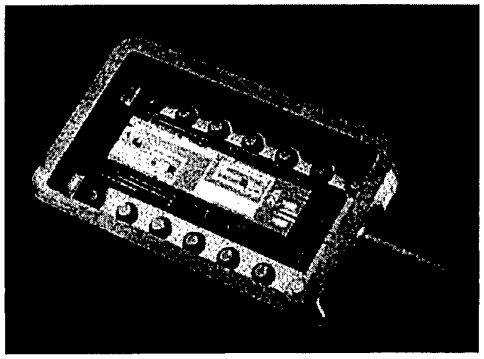

Fig.1b Assembled ASOC™ transceiver

ASOC™ technology and its Application to Optical Sensing

ASOC™ technology provides a number of functional elements which can be combined in different ways, offering a large range of functionality. Apart from the Access and DWM market, we are also working on the application of ASOC™ to optical sensor products. By sharing the same technology basis, significant commercial benefits in this high growth area are expected.

ASOC™ is a manufacturing process based on low loss SOI waveguides. Typical loss figures are ~0.1dB/cm. The waveguides are designed to be single-mode and hence, enabling interferometric sensor designs. Fig.2 is a schematic of the ASOC™ waveguide structure. As the typical waveguide dimensions are in the order of several microns, adiabatic taper structures are employed to achieve mode match to standard optical telecommunications fibre. Precisely etched V-grooves facilitate accurate alignment of the fibre to the waveguide and allow for passive fibre attachment. As a result, low loss coupling between fibre and waveguide can be achieved in a low-cost, high-volume manufacturing environment. Fig.3 shows a optical fibre in a V-groove, aligned to an ASOC™ waveguide.

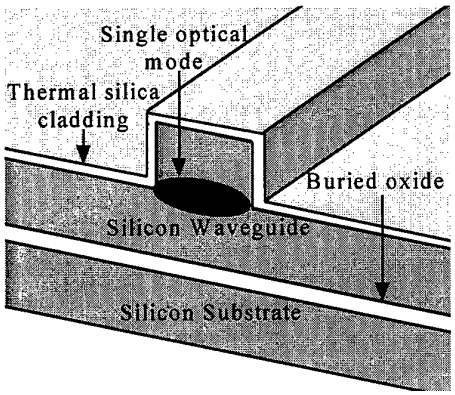

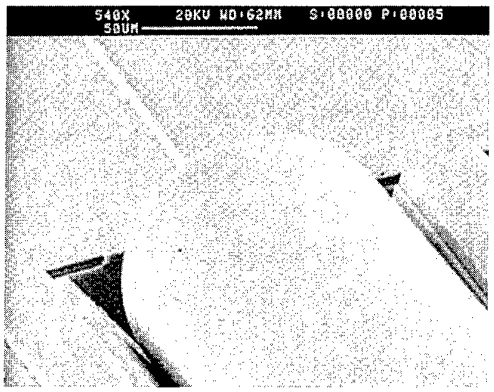

Fig.2 Schematic of ASOC™ waveguide

Fig.3 Fibre to waveguide coupling

Micromachining features on both the silicon chip and light sources/detectors enable accurate passive alignment to the waveguides, providing a cost efficient route for hybridising these elements. A rugged attachment process has been developed by Bookham. Fig.4 shows a laser mounted in front of an ASOC™ waveguide. In addition, couplers and Y-junctions can be formed on SOI, facilitating the design of more complex photonic circuits. Fig.5 provides an SEM picture of a Y-junction employing ASOC™ waveguides.

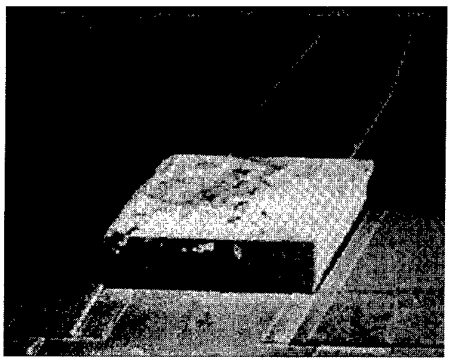

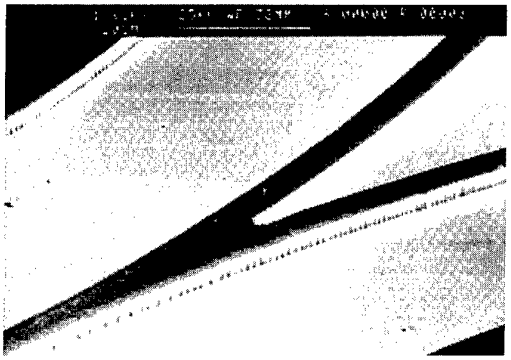

Fig.4 Laser aligned to ASOC™ waveguide

Fig.5 Y-junction employing ASOC™ waveguides

A major benefit of ASOC™ technology is its ability to facilitate phase modulation of the guided beams via free carrier injection or thermal effects. Free carrier injection is provided by placing p and n doped regions on either side of the waveguide. They form a *pin*-diode and electrons and holes are injected into the waveguiding region when the diode is forward biased, changing the effective index of the optical mode. Typical performance figures for the *pin*-phase modulator include the current to achieve a π phase shift (~20mA), optical loss at π phase shift (~0.3dB) and modulation rate (~20MHz). Hence, the ASOC™ phase modulator is ideally suited to meet the requirements of most signal processing requirements in sensor applications.

Taking all these individual building blocks together, ASOC™ technology is very attractive for a large range of optical sensing applications. At Bookham several sensor products are currently being developed:

- Pressure sensor system for applications in automotive in-cylinder pressure measurements in conjunction with a major automobile company. Based on a white-light approach, it offers highly sensitive and accurate measurements combined with inherent lead insensitivity. Both the ASOC™ demodulation scheme and the prototype high temperature sensor heads have been demonstrated successfully.
- Applications in fibre optical gyroscopes offer significant cost reductions together with compact and robust packaging.
- Interrogation of in-fibre Bragg gratings used for structural monitoring employing a low cost ASOC™ optical to electrical interface.
- Biosensors for real time monitoring in biomedical and environmental applications.

The majority of these applications make use of an ASOC™ based white-light system, key components of which are described in the next section.

White-Light Sensing based on ASOC™ technology

A key element of any white-light system is the optical element which analyses the information returned from a remote sensor head in form of a channelled spectrum. The most straightforward option is a processing interferometer, the optical path difference (OPD) of which is matched to the OPD of the sensing cavity. We have developed Mach-Zehnder interferometers based on ASOC™ technology which can be designed to a specified OPD. For the Mach-Zehnder design shown in Fig.6, the OPD can be calculated according to

$$OPD = 4n_{eff}\left\{R\arccos\left(\frac{R-d}{R}\right)-\sqrt{2dR-d^2}\right\},$$

where n_{eff} is the propagation index of the guided mode, R is the bend radius and d is the drop. A number of Mach-Zehnder interferometers with varying OPD have been built and the OPD was measured by evaluating the channelled spectrum. Excellent agreement between the predicted and measured values was achieved (Fig.7).

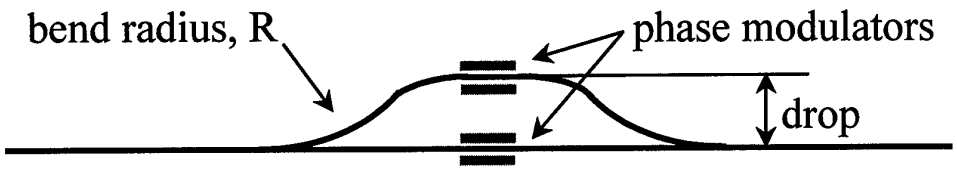

Fig.6 Schematic of ASOC™ integrated Mach-Zehnder interferometer

A typical channelled spectrum produced by an ASOC™ Mach-Zehnder interferometer is shown in Fig.8. As can be seen, a high modulation depth is achieved.

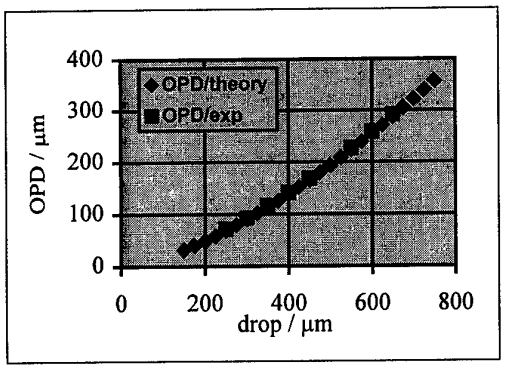

Fig.7 OPD of ASOC™ Mach-Zehnder

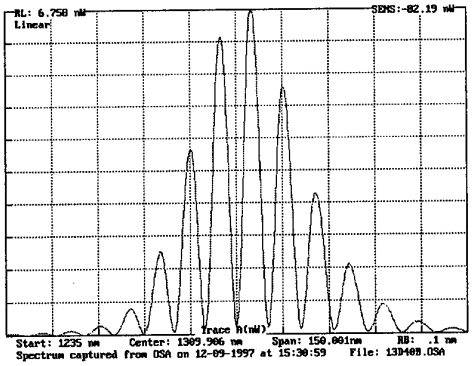

Fig.8 Typical measured channelled spectrum

The ASOC™ interferometer was used to interrogate a Fabry-Perot sensor simulator formed by a vibrating mirror placed in front of a cleaved fibre. Electronics hardware in form of a tracking circuit was built which enables the conversion of displacement into a voltage. Fig.9 shows a typical result measured at a signal frequency of 1kHz, demonstrating excellent linearity and a dynamic range sufficient for a large number of industrial applications. Fig.10 shows the system output using a Fabry-Perot pressure sensor head. The developed system is ideally suited for automotive in-cylinder pressure measurements and high-temperature operation of the sensor head has been demonstrated successfully.

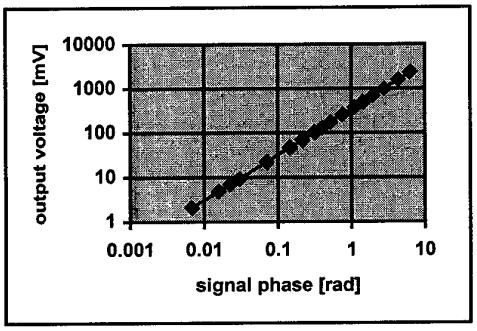

Fig.9 Dynamic system output at 1KHz

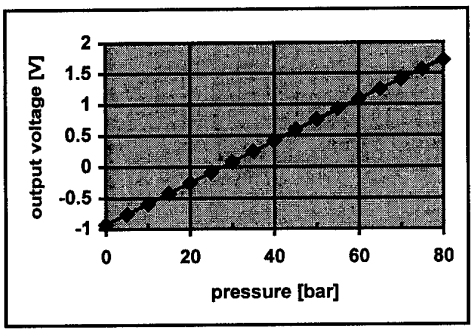

Fig.10 Static system output vs. applied pressure

Conclusions

With ASOC™ a cost-efficient manufactureable integrated optics technology has become available which satisfies the needs of a large range of optical sensing applications. Due to its extreme flexibility, it can be easily adapted to meet specific photonic requirements. We have demonstrated the superior performance of the basic integrated building blocks and shown its suitability in white-light system applications. Further, a white-light pressure system has been developed which is suitable for automotive applications.

References

[1] Rickman AG, (1997), Using the ASOC™ optoelectronic IC process through foundry services, SPIE, Vol 3007, 0277-786X/97.

[2] Gorton S, Barrett P, Dennett N, Morris R, (Sept, 1997), Dual wavelength WDM transceiver meets access network needs, Fiberoptic Product News, Gordon Publications, pp 21,22.

Brillouin based distributed fibre sensor incorporating a Brillouin laser

V. Lecœuche, D.J. Webb, C.N. Pannell and D.A. Jackson,
Applied Optics Group, Physics Laboratory,
University of Kent, Canterbury CT2 7NR
Tel: (0)1227 823288, Fax: (0)1227 827558.

I. INTRODUCTION

Stimulated Brillouin scattering is a unique parametric interaction which offers a simultaneous sensitivity to temperature and strain. Distributed sensing over 50 km with a spatial resolution in the meter range has been demonstrated [1]. Nevertheless, the need for two narrow linewidth laser sources, with a 10 GHz frequency difference controlled to about 1 MHz, is still a major factor limiting the commercial development of a cost effective system. In order to avoid ultrafast electronics which may be used to synthesise a dual frequency source [2-4], we are currently investigating various arrangements incorporating a mode-locked Brillouin fibre ring laser. We have already demonstrated a first application for fire detection with a very simple arrangement [5]. The sensor had an 8 meter spatial resolution over 15 km. In that experiment, the frequency shift between the CW pump and the Stokes pulses was constant and the sensor provided a signal when the fibre reached a threshold temperature. This permitted very fast data acquisition matching with the requirements of an alarm system.

Tuning of the pump/Stokes frequency shift is necessary for the *measurement* of the temperature or strain. We describe here a new arrangement which allows the tuning of the Stokes pulses through phase modulation, and we report some preliminary results.

II. EXPERIMENT

The experimental set-up is schown in figure 1. The Brillouin fibre ring laser, already described in reference [5], generates pulses of about 80 ns and 60 mW peak power at the output of the coupler DC2. When the temperature of the laser is 60°C, the frequency shift between the pump and the Stokes pulse is 12.855 GHz. The repetition time of the pulses (2.9 μs) is smaller than required for

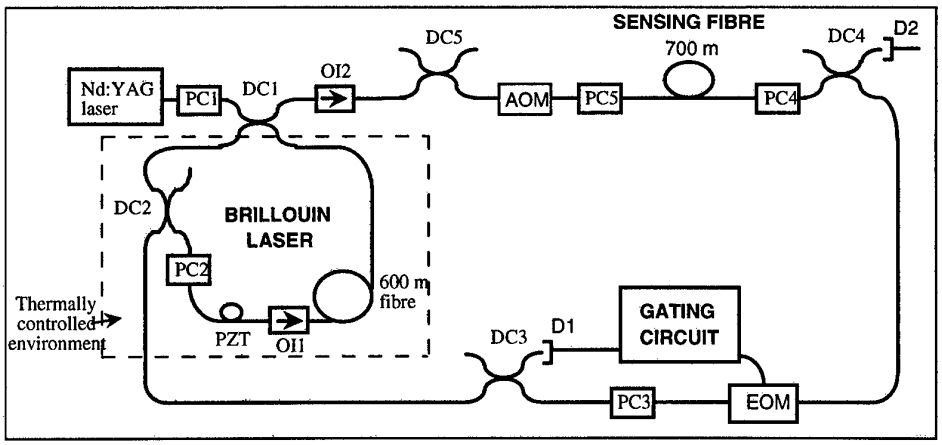

Figure 1: Experimental setup. PC: Polarization Controller, DC: Directional Coupler (1: 55/45%, 2-5: 87/13%), D: Detector, AOM: Acousto-Optic Modulator, EOM: Electro-Optic Modulator, OI: Optical Isolator, PZT: Piezoelectric.

the sensor so the pulses must somehow be gated. In the experiment, only certain pulses are phase modulated (by the EOM) and will therefore interact with the CW pump in the sensor. An electronic circuit was designed to generate a trigger signal once the signal from detector D1 reached a threshold value, indicating the occurrence of a pulse. A phase modulation can then be applied during a short time to produce sidebands in the pulse spectrum. Since the first sideband only should interact with the pump over the whole temperature tuning range, the frequency of the modulation has to, at least, lie around the 200 MHz range. In order to compensate this mean shift, the pump launched in the sensing fibre was shifted by 200 MHz using an acousto-optic modulator. Note that this latter component would be unnecessary if a fibre with higher dopant concentration in the core was used for the Brillouin laser than for the sensor, a shift of a few hundred MHz of the Brillouin gain can be obtained by this method [4].

III. RESULTS

We demonstrated the technique with a 700 meter long sensing fibre. Two lengths of 10 meters in the middle of the sensor were subjected to 0 mε and 74°C, and 1.4 mε at ambient temperature respectively. Another 10 meters of loose fibre at ambient temperature separated them. The result of the frequency scanning for the region of interest is shown in figure 2. Two spikes can be easily identified in the foreground (or left front) of this 3D plot, characterised by a higher Brillouin shift. The one on the left corresponds to the heated fibre, the other corresponds to the fibre under strain.

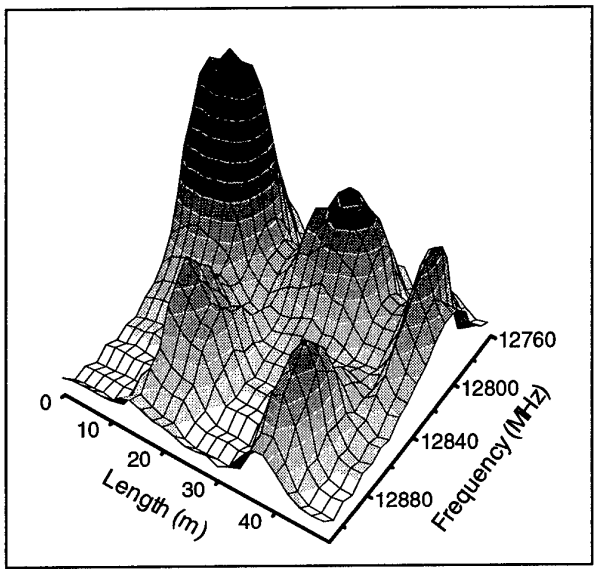

Figure 2: Distributed gain profile of 50 meters of the sensing fibre.

IV. CONCLUDING REMARKS

We have demonstrated the feasibility of a distributed sensor using a Brillouin laser. A 10 meter resolution was demonstrated. Further improvements are however required to ameliorate the signal to noise ratio of our sensor. The high loss of the phase modulator used (6 dB) reduces the power of the Stokes first sideband to about 2 mW peak power. Larger signals could be obtain with a higher probe power, which could be obtained with different phase modulator, or the use of a Brillouin amplifier. Finally, our dual frequency source may also be used for coherent detection of *spontaneous* Brillouin scattering [3], simultaneous measurement of the Brillouin frequency shift and the level of spontaneously backscattered light permits the separation of the temperature and strain information.

V. REFERENCES

1. X. Bao, J. Dhliwayo, N. Heron, D.J. Webb and D.A. Jackson, "Experimental and theoretical studies on a distributed temperature sensor based on Brillouin scattering", J. Lightwave Tech., vol. 13, pp. 1340-1348 (1995).

2. H. Izumita, T. Sato, M. Tateda and Y. Koyamada, "Brillouin OTDR employing optical frequency shifter using side-band generation technique with high-speed LN phase-modulator", IEEE Phot. Tech. Lett., Vol. 8, pp. 1674-1676 (1996).

3. M. Nikles, L. Thevenaz and P.A. Robert, "Simple distributed fibre sensor based on Brillouin gain spectrum analysis", Opt. Lett., Vol. 21, pp. 758-760 (1996).

4. M. Nikles, L. Thevenaz, P.A. Robert, "Brillouin gain spectrum characterization in single-mode optical fibres", J. Lightwave Technol., vol. 15, p 1842 (1997).

5. V. Lecoeuche, D.J. Webb, C.N. Pannell and D.A. Jackson, "A simple and efficient technique for an offset frequency shifter for Brillouin based distributed fibre sensing", Proceedings of OFS 1997, p. 332.

Development of a fully polarimetric optical time domain reflectometer (POTDR)

A.S. SIDDIQUI
Department of Electronic Systems Engineering
University of Essex, Colchester, Essex, CO4 3SQ, UK
Telephone: +44 (1206) 872431; Fax: +44 (1206) 872900; email: ass@essex.ac.uk

1. Introduction

A major development during the last two years has been the deployment of the first *optically amplified* high bit rate (≥ 5 Gb/s) and long haul (TAT 12/13, TPC 5) optical transmission links. A further parallel development over the last few years has been the design, and implementation upto the demonstrator stage, of large scale optically amplified high bit rate fibre communication *networks* [1,2]. Like the long haul point to point links these networks are also to be optically transparent and their end to end size can be several thousand kilometres. In both cases optical transparency (that is, the absence of 3R regenerators, usually less than 100km apart) results in dispersion and non-linear effects accumulating over the entire length of a link. Dispersion shifted (DS) fibres, together with dispersion management schemes, have now essentially overcome the chromatic dispersion problem. These schemes can also keep the penalties due to non-linear effects to within acceptable limits [3]. However, polarisation mode dispersion (PMD) still remains as a significant and now the main dispersion mechanism which limits the maximum attainable bit rate times distance product for these links. This limitation due to PMD applies not just to the new generation of links and networks using DS fibre. They also apply, again as a highly significant limitation now, to upgrading the transmission bit rate over the vast amount of already installed standard step index fibre where the chromatic dispersion at 1.5μm can now be overcome by one or other of a range of dispersion compensation schemes demonstrated over the last few years [3].

Polarisation effects in transmission fibres are therefore an important current topic for experimental and theoretical investigation and in this talk I will attempt to summarise the recent work in this area at Essex.

The initial stimulus for this work was the development of spun fibre to reduce PMD values in fibre cables for use in optically amplified transoceanic links. The main goal of our work was to understand the interaction between the linear and circular birefringences within the fibre and how this leads to the observed PMD behaviour of the fibre, with and without external twist. It will be seen that the role played by fibre twist is a crucial one in determining the PMD behaviour.

2. Differential Group Delay (DGD), Polarisation Mode Dispersion (PMD) and the Maximum Bit Rate

Using the principal states model [4] for polarisation propagation in fibres, we define the differential group delay (DGD) in a *short* fibre link as the difference between the transit times, across the link, of the two orthogonal principle states of polarisation for the link. A convenient

unit for DGD in real fibres is ps/km. In this context a *short* fibre link is defined as one where there is no mode coupling within the link so that the DGD is a direct measure of the (uniform or average) fibre birefringence. For a given fibre the DGD of a short link therefore increases linearly with length as its unit (ps/km) indicates.

If we now progressively increase the length of the link then it is found that, for link lengths greater than a few kilometres, the measured dependence of DGD on link length reduces to being proportional to the *square root* of the link length. This is due to mode coupling coming into play as the link length increases. In this regime of *long* fibre links the differential group delay over the link is referred to as polarisation mode dispersion (PMD), whose value is usually quoted in units of (ps/km$^{\text{TM}}$).

Now because mode coupling is a random process it is not possible to write down a general deterministic relationship between the DGD and PMD values of a fibre. However, for real fibres a rough rule of thumb appears to be that a long link, formed from a fibre with a DGD of say 1ps/km, is likely to have a PMD lying in the range $(0.2 \rightarrow 0.5)$ ps/km$^{\text{TM}}$.

Turning now to the limit due to PMD on the maximum practicable bit rate, we note that the design figure taken for the TAT12 link was that the *total* PMD time over the whole link had to be not greater than 7% of the bit period. TAT12 was designed to allow a maximum PMD of 0.15ps/km$^{\text{TM}}$, which would result in a total PMD of 12ps over its 6400 km length. This in turn leads to a maximum practicable bit rate of 5.8 Gb/s which is comfortably above the target figure of 5 Gb/s.

3. Partially polarisation sensitive OTDR

First experimental attempts to analyse birefringence in fibres used a linear polariser placed in front of the detector in a conventional OTDR arrangement [5]. Although this provided some very useful birefringence information, the interaction between fibre twist and the linear fibre birefringence could not be properly understood by this simple experimental technique, particularly as a theoretical description of the situation was still an unsolved and highly intractable problem.

In [6] the first analytic solution was presented for the DGD of uniform linearly birefringent fibres subject to an external elastic twist and Figure 1 shows the measured and calculated values of DGD against fibre twist. This shows that, for a given fibre, there exists a particular twist rate which nulls the DGD due to the linear birefringence in the fibre and that at higher twist rates the DGD is dominated by the twist-induced circular birefringence. These results also elucidate how the DGD, and therefore the PMD, value is lowered in spun fibres.

In [7,8] an analytical solution was presented for the back-scattered state of polarisation (SOP) from a uniformly linear-birefringent fibre subject to elastic twist which showed that the twist significantly influences the periodicity of the observed signal from the POTDR. Therefore values of PMD inferred from OTDR traces can be significantly in error if even small amounts of twist exists in the fibre. Measurements [7 – 9] confirmed these theoretical results.

4. Fully Polarimetric OTDR

The above, detailed, theoretical and experimental work pointed strongly to an important need for a fully polarimetric OTDR experimental technique. Such a fully polarimetric optical time domain reflector (POTDR) has been developed recently [10 - 11] at Essex and Figure 2 shows the POTDR set up in schematic form.

The POTDR has a spatial beat length resolution of 1 metre with a dynamic range of 30dB. It can therefore measure linear birefringences in fibres too low to be measured, in equivalent terms, by currently available PMD measurement instruments.

At present we foresee two significant applications for the POTDR. The first is in the area of fibre manufacture where the effect of fine tuning the fibre fabrication process in different ways, on the DGD of the resulting fibres, could be determined by examining sample lengths of fibre using the POTDR. The second application could be to examine the birefringence of different sections of an installed standard fibre link to identify sections with abnormally high PMD values. By selectivity replacing these sections only with say DS fibre the overall PMD performance of the whole link could be significantly improved. Work is already well in progress on the first of the above applications [12]. This, as well as the POTDR itself, will be described in more detail in the conference presentation.

5. Conclusion

A summary has been presented of work leading upto the development of a fully polarimetric OTDR and significant potential applications for the POTDR have been indicated.

Acknowledgements

This work was carried out under an EPSRC research grant, Reference GR/K49454. The industrial partners are BT Laboratories, Martlesham Heath and Alcatel Submarine Networks, Greenwich. At Essex the other workers involved are D.H.O. Bebbington, J.G. Ellison, R.E. Schuh, X. Shan and S.D. Walker. At BT Labs the collaborating workers are E.S.R. Sikora and N.G. Walker.

References

[1] M.J. O'Mahony et al., The design of a European optical network, *IEEE Journal of Lightwave Technology*, **13** (1995) 817-829.

[2] G. Hill, Optical networks : From myth to reality. In : G. Prati (ed.)., Photonic Networks. ISBN 3 540-76143-8. Springer-Verlag, Berlin, 1997.

[3] R. Tkach, Dispersion compensation in nonlinear systems, *Conference on Optical Fibre Communications*, OFC '96, San Jose, CA, (1996), Tutorial WO, 131-161.

[4] C.D. Poole et al., Phenomenological approach to polarisation dispersion in long single mode fibres, *Electronics Letters*, **22**, (1986) 1029-1030.

[5] A.J. Rogers, Polarisation optical time domain reflectometry, *Electronic Letter*, **16**, No.13, (1980), 489-490.

[6] R.E. Schuh et al., Theoretical analysis and measurement of the effects of fibre twist on the DGD of optical fibres, *Electronic Letters*, **31** (1995) 1772-73.

[7] R.E. Schuh et al., Theoretical analysis and measurement of the effect of fibre twist on the polarisation OTDR of optical fibres, *Conference on Optical Fibre Communications*, OFC '96, San Jose, California, (1996) paper FA5.

[8] R.E. Schuh et al., Polarisation OTDR measurements and theoretical analysis on fibres with twist and their implications for estimation of PMD, *Electronic Letters*, **32** (1996) 387-388.

[9] R.E. Schuh and A.S. Siddiqui, Measurement of SOP evolution along a linear birefringence fibre with twist using polarisation OTDR, NIST/IEEE/OSA *Symposium on Optical Fibre Measurements*, Boulder, CO, (1996) 159-162.

[10] D.H.O. Bebbington et al., Fully polarimetric optical time domain reflectometer with one metre spatial resolution, *Conference on Optical Fibre Communications*, OFC '97, Dallas, Texas, (1997) paper WL24.

[11] J.J. Ellison and A.S. Siddiqui, "A fully polarimetric optical time domain reflectometer", IEE Photonic Technol. Lett., **10**, No. 2 (Feb 1998), 246-248.

[12] J.J. Ellison and A.S. Siddiqui, "Estimation of linear birefringence suppression in spun fibre using polarimetric OTDR", to be presented at CLEO '98, San Francisco, May 1998.

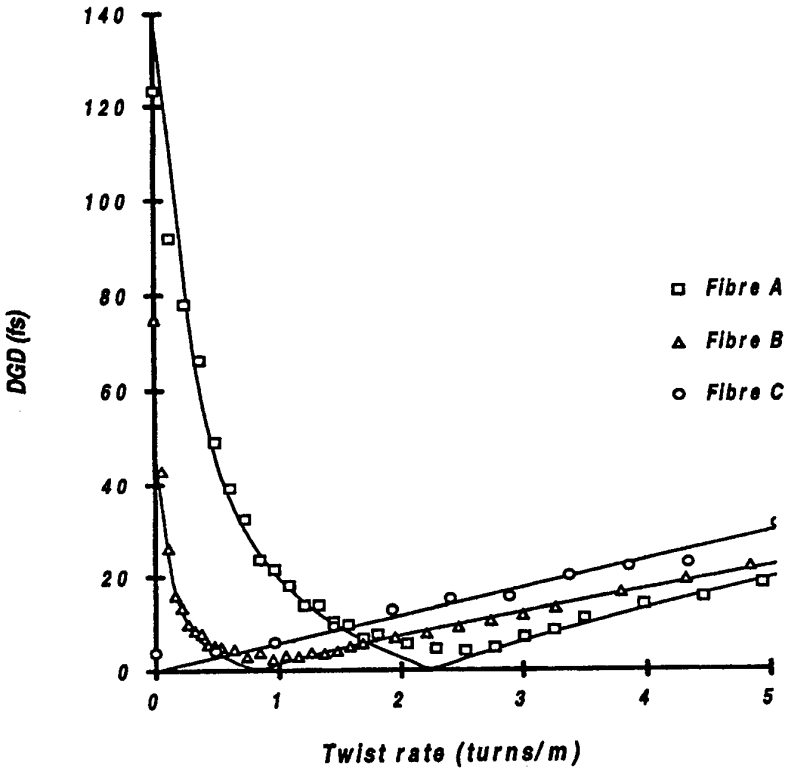

Figure 1. Measured and calculated values of DGD against twist

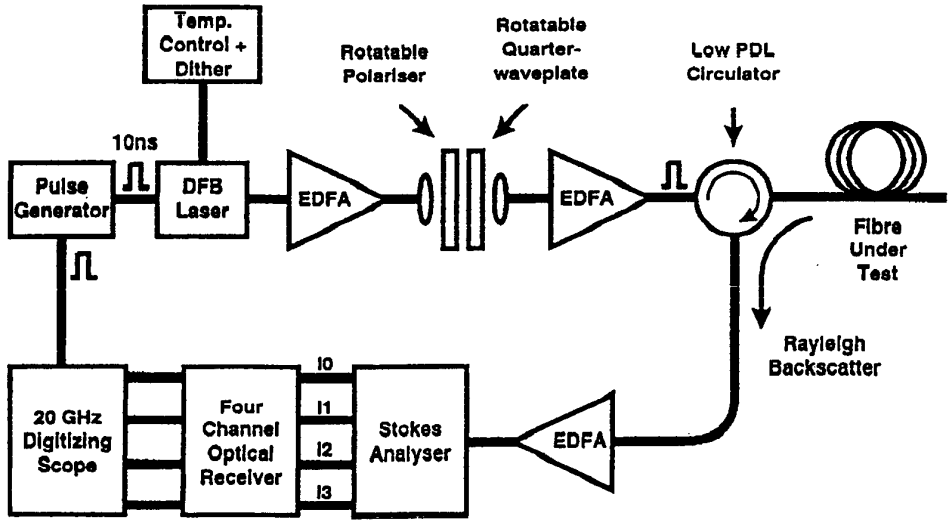

Figure 2. Schematic layout of polarimetric OTDR

Experimental design rules for implementing biconically tapered singlemode optical fibre displacement sensors.

F. J. Arregui, I. R. Matías, C. Bariain and M. López-Amo
Dpto. de Ingeniería Eléctrica y Electrónica. Universidad Pública de Navarra.
Campus de Arrosadía s/n.
31006 Pamplona. Spain
Phone : +34 48 169260, Fax : +34 48 169720, email : parregui@upna.es

Introduction.

Tapered optical fibres are used to design couplers, wavelength division multiplexers [1], near field scanning optical microscopy [2], just to mention a few. Moreover, and due to its strong transmission dependence to external medium the tapered fibre may also be used to sense distinct parameters such as temperature, humidity, PH, etc. In this work bending effects in tapers [3]-[5] are exploited to achieve displacement sensors and to present design rules for implementing these sensors according to the desired both range and sensitivity.

Experimental set-up.

Experiments were performed with 1.3 μm singlemode standard optical fibre pigtails of approximately 2m. long. This optical fibre has core and cladding diameters of 9.4 μm and 125 μm, respectively. For each sample, 2m. of fibre were cleaved with a RXS Siemens AG precision fibre cleaver and the ends were adapted to connectors. Approximately 10 cm. of the fibre cover at the centre were stripped out with an organic solvent. Samples were prepared by stretching the uncovered region using an Ericsson FSU-905 electric splicing unit. In the fig. 1 it can be observed a photograph of one of these tapers. In this case, the insertion losses were about 3 dB. The fibre then was fixed at two symmetrical points respect the tapered zone on a Creative Stars micrometer of 10 μm of resolution. To fix the fibre at these points an adhesive cyanocrilate was used. It was possible to linearly vary the distance between two fixed points of the fibre with the above micrometer device getting the fibre to be bent it. The experimental set-up is shown in fig.2.

A Rifocs 665R laser source (λ = 1310 nm.) or a Rifocs 666R laser source (λ = 1550 nm.), according to the specific experiment, was attached to one fibre connector. The optical power output at the other fibre end was measured with a Rifocs 671 RS optical power meter .

Some experimental results.

In fig. 3 and 4, the output optical power transmission at a wavelength of 1310 nm versus the displacement is presented. In the first one, two samples were made with taper waist diameter of 66 and 56 μm., in distinction to fig. 4 where the tapers had a waist of 38 and 22 μm. Other samples of similar diameters were developed obtaining similar results.

In the fig. 3 it can be seen that the more stretched the fibre the faster decrease the optical power, so the slope of the output optical power versus displacement become more abrupt. With the taper waist of 56 μm a quasi-linear sensor is obtained with a wide measurement range but with low resolution. Actually, the measured range is of 5 mm (0 to -10.55 dBm) in a displacement with a resolution in the worst case of 2.4 e-3 dBm/μm for λ = 1310 nm.

When the waist diameter is smaller, fig. 4, then the output optical power curves become oscillatory. Although apparently a taper with these characteristics could be rejected, it exists an optimal about 22 μm of waist diameter in which it can be obtained a short range, but a high resolution.

In order to improve the sensitivity of the tapers two different wavelengths were probed, although the curve form changes, fig. 5, in the non oscillatory zone we could find that the slope is more abrupt and we obtained more sensitivity to displacement.

A zoom of the zone from 60 to 110 μm. of displacement of this 22 μm sampler is shown in the fig. 6. In this it has been obtained a short range of 50 μm. but with a resolution of 0.247 dBm/μm.

All of these experiments were made by increasing and decreasing the displacement in both directions and no hysteresis was detected. This is because we worked in the elastic zone of the silica material, not in the fluency zone. To give an idea about the fracture points of the tapers in function of the diameter of the waist we have also probed to measure the displacement in these breakpoints (fig. 7). It has been found there is a minimum point that the break is easier, around the 30 μm. of waist. Moreover these tapers of this diameter are the

most sensitive but the non-oscillatory zone is over when the achieved displacement is 130 μm. (fig. 4). The breakpoint is found in 1400 μm. of displacement what implies a big margin. Notice that at least, in this case, measurements until 1000 μm. were made it and no hysteresis was found.

In order to find more sensitivity to displacement it was probed to change the distance between the two fixed points to the micrometer, fig. 8. The graphs are similar but in the 0-200 μm. of displacement zone more abruptness is achieved because the shorter distance between the fixed points the later begins to fall the optical power. Anyway expressing the displacement in microstrains (με) results are similar in the three curves.

Conclusions.

In this work it has been shown the basic rules to make an intensity optical fibre sensor based in biconically tapered single mode optical fibres. To obtain more resolution is better to get a waist around 22 μm. and to use a 1550 nm. wavelength. To obtain a wide range is better to get a waist of around 56 μm.

Acknowledgments.

This work was supported by CICyT Grant TIC-95-0631-C04-02. The authors want to thank to G. Zabalza, I. Goenaga, P. Datta and J.M. Otón for their useful work and discussions.

References.

[1] R. J. Black, S. Lacroix, F. Gonthier, J.D. Love. "Tapered single-mode fibres and devices. Part2 : Experimental and theoretical quantification". IEE Proc.-J. Vol. 138, N°5 , October 1991.
[2] E. Betzig ,J. K. Trautman, "Near field scanning optical microscopy," Sc., vol. 257, p. 189, Mar. 1992.
[3] P.Datta, I. Matías, C.Aramburu, A.Bakas, M. López-Amo, J. M. Oton. "Tapered Optical-Fiber temperature sensor". Microwave and Opt. Tech. Lett. Vol. 11, N°2, Feb. 5, 1996.
[4] Lloyd C. Bobb, P. M. Shankar and Howard D. Krumboltz."Bending Effects in Biconically Tapered Single-mode Fibers". J. of Light. Tech., vol. 8, N° 7, July 1990.
[5] P. M. Shankar, Lloyd C. Bobb, and Howard D. Krumboltz,"Coupling of Modes in Bent Biconically Tapered Single- Mode Fibers". J. of Light. Tech., vol. 9, N° 7, July 1991.

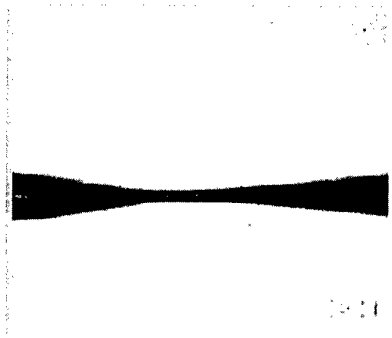

Fig. 1: A photograph of a biconically tapered fibre.

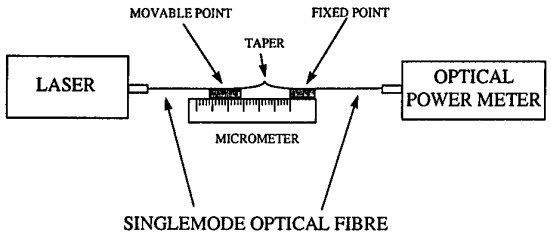

Fig. 2: Experimental set-up.

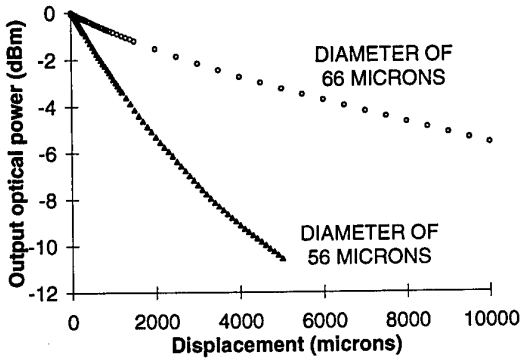

Fig. 3: Experimental measures of the output optical power in tapers of big waists (56 and 66 μm.). Note that the vertical axis initial point has been chosen when displacement is 0. Wavelength λ=1310 nm.

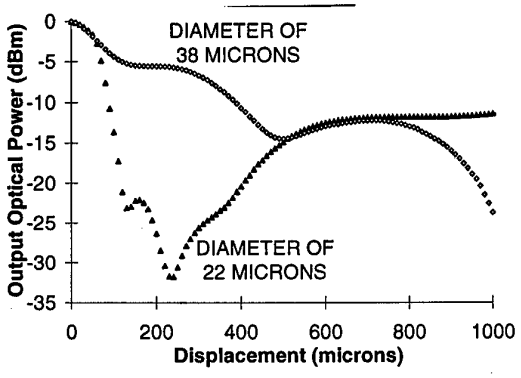

Fig. 4: Experimental measures of the output optical with tapers of smaller waist diameter, 22 and 38 μm., (λ=1310 nm.).

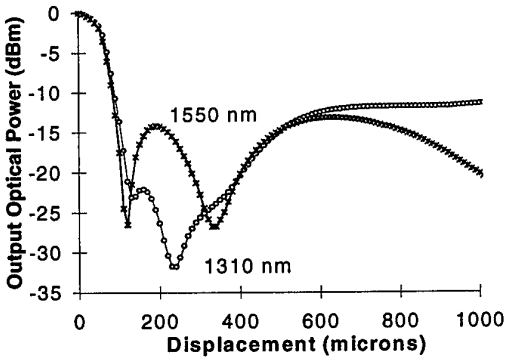

Fig. 5: Output optical power versus displacement in a taper of 22 μm waist diameter.

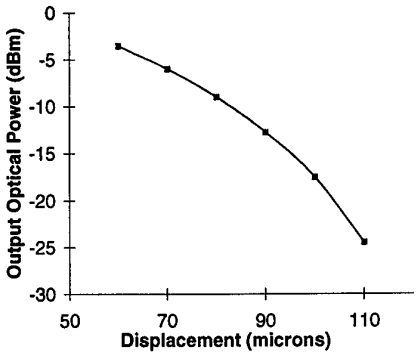

Fig. 6: Zoom of the abrupt zone of the fig.4 (λ=1550 nm.)

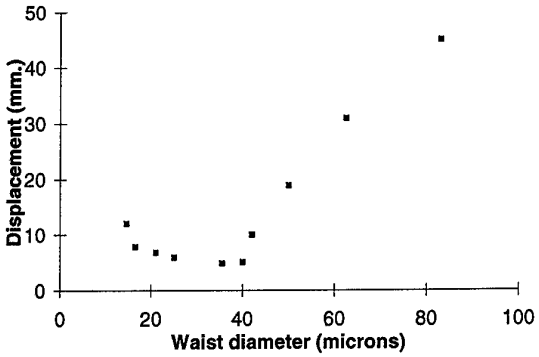

Fig. 7: Fracture points.

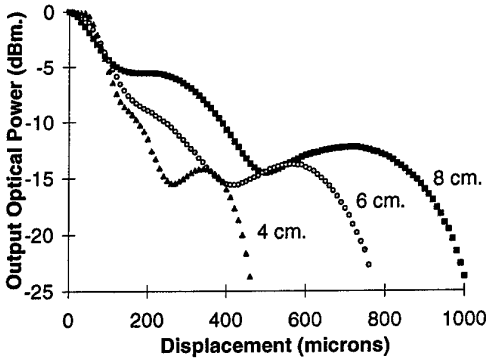

Fig. 8: Output Optical power curves (λ=1310 nm.) vs. different distances between the fixed points at the micrometer

High resolution fringe-counting sensor utilizing the Vernier effect

by
Jan Anders Thorsveen and Kjell Bløtekjær
Department of Physical Engineering
Norwegian University of Science and Technology
N-7034 Trondheim
NORWAY

SUMMARY:

A fringe-counting sensor utilizing the Vernier effect has recently been proposed. The paper presents an experimental verification of the principle. The resolution is $\lambda/5$. This is a proof-of-principle experiment, and the resolution can be improved by careful design.

Introduction

Fringe-counting sensors can usually resolve optical pathlength changes of one or one half wavelength, depending on the interferometer used. Recently, a fiber-optic fringe-counting sensor has been proposed, which may resolve a small fraction of a wavelength [1]. The sensor utilizes the Vernier principle, and is explained here with reference to the setup in Figure 1. Several alternative configurations are possible.

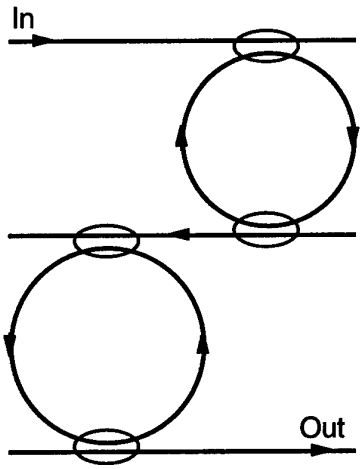

Figure 1: Basic principle of a Vernier sensor realized by two cascaded ring resonators.

The lengths of the two rings are different, their ratio being $n/(n\text{-}1)$, where n is an integer. The upper two figures in Fig. 2 show schematically a section of the frequency response of the two resonators with $n = 6$. The total frequency response of the two rings in Fig. 1 is the product of the individual responses of the two rings. The transmission through both resonators will be high only at the frequencies ω_0 and $\omega_0+\Omega_0$. If one of the resonator lengths is changed, the high transmission peaks disappear. When the length is changed enough to displace the upper response to the lower in Figure 2, the joint response will be the same as initially, only displaced by one free spectral range of the unchanged resonator. The resulting response for the two resonators in tandem is shown in Fig. 3a for the situation when the two resonators share common resonances, as in Fig. 2. Figure 3b shows the response when the response of one sensor is displaced halfway between the upper and lower of Fig. 2. Note that the highest peaks in Figure 3b are two orders of magnitude below those of Figure 3a.

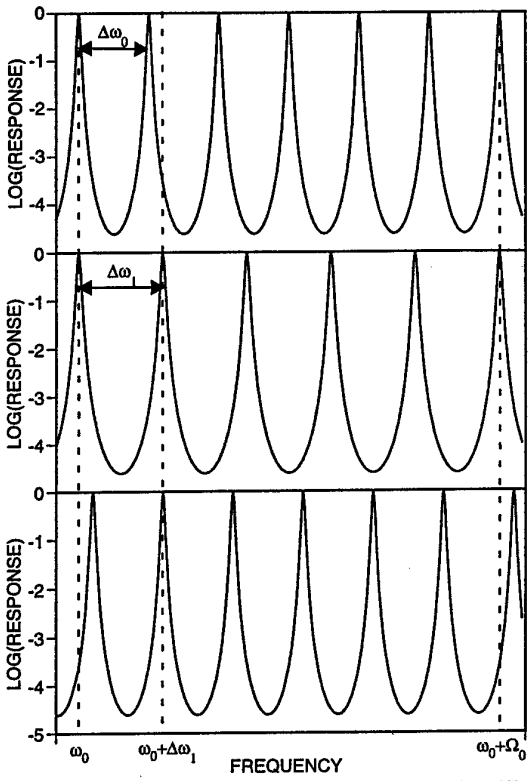

Figure 2: Response of two Fabry-Perot resonators of different lengths. The top and bottom figures represent the same resonator, with a slight change in length.

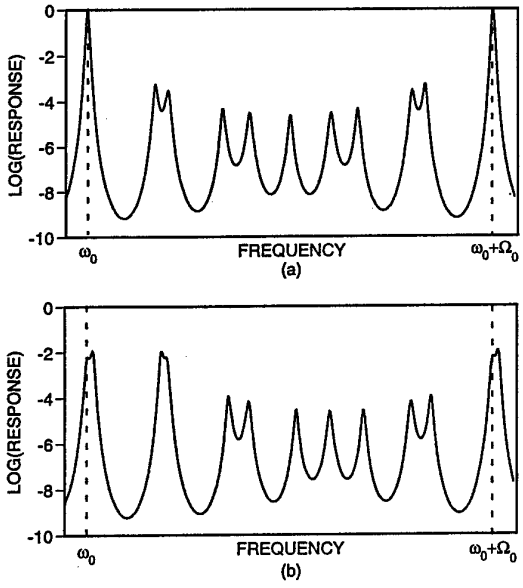

Figure 3: Combined response of two cascaded Fabry-Perot resonators of different length. (a): Overlapping resonances. (b): Non-overlapping resonances.

The present sensor scheme uses a broad-band source with a spectrum that is wide enough to cover one or more periods of the joint response. The output power from the sensor is then determined by the transmission through the two resonators, averaged over the frequency range of the source. This average will vary periodically with the perturbation of the sensing resonator length, with a period which may be a small fraction of a wavelength, depending on the relative difference between the two resonator lengths.

Experiment

The experimental setup is essentially as shown in Fig. 1. The rings are made of single mode fibers. Ring number 1 was measured to be 2.72 cm long. The corresponding free spectral range is 0.433 pm. The length of ring number 2 was adjusted to make the ratio of the free spectral ranges of the two resonators near 6/5, i. e. $n = 6$ in the above notation. The coupling coefficients of the four couplers are nominally 10 %. Polarization controllers are inserted in both rings and in the fiber connecting the two rings.

Figure 4a shows the spectral response of ring number 1, and Figs. 4b and 4c show the response of the two rings in tandem. The free spectral range in Fig. 4b is seen to be approximately 5 times that in Fig. 4a. The fact that the response in Fig. 4b is not perfectly periodic shows that the ratio of the lengths of the two rings is not exactly 6/5. By applying a slight perturbation to one of the rings the response in Fig. 4c is obtained. Figures 4b and 4c correspond to the theoretical curves in Fig. 3a and 3b, respectively.

The setup was tested as a temperature sensor. A broad-band source was synthesized by scanning the wavelength of a single mode 10 mW 1312 nm DFB laser and averaging the output over several scan periods. The wavelength was scanned with a triangular waveform modulation of frequency 9 kHz, with a scan range of approximately 35 pm. The output from the detector was filtered by a 1 kHz low-pass filter.A length of 9 cm of ring number 2 was enclosed in a tube, and heated with an airblower. The output was monitored during cooling, together with the temperature, as measured by a thermistor. Figure 5 shows a typical plot of temperature (upper curve) and output signal (lower curve) vs time during cooling.

There are 18 periods over a temperature range of 2 K. Thus, the resolution is 0.11 K. Using the temperature sensitivity of quartz fibers, a resolution of 0.23 K is calculated. This is a factor of 2 off the experimental result. One reason for the discrepancy is that the temperature measurement is rather inaccurate. The thermistor was placed in contact with the fiber, but the temperature may be highly nonuniform over the 9 cm sensor length. Another explanation for the discrepancy is that the effect of the fiber coating is neglected in the calculation.

The peaks and valleys of the sensor output have different amplitudes. This is due to the fact that the synthesized broad-band source does not have a flat spectrum. The wavelength modulation of the laser did not follow exactly the triangular waveform of the modulation current. There was a rounding of the peaks, which essentially results in an increased spectral density at the extremes of the wavelength range.

Note that the sensor output pattern repeats itself after 5 periods. The response of resonator number 2 has then moved by one free spectral range, and the combined response is back to the original.

The peak-to-peak amplitude of the sensor output is approximately one tenth the dc output. Calculations show that this corresponds to a resonator finesse of 11.5, which is far below the value of 30 expected for coupling coefficients of 0.1, if the system were lossless. Coupler loss, splice loss, and polarization mismatch are responsible for the reduced finesse, and departure from the exact 6:5 length ratio also contributes to the reduction of the amplitude.

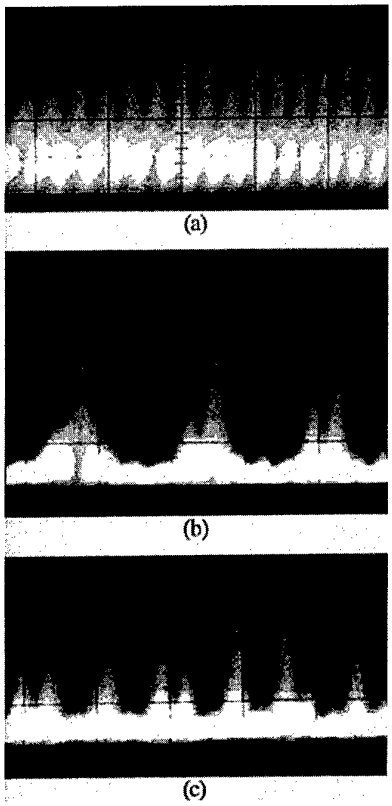

Figure 4: Responses obtained by scanning the laser wavelength. (a): Response of ring number 1. (b):Response of the two rings in tandem, when resonanses of the two rings overlap. (c): Response of the two rings in tandem, when resonanses of the two rings do not overlap.

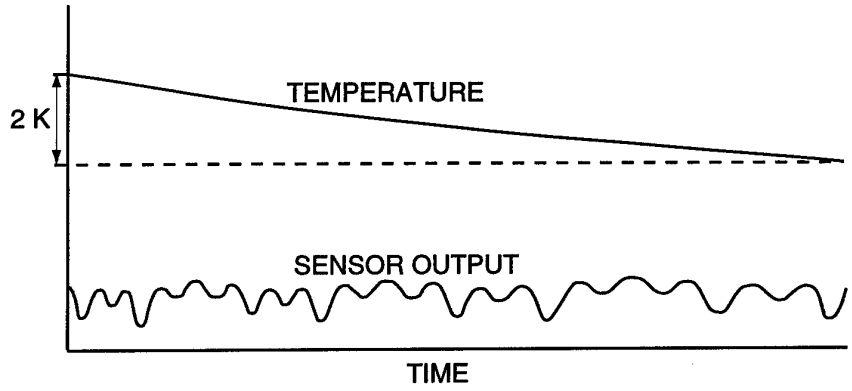

Figure 5: Temperature and sensor output vs time during cooling of 9 cm of ring number 2.

Conclusions

The experiment reported here is a proof-of-principle experiment. A resolution of $\lambda/5$ is obtained. The resolution can be improved by choosing a higher value for n. This will reduce the visibility of the fringes, but this can be tolerated, since fringe counting is possible with much lower fringe visibility than that in Fig. 5. The experiment also shows that a fringe-counting Vernier sensor can be realized even if the broad-band source spectrum is far from flat.

ACKNOWLEDGEMENT

The DFB laser was kindly provided by Kongsberg Defence & Aerospace AS.

REFERENCE

1 K. Bløtekjær, "Theoretical concepts of a novel Vernier-based fringe-counting fibre optic sensor", IEE Proc.-Optoelectron., Vol. 144, pp. 126-129, June, 1997.

Channelled spectrum interrogation of an all-fibre broadband interferometric differential strain sensor

J G Burnett, G R G Erry, R Dickson, R McBride*, M Gander*, J D C Jones*, P M Blanchard, A H Greenaway, A R Harvey

DERA Malvern, St Andrews Road, Great Malvern, Worcs. WR14 3PS, UK
*Physics Department, Heriot-Watt University, Edinburgh EH14 4AS, UK

Introduction

Optical fibre interferometric strain sensors embedded into structures offer a very accurate and robust method for shape measurement [1]. Many schemes have been demonstrated in which strain and/or temperature in a structure are inferred from monochromatic optical phase delay [2]. These techniques have two limitations: phase ambiguity and temperature-strain cross-talk so that for absolute and accurate strain measurement, continuous measurement of optical phase is required and the environment needs to be temperature-controlled or temperature-calibrated by other means.

Phase measurement between two different optical modes (polarisation or spatial) or at two wavelengths permits some discrimination between temperature and strain effects and can extend the range of unambiguous strain measurement. However, the transformations used are typically ill conditioned so that small errors in phase measurement are amplified into large errors in inferred strain and temperature. We have previously described the use of Fizeau fibre sensors with a broadband source where a dispersive Fourier transform spectrometer (DFTS) was used to measure optical phase delay at a large number of wavelengths [3]. This yields absolute measurement of phase and a greatly reduced sensitivity to errors in phase measurement.

The DFTS used in this case employed a mechanically-scanned and optically calibrated air gap to form a temporal interferogram. This technique works well on a vibration-isolated optical table, but for application in harsh environments a more robust method of sensor interrogation is required. We describe here an approach that enables the broadband DFTS technique described above to be transferred from the laboratory to a harsh application environment.

Static Fourier-transform spectrometry is inherently very robust [4] and could readily be used in place of the scanning mirror technique, however we have opted to exploit the convenience of a commercially available miniature spectrometer that fits onto an expansion card within a personal computer. The lack of moving parts for this technique not only offers increased robustness and reliability, but also improved repeatability. The DFTS technique produces two interferograms from a tandem interferometer that are displaced from the zero path difference interferogram. In the spectral domain these correspond to a channelled spectrum, so that when the interferograms are close together, the spectral period of the channelled spectrum is large and as increasing strain and/or temperature difference causes the interferograms to increase in separation, the spectral period reduces. Distortion of the

interferograms (rather than simple translation) in the DFTS technique enables temperature and strain to be inferred with low cross-talk. This dispersion also causes an analogous chirp in the channelled spectrum modulation that can also be used to separately infer temperature and strain.

Sensor description and theory

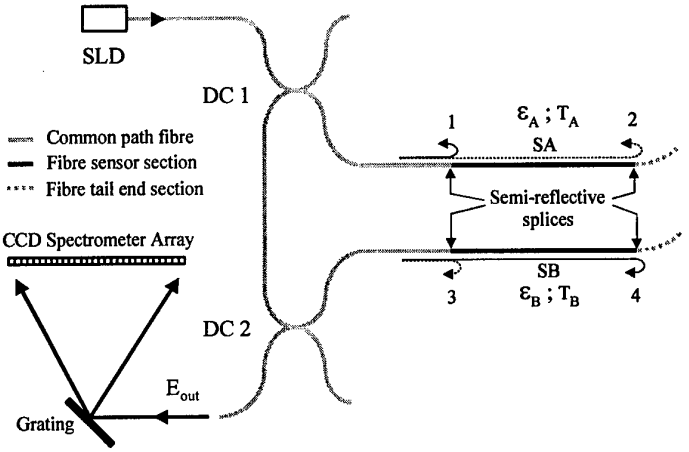

Figure 1. Schematic diagram of a differential fibre strain sensor based on a tandem interferometer configuration. SLD is a super-luminescent diode. See text for explanation of other terms.

The fibre sensor system described in this paper is illustrated in figure 1. In this configuration, known as a tandem interferometer [5], the integrated differential strain ($\Delta\varepsilon=\varepsilon_A-\varepsilon_B$) and integrated differential temperature ($\Delta T=T_A-T_B$) can be determined between the fibre sensor sections SA and SB as shown (in black) where each section is defined between semi-reflective splices.

The output field E_{out}, interrogated by a spectrometer, represents the supposition of four fields defined by the four possible optical paths through the system. The optical paths are defined by reflections off the semi-reflective splices: 1&3, 2&3, 1&4 and 2&4. The mutual phase difference between these fields and the spectrometer resolution will determine whether they interfere coherently. We require that the fields associated with the reflections 1&3 and 2&4 do not interfere coherently with any of the other fields and that the fields described by the reflections 2&3 and 1&4 do interfere with each other.

The conditions above are satisfied provided the effective coherence length is less than twice the sensor length, but greater than the largest difference in optical path length between the fibre sensor sections. Provided there is sufficient difference in optical path length between SA and SB however, a nominally cosinusoidal channelled spectrum of discrete intensities $I(\lambda_i)$ is detected by the spectrometer CCD array:

$$I(\Delta\varepsilon,\Delta T,\lambda_i)=I_o(\lambda_i)\left[C_1+C_2\cos\Phi(\Delta\varepsilon,\Delta T,\lambda_i)\right]$$

where C_1 and C_2 are constants determined by the reflection and transmission coefficients in the system. $\Phi = \phi_A - \phi_B$ is the phase difference between the optical paths 2&3 and 1&4. Due to the common path fibre lengths in the system only phase changes, ϕ_A and ϕ_B, due to strain and/or temperature differences, in the sensor sections SA and SB respectively result in an overall phase difference Φ. For the system as illustrated, the maximum fringe visibility obtainable would be approximately 50% given optimum values of C_1 and C_2.

The phase $\Phi(\lambda_i)$, for a given strain/temperature difference, associated with this intensity distribution as a function of wavelength is determined from its complex analytic signal representation. The real part of this analytic signal representation is just the intensity distribution itself. The imaginary part is determined via a Hilbert transform of the real part such that the real and imaginary components form a Hilbert pair. In practice a band-pass filter is also applied in Fourier space to take out low- and high-frequency artefacts in the spectral signal.

Once the analytic signal is known, the phase is extracted from its argument. Since phase is modulo 2π a phase unwrapping algorithm is implemented to extract the full phase curve as a function of wavelength. A quadratic least squares fit is applied to this phase function and the first and second-order coefficients extracted. Each coefficient may be calibrated against plate deflection and temperature difference. The functional dependence of both coefficients against these measurands is sufficiently different to allow discrimination between plate deflection and temperature difference [3].

In the implementation described here, the sensor sections SA and SB are prestrained and embedded in polyurethane sheets bonded to an aluminium cantilevered plate as shown in figure 2. The sensors are bonded into metal anchors at either end of the sheets. The fibre sections, once embedded, were cleaved at both ends such that the physical lengths SA and SB were nominally identical. Pre-coated semi-reflective ends on fibre down- leads were then spliced to the ends of the sensor section using UV-cure glue. The end of the cantilever plate can be deflected using a micrometer, which enables the fibres to be strained in a controlled manner. In the experimental implementation so far there is no control of temperature differentials although second-order phase coefficients may be calibrated as discussed above to allow temperature discrimination.

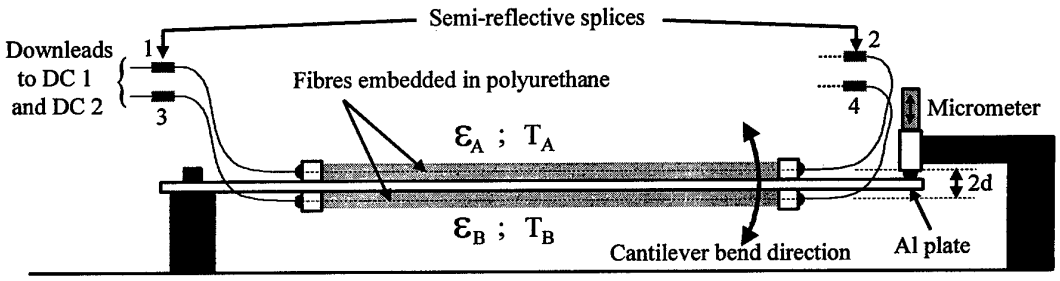

Figure 2. Schematic diagram showing a side/cross-sectional view of the cantilever plate with fibre sensor sections embedded in polyurethane on either side of the plate.

The current super-luminescent diode used (SUPERLUM, SLD-381) emits at a centre wavelength of 850nm and has a nominally Gaussian spectral profile with a FWHM of 20nm. The in-fibre CW power of this device is about 2mW.

A miniature a fibre-connectorised spectrometer on a PC card was used to record the channelled spectrum. This employs a 1024 element linear CCD array giving a spectral resolution of 0.25nm per pixel. The spectrometer output was interfaced to our own signal processing software. The measurement rate of the system is limited to the minimum 8 ms integration time of the spectrometer which, for some applications, would not be fast enough to temporally resolve the channelled spectrum due to fringe 'wash-out'. The dynamic range of the system is improved significantly however by pulsing the SLD with a pulse width narrower than the spectrometer integration period. The current system allows a single pulse, down to 50μs, within the spectrometer integration period.

A series of measurements were made over a 6 mm range of end-of-plate deflection in an isothermal environment, although with a much weaker SLD (12μW). A 128-pixel region on the CCD array centred on the SLD spectrum was used for processing. The results shown in figure 3 show a good linear relationship between the measured first-order phase coefficient and end-of-plate deflection.

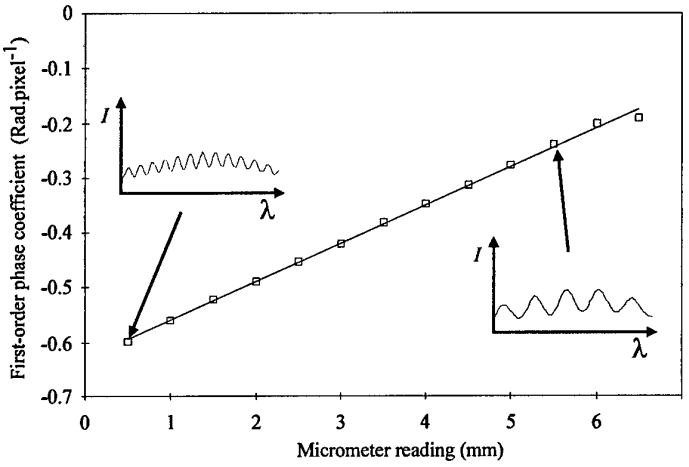

Figure 3. Measured first order phase coefficient against end-of-plate deflection. The two inserts illustrate the raw channelled spectrum output used to determine their respective points on the graph at opposite ends of the measurement range.

Conclusions

Measurement of the deflection of a simple cantilever, into which fibres bonded into a polyurethane layer have been mounted, demonstrates the ability to measure curvature through differential strain measurement using low-coherence techniques. The technique is suitable for use in harsh environments and has applications to other structural monitoring requirements. We are currently testing the system with the higher power SLD-381 which offers the advantage of pulsed mode operation and greater signal to noise to enable calibration of second-order phase with strain and temperature.

References

[1] Measures R M, LeBlanc M, Liu K, Ferguson S, Valis T, Hogg D, Turner R, McEwan K, *Optics and Lasers in Engineering*, **16**, pp 127-152 (1992)

[2] Jackson D A, Jones, J D C, Opt. Acta **33**, pp1469, (1986)

[3] Flavin D A, McBride R, Jones J D C, Burnett J G, Greenaway A H, *Combined temperature and strain measurement with a dispersive optical fiber Fourier-transform spectrometer,* Opt. Lett., **19**, 24, pp 2167-2169, (1994)

[4] Padgett M J, Harvey A R, *A static Fourier-transform spectrometer based on Wollaston prisms*, Rev Sci. Instr. **66**, 4, pp 2807-2811, (1995)

[5] Luke D G, McBride R, Lloyd P, Burnett J G, Greenaway A H, Jones J D C, *Strain and temperature measurement in composite-embedded highly birefringent optical fibre using mean and differential group delay*, Proc. Opt. Fib. Sens.-11, Sapporo, Japan, pp 200-203, 21-24 May (1996)

Large OPD Extrinsic Fabry Perot Interferometers using Thermally Expanded Core Fiber

M. Lequime and J.J. Guérin

BERTIN & Cie – Fiber Optic Systems Division
BP 22000 •13791 AIX-en-PROVENCE Cedex 3 • France
Phone : (+33) 4.42.60.46.00 • Fax : (+33) 4.42.60.00.13

1. Introduction

Extrinsic Fabry Perot Interferometers (EFPI) Sensors have been extensively used for the monitoring of strain and temperature into smart materials and structures[1]. For these applications, the Fabry-Perot cavity used is usually formed by an air gap of few tens of microns located between the extremity of an input single-mode fiber and the reflective extremity of another fiber, either single-mode or multimode. Such gap values provide in fact a good compromise between strain sensitivity, temperature sensitivity and optical performances of the sensor.

For some other applications, like position or linear displacement sensors, the constraints of implementation are not exactly the same and can incite to use larger working distances (for instance one millimeter or more) between the extremity of the single mode fiber and the surface of the reflecting part (fiber, mirror or metallic surface). In such a case, the light power reflected by the surface and back coupled into the core of the input single mode fiber can be very low (typically, less than 0.3% at a wavelength of 1300 nanometers), which makes poorer the intrinsic performances of the distance sensor.

The use of collimating optics is a possible way to increase the working range of such interferometric sensors, but the tolerances applicable to the angular position of the reflecting surface become very stringent and unachievable in most of the cases. An efficient solution can be provided by the replacement of the Fabry-Perot arrangement by a Michelson device, which uses a reference arm and cube corner reflectors instead of plane mirror surfaces[2], but this method leads to larger probe size and more expensive sensor systems.

It is the reason why we have imagined to use single-mode Thermally Expanded Core (TEC) fibers[3] to increase the usefull range of EFPI position sensors to one millimeter or more, without any penalty onto the performances, the size and the cost of the distance probe.

2. Fundamental properties of single-mode TEC Fibers

TEC fibers are fabricated by heating single-mode fibers locally at a temperature comprised between 1300°C and 1600°C with a micro burner (propane/oxygen flame). The duration of this heat treatment varies from 2 minutes up to 60 minutes. This temperature increase induces a radial diffusion of the dopants of the fiber core from the center to the periphery, and, as a consequence, an enlargement of the Mode Field Diameter. The heating region being finite, the longitudinal profile of the fiber core becomes tapered, as shown at the Figure 1.

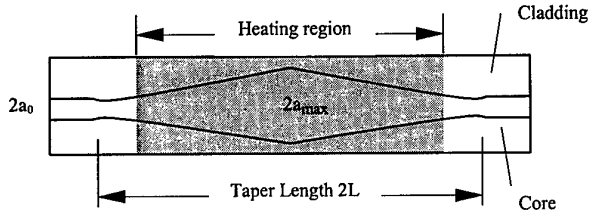

Figure 1 – Schematic illustration of a TEC fiber

This fiber is finally cut in two parts, symmetrically with respect to the center of the heating region, in order to obtain a component whose the untreated extremity can be easily spliced to a standard single-mode fiber, while the enlarged mode field extremity can be used as a part of a low loss connector.

By using the phase-front transformer model[4], it is possible to compute the intrinsic transmission T_0 of the TEC fiber shown at the Figure 1. We found :

$$T_0 = \left[1 + \left\{\gamma_{max}(\gamma_{max} - 1)\frac{\pi n_0 w_0^2}{\lambda L/2}\right\}^2\right]^{-1} \quad (1)$$

where n_0 is the refractive index of the cladding of the fiber, w_0 the fundamental Mode Field Radius (MFR), λ the wavelength, L half the taper length and γ_{max} the maximum core expansion ratio (which is in practical identical to the maximum MFR expansion ratio w_{max}/w_0).

For maximum MFR expansion ratio comprised between 2 and 3, the intrinsic loss of such TEC fibers remains below 0.1 dB for Taper Length greater than 12 mm, which allows the manufacturing of EFPI position sensor of small size (L < 6 mm).

3. EFPI Sensors using TEC Fibers : Theoretical analysis

A schematic description of a distance sensor using TEC/EFPI probe is shown at the Figure 2.

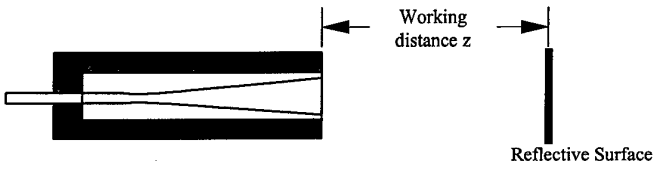

Figure 2 – TEC Fiber EFPI Probe

This probes includes only a TEC fiber and a metallic sleeve to allow its stable and firm fixation in front of the reflective surface.

The optical behavior of the EFPI probe can be described in first approximation by restricting to two the number of reflected waves, i.e. :

- the wave reflected by the silica/air interface at the output of the TEC fiber (reflection coefficient ρ equal to 3,4%)
- the wave reflected by the metallic surface and back-coupled into the same TEC fiber (effective reflection coefficient ηR, where η is the coupling efficiency and R the reflection coefficient of the surface).

In this approximation, the optical transfer function of the probe can be expressed as follows

$$P_R(z,\lambda) = T_0^2 P_0 \left\{\rho + (1-\rho)^2 R\eta(z) - 2(1-\rho)\sqrt{\rho R\eta(z)}\cos\frac{4\pi z}{\lambda}\right\} \quad (2)$$

where P_0 is the incoming light power, P_R the reflected light power, T_0 the intrinsic transmission of the TEC fiber, z the distance between the extremity of the TEC fiber and the reflective surface and $\eta(z)$ the back coupling efficiency defined by[5] :

$$\eta(z) = \left[1 + \left[\frac{\lambda z}{\pi \gamma_{max}^2 w_0^2}\right]^2\right]^{-1} \quad (3)$$

By introducing the normalized working distance $\tilde{z} = z / \gamma_{max}^2$, the optical transfer function of a TEC/EFPI probe can be rewritten as follows :

$$P_R(\tilde{z}, \lambda) = P_0 \Re(\tilde{z}) \left\{ 1 + m(\tilde{z}) \cos \frac{4\pi \gamma_{max}^2 \tilde{z}}{\lambda} \right\} \quad (4)$$

where $\Re$ is the mean coefficient of reflection of the probe and m the index of modulation of the interferometric signal.

The variations of these two last quantities versus the normalized distance $\tilde{z}$ are plotted on the Figure 3 and show that TEC fibers with expansion ratio of 3 allows to manufacture high quality displacement sensors with working distance up to 5 mm.

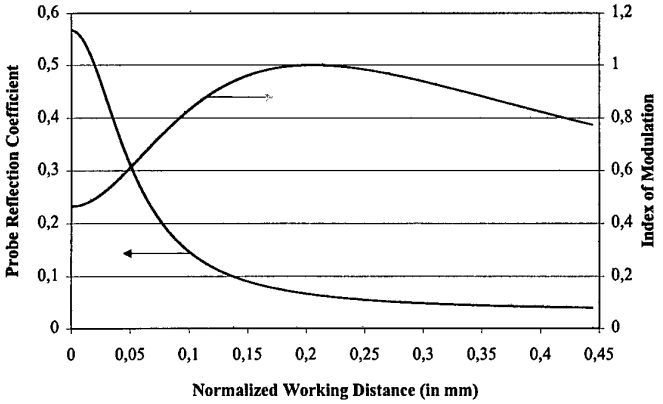

Figure 3 – Main Optical Characteristics of a TEC/EFPI Probe

4. Experimental results

We have purchased TEC fibers manufactured by KYOCERA FineCeramics S.A., single-moded at 1.3 µm and characterized by a Mode Field Diameter around 20 µm (standard products are commercially available at 1.55 µm with expansion ratio between 2 and 3).

The experimental set-up used to perform the optical characterization of the TEC/EFPI probes is described at the Figure 4. It allows to determine the absolute values and the variations of both quantities defined in the previous theoretical section (mean coefficient of reflection, index of modulation).

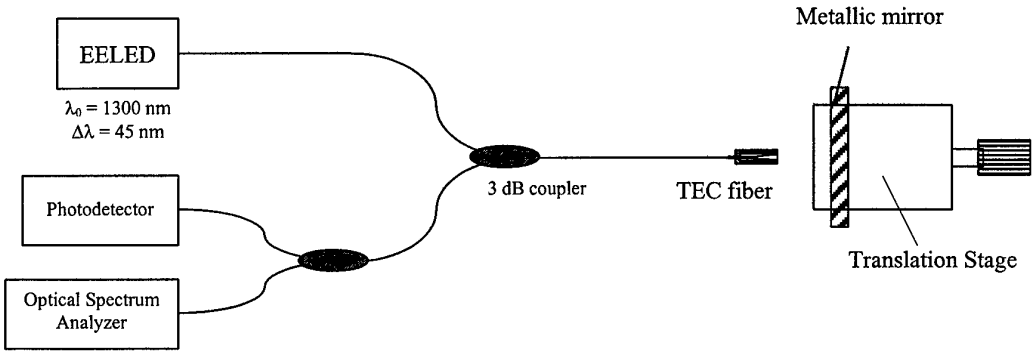

Figure 4 – Experimental set-up

The reflecting surface used here is a flat Invar surface (reflection coefficient around 65% at 1.3 μm) and its position is checked continuously with a .1 μm accuracy electronic displacement sensor .

The Figure 5 shows the variations of the quantity H(z) defined by

$$H(z) = \sqrt{(P(0) - P(z))/(P(z) - P(\infty))} \tag{5}$$

where P(z) is the amount of light power received on the detector when the distance between the extremity of the TEC fiber and the metallic mirror is equal to z.

By combining relations (2) and (3), it is easy to demonstrate that, for working distances greater that the coherence length of the source, H(z) shall be linear with respect to z, the slope being equal to $\lambda / \pi \gamma_{max}^2 w_0^2$.

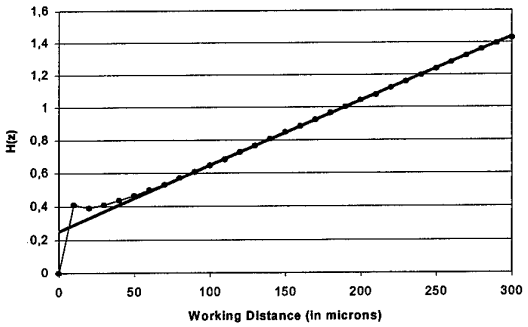

Figure 5 – Experimental results : Variations of the H parameter with the working distance z

The quality of the linear relationship experimentally obtained between H and z for distances greater than the coherence length of the EELED, i.e. 40 μm (black dots : experimental data – black line : linear fitting) confirms that the mode profile at the output of the TEC fiber is always single-moded and allows us to determine the value of the expansion ratio, i.e. 2.2 assuming a 4.65 μm initial MFR.

Figures 6a to 6c show the shape of the spectral profile of the light power reflected by this displacement sensor for three specific working distances, i.e. 70 μm, 315 μm and 800 μm. The index of modulation reached for so large OPD values (for instance 1,6 mm for the Figure 6c) makes the proof that TEC/EFPI probes with expansion ratio between 2 and 3 can be used as accurate displacement sensors even at working distance chosen in the 1-5 millimeters range, and be demodulated through coherence reading with a scanning receiver interferometer.

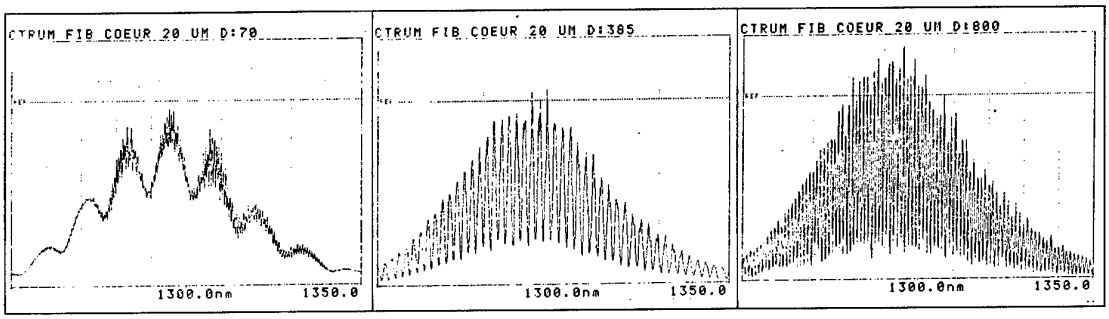

Figures 6 – Spectrum of the light power reflected by TEC/EFPI probe

5. Conclusion

Single-mode Thermally Expanded Core Fibers provide a efficient mean to extend the working range of EFPI displacement sensors in the 1-5 millimeters range. The only constraint applicable to the manufacturing of such components remain the excess loss level, while absolutely no requirements are needed on the repeatability of the MFD value of the expanded region (which is naturally not the case for the low loss connectors applications).

REFERENCES

[1] K.A. Murphy, V. Bathia, R.O. Claus, P. Duncan, M.E. Jones, J.L. Grace, J.A. Greene and T.A. Tran, *Multiplexed Fabry-Perot interferometers and applications*, **SPIE 2507**, Distributed and Multiplexed Fiber Optic Sensors V, pp. 2-13 (1995)

[2] M. Lequime, *Fiber Sensors for Industrial Applications*, Proceedings of the 12th International Conference on Optical Fiber Sensors, Williamsburg, pp. nnn-nnn (1997)

[3] M. Kihara, M. Matsumoto, T. Haidara and S. Tomita, *Characteristics of Thermally Expanded Core Fiber*, IEEE J. Lightwave Technol., **JLT-14**, pp. 2209-2214 (1996)

[4] K. Siraishi, T. Yanagi and S. Kawakami, *Light-propagation characteristics in thermally diffused expanded core fibers*, J. Lightwave Technol., **JLT-11**, pp. 1584-1591 (1993)

[5] see for instance M. Saruwatari and K. Nawata, *Semiconductor laser to single-mode fiber coupler*, Appl. Opt., **18**, pp. 1847-1856 (1979)

Minimisation of thermal effects on the polarisation in a polarimetric sensor using a single-mode fibre optic

E Gaumont, A.Chakari, P.Meyrueis, Michel Clément *.
ENSPS - LSP - ULP, Parc d'innovation, bd Sébastien Brant, 67400 Illkirch.
Tel : (33) 3.88.65.51.50. Fax : (33) 3.88.65.51.60 e-mail : gaumont@sphot.u-strasbg.fr
* SEP division SNECMA, forêt de Vernon BP 802 Vernon cedex
Tel : (33) 2 32 21 72 03 Fax : (33) 2 32 21 76 65
The study is part of a Research & Technology contract between SEP/CNES (France) and Louis Pasteur University (ULP Strasbourg, France)

Optic fibre sensors and especially polarimetric ones provide high accuracy and sensitivity. They are insensitive to electromagnetic perturbations. The simulation of an angular position polarimetric sensor using telecom single-mode optic fibre as a transducer showed a thermal dependence [Manc 95], [Manc 96]. We present a new model of the sensor, taking account of a thermal perturbation ΔT=300 K. Study's aim is to minimise the thermal cycle effects in the fibre. A series of experiments for ΔT = [293 K - 453 K] have been shown to fit well fit the calculated results.

We limit the applied stress field to the bending, twisting and the temperature. For short distances of fibre, for example ten centimetres, we neglect the intrinsic birefringence, as well as its thermal variations. Linear birefringence along a coil of radius, R induces a phase change $\Delta\phi$ [Rash 83] et al :

$$\Delta\Phi = \frac{2\pi^2}{\lambda} C \frac{r^2}{R} \tag{1}$$

Where r is the fibre radius, $C = \frac{1}{2} n^3 \left(p_{11} - p_{12}\right)\left(1 + \nu_p\right)$, $p_{11} = 0{,}121$ and $p_{12} = 0{,}27$ are the elasto-optic coefficients and $\nu_p = 0{,}17$ is the Poisson coefficient. The circular birefringence in a linear part of a fibre that is twisted with an angle, A induces a rotation $\Delta\alpha$ of polarisation direction given by the relation :

$$\Delta\alpha = gA = \frac{1}{2} n^2 \left(p_{11} - p_{12}\right) A \tag{2}$$

These phase changes depend on the temperature through the silica index, n of the fibre, the bending length of the fibre and the Poisson coefficient of the silica. We consider the elasto-optic coefficients P_{11} and P_{12} assuming that the effect of the temperature can be neglected. We equally assume that the thermal variations of n and of the Poisson coefficient, ν_p and the coefficient of linear expansion, dL/L are constant on the considered thermal range, ΔT=300 K :

$$\frac{dn}{dT} = 8.10^{-6}\ 1/°C \quad ; \quad \frac{dR}{RdT} = \frac{dL}{LdT} = 4{,}1.10^{-7}\ 1/°C \quad ; \quad \frac{d\nu_p}{dT} = 6.10^{-5}\ 1/°C \tag{3}$$

In the case of a coil of radius, R the relative phase change per unit temperature is deduced by deriving the expression of the phase change [Wils 89], [Whit 87] :

$$\frac{d(\Delta\Phi)}{\Delta\Phi.dT} = \frac{3}{n}\frac{dn}{dT} + \frac{1}{\left(1+\nu_p\right)}\frac{d\nu_p}{dT} - \frac{dR}{RdT} \approx 6{,}5.10^{-5}\ 1/°C \tag{4}$$

In the case of a twisted fibre, using the same method gives [Cohe 79] :

$$\frac{d(\Delta\alpha)}{\Delta\alpha.dT} = \frac{2}{n}\frac{dn}{dT} \approx 1{,}1.10^{-5}\ 1/°C \tag{5}$$

The spatial path of the "telecom" single-mode fibre used in the sensor is presented below (Fig.1).

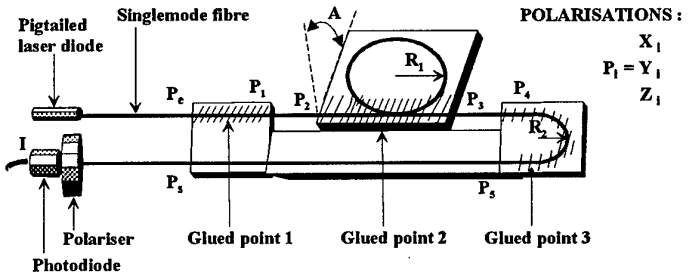

Fig.1 : schematic diagram of the angular displacement polarimetric sensor.

The two twisted parts ([P_1P_2], [P_3P_4]) with angle, A in opposite directions, induce rotations $\Delta\alpha$ and $-\Delta\alpha$ of the polarisation. The coil of radius, R_1 causes a phase change $\Delta\phi_1$. We add half a coil of radius R_2 so that the entrance and the exit of the sensor were the same side, this added bending induces a phase change $\Delta\phi_2$. Starting with the co-ordinates X_i, Y_i, Z_i of the polarisation P_i on the Poincaré sphere, we calculate the co-ordinates X_{i+1}, Y_{i+1}, Z_{i+1} of the polarisation P_{i+1} issued of the constraint G_i in between by the relation [Manc 95] :

$$\begin{bmatrix} X_{i+1} \\ Y_{i+1} \\ Z_{i+1} \end{bmatrix} = \cos\Delta\Phi(G_i)\begin{bmatrix} X_i \\ Y_i \\ Z_i \end{bmatrix} + \left(1-\cos\Delta\Phi(G_i)\right)\begin{bmatrix} \alpha_i \\ \beta_i \\ \gamma_i \end{bmatrix}\left(\alpha_i X_i + \beta_i Y_i + \gamma_i Z_i\right) + \sin\Delta\Phi(G_i)\begin{bmatrix} \beta_i Z_i - \gamma_i Y_i \\ \gamma_i X_i - \alpha_i Z_i \\ \alpha_i Y_i - \beta_i X_i \end{bmatrix} \tag{6}$$

The entry polarisation P_e corresponds to P_1 for a longitude 2ϕ and for latitude 2ψ. The principal axe, Γ_i of each birefringent part of the material links the two diametrically opposite points with a longitude $2\{\phi_{\Gamma i}\ (+\ \pi/2)\}$ and with latitude $2\{\psi_{\Gamma i}\ (+\ \pi/2)\}$ representing the eigenstates of this material (silica in this case), so :

$$\begin{bmatrix} \alpha_i \\ \beta_i \\ \gamma_i \end{bmatrix} = \begin{bmatrix} \cos 2\psi_{\Gamma i}\cos 2\phi_{\Gamma i} \\ \cos 2\psi_{\Gamma i}\sin 2\phi_{\Gamma i} \\ \sin 2\psi_{\Gamma i} \end{bmatrix} \qquad \begin{bmatrix} X_1 \\ Y_1 \\ Z_1 \end{bmatrix} = \begin{bmatrix} \cos 2\psi\cos 2\phi \\ \cos 2\psi\sin 2\phi \\ \sin 2\psi \end{bmatrix} \tag{7}$$

That is a rotation with an angle $\Delta\Phi(G_i)$ of the point P_i around the principal axe Γ_i. Evolution of the exit polarisation $P_s = P_5$ permits the deduction of the normalised intensity, I through the polariser oriented in the direction, p by the relation :

$$I(P_s, p) = \tfrac{1}{2}\left[1 + (\cos 2p) X_s + \tfrac{1}{2}(\sin 2p) Y_s\right] \quad (8)$$

The intensity through the polarisor increases from minimum value, I_m to maximum value, I_M from the angular position, A_m to the angular position, A_M for a given position p of the polariser. The thermal variation ΔT results in the enhancement of the phase changes $\Delta\Phi_1$ and $\Delta\Phi_2$ and in a thermal modulation of the dynamic of the response ($\Delta I = I_M - I_m$, fig.2). This modulation is represented by the modulation of the polarisation degree d_{Am} or d_{AM} of the light which intensity is I_m or I_M. A linear entry polarisation P_e provides a 48,75° angular range. And if P_e is circular, the angular range is 97,5° [Manc 96]. When P_e is elliptical, the angular range may decrease (60° for example) or enhance (110° for example). In order to have the dynamic, ΔI enlarged and its thermal modulation partly minimised, the direction p must be superposed or perpendicular to the rotation direction of the coil, $A = p_0 = 0°$. Also, I_m and $(1-I_M)$ are equal and correspond respectively to the minimum and the maximum of the intensity transmitted through the polariser, for a given polarisation. The choice of the value of the radius of the coil, R_1 permits to have this dynamic, ΔI maximum. So the normalised intensity of the response when $\Delta T = 0$ K vary between 0 and 1, the sensitivity of the sensor is maximum, the trajectory of the exit polarisation P_s follow the equator of the Poincaré sphere. Therefore the polarisation degree, d_A in front of the half coil, for each angular position A, is equal to 1. Especially, the thermal modulation of the polarisation degree is symmetric and minimum, every side of the angular position p_0. For that, the coil must be equivalent to a quarter-wave plate if P_e is circular or to a half-wave plate if P_e is linear (Fig.2).

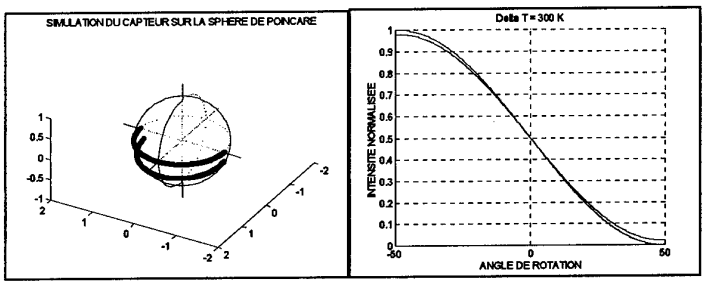

Fig.2 : optimised sensor responses. P_e is circular. $\Delta\phi_1 = 9.\pi/2$. $d_{Am}(\Delta T = 300K) = 0.9595$.

In this case, relation (1) allows the calculation of (N+1)/2 values of R_1 whose corresponding phase change $\Delta\Phi_1$ is equal to $(2q-1).\pi/2$ where N=2q-1 (Fig.3). The value of radius, R_2 of the half coil should induce a phase change $\Delta\Phi_2 = q.\pi$. The amplitude of the thermal modulation of the polarisation degree d_{Am}, for each value of R_1 is given by the relation :

$$\Delta d_{Am}(\Delta T) = |\, d_{Am}(\Delta T = 0K) - \Delta d_{Am}(\Delta T)\,| \quad (9)$$

N =2q-1	**$\Delta\phi$**	**R_1 mm, $\lambda_1 = 0.6328$ µm**	**$\lambda_2 = 0.780$ µm**	**$\lambda_3 = 1.3$ µm**	**$\Delta d_{Am}(\Delta T)$, 30K**	**100K**	**200K**	**300K**
1	$\pi/2$	83.657	67.403	39.880	.0000	.0001	.0002	.0005
9	$9\,\pi/2$	9.295	7.489	4.431	.0004	.0045	.0180	.0405

Fig.3 : optimal dimensions of the coil for N=1 and N=9, with the radius of the fibre r =125 µm.

Relation (4) shows that $\Delta(\Delta\phi_1)/\Delta T$ is inversely proportional to R_1. Therefore, $d_{Am}(\Delta T=300K)$ increases when N reduces and R_1 increases. The more optimal value is for N = 1 and $\Delta\phi = \pi/2$. In this case, the angular error commit in a simple calibration of the response at ΔT = 300 K remains **below to 0,1°** on a 90° angular range. Wavelength λ allows the reduction of both order, N of the phase change $\Delta\phi_1(N)$ and the amplitude of the thermal modulation. Practically, if the dimensional background of the sensor limits the radius of the coil to a value of about 7,7 mm, it is preferable to choose the wavelength λ_3 = 1,3 µm so that $\Delta\phi_1 = 5.\pi/2$ instead of choosing λ_1 = 0.6328 µm leading to $\Delta\phi_1 = 11.\pi/2$ (Fig.3). Thermal modulation of the polarisation degree is $\Delta d_{Am}(\Delta T=300K)$ = 0,0126 instead of 0,0609.

Series of experiments are presented where wavelength λ = 1,3 µm. The sensor has no half coil. R_1 is chosen for having $\Delta\phi_1 = 5.\pi/2$ and obtaining a 97,5° angular range and a polarisation degree $d_A(\Delta T=0K) = 1$. The coil is heated using hot air ; glued points are kept off the thermal perturbation zone. The coil is glued with cyano-acrylate glue along its rotation axis ; major part of its circumference is in the air. We recorded two responses at T = 293 K and at T = 453 K (Fig.4).

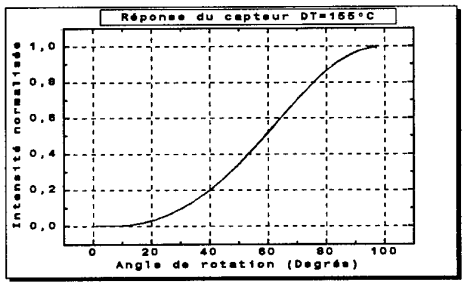

Fig.4 : sensor responses at T = 293 K and T = 453 K. λ = 1,3 µm. P_e is circular, $\Delta\phi_1 = 5.\pi/2$.

A weak thermal modulation of the dynamic of response has been observed by direct reading on the detection amplifier. But the shift of minimum intensity of the response is below the 5mV voltage sample of the data acquisition card of the experiment system. These records well fit the calculation results.

In conclusion, all of the thermal effects applied on the "telecom" single-mode fibre have been considered in the simulation of the angular position polarimetric sensor. Optimisation of calculation shows that it is possible theoretically to minimise the thermal modulation of the dynamic of the sensor response, so that the polarisation degree $d_{Am}(\Delta T=300K)$ calculate at the angular position of the minimum intensity is equal to 0.9995. In this case, the angular position error ΔA would be below 0,1° along an angular range of 90°. The entry polarisation P_e, the choices of the wavelength λ and of the radius R_1 of the rotation coil are the essential parameters useful for optimising the response. An experimental system has been developed. The results obtained in the experimental thermal range [293K - 453K] have been shown to agree well with the theoretical simulation of the sensor.

BIBLIOGRAPHIE :

[Manc 95] N.Mancier : « Etude de la biréfringence induite par contrainte externe dans une fibre optique. Application à la réalisation d'un capteur de position angulaire à basse température ». Thèse, 1995.

[Manc 96] N.Mancier, A.Chakari, M.Clément, P.Meyrueis : « Angular displacement fibre-optic sensor : theoretical and experimental study », Applied Optics, vol 34, n°.28, pp 6489-6495, 1996.

[Rash 83] S.C.Rashleigh : « Origins and control of polarization effects in single-mode fibers ». J.Light. LT-1, 1983, pp 312-330.

[Wils 89] S.J.Wilson : « Temperature sensitivity of optical fiber path length », Opt. Commun. 71 n°6, pp 345-350, 1989.

[Whit 87] B.J.White, J.P.Davis, L.C.Bobb, H.D.Krumboltz, D.C.Larson : « Optical-fibre thermal modulator ».IEEE J.Lightwave Technol. LT-5, n°9, pp 1169-1175, 1987.

[Cohe 79] L.G.Cohen, J.W.Fleming : « Bell Syst. Tech.J.58, pp 945-954, 1979.

[Aude 97] P.Audebert, F.Bresson, S.Bertrand, G.Tribillon : « Stable and adhesive hybrid fluorescant sol-gel coating on pre-treated stainless steel. Application to the realisation of optical fluorescence sensor », Applied Surface Science, (1997).

[Aude 96] P.Audebert, F.Bresson, R.Devillers, G.Tribillon : « Inclusion of fluorophore in hybrid sol-gel coating ; application to in-situ temperature measurement », Synth. Met 81, 1996, pp. 315.

Systems Applications and Field Trials

Thursday–Friday, 9–10 July 1998

Chair: Robert A. Lieberman, Physical Optics Corporation (USA)

The stable class 0.2 Sagnac Current Sensor using annealed fiber sensor coil

T.G. Nielsen[1] , Institute of applied physics, university of Bern, sidlerstr. 5 CH-3012 Bern,
Tel. +41 31 631 89 25.
K. Bohnert, ABB Corporate Research Center, CH-5405 Baden-Dättwil,
Tel. +41 56 486 80 44.

Summary

I. Introduction

Optical fiber current sensors are of considerable interest to the electric power industry. Particularly attractive features as compared to conventional current transformers include inherent galvanic isolation of the sensor head from ground potential, less sensitivity to electromagnetic interference, smaller size and weight and higher safety.

A particular sensor configuration is a Sagnac all-fiber interferometer which is used to detect the magnetic-field-induced Faraday phase shift between two circularly polarized light waves counterpropagating in a circular fiber coil [1]. When a magnetic field is present along the direction of propagation of the light in the coil, the two counterpropagating waves will have different phase velocities, the difference being proportional to the magnetic field in the coil. The interference of these waves provides the sensor signal.

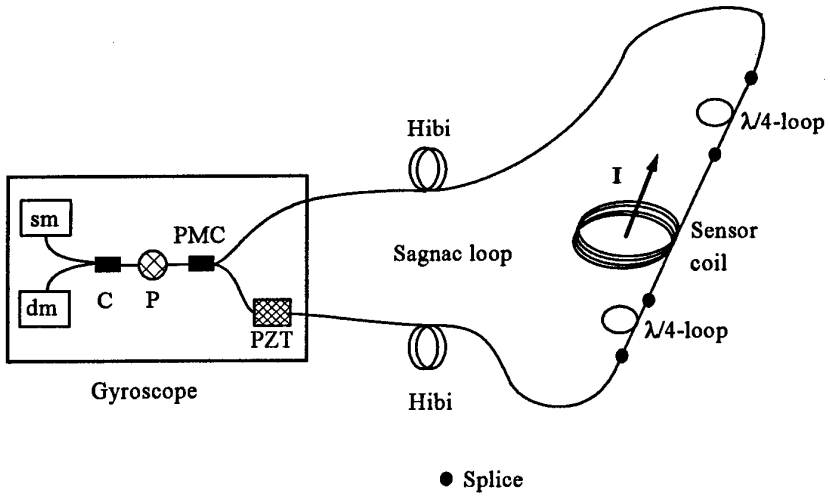

Figure 1 Exploitation of the fiber optical gyroscope for assembly of an all-fiber Sagnac current sensor. sm: source module, dm: detection module, P: polarizer, PMC: phase maintaining coupler, PZT: piezo electric modulator, I: current to be sensed, Hibi: *hi*gh *bi*refringence fiber.

[1] Work at ABB Corporate Research Center (Baden, Switzerland) to obtain the Cand. of Science degree from the University of Copenhagen

An important advantage of this type of sensor is that noise will have the same effect on the two counterpropagating waves and will be canceled out, while the magnetic field influences the waves oppositely. Moreover, the technology developed for optical fiber gyroscopes (based on the Sagnac effect) can be exploited. Thus, the scope of this work was to build and test a Sagnac Current Sensor by modifying a commercial available and cheap (~1000$) fiber optical gyroscope.

II. The components of the sensor

The sensor (Fig.1) is a minimum configuration of an all-fiber Sagnac interferometer and consist of a modified commercial open-loop fiber gyroscope, a 20 loop fiber sensor coil with a diameter of 80 mm, and two off-coated fiber loop quarterwave retarders (converting linearly polarized light into circularly polarized or opposite) whose retardance error were within 2°. Both quarterwave retarders and the sensor coil consist of ultra-low birefringence fiber (York). In other words, the high birefringence (hibi) fiber loop of the gyroscope has been cut and supplied with the quarterwave retarders and the sensor coil (Fig.1).

The retardance of the sensor coil, before annealing, was from theory [2] about 300° due to the bending of the fiber into a coil. In order to make the present current sensor sufficient temperature stable and fulfilling the requirements on accuracy of a class 0.2 sensor [3], the retardance of the sensor coil must be reduced to well below 100°. This is done with a specific annealing cycle [4] in a temperature controlled oven.

The experiments showed that in order to prevent a very brittle coil, gaseous Nitrogen must be blown into the oven during the annealing cycle. As it turned out, an acceptable sensor coil was made by adding this substantial step to the specific procedure and by stating the procedure more exactly, namely, by soaking the fiber in dichloromethane for only about 1 minute prior to annealing. Finally, an annealed sensor coil with a retardance of only 40° was attained. Thereby, the annealing procedure has reduced the retardance of the sensor coil by more than a factor of 7. This ideal sensor coil and quarterwave retarders are then assembled with the Sagnac interferometer.

III. Measurements on the sensor

A. Stability in time- and dynamic range.

The sensor was tested for the measurement of 50 Hz currents up to 1200 A_{rms}. A high quality inductive coil was used as conventional reference. The results are shown in Fig. 2. The large standard deviation for each measurement is due to the fact that the electronics of the gyroscope for signal processing was lacking at the time of experiment, and alternatively spectrum analyzers were used for signal processing. In spite of these large standard deviations, any *tendency* of deviation of sensor measurement from conventional measurement would be seen with this method. In Fig. 2 it is seen, that the accuracy, in the dynamic range, of this Sagnac sensor stays within the requirements of a class 0.2 current sensor.

The stability, in the time range, of the Sagnac sensor was also tested. A measurement was made every 5. minute during 30 hours. The results are shown in Fig. 3, where it is seen that the sensor is time-stable within 0.2 %, which fulfills the requirements for a class 0.2 sensor.

B. Mechanical perturbations

The stability of the Sagnac sensor to strong vibrational perturbations on respectively the hibi fiber and the sensor fiber of it was tested. Both low (100 Hz) and high frequency (24 kHz) perturbations were applied respectively in both cases, the 100 Hz vibrations with a much higher amplitude.

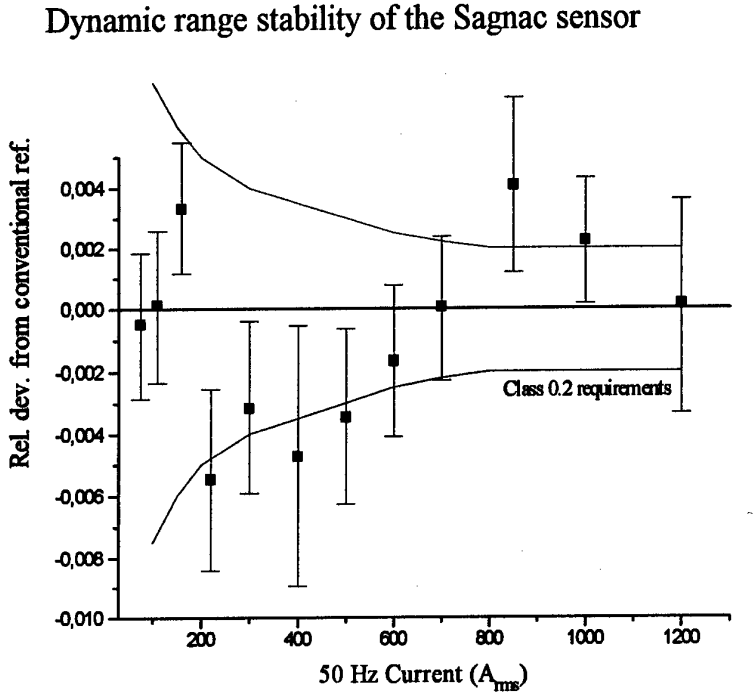

Figure 2 The accuracy in the dynamic range of the Sagnac sensor. For each current value, the black square corresponds to the average value of 12 measurements and the bar corresponds to the standard deviation.

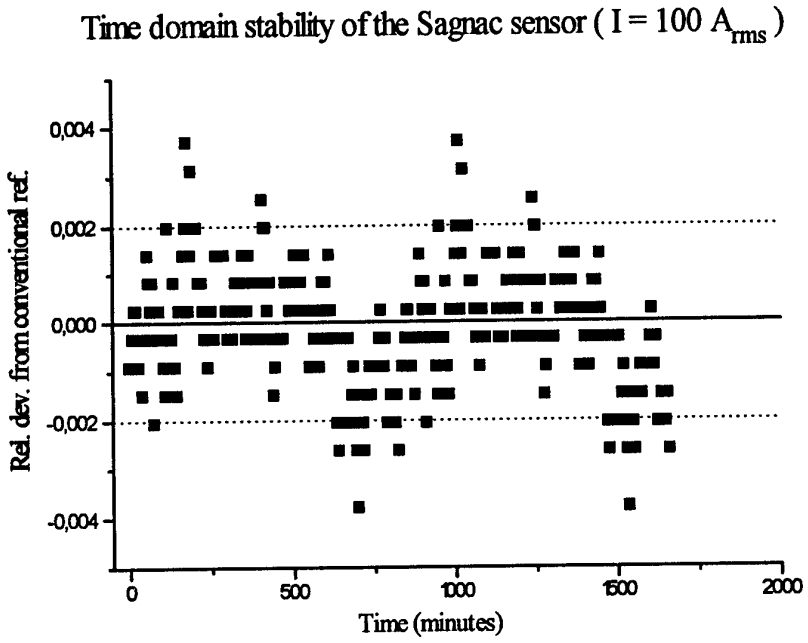

Figure 3 Stability of the Sagnac sensor in the time domain. All measurement made for the current, $I \approx 100\ A_{rms}$.

When applied to the sensor fiber, the 100 Hz vibrations nevertheless caused a noise signal at 100 Hz equivalent to only 1 A_{rms}, while the 24 kHz vibrations caused a noise signal at 24 kHz equivalent to 10 A_{rms}. So it is seen that the Sagnac sensor is much more sensitive to high frequency vibrations, which might be due to the non-reciprocity of high frequency phenomena. The Sagnac sensor showed no sensitivity to any of the perturbations on its hibi fiber.

For the sake of comparison, stability to analogous perturbations was tested for an all-fiber optical current sensor using the *polarimetric detection scheme*. Also for this sensor, there was no effect of perturbations on the hibi fiber of it. Here, the 100 Hz vibrations caused a noise signal at 100 Hz equivalent to 5 A_{rms}, and the 24 kHz vibrations caused a noise signal at 24 kHz equivalent to 20 A_{rms}.

IV. Conclusion

The results given above can be concentrated in 3 important steps toward developing a competitive Sagnac optical current sensor :

- With the aid of thermal annealing, the retardance of the sensor coil was reduced by almost a factor of 8 (from 300° to 40°). Thereby a nearly ideal sensor coil for the Sagnac sensor was constructed. Also nearly ideal quarterwave retarders (Retardance = 90° ± 2°) were constructed by bending a piece of fiber into a circular loop (λ/4-loops).

- By assembling of the given nearly ideal sensor coil and $\lambda/4$-loops with a already developed Andrew gyroscope, it was shown that one can accomplish a Sagnac optical current sensor fulfilling the requirements of a class 0.2 current sensor.

- It was demonstrated that to both high and low frequency perturbations, the Sagnac sensor is less sensitive than an optical current sensor using the polarimetric detection scheme. It is especially less sensitive to low frequency vibrations, namely a factor of 5, who can disturb the 50 Hz current measurement directly. The strong low frequency perturbations causes a noise signal equivalent to 1 A_{rms} in the Sagnac sensor. Since the purpose of this sensor is current measurement in the range of 1000 A_{rms}, such a noise signal will hardly be of any importance.

References

[1] G.Frosio, "All-fiber Sagnac current sensor", Opto 92 Proceedings, Paris, 560-564 (1992).

[2] R. Ulrich, S. C. Rashleigh and W. Eickhoff, 'Bending-induced birefringence in single-mode fibers', Optics Letters Vol. 5, No. 6, pp. 273-275, (1980).

[3] R. Stierlin , 'Faseroptische Sensoren', Bulletin SEV/VSE 82, (1991).

[4] Dingding Tang, A. H. Rose, G. W. Day, and S. M. Etzel, 'Annealing of linear birefringence in single-mode fiber coils: Application to optical fiber current sensors', J. Lightwave Technol., Vol. 9, No. 8, pp. 1031-1037, (1991).

Composite plate drop test using a 16 channel fibre Bragg grating strain sensor system

G.B. Havsgård[1], K. Pran[1], S. Knudsen[1], P.O. Baalerud[1], G. Wang[1],
S.T. Vohra[2], M.A. Davis[2], A. Dandridge[2] and A.E. Jensen[3]

1 - Norwegian Defence Research Establishment (FFI), P.o. Box 25, N-2007 Kjeller, Norway
Phone: 47 6380 7380, Fax: 47 6380 7212, E-mail: geir-bjarte.havsgard@ffi.no
2 - Code 5600, Naval Research Laboratory (NRL), Washington, D.C. 20375, USA
3 - Division of Applied Mechanics, NUST, N-7034 Trondheim, Norway

Introduction: Under the Composite Hull Embedded Sensor System (CHESS) program, which is a co-operative program run jointly by FFI and NRL, a drop test with a composite sandwich plate has been performed [1]. The plate was designed to have similar mechanical properties to a bottom panel in the Norwegian Navy's new fast patrol boat (MTB). The goal of the drop test was to enable us to choose sensor locations and sensor readout system for the final tests in the CHESS program, which are going to take place on the MTB.

The MTB is an Air Cushion Catamaran made from composite materials. Under high sea conditions, the area between the two hulls of the catamaran, called the wetdeck, can experience wave slamming. This transient loading results in high forces acting upon the structure, and can lead to delamination and damage in the wetdeck. In order to study the effects of wave slamming, the dynamics of the composite plate was measured during many drops in a controlled environment at MARINTEK in Trondheim. The MARINTEK site is equipped with a large towing tank with a wave generator and a drop rig that enabled us to drop the plate on a prescribed position on the waves.

In addition to the fibre optic sensor system, the plate was equipped with a range of conventional sensors like electrical strain gauges, pressure sensors, force sensors, accelerometers and a displacement sensor.

Sensor system: The fibre optic sensor system was a 16 channel system with a combination of wavelength division multiplexing and spatial multiplexing, see Figure 1. A total of 16 Bragg gratings were divided between three arrays, two with four gratings each, and one with eight gratings. The light reflected from each grating array was sent through a slightly unbalanced Mach Zehnder interferometer in order to convert the wavelength changes induced by the strain into phase changes $\Delta\phi$ given by

$$\Delta\phi = -2\pi nd\frac{\Delta\lambda_b}{\lambda_b^2} = -2\pi nd\frac{1-p_e}{\lambda_b}\varepsilon, \qquad (1)$$

where n is the fibre index, d is the geometrical path imbalance, λ_b is the Bragg wavelength, $p_e = 0.22$ is the effective photoelastic constant and ε is the longitudinal strain. The optical path imbalance (nd) of the interferometers was ca 2 mm for all the interferometers. The channels were demultiplexed in the WDM filters, splitting the light into 16 fibres, where each channel was detected and the phase retrieved using Phase Generated Carrier (PGC) modulation and a Differentiate and Cross Multiply (DCM) demodulation technique [2]. The PGC implies a high frequency modulation of the phase, which was done by applying voltage to a fibre-wrapped piezoelectric cylinder in one of the interferometer arms. Both the

demodulated output and the quadrature (sine and cosine) signals were recorded during the tests. The quadrature signals have been post-processed in order to check for amplitude variations. Additionally, the quadrature signals were demodulated using an inverse trigonometric technique [3], producing phase signals less influenced by amplitude variations in the quadrature signals. The results presented in this paper are from this processing.

The 1x4 WDMs had passband widths of about 5.5 nm for all channels, thus limiting the maximum strain to ±2300 με. The 1x8 WDM had passband widths ranging from 1.6 nm to 2.9 nm with corresponding maximum strain amplitudes from ±700 με to ±1200 με. The Bragg gratings were designed to have Bragg wavelengths in the passband centres. The system noise floor was less than $10n\varepsilon/\sqrt{Hz}$ @ $1\ kHz$, and the system bandwidth was 7 kHz.

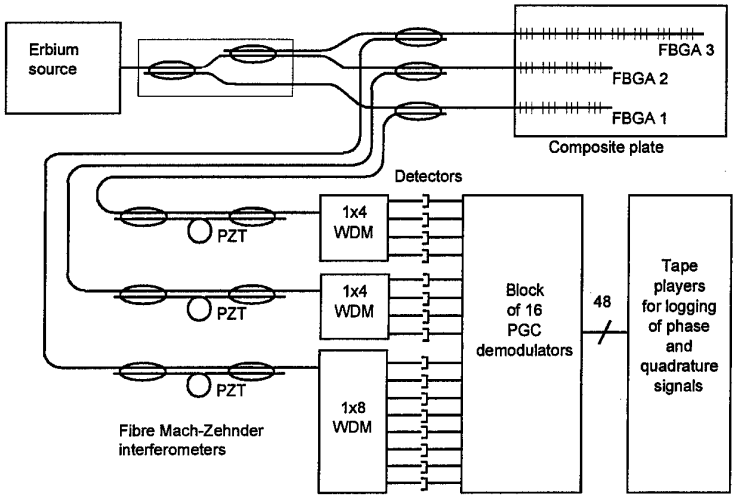

Figure 1 The Bragg grating strain sensor system used in the drop tests

Composite panel and test sequence: The composite plate measured 1000x600x29 mm, and consisted of a core made from Divinycell H200, and laminates made from layers of Glass Reinforced Polyester (GRP) on each side. The Bragg gratings were attached to the plate surface using a cyanoacrylate based glue called M-bond, and were then protected by covering all the optical fibre with a glass fibre tape which was saturated with epoxy. We put eight gratings on each side of the plate, located in the same positions on the lower (wet) and upper (dry) side of the plate as shown in Figure 2.

During the tests, a total of 16 different drops were carried out, varying the drop velocity (i.e. the vertical velocity of the plate when it hit the water surface), and the drop angle (i.e. the angle between the plate and the water surface).

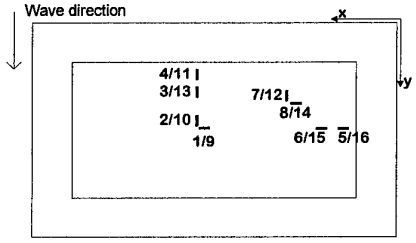

Figure 2 Sensor locations. Gratings 1-8 are on the wet side and 9-16 on the dry side

Results: Measurements of maximum strain in hull panels during oscillations excited by wave impacts are important for hull health monitoring systems, and some of the main results concerning strain amplitude and vibration frequencies are reported here. The maximum strain amplitudes are shown in Figure 3 along with the strain signals from one drop. Not

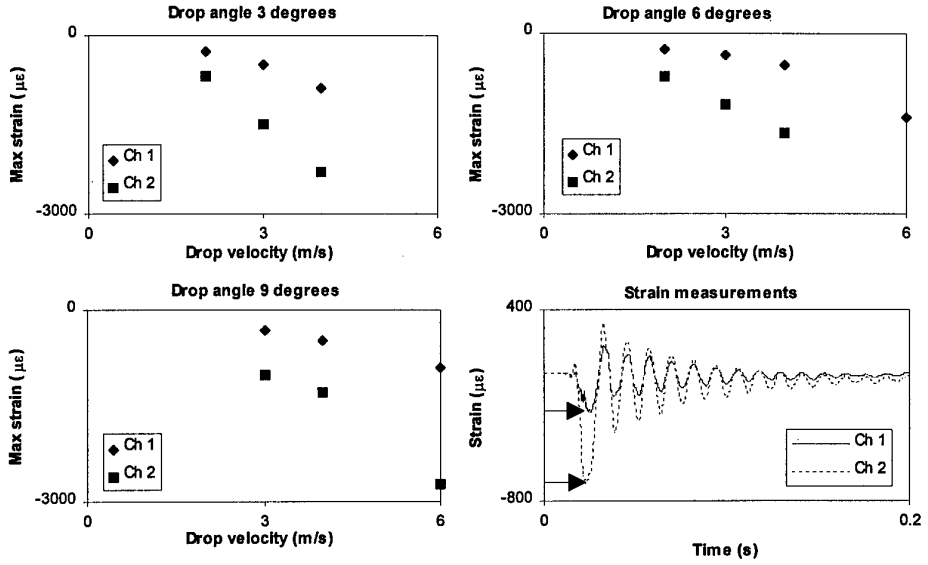

Figure 3 *Maximum strain amplitude versus drop velocity for Bragg gratings 1 and 2 for different drop angles. The lower right hand plot shows the strain signals from gratings 1 and 2 for a drop with angle 3 ° and velocity 2 m/s. The arrows indicate the maximum strain levels shown in the other plots*

surprisingly, the strain amplitudes increase when the drop velocity is increased. The growth seem to have a linear trend. Furthermore, we see that as the drop angle is increased, the maximum strain values are decreased. This is in general agreement with previous experiments with steel beams at MARINTEK and hydroelastic simulations, which show that peak strain during slamming increases linearly with velocity [4].

The vibration frequency of the plate was shown to vary a lot depending on the type of impact, see Figure 4. The frequency of the fundamental mode was determined by Fourier transforming the 0.2 s long strain signal from Bragg grating number 2. As we can see, the vibration frequency decreases with increased drop velocity, and decreased drop angle. This shows that the hydroelastic behaviour of the plate, which determines the vibration frequency, becomes more pronounced as the drop velocity increases and drop angle decreases [5].

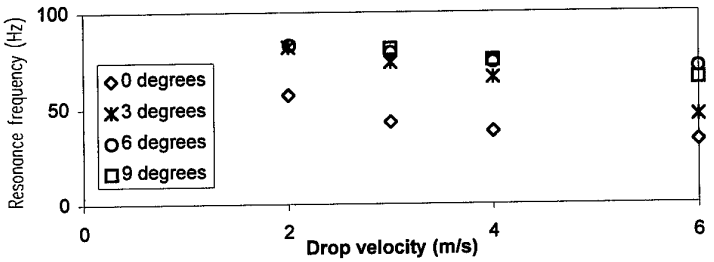

Figure 4 Plate resonance frequency versus drop velocity for different drop angles

Sensor performance: As mentioned in the sensor description, the maximum strain amplitude is limited by the WDM filter passbands. In the drop tests, the maximum strain values turned out to be larger than expected, and channel drop-outs occurred. This can be seen from the amplitude of the quadrature signals, A, given by $A = \sqrt{S^2 + C^2}$, where S and C are the recorded quadrature signals. A is proportional to the transmission in the WDM filters, and is fairly constant when the grating wavelengths are within the WDM passbands. In Figure 5 the demodulated strain signals from gratings number 2 and 3 are shown along with the amplitude A for the same channels. These results are from a 6 m/s drop on flat water, which induced the largest strain values in the test sequence. As we can see, the amplitude for channel 3 is low and constant for a period in the initial peak, which shows that a channel drop-out has occurred. For channel 2, the amplitude goes low due to a channel drop-out, then increases due to light from the neighbouring channel (grating number 3) entering the channel 2 passband. The peak strain amplitude is not retrievable for channel 2, but possibly retrievable for channel 3. It should be noted that it is only the peak strain amplitude that in some cases were lost, the rest of the signals are OK. The solution to the drop-out problem in this sensor system would be to increase the passband width of the WDMs, and if necessary reduce the number of channels.

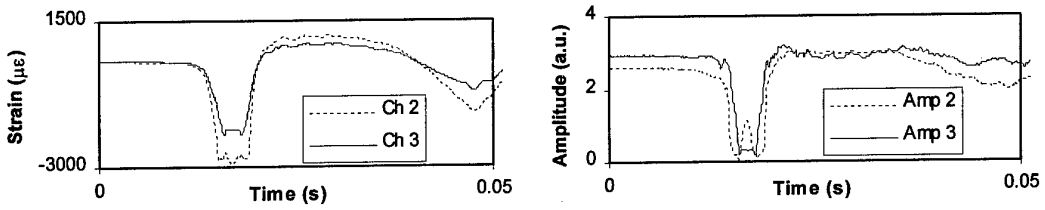

Figure 5 Strain signal and quadrature signal amplitudes for a 6 m/s drop on flat water

The peak pressure on the plate for some of the drops were on the order of 600 kPa, so although the gratings were well protected, the pressure lead to amplitude changes in the quadrature signals, as indicated by the arrows in Figure 6. We believe that these amplitude dips are due to induced birefringence in the fibre, and thus changes in the interferometer visibility. The amplitude A is also proportional to the interferometer visibility. However, even under these circumstances, the strain signals were correctly demodulated, demonstrated by the fact that the strain signals were similar to those measured in the same locations on the dry side of the plate, except for the opposite sign.

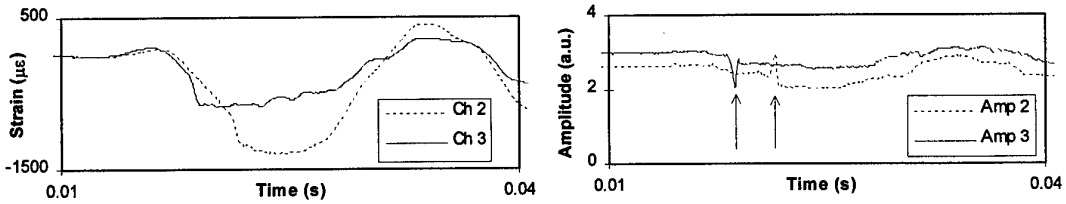

Figure 6 Strain signal and quadrature signal amplitudes for a 4 m/s drop with angle 9°

This work was partly supported by MARINTEK.

References: [1]: S. T. Vohra et al.: OFS 12, Post deadline session (1997)
[2]: A. Dandridge et al.: J. Quantum Electronics, vol 18, p. 1647 (1982)
[3]: I. J. Bush et al.: SPIE vol 1797, p. 242 (1992)
[4]: J. Kvålsvold et al.: PRAD, The sixth international symposium on practical design of ships and mobile units (1995)
[5]: O.M Faltinsen: Sea Loads, Oxford University Press (1991)

Miniature Fibre Optic Pressure Sensor for High Resolution Measurements in Turbomachinery Applications

W.N. MacPherson, J.M. Kilpatrick, J.S. Barton, J.D.C. Jones
w.n.macpherson@hw.ac.uk, j.m.kilpatrick@hw.ac.uk, j.s.barton@hw.ac.uk, j.jones@hw.ac.uk
Physics Department, Heriot-Watt University, Riccarton, Edinburgh EH14 4AS, UK

K.S. Chana, J.S. Anderson
DERA Pyestock, Hampshire GU14 0LS, UK

T.V. Jones, D.R. Buttsworth
Department of Engineering Science, Oxford University, Parks Road, Oxford OX1 3PJ, UK

Introduction

There is considerable demand in the field of turbomachinery research to make in-situ measurements of temperature, heat flux, and pressure in large-scale flow rigs. This is driven by the desire to increase engine efficiency and reliability by improving our understanding of the flow regimes within compressors and turbines. Thus aerodynamic probes are required that are capable of making localised, high bandwidth measurements in test facilities. In the measurement of pressure, sub-mm spatial resolution is required at frequencies of tens of kHz. For example, high spatial resolution is needed to probe between blade rows or to distinguish structure in complex flow fields. High measurement bandwidth is required to resolve pressure changes within the timescale of the passage of a single turbine or compressor blade at operating speeds.

There has been considerable development of silicon micromachined electrical sensors [1] (e.g. the Kulite piezoresistive range of pressure transducers); however, they exhibit limited spatial resolution — typically in excess of 1mm — and have a limited frequency response [1], exacerbated when it is necessary to protect the sensor from high speed particle impact, i.e. oil or dust suspended in transonic flows. Optical pressure sensors based upon diaphragm strain measurement, cantilever oscillations [2], or diaphragm displacement [3,4,5] have been demonstrated, but do not achieve the spatial and temporal resolution required for many aerodynamic measurements.

We consider the design, and performance of an experimental fibre optic pressure sensor that aims to meet these requirements, and present results obtained in an aerodynamic test facility

Sensor Design

The fibre optic pressure sensor consists of an extrinsic air cavity formed between the Fresnel reflection from the cleaved end of the single mode addressing fibre, and a reflective metal diaphragm (Figure 1). The transduction mechanism is the distortion of

the diaphragm caused by a differential pressure across it, which changes the path length of the air cavity. The sensor characteristics — pressure range, sensitivity, and frequency response — are determined by the diaphragm dimensions, which may be optimised for a given flow regime by choosing an appropriate diaphragm material and thickness.

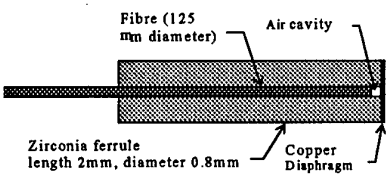

Figure 1 Pressure sensor construction details

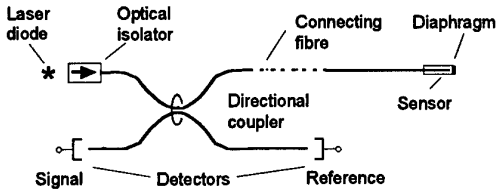

Figure 2 Optical interrogation system

The sensor is interrogated by a 780nm diode laser source, utilising a bi-directional coupler to enable measurement of the reflected signal (Figure 2). The reflected signal, I, is a measure of the interferometric cavity phase, and is described by the two beam approximation, given in equation (1). I_0 is the incident light intensity and ϕ, the optical phase is related to the cavity length l by $\phi = 4\pi nl/\lambda$, where n is the cavity refractive index (~1.0 for air) and V is the cavity visibility.

$$I = I_0(1+V\cos\phi) \tag{1}$$

The relationship between phase and pressure can also be determined. When subject to a differential pressure, the diaphragm experiences, at radius r, a surface deflection described by a quartic function $y(r)$ from which the pressure sensitivity may be estimated [6]. The optical phase change due to a change in cavity length $\Delta l = y(0)$ arising from a pressure change ΔP is given by

$$\frac{\Delta\phi}{\Delta P} = \frac{\Delta\phi}{\Delta l}\frac{\Delta l}{\Delta P} = \frac{4\pi n}{\lambda}\frac{3(1-\mu^2)a^4}{16Eh^3} \tag{2}$$

where a,h are the diaphragm radius and thickness, E is Young's modulus and μ Poisson's ratio for the diaphragm material. The pressure sensitivity is independent of the sensor cavity length. For a circular diaphragm, fixed around its circumference, the lowest resonant frequency of the diaphragm is given by [6] :

$$f = \frac{10.21}{2\pi a^2}\sqrt{\frac{D}{h\rho}} \quad \text{where } D = \frac{Eh^3}{12(1-\mu^2)} \tag{3}$$

which gives an indication of the maximum measurement frequency. The sensor's performance can be modelled by evaluating the bursting pressure and the resonant

frequency as above. For our application copper was the chosen diaphragm material as it is relatively easy to produce circular diaphragms of controlled thickness in the μm range by vacuum evaporation.

Density	ρ	8920	kg m^{-3}
Young's Modulus	E	130 x 10^9	Pa
Poisson's ratio	μ	0.34	–
Max. tensile stress	σ_m	220 x 10^6	Pa

Table 1 Copper diaphragm properties

The material properties of copper are given in table 1. A diaphragm thickness $h = 3$ μm and radius $a = 62.5$ μm will permit a bandwidth of ~ 1MHz set by the resonant frequency, a range set by the bursting pressure of 10 bar, and a pressure sensitivity of ~1.1 rad bar^{-1} for an illumination wavelength $\lambda = 800$nm.

The spatial resolution is inherent in the sensor construction, in which the active diaphragm area has the same radius as the addressing fibre, with the external dimensions limited only by the support ferrule. Our particular design utilises precision zirconia fibre connector ferrules as a basis for the sensor. These are machined to an outside diameter of less than 1mm. Commercially available pressure sensors are typically >1mm diameter.

Pressure Calibration

The pressure sensor has been calibrated in the range 3 bar down to rough vacuum (~1mbar). Low pressure calibration was carried out in a vacuum chamber fitted with a fibre feedthrough, and the high pressure calibration was carried out within a pressure chamber, fitted with a low bandwidth electrical gauge for comparison. Results indicate a cavity phase response of ~2.85 radians/bar (Figure 3).

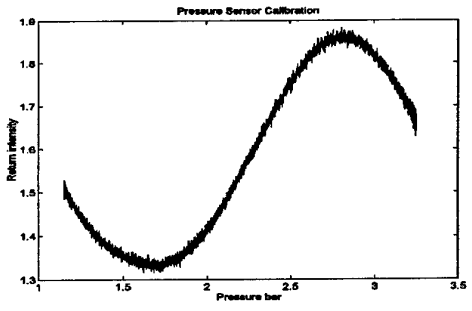

Figure 3 Sensor response versus pressure

Experimental Results

The pressure sensor was embedded in the 'total pressure' forward-facing position in an aerodynamic probe (Figure 4), which we then evaluated in a large scale aerodynamic test rig. The Isentropic Light Piston Facility (DERA Farnborough) is a transient flow facility, consisting of a stator and turbine rotor upstream of the probe. The 60 blade rotor stage rotates at ~10,000 rpm during the 0.5 s flow transient. The probe signal reveals structure of pressure oscillations at blade passing frequency and its harmonics.

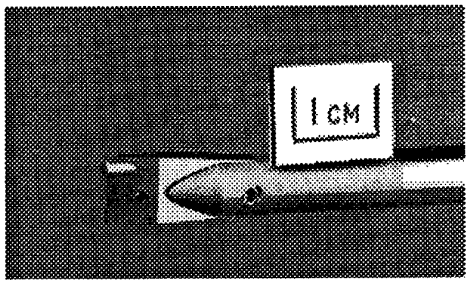

Figure 4 Optical pressure probe

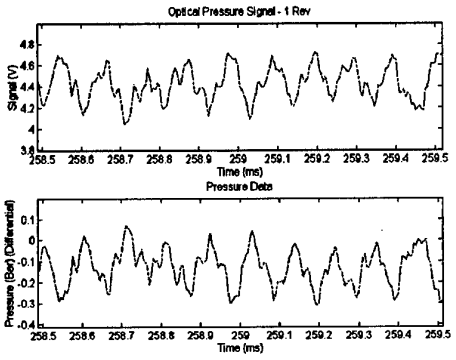

Figure 5 Pressure sensor data

The pressure signal may be averaged over several rotor revolutions to compensate for any time varying flow effects. Analysis of such data reveals frequency components in excess of 200kHz.

Conclusion

Using a fibre based pressure sensor embedded in an aerodynamic probe we have demonstrated the measurement of high bandwidth pressure fluctuations, of the order of 0.2 bar at 10 kHz, with 0.05 bar resolution and frequency components in excess of 200 kHz. This transducer exhibits the range, resolution, and frequency required for aerodynamic measurements, whilst maintaining the ability to provide high spatial resolution.

Acknowledgements This work was supported by the Engineering & Physical Sciences Research Council, whom WNM thanks for the provision of a studentship.

References

[1] R W Ainsworth, A J Dietz, T A Nunn, The use of semi-conductor sensors for blade surface pressure measurement in a model turbine stage, Trans. ASME J. of Eng. for Gas Turbines & Power, **113**, 261 - 268, 1991
[2] D Angelidis and P Parsons, Optical micromachined pressure sensor for aerospace applications, Optical Eng., **31**, 1638 - 1641, 1992

[3] Y J Rao and D A Jackson, Prototype fiber-optic-based ultrahigh pressure remote sensor with built-in temperature compensation, Rev.Sci.Instrum. **65**, 1695 - 1698, 1994
[4] Y Kim and D P Neikirk, Micromachined Fabry-Perot cavity pressure transducer, IEEE Photonics Technol. Lett. **7**, 1471 - 1473, 1995
[5] J Castracane, L P Clow, G Seidler, Optical multichannel transducer array for wind tunnel applications, Optical Eng. **35**, 2627 - 2633, 1996
[6] M Di Giovanni, Flat and Corrugated Diaphragm Design Handbook (Marcel Dekker, New York 1982)

Quasi-Static Strain Monitoring During the 'Push' Phase of a Box-Girder Bridge Using Fiber Bragg Grating Sensors

Sandeep T. Vohra, Bryan Althouse, and Gregg Johnson
Naval Research Laboratory, Code 5670, Washington DC 20375, USA
and
Samuel Vurpillot and Daniele Inaudi
Stress Analysis Laboratory, EPFL, 1015 Lausanne, Switzerland

Introduction: An interesting and increasingly popular method of building steel and concrete composite bridges involves the use of a large steel based structure called a box-girder. These massive structures, which have dimensions on the order of 5m x 5m x 150m with wall thickness sometimes exceeding 5 cm, are assembled by welding together many shorter (e.g. 5m x 5m x 5 m) box-girder pieces near a bridge building site. The massive and long box-girder structure thus created, is then 'pushed' from one end of the bridge pier to the other. A concrete deck is eventually built on top of the box-girder to complete the bridge structure. This bridge building approach apparently holds advantages in the sense that it requires far fewer on-site workers and also allows for rapid building of large scale bridges over difficult terrain. One of the more interesting (and potentially dangerous) phases during the construction process of a box-girder bridges is the so-called 'push' phase. During this phase, the long box-girder structure, which prior to the push rests on a pier closest to land, is literally pushed from one bridge pile-on to the next, requiring it to travel a distance of over 100 meters. The far pile-on typically is built in a ravine or a deep valley over which the bridge is being built. During the push, the steel box-girder structure is subjected to static strains at various locations, depending upon the position of the box-girder at any given time. For instance, the far end of the box girder would be subject to cantilever motion, which may be driven into oscillations due to winds in the ravine. Monitoring the strain at various locations in the box-girder during the push phase of the bridge construction has potential benefits in future infra-structure modeling efforts as well as in determining construction safety factors. In addition, utilizing enabling technologies (e.g. fiber Bragg grating strain sensors) for strain monitoring during an actual construction phase of a real world structure allows determination of the maturity of: (i) the instrumentation system, (ii) sensor packaging, and (iii) installation approaches [1].

This work reports the results of a 32 element fiber Bragg grating (FBG) array used to monitor strain at various locations in box-girder vaux viaduct being constructed near Lausanne, Switzerland. The entire push phase of the box-girder bridge, which took about a day, was monitored using several FBGs whose responses were interrogated using the scanning Fabry-Perot (FP) method [2]. Preliminary quasi-static strain sensing data shows fine as well as gross details of the push phase. The sensors are planned to operate during many phases of the box-girder bridge construction including the push, the concrete deck pouring, and eventually traffic monitoring. We report here on the push phase only.

SPIE Vol. 3483 • 0277-786X/98/$10.00

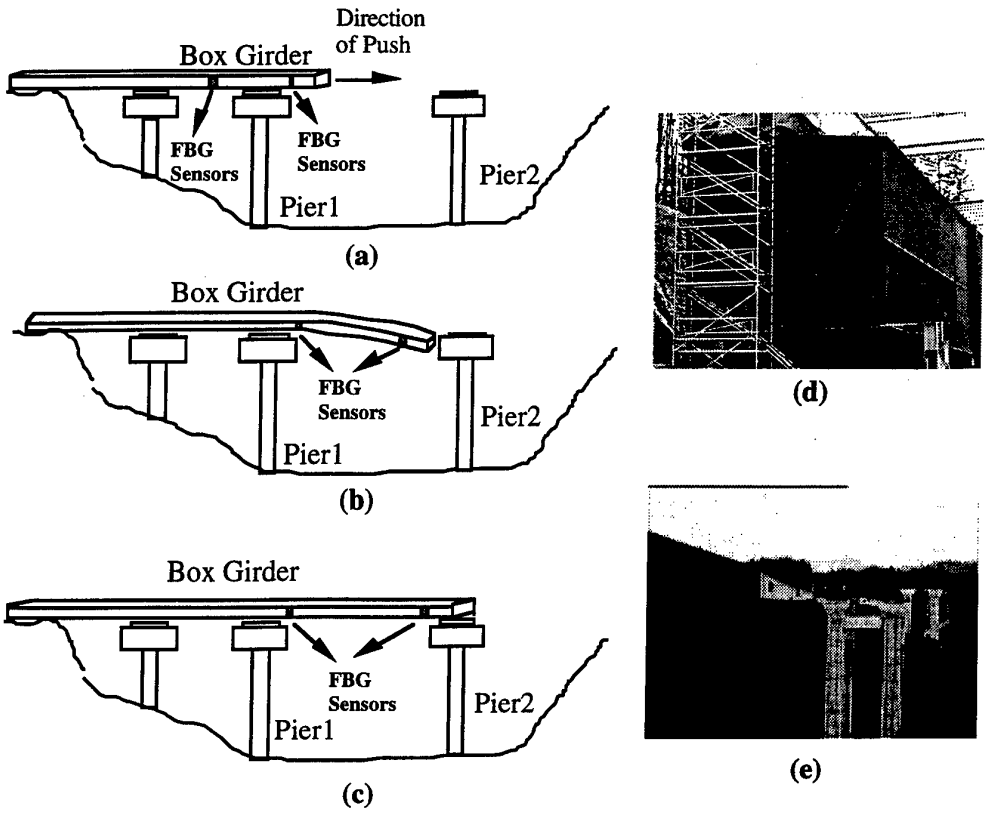

Figure 1 A simple sketch depicting the three push phases of the box-girder bridge (a), (b) and (c), along with a set of photographs showing the cross-section of the box-girder (d) and the box-girder prior to reaching pier 2 (e). The box-girder super-structure also has I-beams attached towards the far end which are not shown here.

The three phases of the box-girder bridge push are shown in Figure 1. Initially, the box-girder structure, which is built on land by welding shorter box-girders pieces together, rests on land and one of the piers (Figure 1a). The FBG sensors were attached on the inside of the girder during this phase. The two locations of the FBG arrays are indicated in Figure 1. Once a sufficiently long box-girder section has been assembled, it is pushed with hydraulic equipment from one pier to another, as shown in Figure 1b. During this phase the end of the box girder ends up in a position which could induce cantilever type motion (Figure 1b). In other words, we expect to see strain data from both arrays during this part of the push. The final phase of the push involves attaching a machine to the end of the box-girder to 'pull-up' the structure on pier 2. This phase also results in significant strain variations in the structure. The photographs in Figure 1 show the cross-section of the box-girder (Figure 1d) and the bridge during the push from pier 1 to pier 2 (Figure 1e). Pier 2 is approximately 100 meters tall.

Sensor Location and Attachment: Two arrays of 16 FBG sensors were attached circumferentially at two different locations inside the box-girder (Figure 1). The first array was located inside the box-girder approximately 10 meters from the far end (i.e. the end facing pier 2), while the second array was located approximately 65 meters from the far end of the box-girder (Figure 1a). The first array (closer to the end of the box-girder) had FBG sensors located on the floor, the ceiling and on the side walls while the second array had sensors located on the floor and side walls only. Since static and quasi-static strains are of interest in this work, any wavelength shift in FBGs due to thermal drifts must be compensated. This was accomplished by providing two FBGs at each sensing location, one of which was in mechanical contact with the structure while the other was in thermal contact only. In other words, strain measurements were made at eight points along the circumference of the box-girder at the two aforementioned locations. The FBGs for measuring strains were attached to the structure using an cyno-acrylate based bonding agent (e.g. M-Bond 2000). A small area of the box-girder was scrubbed clean and sanded smooth. The FBGs were bonded to the area after applying a small amount of pre-strain (< 50 micro-strain). All FBGs were attached to measure strain along the length of the girder. The second grating (for temperature compensation) was placed in thermal contact with the structure using a heat sink compound. However, making proper thermal contact without also making mechanical contact with the structure proved to be difficult considering the low ambient temperatures which tends to stiffen the thermal compound. Fortunately, since the metallic box-girder is massive, it undergoes minimal temperature changes during the actual measurement period (a few hours), thus not necessitating thermal compensation of FBG strain data. The FBG pairs (for both mechanical and thermal measurements) will become much more significant during the concrete deck pouring phase (to occur in the future) of the box-girder bridge construction when exothermic reactions are expected to provide localized heating as well as localized static strain .

The FBG sensor responses were interrogated using a scanning Fabry-Perot (FP) system [2,3]. Light from two ELEDs (operating at 1.3 μm) was directed through a pair of 2x2 couplers connected to the two FBG arrays. The reflected light is combined with a third coupler and directed to a single FP filter. Even though the FP filter is capable of achieving scan rates of 360 Hz, the system was effectively scanning at about 3 Hz since only static strains were being measured. This allowed for continuos monitoring of strain data during the push phase of the box-girder without exhausting the storage space on the computer hard drive. The FBGs were spaced about 2.5 nm apart, thus allowing ±1200 με to be easily measured. The internal system noise was measured to be about 1 με.

Results: The strains as seen by the three floor sensors of the second FBG array (sensor set 2) during the push are depicted in Figure 3a. This part of the push phase lasted about one hour, at the end of which the box-girder attained the position shown in Figure 1b.

During this part of the push phase, the FBG sensor set 2, traveled over pier 1 thus inducing compressive strains in FBG sensors located on the floor. The data are shown in Figure 3a. The FBG sensor set 1 undergoes fairly complicated strain changes as it sees a combination of compressive loads during the early part of the push, after which loading effects due to cantilever type motion induces more complex strain responses. This data is currently being analyzed and is not shown here. After the box-girder reaches close to the second pier, the end closest to pier 2 is attached to a machine which lifts it up on to pier 2 where it is permanently fastened. This 'pull-up' and fasten phase is the final phase of the box-girder push (Figure 1c). The pull-up phase also induces large strains at various locations on the box-girder which as measured by both FBG arrays are shown in Figure 3b. Not surprisingly, the ceiling and floor FBGs measure strain with opposite sign. Also the magnitude of the strain in array 1 is larger than that in array 2. The strain data clearly shows the stop and go motion utilized by the operators during the pull-up phase.

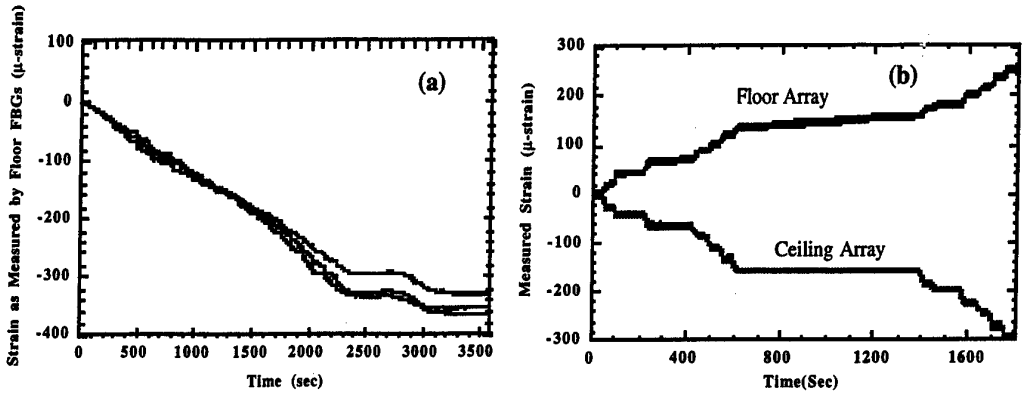

Figure 2 (a) Strain data from floor sensors in FBG array 2 (one closer to land) during the push phase. (b) Strain data from floor and ceiling sensors of FBG array 1 (closer to pier 2) during the 'pull-up' phase.

Conclusions: An array of 32 FBG sensors were used to measure strains at various locations in a box-girder bridge during an actual push phase of an in-construction bridge. The quasi-static strains in the FBGs were successfully measured with a scanning FP system which is sufficiently ruggedized to handle real-world conditions (e.g. low temperatures, winds and rough handling). The field test demonstrated that appropriate packaging of FBG sensors, which allows both mechanical and thermal sensing as well as allows for easy and quick installation on large scale steel structures, is required.

1. D. Inoudi, Proceedings of 12th OFS Conference, Williamsburg, USA, p. 596 (1997).
2. A.D. Kersey et.al., Optics Letters 18(16), p. 1370 (1993).
3. S.T. Vohra et.al., Proceeding of Workshop on Fiber Optic Sensors for Construction Materials and Bridges, Newark, NJ, May 1998 (to be published).

A Fibre-optic Microsensor for Measurement of Temperature Dynamics in Gas Turbine Systems

J.M.Kilpatrick, W.N.MacPherson, J.S.Barton, J.D.C.Jones
Physics Department, Heriot-Watt University, Edinburgh EH14 4AS, UK

D.Buttsworth, T.V.Jones
Dept. of Engineering Science, University of Oxford, Parks Road, Oxford OX1 3PJ, UK

K.S.Chana, J.S.Anderson
DERA Pyestock, Farnborough, Hampshire GU14 0LS, UK

1. Introduction.

The use of computational fluid dynamics (CFD) to model the temperature and pressure distributions which drive complex thermodynamic processes in gas turbine systems contributes to more cost efficient turbine design and development. However, experimental measurements are still required for validation of full-field CFD models, particularly in regions of highly unsteady flow where model stability is most severely tested. This work concerns the development of fibre optic temperature and pressure microsensors for measurements combining high spatial resolution and high bandwidth in unsteady gas flows. The objective of the work presented in this paper was to measure *gas total temperature* in a large-scale turbomachinery test-rig at DERA Pyestock, known as the Isentropic Light Piston Facility (ILPF). We have accordingly designed a dual sensor system, in which one of the elements is heated, so that gas total temperature can be measured independently of the convective heat transfer coefficient. Whilst such dual element probes based on thin-film resistance gauges have been developed previously for aerodynamic studies [1], this is the first report of their development using optical sensors.

2. Sensor Design and Characteristics

The temperature sensor comprises a 1.5μm 3-layer film structure which is vacuum deposited onto the end of a single mode optical fibre. It has an external diameter of 125 μm, with a central active area defined by the core diameter of 5μm. It operates via the thermo-optic effect in the main etalon and has negligible cross-sensitivity to pressure, which is critical for the proposed application. The external mirror provides isolation from flow particulates and, together with the interior semi-transparent mirror, forms an asymmetric Fabry-Perot structure with the response shown in Fig.1. [2]

SPIE Vol. 3483 • 0277-786X/98/$10.00

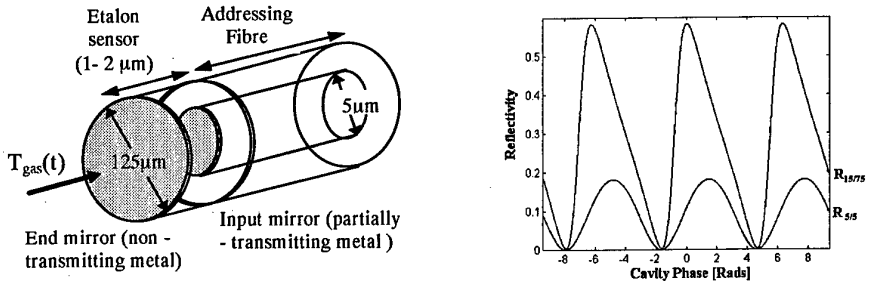

Fig.1. (a) Fibre Fabry-Perot temperature sensor. (b) Reflection response (upper curve) compared to cosinusoid response of a lower finesse single layer etalon. (lower curve)

3. Temperature Sensor Calibration

Compared to the more commonly encountered low finesse fibre Fabry-Perot sensor, the configuration of Fig.1(a) is more suited to operation in a harsh environment with physical protection afforded by overcoating of the exposed face. In addition, the higher reflectivity and asymmetric response can enhance the temperature sensitivity by up to 7 times that of an equivalent low finesse device. When suitably phase biased, the sensor also has a linear response well beyond the intended operating temperature limits, as shown in Fig.2.

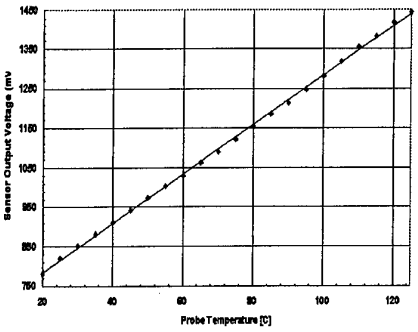

Fig.2.Calibration curve for a 1.5μm sensor of the type shown in Fig.1(a)

Generally, for phase shifts which approach or exceed the unambiguous range of the sensor, a homodyne phase recovery scheme is employed by current modulation of the laser diode to generate 3 discrete wavelengths. However, for the purpose of the measurements described here, operation within the linear range of the transfer response permits a straightforward recovery based on single wavelength interrogation with temperature obtained directly from the sensor data and calibration curve.

4. Dual Sensor Gas Total Temperature Measurement

Recovery of the *gas* flow temperature from the sensor temperature data requires some knowledge of the convective heat transfer coefficient. For sufficiently well characterised flow conditions and known geometries the latter can be modelled. [3] In unsteady flow conditions where the heat transfer coefficient cannot be assumed constant this approach is susceptible to error. An alternative method which avoids this difficulty employs

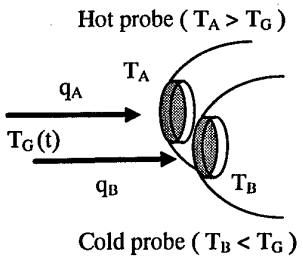

two sensors operating at different temperatures. From the expressions which relate the convective heat transfer to the gas and optical sensor temperatures, the heat transfer coefficient, may be eliminated to give an expression for the gas total temperature.

$$T_G = T_A + \frac{q_A (T_B - T_A)}{q_A - q_B} \qquad [1]$$

where T_A is the hot probe temperature, T_B the cold probe temperature and T_G the gas temperature. Convective heat flux for the hot and cold probe, q_A and q_B, was inferred from the measured surface temperature history, according to a finite difference method. [1] Gas total temperature was then determined from the dual sensor temperature data and the derived heat flux according to equation 1.

5. Gas Temperature Measurements in the Isentropic Light Piston Facility

The ILPF is a transient flow facility used for aircraft engine turbine research and development and provides the principal test bed for these sensors. It comprises a stator and rotor stage, simulating a high pressure turbine. The rotor is spun up to design speed before a transient hot air flow is released through the stage. To measure gas temperature variations in the wake of the rotor blades a dual sensor fibre-optic temperature probe, Fig.4, was installed downstream, approximately 10-20 mm behind the trailing edge of the rotor blades.

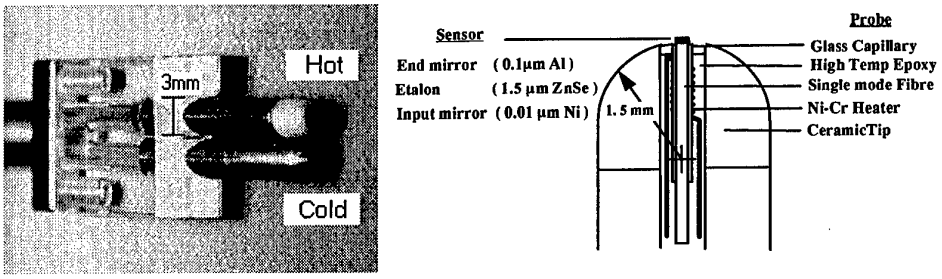

Fig.4. (a) Fibre-optic gas temperature probe. (b) Hot probe construction

The hot probe construction incorporated a 250 μm diameter 15W nichrome resistive heater embedded close to the sensor, Fig4(b). Heating was applied approximately 30 seconds prior to the run commencing, producing a temperature differential of around 50^0C between the hot and cold probe prior to arrival of the shock front.

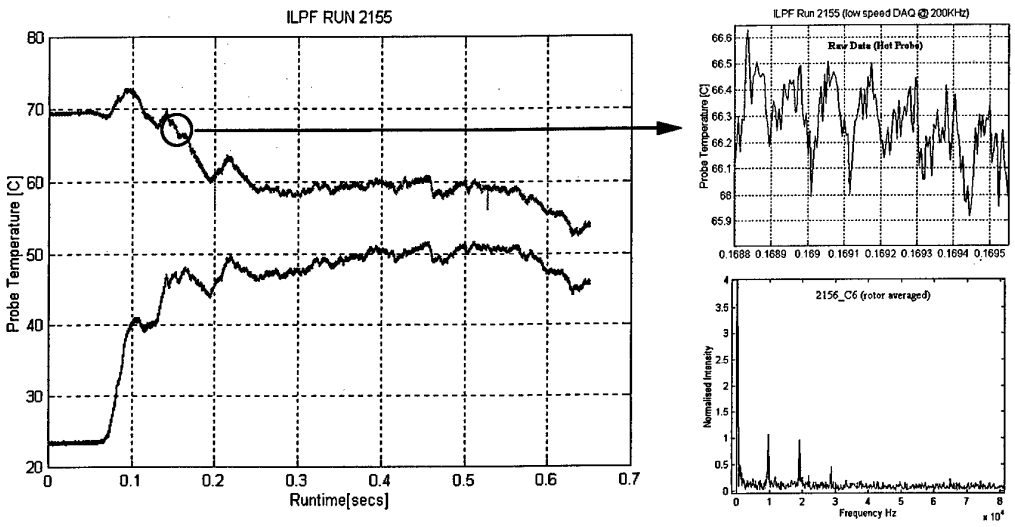

Fig.5 Raw data from hot and cold fibre optic sensors in ILPF flow. Inset shows unsteady component of 0.4K amplitude at 9.5kHz. (blade passing signal) with frequency spectrum below.

Data from a typical measurement are shown in Fig.5 and indicate a general convergence of the hot and cold sensor temperatures towards the mean gas temperature as steady state flow conditions are established. The raw data show higher frequency structure comprising unsteady (sensor) temperature fluctuations of 0.4 K amplitude associated with the individual rotor blades passing the sensor at a rate of 9.5kHz. The frequency spectrum indicates the presence of components in the second harmonic of the blade passing signal to around 30kHz.

6. Data Processed for Gas Total Temperature

The raw data shown in Fig.5 were processed according to equation 1. The temperature and convective heat flux history of the ILPF run are shown in Fig. 6, together with the recovered gas total temperature. The data indicate a mean gas temperature of around 328 K and underlying gas temperature oscillations of amplitude 12K at 9.5kHz, a factor of 30 greater than the dynamic temperature changes recorded by the sensor.

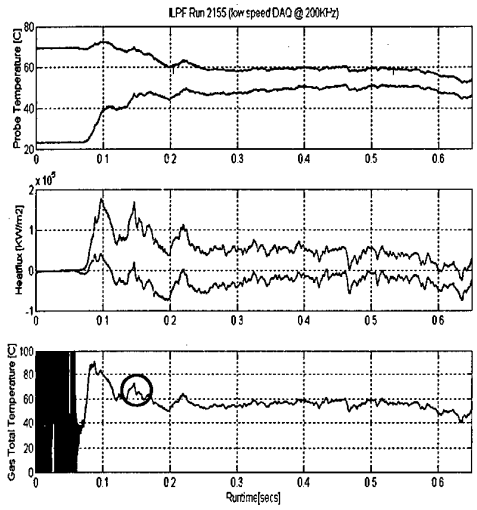

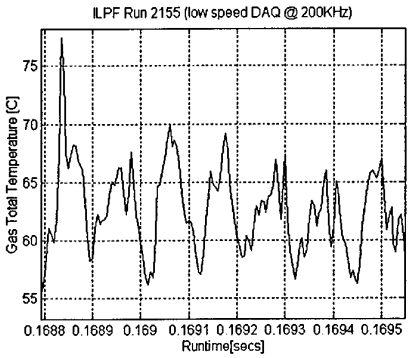

Fig.6 Heat flux and gas total temperature in the ILPF flow. Inset shows average gas temperature oscillations of 12 K at 9.5kHz and structure in blade passing signal.

7 Summary and Conclusions

We have demonstrated a robust fibre-optic microsensor for gas temperature measurements in aerodynamic flow facilities, although this application is by no means exclusive. The sensor has an active area of approximately 5 microns, a temperature resolution of less than 0.1K and a dynamic response up to 30kHz. Future work will explore the issues of measurement sensitivity, bandwidth and probe miniaturisation, with a view to further and more detailed study of structure in the blade passing signal.

8. References

[1] D.R.Buttsworth, T.V.Jones and K.S.Chana. "Unsteady Total Temperature Measurements Downstream of a High Pressure Turbine", 42nd ASME International Gas Turbine and Aeroengine Congress, June 2-5th, Orlando, Florida, 1997.

[2]. J.M.Kilpatrick, W.N.MacPherson, J.S.Barton, J.D.C.Jones "Reflection transfer characteristics of an optical fibre Fabry-Perot interferometer" *Sensors and their Applications VIII*, A T Agousti, N M White (eds), 263 - 268, IOP Publishing 1997, ISBN 0 7503 0421 9

[3] Kidd S.R., Barton J.S., and Jones J.D.C., Demonstration of optical fiber probes for high bandwidth thermal measurements in turbomachinery. Journal of Lightwave Technology, Vol.13, No.7, p1335-1339, July 1995.

Bragg Grating Extensometer Rods (BGX) for Geotechnical Strain Measurements

C. Schmidt-Hattenberger, G. Borm
GeoForschungsZentrum Potsdam, Telegrafenberg, D-14473 Potsdam, Germany

Abstract

We report on a new type of optical extensometer for strain measurement in geotechnical and civil engineering applications. The system key elements are Fiber Bragg Gratings (FBG) embedded in glassfiber reinforced polymer (GRP) rockbolts. In order to monitor rock deformations in tunnels, a prototype sensor rockbolt was designed. First measurements have been made to demonstrate the characteristics of the sensor system.

Introduction

The interest on Fiber Bragg Grating (FBG) sensors is increasing considerably in recent years. It has been successfully demonstrated that FBG sensors have great potential for a wide range of applications where quasi-distributed measurement for important physical quantities, such as strain, temperature, pressure, and force, are required [1]. The most important advantage of this type of sensor is that the signal is directly related to an absolute wavelength change. Thus, the sensor can be made independently of source intensity variations and losses in the experimental setup.

One focal point of interest is the application of FBG sensors in underground structures, such as tunnels and mines [2]. Measurement of geomechanical rock deformation is a major concern in these environments. Underground excavations and blasting works cause changes in the stress regime of the surrounding strata. Depending on the geologic structure and material properties of the rock mass, these stress changes may create unstable conditions. Therefore, overbreak, caving and flooding can occur which can threaten workers safety, and can cause damage or loss of the equipment.

A desirable solution is prevention by accurate prediction of the geologic structure and its stability. Hence, an essential part of tunneling is the periodical monitoring of the rock deformations. The commonly used methods such as triangulation, water levels, mechanical extensometers etc. exhibit a variety of measurement problems, i.e. their installation needs specialized operators, the obtained spatial resolution is generally low, and they consist of only single-point sensors. Therefore, a real demand exists for a monitoring tool which is easy to install, and allows static and dynamic strain measurement with high spatial resolution.

Rockbolts are typical elements of stabilization at the construction of a tunnel. In combination with the application of shotcrete, they are mounted in boreholes radially to the tunnel axis. Now, the idea was to exploit these rockbolts as an ensemble of sensors for monitoring the straining of the rock by implementing Bragg gratings in the anchor rods. Furthermore, assembled with several distributed gratings, one single anchor rod can perform as a multipoint-sensor with the ability for measuring also the gradients of strain close to the tunnel wall. This offers a great advantage of that new type of Bragg Grating Extensometer (BGX) sensor against conventional strain detection systems, and also against competitive fiber optic strain monitoring systems [3,4].

Technical Realization

Laboratory tests were performed with a 1.50 m glassfiber reinforced polymer rockbolt. The rod diameter is 22 mm, the Young's modulus amounts to 44 kN/mm^2. A groove of 1mm width and 2mm depth was cut into the rod surface. A grating was embedded into this groove and fixed by a special two-component Epoxy which was provided by the rockbolt manufacturer. In addition, a resistance thermometer element Pt1000 was implemented in the rod for controlling its temperature. At the head of the rockbolt a FC-APC connector (8° angle polishing) was mounted in order to connect the sensor head via fiber cable with the light source and the corresponding optical setup. The complete sensor head is shown in Figure 1.

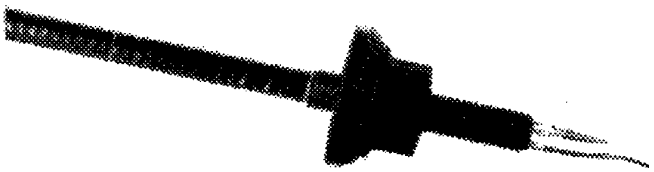

Fig. 1 GRP-rockbolt, with FC-APC connector to embedded Bragg grating, and SMC connector to Pt1000 element.

As shown schematically in Figure 2, first static strain experiments have been performed in order to test the feasibility of the anchor rod sensor. At one side, the rockbolt was fixed by a special mechanical mount. The other side is remaining unfixed but loaded via a threaded bolt which produces a defined force onto the rock-bolt.

The theoretical description of this experiment can be derived from elasticity theory [5].

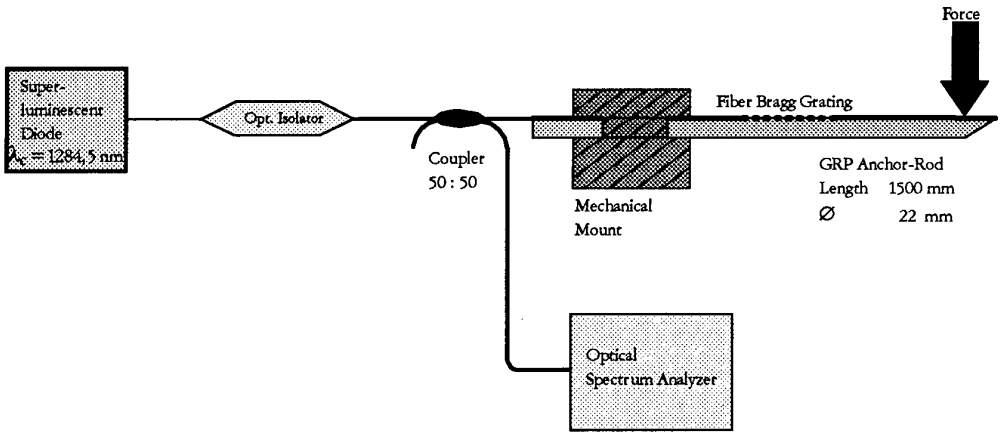

Fig. 2 Scheme of experimental setup for investigation of static strain of a glassfiber reinforced polymer (GRP) anchor rod.

Results

Figure 3 shows the experimental results of the static strain experiment. According to the theory [5] it can be demonstrated that by bending of the rod, the fibers at the concave side are stretched which causes a positive Bragg-wavelength shift ($\Delta\lambda$=0.60 nm), and the fibers at the convex side are compressed which causes a negative Bragg-wavelength shift ($\Delta\lambda$=-0.60 nm). This has been simulated by mounting the rod in such a way that the groove with the embedded FBG was directed with 0° angle with respect to the acting load, and after that rotated axially by 180 °.

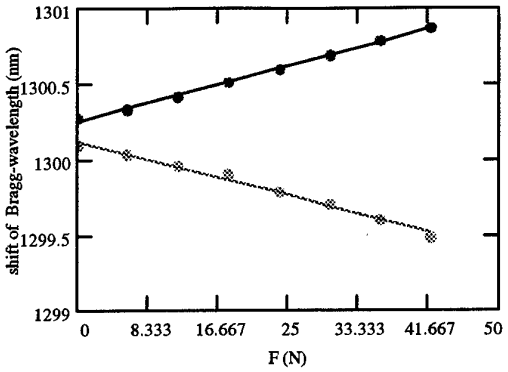

Fig. 3 Experimental data of the bending test on the rockbolt. The groove with the embedded Bragg grating (λ_B=1300.3 nm) was orientated under 0° (upper graph) and 180° (lower graph) with respect to the bending force F.

The characteristics of Fig.3 demonstrate the bending sensitivity of the anchor rod, which has been verified in further measurements where the groove with the grating was turned into definite angular positions between 0° and 360° with respect to the applied load.

While the above setup utilizes only Bragg gratings which are directed along or parallel to longitudinal axis of the rockbolt, in another test an additional Bragg grating was directed perpendicular to the symmetry axis of the rod. Here, the strain is defined by the Poisson-relation [5]. Accordingly a negative radial strain was observed when a positive longitudinal strain was measured, and vice versa. The corresponding Poisson number was close to the number specified by the rod manufacturer.
Currently, a rockbolt with 3 grooves with simultaneously detecting Bragg gratings is under investigation.

The following theoretical approach can describe the results of Fig.3:
The bending momentum M of the applied force on the single-side fixed rod is:

$$M(x, y_0, r, l, E) := P(y_0, r, l, E) \cdot x \qquad (1)$$

where y_0 is the deflection of the rod in the bending test, r is the radius of the anchor rod , l is the free length of the rod, and E is the Young's modulus. In the present case, the maximum force F was 42 N, and x represents the spatial coordinate along the rod.

The stress as a function of coordinates x and y, with y as distance from the "neutral layer" of the rod [5] is given by

$$\sigma(x, y, y_0, r, l, E) := \frac{\sigma_{max}(x, y_0, r, l, E)}{r} \cdot y \qquad (2)$$

The corresponding axial strain reads

$$\varepsilon(x, y, y_0, r, l, E) := \frac{\sigma(x, y, y_0, r, l, E)}{E} \qquad (3)$$

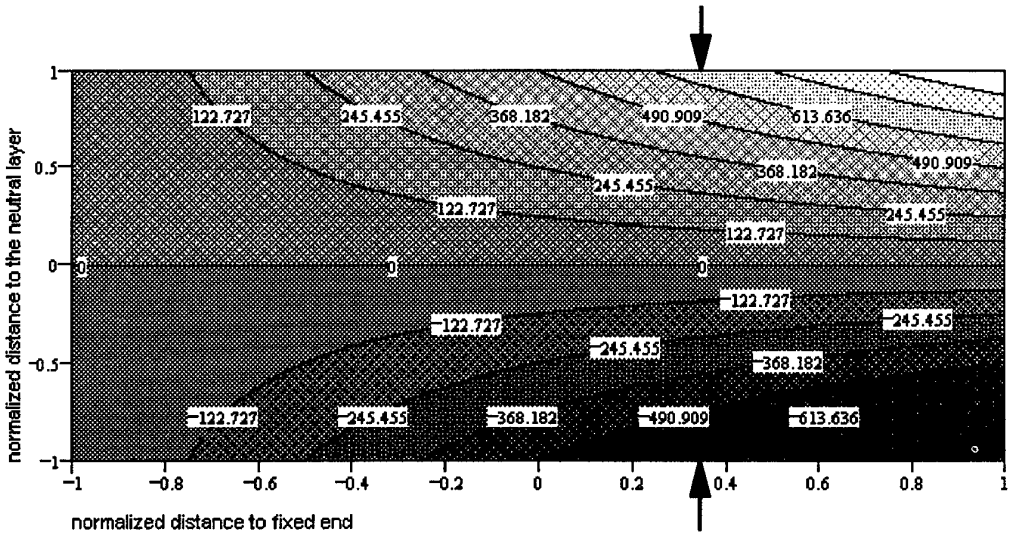

Fig.4 Theoretical strain distribution along the anchor rod, calculated by eq. (3). The solid lines are isolines of strain (in με) in the axial cross section of the rod geometry. The maximum strain levels from Fig. 3 measured experimentally by the wavelength-shift ($\Delta\lambda = \pm$ 600 pm $\Rightarrow \pm$ 600 με @ λ_B=1.3 μm) of embedded FBG (located at normalized position x=0.35) are marked by arrows.

Conclusions

First investigations on a glassfiber reinforced polymer rockbolt have proven that the newly-designed BGX sensor head can precisely measure applied static strains. Moreover, due to its geometry, the anchor rod shows also a sensitivity with respect to angular rotation. This experimental study will be followed by finite-element approaches to model numerically the response of the BGX rockbolt when embedded in the wall at the tunnel.

Additional types of rockbolts are currently under development, and will be applied for field measurements at various tunnel construction sites.

References

[1] A. D. Kersey, "A review of recent developments in fiber optic technology ", Optical Fiber Technol., vol. 2, 291 (1996)

[2] P. Ferdinand *et al.*, "Mine operating accurate stability control with optical fiber sensing and Bragg grating technology: The European BRITE/EURAM STABILOS Project", J. Lightwave Technol., vol. 13,1303 (1995)

[3] S. C. Blair *et al.*, "A new reflective optical extensometer (ROX) system for geomechanical deformation measurements ", Int. J. Rock Mech. & Min. Sci., 34:3-4, paper No. 029

[4] K. A. Heasley *et al.*, "Development of a fiber optic stress sensor ", Int. J. Rock Mech. & Min. Sci., 34:3-4, paper No. 066

[5] S. P. Timoshenko, J. N. Goodier, "Theory of Elasticity", McGraw-Hill, 1982

SURVEY OF US PATENT ACTIVITY IN OPTICAL FIBRE SENSORS

Z Y Zhang, K T V Grattan
Department of Electrical, Electronic and Information Engineering
City University, Northampton, London, EC1V 0HB

1. Introduction

A range of reports and most significantly several surveys of commercial optical fibre sensor technology have been carried out and published in recent years. In 1988 ERA Technology Ltd [1] issued a report to the Optical Sensors Collaborative Association (OSCA) in the UK on a world-wide survey of manufacturers in the field and in 1994 this work was extended in a further document [2] adding to the data available though a report based on interviews (mostly in the USA) and a questionnaire to major manufacturers. A number of other commercial organizations have produced reports and perspectives, often selling for several thousand dollars.

It is thus timely to survey the situation, not on the basis of responses to questionnaires or interviews, but using the rapidly developing availability of data obtained by electronic means, through E-mail and the Internet. Such techniques were much more in their infancy for previous reports, and their use removes some of the subjective factors relating to questionnaires. These include the extent to which full and solid responses were received (or not at all as the case may be), influencing the accuracy of the data obtained.

This led to the decision to focus heavily in this report upon patent information, being representative of both real commercial potential and exploitation and also being more readily quantifiable than much of the more research-oriented information available in the open scientific literature. The former is seen as being much closer to, or actually representative of the market, rather than showing the typical development period of perhaps up to 10 years that could be expected for the exploitation of more purely research data.

The aims and objectives of the approach were as follows:

- survey available data from a range of electronic sources from manufacturers, patent sources and researchers in the broad field of optical fibre sensor technology
- access and categorize this information in a meaningful form in relation to measurands, geographical factors and trends
- build upon previous work [1,2] in the presentation of the information. To that end, as far as possible, similar categorization criteria and headings were used and data are presented in summary and tabular form for ready access and comparison.

The results of the survey are presented together with an analysis of the data.

2. Results of the OFS product survey

2.1 *OFS suppliers*

An earlier report [1], which was completed in May 1988, identified over 213 companies as being potential manufacturers of OFS and information was obtained from over 100 of these. This work was updated in 1994 by Crossley [2], adding to the group of companies identified in 1987.

Up to this time, a total of around 350 companies have been revealed as potential OFS manufacturers or suppliers, with 101 of these companies actually located as OFS manufacturers. The geographical distribution of these OFS manufacturers shows that the USA is the dominant player in the OFS market under this criterion, with the UK and Europe a strong second.

2.2 *OFS sensor products*

The distribution of the OFS products offered by these 101 manufacturers located is illustrated in Figure 1, where sensors are categorized by their measurands. Of the 164 sensors whose details appear here, temperature (30), displacement (28) and pressure (12) sensors account for ~ 43%, with gas (12) and chemical (22) sensors, mostly based on absorption spectroscopy techniques and liquid level sensors (10), representing another 26% of the total. The remainder accounts for 31%. This shows no significant difference from the results of previous work[2] in spite of the updating of the data used.

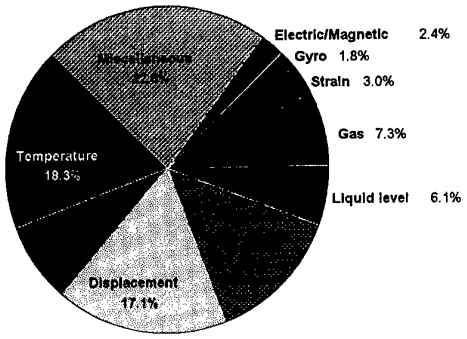

Figure 1: Measurand distribution of OFS products surveyed.

3. US patents in the OFS field

3.1 *Technology development mirrored by patents issued (1980-97)*

A total of 1310 US patents issued between 1980 to the end of 1997 have been located and identified to be in the field of optical fibre sensors. The numbers of such patents issued over these years are illustrated in Figure 2, on an annual basis. This has shown the general trend of a clear increase in the number of OFS patents issued each year from 1980 to 1994 (by almost an order of magnitude, over that period), followed by a noticeable decline thereafter.

Statistics gleaned from the patent information show that the average length of time from a patent application being filed to it being issued is about 2 years. Thus, the number of successful OFS patent applications filed each year could be estimated to follow the thick line in Figure 2. It indicates that the development of OFS technology was most active in the period around 1992. This may indicate a decline in investment in research and development in the late 1980s, feeding through in this way.

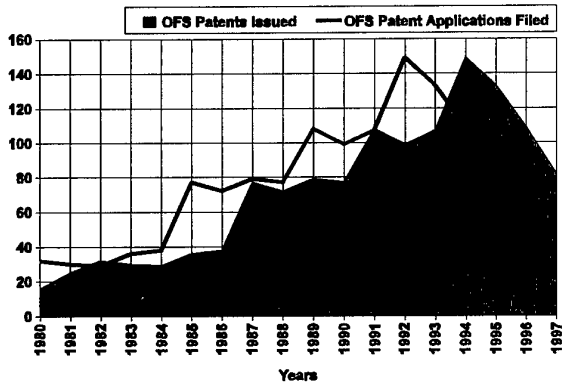

Figure 2: Numbers of US patents in OFS field issued from 1980 to 1997.

3.2 *Geographical distribution of OFS patent assignees (1994-97)*

Particular attention has been paid to the period of the 4 years from the start of 1994 to the end of 1997. There were 486 US patents issued from 1994 to September 1997 located in the OFS field, and the geographical distribution of their assignees, who normally are the owners of these intellectual properties, is illustrated in Figure 3 by countries of origin.

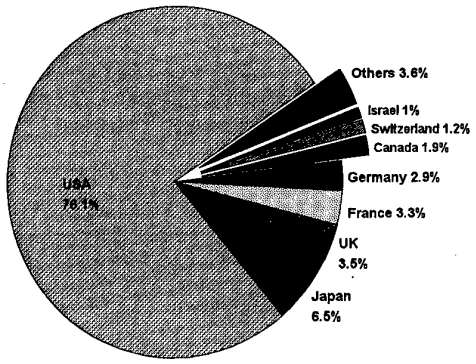

Figure 3: Geographic distribution of OFS patent assignees by countries.

This shows again that the USA is by far the biggest player in OFS technology development. Japan is second only to the USA with a share of 6.5%. The UK also has a significant impact but is contributing a mere 3.5% of those OFS patents, this being, however, a percentage slightly higher than those of any other of her European counterparts with France and Germany, as expected, being the other major contributors to an EU total of around 12%.

3.3 *Measurand distribution of OFS patents*

A further analysis of the data was carried out and a measurand distribution of those 486 OFS patents issued from 1994 to the end of 1997 is illustrated in Figure 4, where the patents are classified according to the measurands of interest.

There are several points to note:

- Patents which were not associated with a specific measurand and claimed to be of "general purpose", and those falling into the miscellaneous measurand category account for a total of 36.4% of those 486 OFS patents. This illustrates the great variety in the OFS devices and is characteristic of the technology itself;
- In contrast to the meager share (1.8%) for fibre optic gyros in the OFS product survey (see Figure 1), fibre optic gyro technology accounts for a very significant proportion (14.4%) of the total of the OFS patents surveyed. It is most probably due to the military origin of the early developmental work of this specific technology and an indication of the anticipated early market. With the exploitation of the technology in non-military applications, e.g. the car navigation gyro developed by Hitatchi Cable for Nissan Motors, more commercial fibre optic gyros are likely to appear in the market place and at comparatively high volumes;
- The figure shows the normalized (to 100% : annual total) measurand distribution of US patents in the OFS field issued over the years from 1994 to 1997, illustrating the comparative level interest of each. Noticeable is the rising trend in the chemical sensor field from 1995, and the significant proportion of strain/stress sensor patents being maintained over these years. Declines in the proportions of other measurands commonly encountered

in process control, e.g. liquid level, pressure and temperature are obvious, though temperature sensor technology has still attracted a relatively high level of interest following a decline from 1994 to 1995, possibly due to the interest in measuring temperature specifically to deconvolve its effect from that of other measurands.

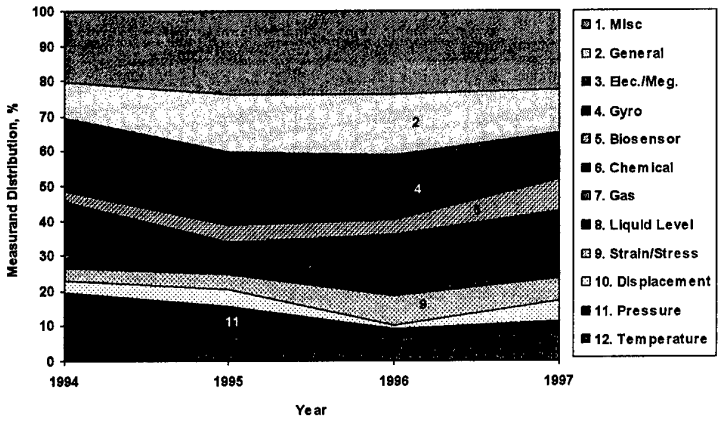

Figure 4: Measurand distribution of US patents in OFS issued over the years from 1994 to 1997.

4. Summary and Trends

It can be seen that displacement/position/proximity sensors have in the past contributed the majority of the revenue from fibre optic sensors, and it would appear likely that they will still do so, as stated by the Frost & Sullivan [3] report, at least in the short term. According to other data on sensor markets from BCC[4] recently published, the share of displacement/proximity sensors in terms of the worldwide OFS sensor revenues was 50% in 1993. The next important in revenue terms is the group of temperature sensors, which shared 15% of the revenues in 1993. The image depicted by the OFS technology development activities disclosed in the study reported herein shows the contrast between revenue earning and patent activity, where only 3.5% of US patents issued from 1994 are for displacement measurement compared to 8.4% for temperature sensing. BCC predicted that a rise in temperature sensor revenue to 18% will be seen in 1998, while the share of displacement/proximity sensors will decline to 45%. The most obvious lesson to be drawn is the time from patent activity to revenue stream, and the technology associated with many, if not most of the commercial displacement sensors is 'tried-and-tested', and the subject of patents of the early 1980s, for example. The BCC prediction is for a trend away from the dominance of displacement sensors, and this is confirmed in the current patent activity, which will be reflected more closely in market share over the next decade, it is expected.

An interesting 'snapshot' of activity is seen in the analysis of papers presented the major International Conference in the field at the end of 1997, coinciding with the end point of this survey. Among all the technical papers presented in the 12th International Conference on

Optical Fibre Sensors (OFS'12) held in Williamsburg, Virginia, more than 28% were dedicated or related to FBG technology. Consequently, strain was the most discussed measurand at the OFS'12.

These statistics illustrated in Figure 5 compare interestingly with Figure 4, showing patent activity over the recent period. It can be seen that research activity, of which they are representative, correlates more closely to patent activity than do sales and associated revenue generation, based as they are on "older" technology. This clearly shows the trends for the future - not all patents will be products - but some will, and be commercial successes with their impact on revenues for the first decade of the 21st century.

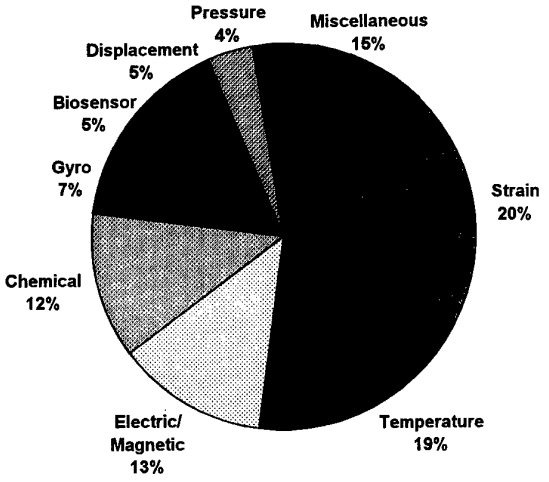

Figure 5: Distribution of papers presented in OFS'12 by measurand-of-interest.

Acknowledgement

The authors are pleased to acknowledge the support of the Optical Sensors Collaborative Association (OSCA) and their permission to publish this work.

References

1. ERA Technology Ltd, Report to Optical Sensors Collaborative Association, Chislehurst, Kent, UK (1988)
2. Crossleys, Report to Optical Sensors Collaborative Association, Chislehurst, Kent, UK (1994)
3. Frost & Sullivan, Commercial Report, 2525 Charieston Road, Mountain View, CA 94043 USA (1997)
4. Business Communications Co. Inc., 25 Van Zant Street, Norwalk, CT 06855 (1997)

Optical Fiber and Integrated Optics Accelerometers for Real Time Vibration Monitoring in Harsh Environments: In-Lab and in-Field Characterization

J. M. López-Higuera, P. Mottier, *A Cobo*, E. Ollier, *M. A. Morante*, Cl. Chabrol, *F. J. Madruga*, & P.Philippe.

Photonics Engineering Group /University of Cantabria
Avda. los Castros s/n, E-39005 Santander (Spain)
Tel.: +34-42-201498; Fax: +34-42-201873
e-mail: higuera@teisa.unican.es

LETI/CEA/Département de Microtechnologies
CEA-Grenoble, 38054 Grenoble Cedex 9, France
Tel.: 33 4 7688 57 35; Fax: 33 4 7688 94 56
e-mail: Patrick.Mottier@cea.fr

Introduction

The reliability of rotating machines such as electrical generator is critical to the overall reliability and operation of electrical power plants. The very high cost of these machines, makes it necessary to improve the lifetime of a wide set of currently installed hydrogenerators around the world and avoid costly maintenance [1]. Vibration monitoring is essential in maintenance and protection programs [2]. However, due to the harsh environment (high electromagnetic fields and high temperature) and the very low frequency spectrum of the vibrations, the above mentioned machines cannot be appropriately monitored by piezoelectric sensors. Several approaches of optical sensors have been already developed either in fiber optics [3], or combination of optical fiber with silicon microstructures [4] or in integrated optics [5], but because of technical or economic reasons, up to now, these sensors are not fully suited for the above-mentioned applications.

In this paper both optical fiber and integrated optics accelerometers developed in order to satisfy specifications required for these applications are presented. Their developments were a part of a European project dedicated to real time defect detection and predict forthcoming failures of a generator group in an electric power plant in Spain. In- laboratory and in-field tests are reported.

Sensor System Description

The systems are basically composed of a transducer head and of an analogue electronic unit linked by optical fibers. Both sensors are based in the same modulation technique but the transducers are developed in fiber optic technology for low frequency vibrations (shaft bearing), and in integrated optics technology for the medium frequency range (winding).

They detect vibration levels by means of a moving fiber or of an integrated waveguide in cantilever configuration that modulates the transmitted light intensity through two output fibers or two integrated waveguides, according to the acceleration of the place where are located. After the corresponding modelisations [7, 5], the optical sensor heads were fabricated. The optical path and the seismic mass of the integrated transducer were made of the same silica material using the integrated optics LETI's technology. Three silica layers with different phosphorus

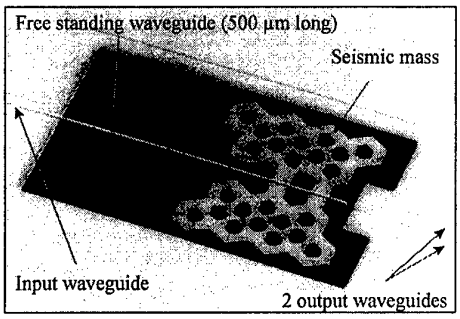

Figure 1. A SEM photograph of the optical transducer developed in integrated optic technology.

doping levels were used to define the waveguide structure. The device was fabricated in five main steps. The first step is the optical path fabrication. It is performed using PECVD and reactive ion etching technology. The second step is the mechanical structure fabrication.

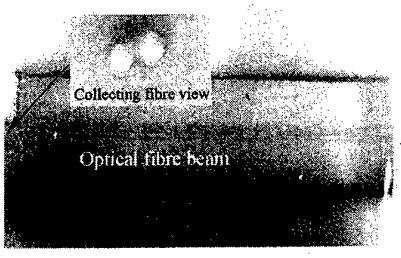

Fig.2.- Nomarski optical photograph of the optical fiber transducer head

This step is divided in two parts: RIE anisotropic etching of the three silica layers (about 15 microns thick) and anisotropicetching of silicon using an isotropic reactive ion etching. Groves for sturdy fiber connection were simultaneously etched in front of the input and output waveguides. A photograph of the sensitive part of the transducer (developed is shown in figure 1.

The main components of he optical fiber transducer head are the input optical fiber cantilever, the two receiving fibers and the housing, as is depicted in Fig. 2. The optical fiber transducer head has been fabricated using only insulated materials. The optical fibers (100/140 type) were positioned on an aluminum plate that had laser micromachined grooves suitably dimensioned and aligned, and they were led to their exact place with the help of a four-degree-of-freedom micropositioning system. They were fixed by means of a low shrinkage optical adhesive that meets U.S. Federal Specification Mil-A-3920. Apart from curing them with ultraviolet light, the optical heads were subject to temperature shocks in an *ACS* Hygros-15 climatic chamber, in order to reduce the infantile life period as much as possible.

The optoelectronic unit is the part of the sensor system that generates, receives and processes the optical signals occurring in the acceleration transduction. It communicates with the optical head by means of a fiber optic link so it can be located far away if the transducer operates in a harsh environment. The basic functions are: generation of the optical signal sent to the transducer, detection and pre-amplification of the return optical signals, differential processing, band-pass filtering, and conditioning of the output signal to its output scale. The light generation subsystem consists of a optical source and its driving electronics. An LED diode and a laser diode were chosen as the light sources for the optical fiber and the integrated optic sensor respectively.

Commercial low cost PIN photo-detectors, pre-amplifiers, processing, filter, and another electronic components were used for the implementation of the opto-electronic unit. Because of the differential nature of the processing carried out on the 2 optical intensities the output signal (voltage following the acceleration on the transducer) is compensated for environmental and other undesirable perturbations.

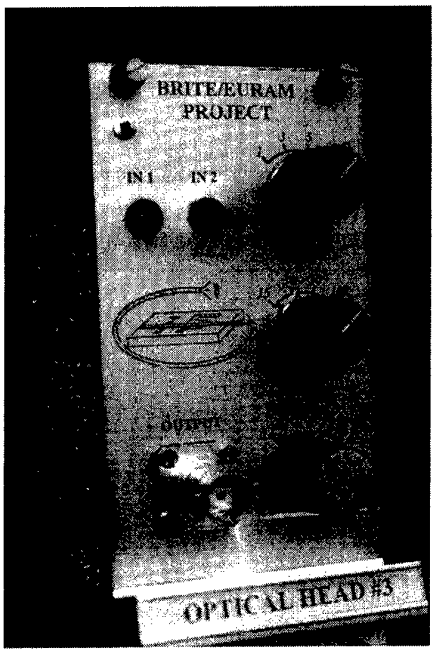

Fig. 3 . Photograph of one plug-in optoelectronic unit.

In figure 3, a view of one plugging optoelectronic module is shown. For its installation in the power plant, six optical fiber sensor heads for low frequency shaft-bearing and three integrated optics sensor heads for winding vibration monitoring were fabricated and their associated electronic boards, including their power supply, were integrated in a 19'' rack. A custom optical channel that meets the requirements of international specifications such as B56724 and VDE-0207 was built to link the 19'' rack with the optical distribution boxes at each turbine level, and to connect the sensor heads to these boxes.

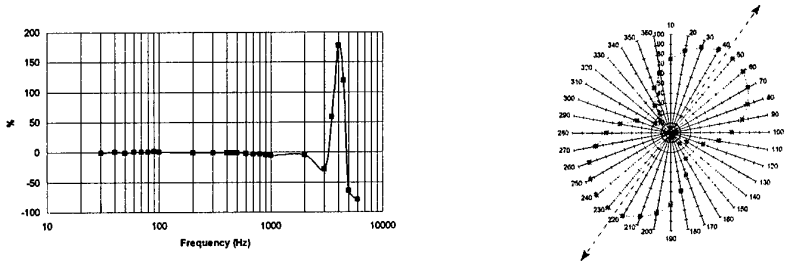

Fig. 4 Examples of in-lab Characterization: frequency response and transverse sensitivity of the integrated optic transducer

The system was fully tested and calibrated in the laboratory prior to its installation in the plant. The frequency response and the transverse sensitivity of the integrated sensor head are shown in figure 4.

Field Operation

The system was installed and fixed for its operation in the hydroelectric plant for more than one year, and, since that time, it has been working continuously. Figure 5 shows a view of accelerometer for winding monitoring.

The signal generation and detection unit for the optical sensors was located 40 meters away from the turbine, where the intensity of the electromagnetic field is no more significant.

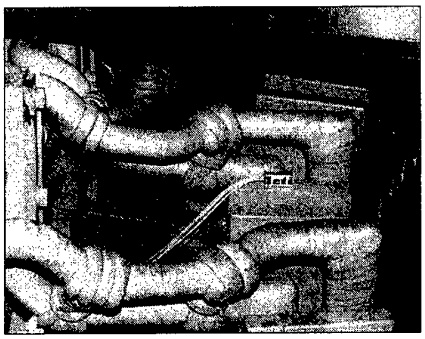

Fig.5. Integrated sensor head installed on the winding of a hydrogenerator.

Figs. 6a and 6b, show a picture of the vibration spectrum of both accelerometers in the same working generator machine conditions. Improvements of some parts of the optical accelerometers were done according with the field obtained data. At last the technical characteristics of the developed and validated sensor systems are summarized in table I.

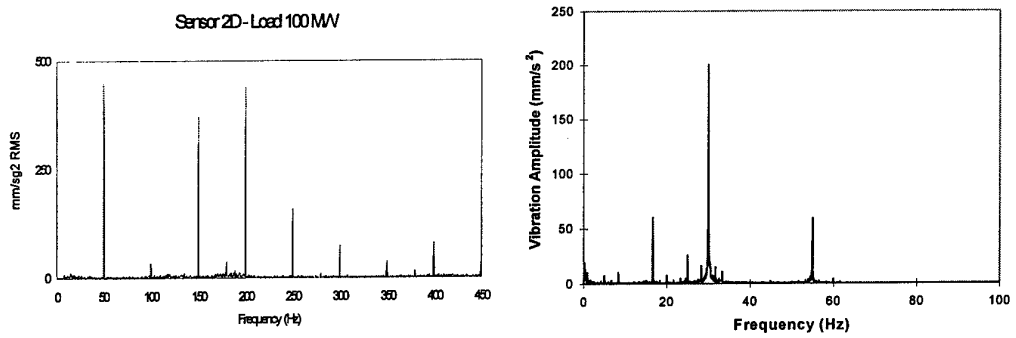

Fig, 6. Winding (a) and shaft bearing (b) vibration spectral features obtained in one field test

Characteristics	Integrated optic	Fiber optic
Frequency range	30-2000 Hz	0.2-140 Hz
Frequency response	<±5%	<±5%
Amplitude range	0.5-600 m/s^2	0.025-10m/s^2
Amplitude linearity	<1%	0.04% (0...1G)
Resolution	0.5 m/s^2	0.02m/s^2
Transverse sensitivity	<5%	<4%

Table I. Summary of the final behaviors of both sensor systems developed.

Conclusions

An optical accelerometer system composed of six fiber low frequency, and three integrated optics medium frequency transducer heads has been fully developed and tested, both in-lab and in-field conditions with very good agreement with their specifications.

The long-term stability of the system was surveyed. The signals from the optical sensors were analyzed for a long period in which the generator group operated in actual production conditions, and no significant time drift has been found, what validates the system for real time field operation in a harsh environments.

At last, many potential similar applications could be considered such as pressure sensor, microphone.... for applications to electrical power nuclear or chemical plants.

Two patents related to this work are pending.

Acknowledgement

This work has been partly funded by the European Economic Community and the Spanish CICYT Commission through the Brite Euram 7289 and the TIC95-0631-c0401 projects respectively. The authors are grateful to the European partners. The industrial power is managed by Iberdrola (Spain).

References

[1]F. Arregui, C. Mazzieri, C. Pantaleón, E. Gómez, P. Mottier, J. Marcou, J.L. García, I. Santamaría, J.M. López Higuera, F. Viadero, "Protection an d monitoring system for hydroelectric generating sets", EUROMAINTENANCE'96, Copenhagen (Denmark), May 1996.

[2] H. P. Bloch and F. K. Geitner, "Machinery Failure Analysis and Troubleshooting", 2nd Edition, Gulf Publishing Company, Houston, Texas, 1994.

[3] D.R. Miers, D. Raj, J. W. Berthold, "Design and characterisation of fiber optic accelerometer" Fiber optic and laser sensor V, Proc. Soc. Photo-Opt. Instrum. Eng. 938, pp 421-423, 1987.

[4] A. Malki, P. Lecoy, j. Marty, c. Renouf, P. Ferdinand, "Optical fiber accelerometer based on a silicon micromachined cantilever", Applied optics, vol 34, N°34, pp 8014-8018, 1995.
[5] M. Hoffmann, H. Bezzaoui, E. Voges, "Micromechanical cantilever resonators with integrated optical interrogation", Sensors and Actuators A, 44, pp 71-75, 1994.
[6] E. Ollier, P. Philippe, E. Entressangle, C. Chabrol, P. Mottier, "Micro-opto-mechanical vibration sensor integrated on silicon", MOEMS'97, Nara (Japan), November 18-21, 1997.
[7] J. M. López-Higuera, M. A. Morante, and A. Cobo, "Simple low-frequency optical fiber accelerometer with large rotating machine monitoring applications", to be published in the IEEE Journal of Lightwave Technology, July 1997.

Applications for optical fibre sensors in gaseous electronics

G.A. Woolsey[1] and G.B. Scelsi[2]

Division of Physics and Electronics Engineering

University of New England, Armidale, NSW 2351, Australia

[1] Tel: +61 2 6773 3450 Fax: +61 2 6773 3413 Email: gwoolsey@metz.une.edu.au

[2] Tel: +61 2 6773 2426 Fax: +61 2 6773 3413 Email: gscelsi@metz.une.edu.au

1. Introduction

Optical fibre sensors have many attributes that make them attractive for diagnostics in gaseous electronics systems involving electrical discharges and plasmas. These systems often use high voltages and generate electromagnetic noise, so that optical fibres have advantages over the more conventional electric and magnetic probes used to measure discharge parameters. The small fibre dimensions are a further advantage in that they allow much better spatial resolution than measuring techniques such as optical spectroscopy and light scattering. Furthermore, the facility for remote sensing provided by optical fibres can be particularly useful when working with large-scale fusion plasmas and high voltage sparks.

Electrical discharges and plasmas come in numerous forms, and have wide practical application. Low pressure dc and pulsed glow discharges are used as light sources and are the fundamental unit in most forms of gas discharge laser. Coronas, which are produced at high voltage points or along fine wires, provide the ion charge in photocopiers and laser printers, and the ozone in air purifiers. High voltage corona wires generate the charge for the electrostatic precipitators used to extract particulate matter from flue gases. Coronas are a recurring problem in high-voltage switchgear and it is important to be able to detect them in order to minimise damage to conductors and insulators and to prevent their development to catastrophic electrical breakdown. High current dc and ac arc discharges are used as high-intensity light sources and in welding, while rf-induced plasmas are being exploited for plasma processing; and of course, high-current, high temperature, magnetically-confined plasmas provide the best hope for controlled nuclear fusion. In all of these, it is necessary to be able to measure, control and monitor the critical electrical parameters of current, voltage, electric field and charge concentration, as well as the gas properties of temperature, pressure, flow rate and chemical composition.

Apart from our work at the University of New England, the application of optical fibre sensors to gaseous electronics systems has been limited to some early measurements of fusion plasma current using Faraday rotation [1,2], and a range of monitoring probes for circuit breakers developed by Professor G. R. Jones and his group at the University of Liverpool [3,4,5]. We have applied established optical fibre sensing techniques to the study of dc glows, dc coronas and rf plasmas, and have developed some new sensors specifically for discharge study. This paper provides a review of our work.

2. Temperature

In dc gas discharges, gas temperature data are significant, because in conjunction with information on gas pressure, they allow gas densities (N) to be determined. N, in turn, when combined with measurements of electric field (E), allows the ratio E/N to be calculated. E/N is a critical parameter in discharge physics since it controls the electron energies and hence the rates of gas ionisation and excitation. For a glow discharge with cylindrical symmetry, we have used a Fabry-Perot interferometer sensor to measure the integral of the temperature along different chords of a discharge cross-section, and by carrying out Abel transformations, to produce temperature distributions as in Fig. 1 [6]. A fibre temperature probe has been used also in a highly ionised plasma, such as that used in fusion studies, to measure the ion temperature.

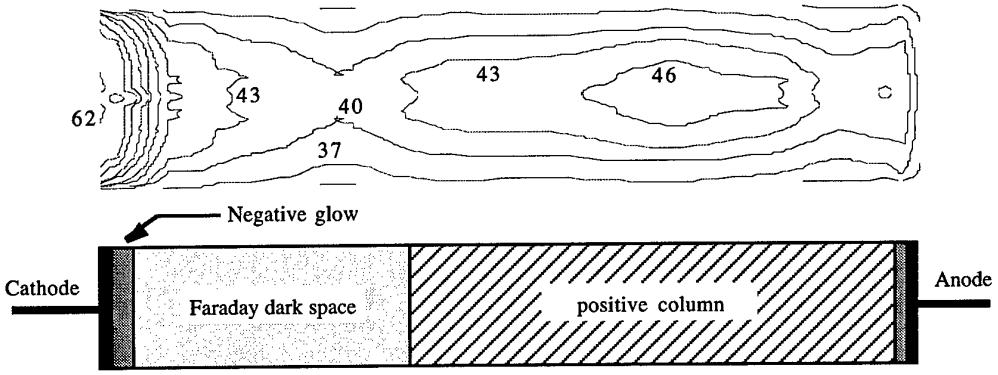

Fig. 1 Axial temperature profile measured in a glow discharge in Argon: pressure = 1 Torr, current = 4 mA, voltage = 370 V, electrode spacing = 150 mm, electrode radius = 21 mm. Temperature contours are labelled in °C.

3. Electric Field/Charge

The significance of electric field measurement in discharges was discussed in §2. An established optical fibre sensing technique for electric field measurement is that of bonding the sensing arm of an interferometer fibre to a film of piezoelectric material, or coating the fibre arm with the material. We have made measurements of electric field in an air corona with this method using a film of polyvinylidene fluoride (PVDF) [7]. We are now working on a double integrating probe, where one arm is coated with PVDF. Simultaneous measurement of temperature and electric field will allow E/N distributions to be determined.

To obtain useful sensitivity with a piezoelectric probe, an active sensor length of several mm is needed, and this limits the spatial resolution. As an alternative, we have developed an electric field sensor which relies on the deflection of a small cantilever [8]. This sensor is based on the principle of the gold-leaf electroscope, and is interrogated in the same way as an optical fibre pressure sensor involving deflection of a membrane. The sensor details are shown in Fig. 2.

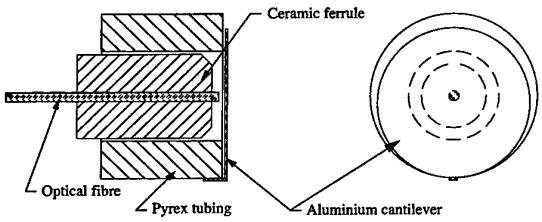

Fig. 2. Structure of the electric field sensor.

When the sensor is placed in an electric field, induced charging produces deflection of the cantilever, which is measured using low-coherence Fabry-Perot interferometry. The sensor has been used to measure electric fields in the vicinity of a Van de Graaff generator, within a pair of plane-parallel plates and in a point-plane gap similar to that used to produce coronas [9]. Whereas the final cantilever deflection in the corona is a function of the local electric field, the time taken to reach the equilibrium charge condition depends on the charge concentration in the vicinity of the sensor. This fact will be exploited to measure charge-density distributions generated, for example, by a corona discharge. Presently we are seeking to miniaturise the sensor to provide a probe with dimensions of less than a mm.

4. Gas Flow

In a corona discharge produced at a high-voltage point, ions of the polarity of the point move rapidly away from it, and transfer their momentum to neutral gas molecules to produce a jet-like flow known as the corona wind. The corona wind plays a role in electrostatic precipitators and has applications for localised heat transfer. Because of the high voltages and large charge densities in the corona environment, measurement of the speed of the corona wind has always been difficult using conventional flow sensing techniques. Our flow sensor has been successfully applied to laboratory coronas in air [6] and in sulphur hexafluoride (a gas widely used for insulation in high voltage systems) and to an electrostatic precipitator [10].

The principle of the sensor is illustrated in Fig. 3. A pulse of CO_2 laser radiation heats a short length of the fibre (2-4 mm) in a Fabry-Perot interferometer arm. The corona wind cools the fibre by forced convection so that the temperature rise of the fibre, and hence the interferometer phase shift, is a function of the speed of flow. Absolute data are obtained through calibration or analysis of the heat balance of the system. The sensor has been used successfully to obtain three-dimensional profiles of corona wind speed in air and SF_6 coronas. Indeed, our data on SF_6 are the first on this gas: other sensors for corona wind speed measurement cannot be used in a vacuum vessel, and so are suitable only for studies in atmospheric air.

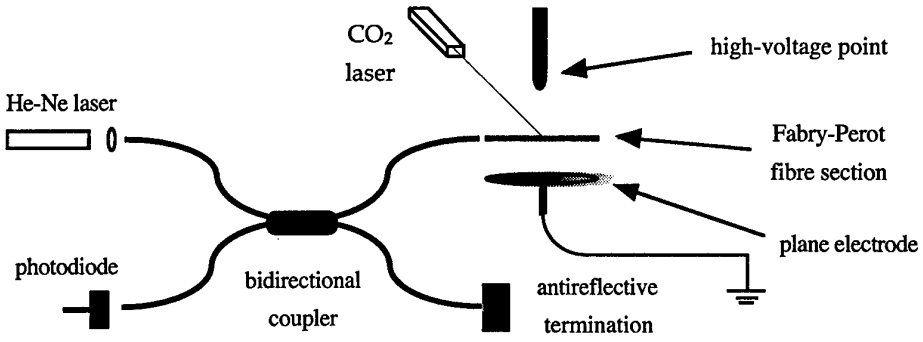

Fig. 3 Corona wind sensor.

5. Gas decomposition

Most gas-insulated switchgear use high pressure SF_6 as the insulating medium. Switching arcs and unwanted low-current coronas which occur from time to time in these devices cause some dissociation of the SF_6, which leads to degradation of insulating efficiency. It is important therefore to monitor the level of SF_6, in order to be able to shut down the system before a catastrophic breakdown occurs. We have developed two optical fibre techniques which have the potential for monitoring practical SF_6-insulation systems. One is for sulphur, a product of the degradation process in SF_6 discharges: the sulphur deposits onto any surface adjacent to the discharge. The level of deposition can be monitored by measuring evanescent-wave absorption of light transmitted through a fibre in or near the discharge. Using both white light and 633 nm laser radiation with silica fibres, we have been able to examine the rate of sulphur deposition [11]. The second sensor monitors the SF_6 gas concentration by evanescent-wave attenuation using a silver halide fibre and the 10.6 μm radiation of a CO_2 laser. This exploits the strong infra-red absorption of SF_6 at 10.55 μm. This sensor has revealed, for example, that the level of SF_6 falls at a rate of 2% per day in a typical SF_6 corona [12].

6. Conclusion

Many of the discharge/plasma parameters discussed here can be measured in other ways, but clearly, the major advantage for gaseous electronics systems of the optical fibre sensors described above is their immunity to high voltages and electromagnetic noise. This should make them attractive to the gaseous electronics community, and indeed, following some early resistance, we feel that acceptance of optical fibre sensing by researchers in discharge/plasma fields is starting to occur. We now need to convince those involved in the development and manufacture of gaseous electronics devices, such as photocopiers, static control systems, electrostatic precipitators, discharge lamps, gas lasers and circuit breakers, of the virtues of optical fibre sensing.

Acknowledgements

We are very appreciative of the contributions of our postgraduate students: Kate Jones, Dragan Vukovic, Tim Priest and Vernie Everett, and technical officer: Graham Hyde.

References

[1] G.I. Chandler, and F.C. Jahoda, Rev. Sci. Instrumen. **56**, 852-854, 1985.

[2] G.I. Chandler, P.R. Forman, F.C. Jahoda and K.A. Klare, Appl. Opt. **25**, 1770-1774, 1986.

[3] L. Issac, J.W. Spencer, J. Humphries, G.R. Jones and W. Hall, in *Proc. 12th Int. Conf. on Gas Discharges and their Applications*, 86-89, Greifswald, 1987.

[4] M.G. Ennis, J.W. Spencer, D.R. Turner and G.R. Jones, in *Proc. 12th Int. Conf. on Gas Discharges and their Applications*, 123-126, Greifswald, 1987.

[5] J. Cosgrave, J.E. Humphries, J.W. Spencer, G.R. Jones, P.C. Russell, W. Hall and K.G. Lewis, in *Proc. 12th Int. Conf. on Gas Discharges and their Applications*, 512-515, Greifswald, 1987.

[6] V. Everett, K.T. Jones, G.B. Scelsi and G.A. Woolsey, Aust. J. Phys. **48**, 527-541, 1995.

[7] G.A. Woolsey, D.W. Lamb and M.C.H. Woerner, in *Fibre Optic and Laser Sensors IX* (Eds: R.P. DePaula and E. Udd), Proc. SPIE 1584, 243-253, 1991.

[8] T.S. Priest, G.B. Scelsi and G.A. Woolsey, Appl. Opt. **36**, 4505-4508, 1997.

[9] T. Priest, G.B. Scelsi, and G.A. Woolsey, Proc. OFS-12, 241-244, Williamsburg, 1997.

[10] G.B. Scelsi, K. T. Jones, G. A. Woolsey, and R. Morrow, Proc. OFS-11, 120-123, Sapporo, 1996.

[11] G.A. Woolsey, D. Vukovic and G.B. Scelsi, Proc. OFS-11, 474-477, Sapporo, 1996.

[12] D. Vukovic, G.B. Scelsi and G.A. Woolsey, Proc. OFS-12, 269-272, Williamsburg, 1997.

Comparison between Flint Glass Fiber and Twisted/Bent Single-Mode Fiber as a Faraday Element in Interferometric Fiber Optic Current Sensor

K. Hotate, Bao T. Thai, and T. Saida

Department of Electronic Engineering, School of Engineering, The University of Tokyo
7-3-1 Hongo, Bunkyo-ku, Tokyo 113-8656, Japan
Phone: +81-3-5684-3264, Facsimile: +81-3-5684-3643, Email: hotate@sagnac.t.u-tokyo.ac.jp

1 Introduction

All-fiber current sensor based on the Faraday effect has significant advantages over the conventional current sensors, including a high electric insulation, an immunity to electromagnetic interference, a wide dynamic range, a small size and a low cost. The configuration of all-optical fiber-optic current sensor can be classified into polarimetric-type[1] and interferometric-type[2][3]. The polarimetric-type measures the polarization state changes through the sensitive fiber, while the interferometric-type measures the nonreciprocal phase differences of counter- or co-propagating waves through the sensitive fiber.

The interferometric fiber-optic current sensor, employing the phase modulation/demodulation schemes developed for use in the interferometer fiber optic gyro, has a possibility to achieve high sensitivity of μ rad phase differences. The major difficulties are sensitivity to time-varying mechanical and thermal disturbances (Shupe effect errors), and scale-factor quenching due to intrinsic and bend-induced birefringence in the sensitive fiber. The Shupe effect errors can be suppressed by employing an in-line Sagnac reciprocal interferometer[3]. On the other hand, the scale-factor quenching has been overcome by twisting the sensing fiber. When the bending radius is less than 10 cm, however, this contermeasure is not enough to realize a stable sensitivity, as shown in this paper.

Recently, a flint glass fiber has been developed for use in the fiber-optic current sensor jointly by Tokyo Electric Power Company and HOYA[4]. The flint glass fiber has a small intrinsic linear birefringence ($\sim$1.2 degree/m), extremely small photo-elastic constant ($\sim$-6×10^{-15} /Pa), and a large sensitivity to magnetic field (Verdet constant is about 3.8×10^{-6} rad/A turn@1.55 μm)[4]. Compared with a silica glass, the photo-elastic constant is about thousandth smaller, and the Verdet constant is about 6 times larger. Hense, the fiber-optic sensor employing the flint glass fiber as the sensing fiber has a stable and high sensitivity, and is insensitive to bend-induced birefringence. In addition, due to its diamagnetism, temparature dependance of the Verdet constant in the flint glass fiber is small. These advantages of the flint glass fiber has already been confirmed in the polarimetric configuration[1].

In this paper, we demonstrate, for the first time, an interferometric fiber-optic current sensor employing the flint glass fiber. Performance in the proposed system are discussed. The scale factor of the interferometric sensor with a twisted/bent single mode fiber is analyzed considering both the intrinsic birefringence and the bend-induced birefringence. It is shown that the system with the fling glass fiber has more stable scale factor compared with the ordinally system with the twisted/bent fiber. Experimental results are also shown.

2 System configuration

The developed system is shown in Fig.1. We have adopted an in-line Sagnac interferometer configuration[2][3], being combined with the flint glass fiber. Light from a superluminescent diode (SLD) is directed to a polarizer through a single mode 3dB coupler. The resulting linearly polarized light, via a 45 ° polarization-axis tilted splice between the polarizer and a polarization maintaining (PM) fiber, excites equally x and y polarization modes in the PM fiber. The portion of the PM fiber

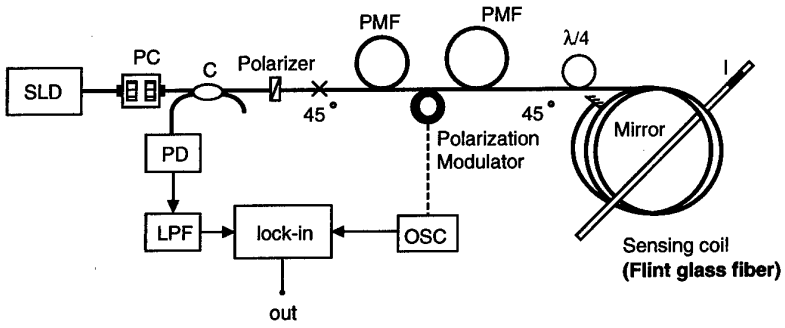

Figure 1: Experimental configuration of in-line Sagnac interferometer fiber-optic current sensor employing flint glass fiber.

prior to a polarization modulator is for decreasing the bias resulting from the parasitic polarization coupling modulation in the polarization modulator[3], while the portion posterior to the polarization modulator is for decreasing the bias resulting from the intrinsic linear birefringence in the sensing fiber. Here, the polarization modulator is driven with sinusoidal waveform for the quadrature detection scheme. These orthogonal linear polarizations are converted to right and left hand circular polarization (RHCP and LHCP), respectively, by a quater wave plate (QWP). The RHCP and LHCP light waves go through the flint glass fiber used as the sensing fiber, experiencing the phase shift due to the Faraday effect. When they reflect at the mirror located at the end of the flint glass fiber, their states of polarization are swapped (RHCP becoming LHCP and vice versa), and they retrace their way through the flint glass fiber. Since the Faraday effect is nonreciprocal, the phase difference between the both waves is doubled on their return trip. They are returned to linear polarization states at the QWP, and coupled to the photo detector via the PM fiber and the 45 ° tilted splice. Because the outbound wave in x-axis in the PM fibers returns along y-axis and the outbound wave in y-axis returns in x-axis, the phase difference resulting from the polarization mode dispersion in the PM fiber are completely compensated[2]. The phase difference between their waves, due to the Faraday effect in the flint glass fiber, is demodulated by a lock-in amplifier. The phase differnce, $\Delta\phi$, can ideally be written as$\Delta\phi = 4VNI$, where N is the number of turns of the sensing fiber, and I the current carried in the wire.

3 Scale factor stability

Although the sensitivity of the current sensor is required to be stable, the intrinsic and bend-induced birefringence quenches the scale factor. We evaluate the scale factor by the Jones matrix calculations.

System with flint glass fiber

The flint glass fiber can be treated as a birefringent fiber with an extremely low birefringence. In this case, the scale factor F can be written as $F = \sin\Delta\beta_0/\Delta\beta_0$[3], where $\Delta\beta_0$ is the linear birefringence in the flint glass fiber. The scale factor, calculated as a function of the linear birefringence, is shown in Fig.2, where the sensing fiber length is assumed to be 3 m. Since typical value of the birefringence in the flint glass fiber is 1.2 °/m, namely the beat length is 300 m, it can be seen that the scale factor of 99. 7 % is achievable.

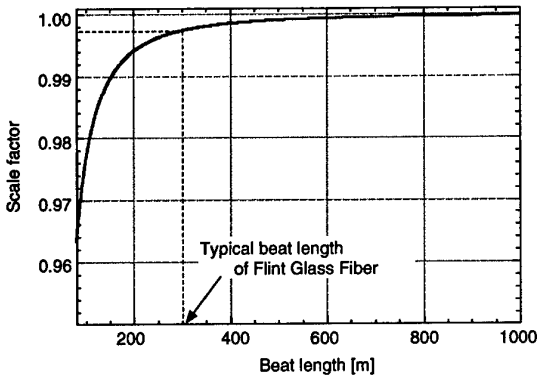

Figure 2: Scale factor performance of in-line Sagnac interferometer fiber-optic current sensor employing the flint glass fiber as a function of linear birefringence in the sensing fiber.

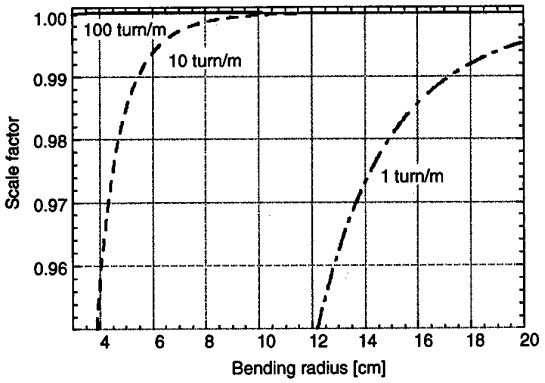

Figure 3: Scale factor performance of in-line Sagnac interferometer fiber-optic current sensor employing twisted/bent fiber as a function of bending radius of the sensing coil.

System with twisted fiber

In the calulation of the scale factor in the system employing the twisted/bent fiber, we must distinguish the bend-induced birefringence from the intrinsic birefringence, because the bend-induced birefringence is fixed to the space, while the intrinsic birefringence rotates along the fiber with twisting.

Using the coodinate (x, y) that chases the local birefringence axis of the fiber, the polarization properties of the twisted/bent fiber can be written as

$$\begin{aligned}
\frac{d}{dz}\begin{pmatrix} E_x \\ E_y \end{pmatrix} &= -\mathrm{j}\begin{pmatrix} \Delta\beta_{total} & 0 \\ 0 & -\Delta\beta_{total} \end{pmatrix}\begin{pmatrix} E_x \\ E_y \end{pmatrix} + \begin{pmatrix} 0 & -(\Phi-\phi\alpha) \\ (\Phi-\phi\alpha) & 0 \end{pmatrix}\begin{pmatrix} E_x \\ E_y \end{pmatrix}, \quad (1) \\
\Delta\beta_{total} &= \sqrt{\Delta\beta_0^2 + \Delta\beta_{bend}^2 + 2\Delta\beta_0\Delta\beta_{bend}\cos(2\phi z)}, \\
\Phi &= \frac{1}{2}\frac{d}{dz}\left[\tan^{-1}\left(\frac{\Delta\beta_0 \sin 2\phi z}{\Delta\beta_0\cos 2\phi z + \Delta\beta_{bend}}\right)\right],
\end{aligned}$$

where ϕ is the twisting angle per unit length, α is the optical activity, $\Delta\beta_0$ is the intrinsic linear birefringence, and $\Delta\beta_{bend}$ is the bend-induced birefringence[5]. Here, $\Delta\beta_{total}$ means the net linear birefringence, and Φ means the rotation angle of the net linear birefringence. Solving Eq. (1) numerically, we can obtain the scale factor of the system as a function of the bending radius, as shown in Fig.3. In Fig.3, we assume that the sensing fiber length is 3 m and the intrinsic birefringence is $\pi/15$ rad/m. The scale factor when the twist rate is 100 turn/m, 10 turn/m, and 1 turn/m are shown

in the figure. We can see that, for the scale factor better than 0.997, the bend radius needs to be larger than 20 cm if the twist rate is 1 turn/m, and larger than 7 cm if the twist rate is 10 turn/m. In the case that the twist rate is 100 turn/m, which is the physical limit of twisting, quenching in the scale factor is hardly observed. However, highly twisted fiber has difficulty in treating, and tends to untwist over time.

4 Experiments

We have carried out, for the first time, the experiments of the interferometric fiber optic current sensor with the flint glass fiber. The setup is shown in Fig.1. The length of the sensing fiber is set to be 3.6 m, which is the optimum length determined by the loss of the flint glass fiber of 1.2 dB/m. A fiber-wrapped piezoelectric ring modulator is used as the polarization modulator, whose

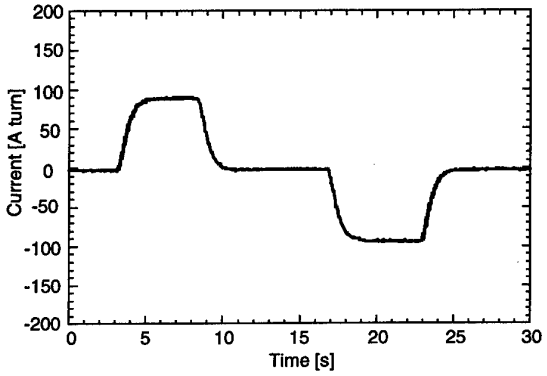

Figure 4: Current Measurement performed by the interferometric fiber optic current sensor with the flint glass fiber.

drive frequency is 22 kHz. The length of the PM fiber prior to the polarization modulator is 15 m, while that posterior to the polariztation modulator is 200 m. The length of the former PM fiber can be shortened by employing higher modulation frequency. It should be noted here that the length of the PM fiber is set to avoid subpeaks in the optical coherence function of the SLD. In this system, the detected optical power is about 200 nW, corresponding to the shot-noise limited sensitivity of 2.3 μrad with 3.3 Hz bandwidth.

The result of the current measurement is shown in Fig.4, where the wire coil is used as the current carrying conductor to simulate large values of current. In Fig.4, the current of about 90 A·turn is clearly measured, while the minimum sensitivity is less than 0.3 A·turn.

5 Conclusion

We newly developed an interferometic type fiber-optic current sensor using the flint glass fiber. Numerical analysis has been done, considering both the intrinsic birefringence and the bend-induced birefringence of an ordinary single mode fiber. The analysis told us that the configuration with the flint glass fiber can realize exceptionally stable scale factor compared with the conventional one with twisted/bent single mode fiber. Experimental demonstration with the flint glass fiber were also shown.

The authors would like to thank Dr. Kurosawa of Tokyo Electric Power Company and Dr. Yamashita of HOYA for providing the flint glass fiber.

References

[1] K. Kurosawa, "Optical Current Transducers Using Flint Glass Fiber as the Faraday Sensor Element," Proc. *OFS-11*, We1-S3, pp. 134-139, 1996.

[2] G. Frosio and R. Dändliker, "Reciprocal reflection interferometer for a fiber-optic Faraday current sensor," Appl. Opt., vol. 33, pp. 6111-6122, 1994.

[3] J. Blake, P. Tantaswadi, and R. T. de Carvalho, "In-Line Sagnac Interferometer Current Sensor," IEEE Trans. Power Delivery, vol. 11, pp. 116-121, 1995.

[4] T. Yamashita, A. Watabe, I. Masuda, K. Sakamoto, K. Kurosawa, and S. Yoshida, "Extremely Small Stress-Optic Coefficient Glass Single Mode Fibers for Current Sensor," Proc. *OFS-11*, We2-4, pp. 168-171, 1996.

[5] H. C. Lefevre, "Single-mode fiber fractional wave devices and polarization controllers," Electron. Lett., vol. 16, pp. 778-780, 1980.

A 32 element TDM optical hydrophone array

P.Nash, G. Cranch, Defence Evaluation and Research Agency, Winfrith Technology Centre, Dorchester, Dorset, DT2 8XJ, UK
L. K. Cheng, D. de Bruijn, TNO Institute of Applied Physics (TPD), P. O. Box 155, 2600 AD Delft, The Netherlands
I. Crowe, Thomson Marconi Sonar Systems, Throop Road, Templecombe, Somerset, BA8 0DH, UK

Introduction

This paper describes the design and development of an optical hydrophone array for a seabed application. Optical hydrophones have been under development in a number of countries [1] as alternatives to piezoelectric based sensors, and the technology has now reached the stage where arrays with significant numbers of sensors can be constructed and deployed in realistic (and frequently hostile) environments. The array described in this paper is being constructed under a collaboration between the Defence Evaluation and Research Agency in the UK and TNO/TPD in the Netherlands (The TNO/TPD work is being funded by the Royal Dutch Navy). The system is modular in form and comprises up to 32 hydrophone elements in a time division multiplexed (TDM) reflectometric architecture. The array has been designed to act as a testbed for different hydrophone technologies and to explore their use in an at-sea trial.

System architecture

The array is designed to be used in conjunction with an optoelectronic interrogation unit developed under a previous project. The array is intended to be deployed from a surface vessel onto the seabed and interrogated through a 5km fibre datalink. The array is designed for operation in depths of up to 200m, and will initially be deployed for periods of up to 2 weeks. The array will require no electrical power and will contain only passive optical components.

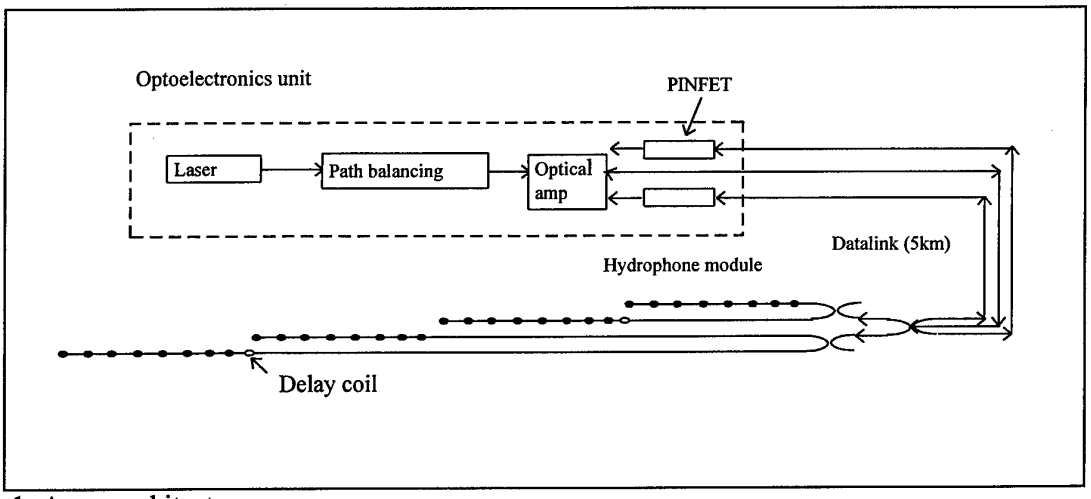

Fig. 1: Array architecture

The array architecture is shown in fig 1. The array consists of up to 4 modules of 8 hydrophones each, arranged in a tree configuration. The system is based on the TDM reflectometric architecture originally developed by Plessey [2]. The hydrophones in each module are time multiplexed on a single line, and are separated by semi-reflective elements which are constructed by silvering one port of a fibre x-coupler. Although the 4 branches are effectively parallel, they are physically arranged to form a single continuous line of 32 hydrophones. The total length of fibre between reflective elements is 100m. The array is interrogated through a single output and 2 return fibres.

Hydrophone design

The array contains hydrophones of 2 designs, one module using a TNO/TPD design while the remaining modules use a DERA designed hydrophone. These hydrophones use different design approaches but have been designed to be integrated into the common optical architecture. One of the purposes of the programme is to compare the performance of the different hydrophones.

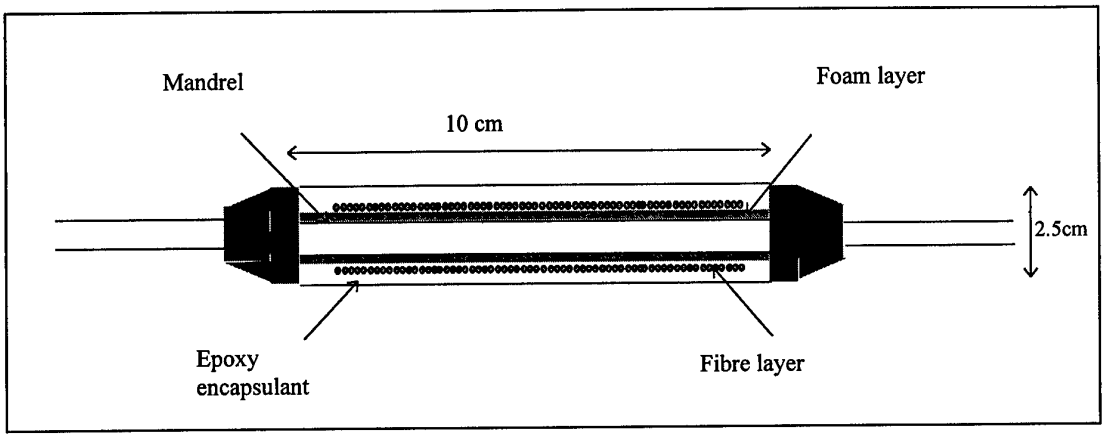

Figure 2: Hydrophone design

The DERA hydrophone design is shown in fig. 2. The hydrophone is an air backed mandrel design, containing 100m of fibre with an overall diameter of 2.5 cm and a length of 10 cm. The fibre coil is encapsulated in a layer of epoxy resin. The hydrophone responsivity has been measured to be -8 dB re 1 rad/Pa, and is flat up to frequencies well in excess of 1 kHz. Although air-backed, the mandrel is comparatively stiff and so the pressure tolerance of this hydrophone is intrinsically quite high.

The TNO/TPD hydrophone is based on a flexural disc design, which is highly compliant and gives a very high gauge sensitivity. This means that a responsivity of -7 dB re 1 rad/Pa can be achieved with a sensor length of just 4m. To achieve compatibility with the overall array architecture, the sensor also contains a 96m delay coil which is shielded from the acoustic signal within the centre of the hydrophone. The high compliance of the disc means that it is inherently prone to collapse under pressure, so the sensor incorporates a pressure compensation mechanism which allows it to operate down to the required 200m depth. The hydrophone has a diameter of 5cm.

Array design

The array is designed to be lightweight, small diameter and easily repairable. Simplicity of manufacture was also a significant requirement. Construction of a system which meets these requirements, while at the same time being able to survive the often hostile environments and handling encountered during deployment and recovery, is a significant challenge. The basic array structure is shown in fig.3. Individual hydrophone elements are joined together using a rigid metal enclosure which contains the reflective x-coupler and associated fusion splices, together with sufficient spare fibre to enable additional splices to be made in the case of hydrophone replacement. This enclosure is 15cm in length and 3.5 cm in diameter. The fibre between spice enclosures and hydrophones is protected in a loose tube cable which contains a Vectran strength member, and has an external diameter of 8mm. Fibres for other array modules are contained within a separate fibre cable which is attached to the array. The 5km datalink attached to the array has a diameter of 8mm and contains 6 fibres, although only 3 are actually used. The array and datalink are normally stored on a 1.5m diameter drum.

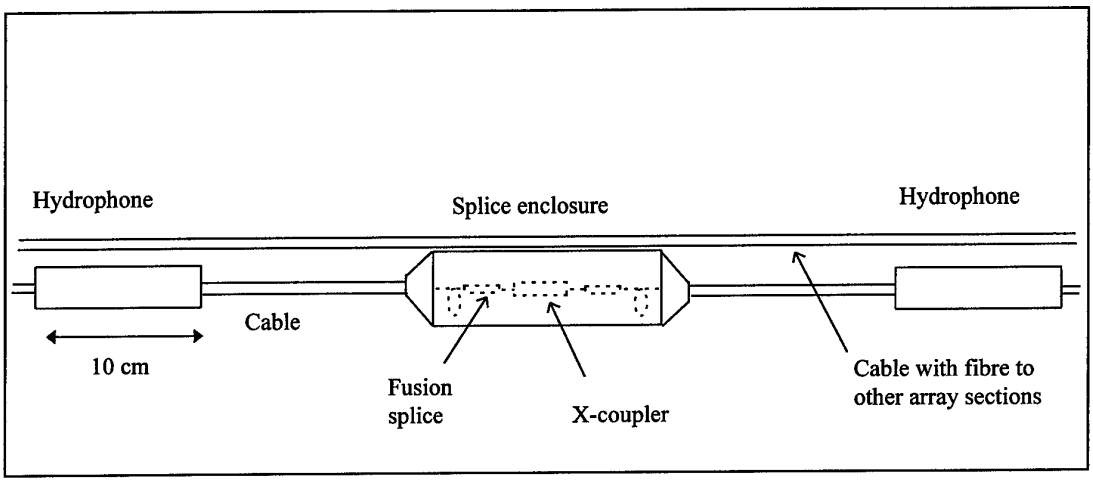

Figure 3: Array structure

Optoelectronic interrogation system

The interrogation system has been previously developed by Thomson Marconi Sonar under DERA funding. The optics and electronics are contained in a compact and rugged unit. The optical circuit is shown in fig. 4, and comprises a fibre laser, followed by a path balancing interferometer and an erbium doped fibre amplifier. A frequency difference is imposed on the light travelling through the two interferometer arms using two acousto-optic modulators. The output of the interferometer consists of 2 pulses, separated by a delay equal to twice the transit time of light through a hydrophone, and with a frequency difference equal to the heterodyne frequency. These pulses are then routed to the array through the single input fibre.

Optical signals returning to the array pass through the two return fibres and are routed onto 2 photodiodes. The signals are then demultiplexed and demodulated using 32 parallel analogue demodulators.

The optoelectronic system has been tested with a previous 32 element array constructed by Thomson Marconi Sonar. The system noise floor obtained with the original system is shown in fig. 5. The noise floor achieved is approximately equivalent to Deep Sea State Zero (moderately rough ocean conditions). The responsivity of the hydrophones in the new array is 4 dB higher than those in the original system, which will lead to a corresponding reduction in the noise floor in fig. 5. The noise floor achieved is higher than theoretically predicted, and further improvements to the electronics and to the acoustic isolation of the reference coil in the interferometer is expected to reduce this level.

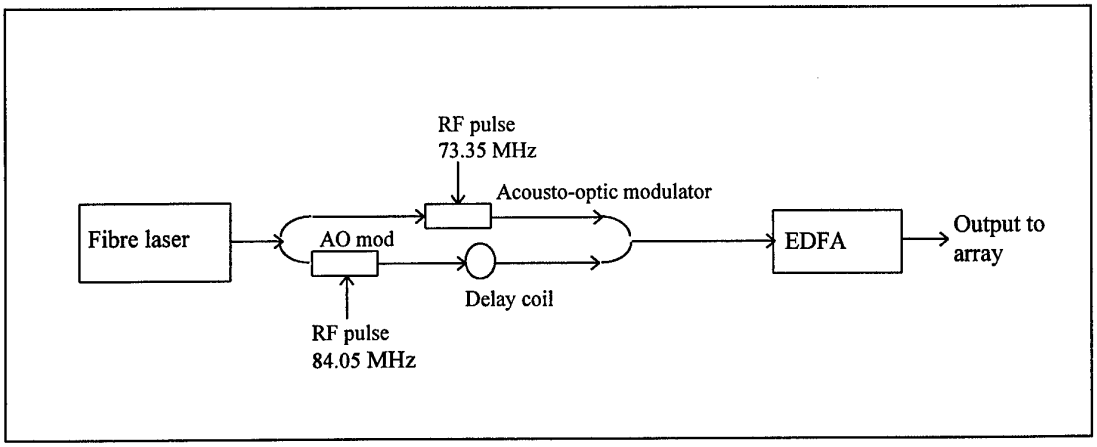

Figure 4: System optical architecture

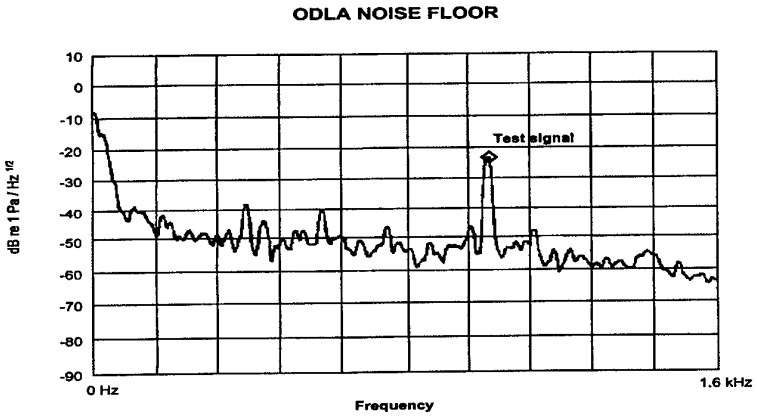

Figure 5: Optoelectronic system noise floor

Experimental programme

The array is being assembled during the first part of 1998 and will be tested during a sea trial in May 98. During this trial, which will be jointly conducted by DERA and TNO/TPD, the array will be deployed onto the seabed and interrogated from the deployment vessel. The performance of the array will be fully characterised in terms of noise floor, system dynamic range and beamforming performance, and the results from the different array hydrophones will be compared. Results from the trial will be presented at the workshop.

References

1. A. Dandridge, "Development of Fibre Optic Sensor Systems, 10th Optical Fibre Sensors Conference, Glasgow 1994

2. M. Henning et al, "Optical Fibre Hydrophones with Downlead Insensitivity", 1st Optical Fibre Sensors Conference, London 1983

A New Optical Fiber Voltage Transformer

Miaoyuan Ye Jianying Zhou Ying Cui Zhiping Chen
Dept. of Electrical Power Engineering, Huazhong University of Sci. & Tech. P.R.C.

Abstract: This paper deals with the design, testing results and practical application of a new type of optical voltage transformer(OVT). It's different from the exist OVTs. The high voltage (beyond 110KV) is directly applied on the electrooptical crystal ($Bi_4Ge_3O_{12}$) sensor, without the divider. And a new type of the silicon rubber insulator, SF_6 gas filled ,is employed for high voltage insulation. Its precision is $\pm 0.2\%$ from 80% to 120% of the rating voltage, between -10℃ and +40℃. All parts of the OVT are developed according to the requirement of products.

Introduction

The optical voltage transformer(OVT), based on the Pockels effect, offers substantial advantages in comparison with conventional type voltage transformer, such as rapid response, immunity to electromagnetic induction noise. And our new OVT, in comparison with former OVTs, has better linearity and temperature stability for its new type sensor, analog signal processing unit and digital processing unit.

In the sensor, the Pockels cell ($Bi_4Ge_3O_{12}$) has been purified for three times to eliminate the impurities. And annealing processing has been used to relieve stress causing birefringence. there are two light paths in it to compensate the effects of birefringences ,which are sensitive to temperature and stress(or pressure).

In the analog processing unit, a servo-control circuit is used to equalize the DC values on the photodiodes(PINs) , then to process the two modulated lights of the sensor.

And in the digital processing unit, a high speed data acquisition system, based on a microprocessor MCS-80C196 ,is presented. It can realize the automatic calibration of the OVT and the data communication within power system through a serial port.

Principle

Fig.1 shows a schematic diagram of the detection system in the newly developed optical transformer. Light emitted by a LED (wavelength 850nm) is transmitted by the fiber to the Pockels sensor unit. Light from the end of the fiber is transformed into linearly polarized light by a polarizer, then passes through a prism, a $Bi_4Ge_3O_{12}$ Pockels crystal, and another prim. The two prisms have the same effect as a quarter wave plate. Then the light is divided into two by a analyzer. This two-light-path system is to eliminate the temperature birefringence and the change of the light source power.

Fig.2 shows the analog signal processing unit. To process the two intensities collected by the return fibers correctly , we have to mention two different gains on the two channels .

The analog signal processing system equalize the DC values on the two photodiodes, then do sum and difference of the two signal. In the end , the voltage output

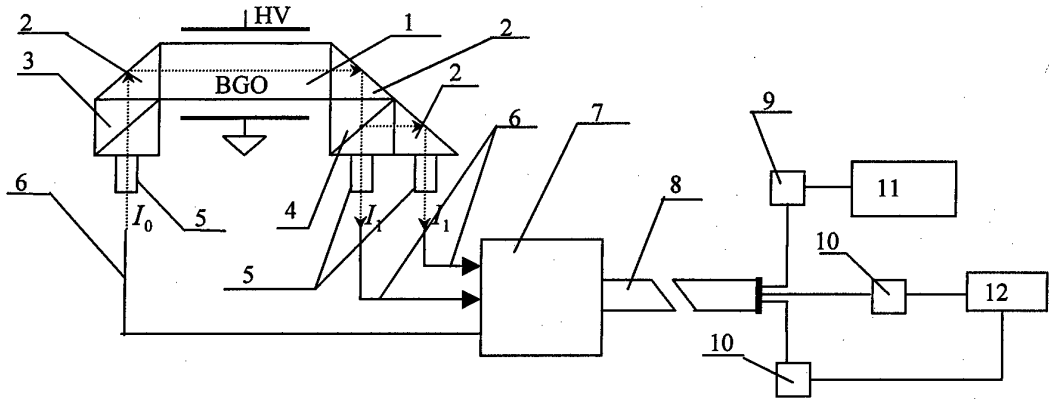

1-BGO crystal, 2-90°prism, 3-Polarizer, 4-Analyzer, 5-Collimating lens, 6-Fiber, 7-Fiber connectors, 8-Fiber cable, 9-ligth source, 10-Photodiode(PIN), 11-Constant current source, 12-Signal Processing Unit

Fig.1 Voltage sensor structure

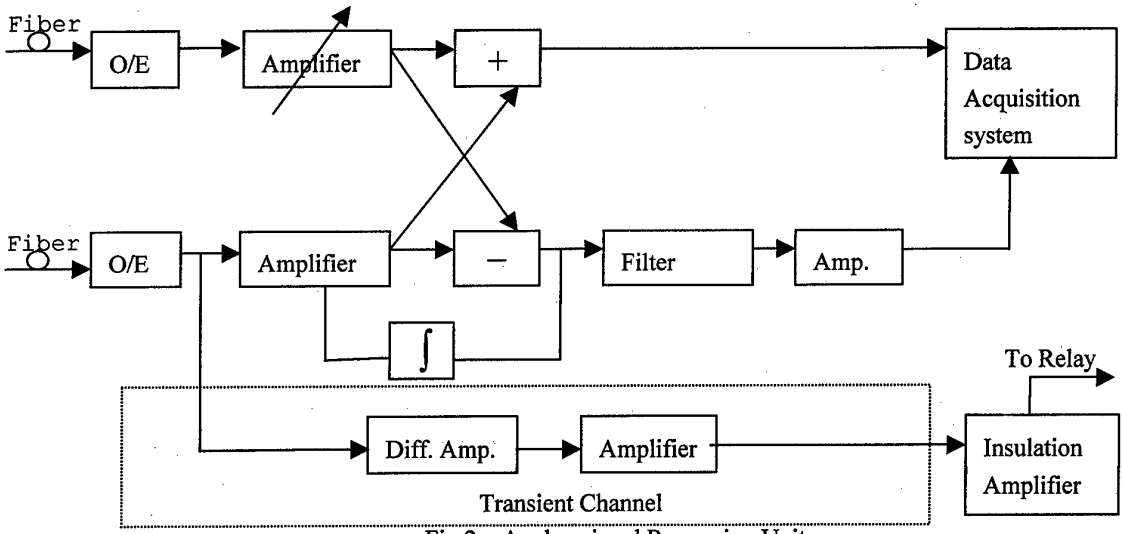

Fig.2 Analog signal Processing Unit

of this circuit is translated to the digital unit to measure the RMS value and store the wave of signal. To gain a stable value , there are several filters to repress the noise, so they cause a delay , but this delay is not admitted by a relay protection.

Thus the signal for microcomputer relay protection is provided by the transient channel, which is insulated from the protection system by an insulating amplifier.

Fig.3 shows the digital signal processing unit. Besides the signal of the OVT, it gets signal from temperature probes, pressure sensors, and the conventional potential transformers, to monitor the status of OVT in experiments.

With the automatic calibration program , no adjustable components are needed in analog processing. It increases the reliability of the whole system, and makes

the calibration and factory test easy.

With the function of communication in power system, this OVT is fit for the need of power station automation .

And Fig.4 shows the whole system of our OVT.

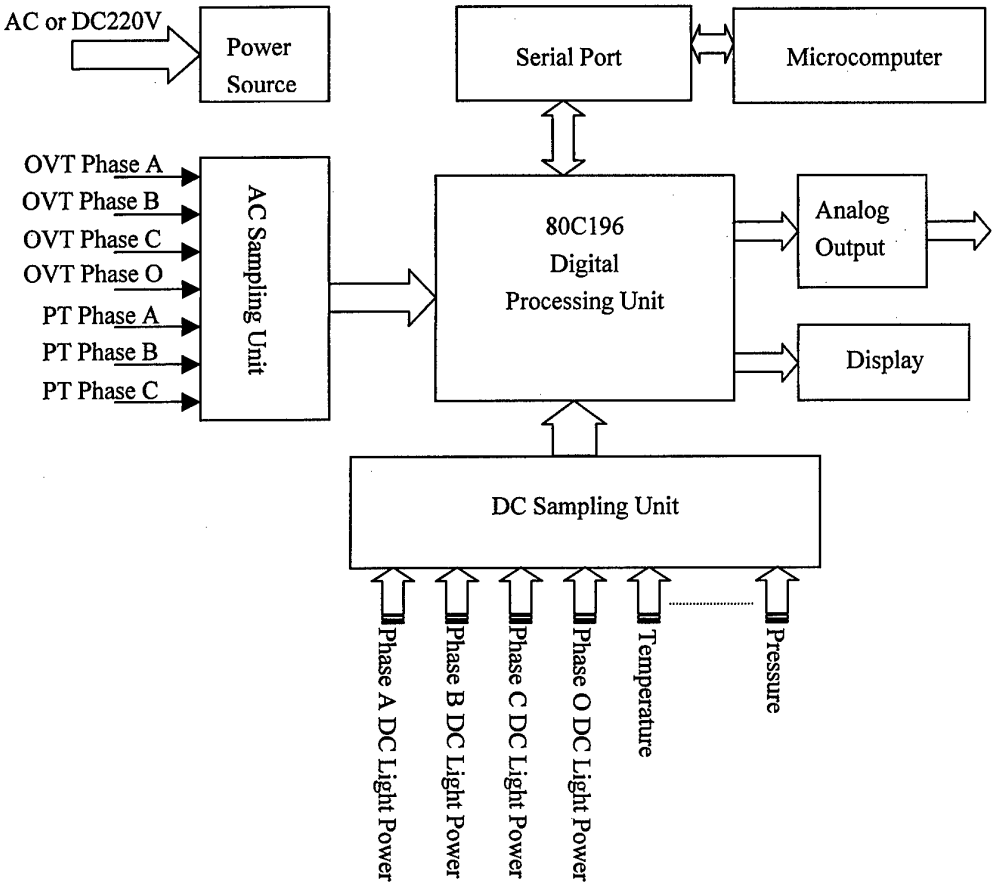

Fig.3 Digital Processing Unit

Testing Results

In order to evaluate the characteristics of the OVT, we have done some important experiments in China Electric Devices Testing Center, and some in our laboratory. The result of major test items are as follow:

1. Linearity test

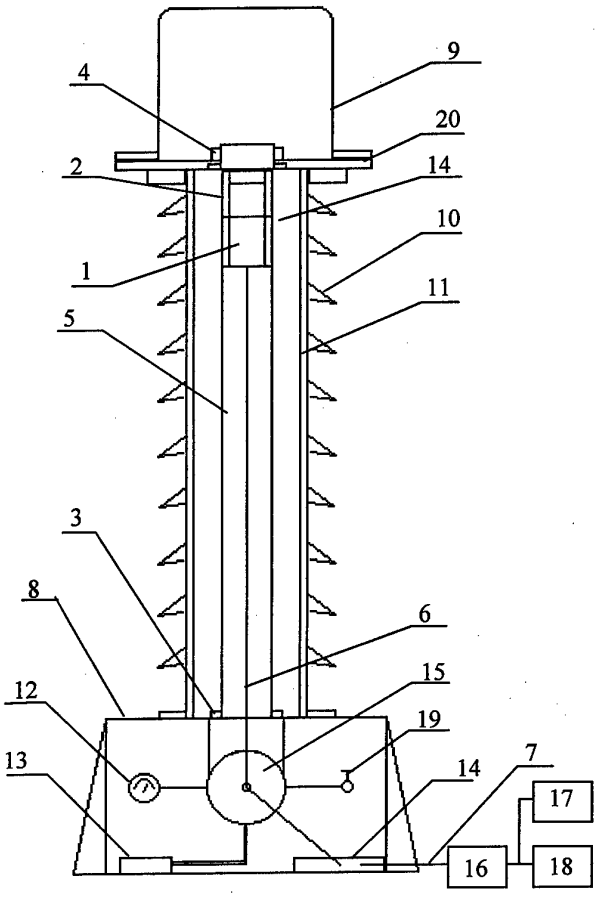

1、 Voltage sensor;
2、 Insulator;
3、 Down flange;
4、 Upper flange;
5、 Metal tube;
6、 Fiber;
7、 Fiber cable;
8、 Bed;
9、 Cap;
10. Silicon rubber skirt;
11. Epoxy tube;
12. Pressure instrument;
13. Density relay;
14. Fiber connectors;
15. Seal plate;
16. Signal processing unit;
17. Metrology unit;
18. Microcomputer relay protection

Fig.4 POVT-110-I Optical fiber transformer structure

Fig.5 shows the linearity test over the input voltage range from 10% to 120% of the rating voltage(110KV).

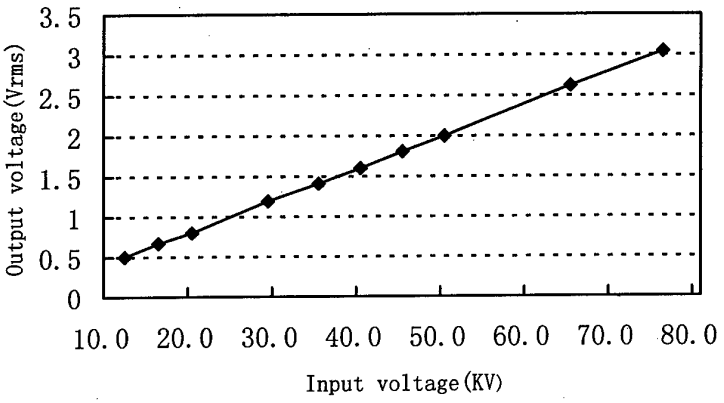

Fig.5 The output characteristic of voltage measuring system

2. Ratio error

Tab.1 shows the relation between the ratio error and the input voltage.

Applied Voltage (KV)	50.6	63.5	75.9
Digital Output (KV)	50.7	63.4	75.8
Ratio Error (%)	+0.20	-0.16	-0.13

Tab.1 Ratio error between digital output and applied voltage

3. Temperature Characteristics

To investigate temperature dependency , the Pockels sensor was placed in a thermostat oven , the temperature varied from 0-50℃ at the rate of 0.5℃/min, and the ratio error corresponding to the rated applied voltage of the sensor was measured during the period , data showed that the ratio error variations were within ±0.2% .

The entire apparatus was the placed in a thermostat oven , the temperature was varied from -10 to 60 ℃ , and the temperature dependency of the ratio error corresponding to 100% and 80% of the rating voltage(110KV) was measured. The results of this test indicated that the variations of the ratio error were within ±0.2%.

4. The Pressure Characteristic

To investigate pressure dependency, we decrease the pressure of SF_6 inside the OVT from 0.3Mpa to 0.2Mpa, then increase the pressure to original value. Fig.6 shows the relation between ratio error and the gas pressure.

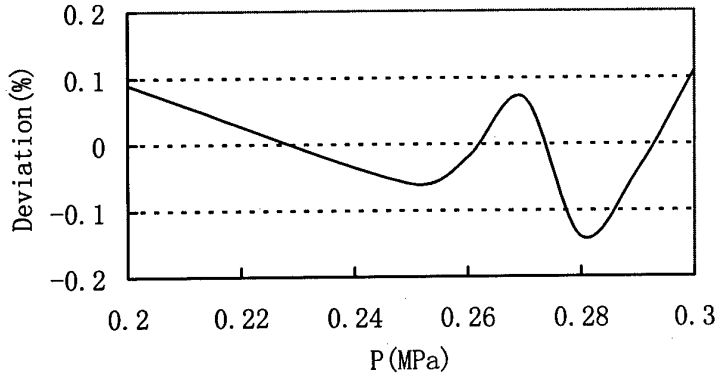

Fig.6 Pressure characteristic of voltage measuring system

5. The Stability Of The OVT

Fig.7 shows the relation between the ration error and time.

6.Response of the Transient Channel

the measured voltage is varied from 0 to rating voltage. The delay time of the optical system is about 60μs.

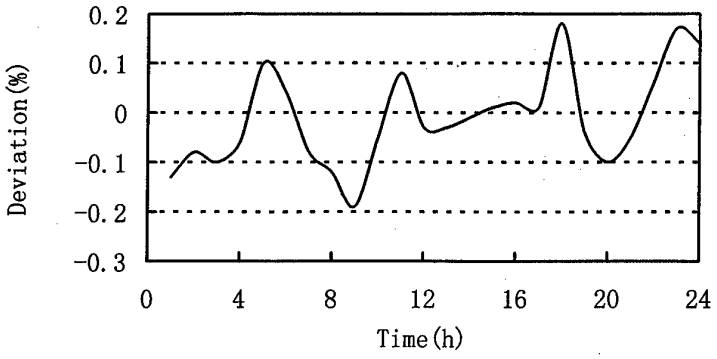

Fig.7 The stability of voltage measuring system

Conclusion

The OVT based on $Bi_4Ge_3O_{12}$ crystal was evaluated. The methods to deal with the crystal by annealing and purifying are very important. The compensation of stress birefringence and temperature birefringence is accomplished by the two-light-path system and the analog signal processing unit. The digital processing unit is used to calibration and factory test of the OVT, and to transmit data within power system.

The results of experiments on the OVT shows that the OVT is reliable and can be applied in power system to replace the conventional potential transformers.

References

1) M. Kanio, G. Takahashi, T. Sato ,"Optical Voltage and Current Measuring System for Electric Power System",IEEE Transaction on Power Delivery, Vol. PWRD-1, No.1, pp.91-97, January 1986.

2) A. Cruden, Z. J. Richardson, J. R. McDonald, I. Andonovic, "Compact 132kV Combined Optical Voltage and Current Measurement System ", IEEE Instrumentation and Measurement Technology Conference, pp.1399-1402, May 19-21, 1997.

3) Kyung Shik Lee, "Electrooptical sensor: birefringence effects and compensation method ",Applied Optics, Vol.29, No. 30, pp.4453-4461, 20 October 1990.

4) L. H. Christensen, "Design, constriction and test of a passive optical prototype high voltage instrument transformer", IEEE Transactions on Power Delivery, Vol.10, No.3, pp.1332-1337, 1995.

5) A. Cruden, Z. J. Richardson, J. R. McDonald, "Optical Crystal Based Devices for Current and Voltage Measurement ",IEEE Transaction on Power Delivery,Vol.10,No.3,pp.1217-1223,July 1995.

6) T. W. Cease, "Optical Voltage and Current Sensors Used in a Revenue Metering System", IEEE trans, Power on Delivery,Vol.67,No.4,Oct.,1991.

7) G. Montemezzani, St. Pfandler, P. Gunter, :Electro-optical and photo-refractive properties of BGO crystals in the ultraviolet spectral range", J.Opt.Soc.Am.b,Vol.9,No.7,July 1992.

In-Fibre Gratings

Friday, 10 July 1998

Chair: Michel Lequime, Bertin et Cie (France)

High resolution strain sensing by locking lasers to fiber-Bragg gratings

B. Lissak, A. Arie and M. Tur
Faculty of Engineering, Tel-Aviv University, Tel-Aviv 69978, Israel

By locking a diode laser wavelength to the mid-reflection wavelength of a fiber-Bragg grating, dynamic strain sensing resolution of $\approx 45\ p\varepsilon/\sqrt{Hz}$ at *3 kHz* is achieved. The error signal provides direct electronic demodulation.

1. Introduction

Fiber Bragg gratings (FBG) offer an attractive method of strain sensing owing to their fiber-based, wavelength encoded operation. In this paper we present a novel passive narrowband interrogation method for FBG strain measurements. The advantages of this method are high sensitivity and high resolution: Experimentally we reached $\leq 10^{-10}\varepsilon/\sqrt{Hz}$, whereas higher resolution and sensitivity can be attained using lasers with lower frequency noise, e.g. diode-pumped solid-state lasers. Furthermore, since the strain signal directly alters the optical power reflected from the FBG, it can be electronically demodulated.

The principle of operation is the following: The wavelength of a single longitudinal mode laser is tuned to the mid-reflection wavelength of a FBG and the reflected light is measured using a photodetector, see Fig. 1. A low-gain servo alters the laser wavelength in order to keep it locked to the mid-reflection wavelength of the FBG. However, the laser frequency will not track dynamic strain variations at frequencies above the unity gain frequency of the servo. The dynamic strain will shift the reflection curve of the FBG, hence the reflected power from the grating will vary with proportion to the applied strain. Observing the error signal of a locked system - as done here - is often used in fiber-optic sensors, e.g. in balanced homodyne Mach-Zehnder interferometers [1] in which the laser is actively held at the quadrature point. However, to the best of our knowledge, our method of interrogation was never applied to FBG sensors.

In Section 2 we theoretically analyze this system and derive the sensitivity limits imposed by the shot noise and laser frequency noise. The experimental setup and results are presented in Section 3. Possible modifications and improvements are discussed in Section 4.

2. Theory of FBG strain sensor

Let us assume a linearized reflection curve of the FBG, in which the reflection coefficient on one side of the curve can be modeled as:

$$R(\nu) = R_{max}\cdot(\nu - \nu_0)/\Delta\nu \qquad \text{for } \nu_0 \leq \nu \leq \nu_0 + \Delta\nu \qquad (1),$$

where ν is the optical frequency, ν_0 and $\Delta\nu$ are the starting wavelength and bandwidth of the linear range of FBG reflection, respectively and R_{max} is the reflection at $\nu_0 + \Delta\nu$. An input beam with a power level P_0 is sent towards the grating. The reflected power is detected by a photodetector with responsivity of R, thus the detected photocurrent is $I_r(\nu) = R_{max}\cdot R\cdot P_0\cdot(\nu - \nu_0)/\Delta\nu$. When no strain is applied, the servo keeps the laser frequency at the mid-reflection frequency $\nu_0 + \Delta\nu/2$. In this case the photocurrent is simply $0.5\cdot R_{max}\cdot R\cdot P_0$. When a strain ε is applied to the FBG, we assume that it will only induce a frequency shift of the reflection curve by $\Delta\nu_s$. The reflection curve of the strained fiber is therefore $R_s(\nu)=R(\nu - \Delta\nu_s)$. The relation between the strain and the frequency shift in our FBG was measured to be $\Delta\nu_s/\nu = -0.79\ \varepsilon$. For

a dynamic strain at a frequency which exceeds the unity gain point of the servo, the laser frequency will not track the frequency shift of the reflectivity curve, and will remain at $\nu_0 + \Delta\nu/2$. Hence, the reflectivity curve shift will change the reflected photocurrent by:

$\Delta I_r = \{R(\nu_0 + \Delta\nu/2) - R_s(\nu_0 + \Delta\nu/2)\}R\cdot P_0 = -0.79\cdot\nu\cdot R_{max}\cdot R\cdot P_0\cdot\varepsilon/\Delta\nu$ (2).

The strain can be determined directly from the measured photocurrent as

$$\varepsilon = -\frac{\Delta I_r \cdot \Delta\nu}{R\cdot P_0\cdot\nu\cdot 0.79\cdot R_{\max}} \quad (3).$$

Let us investigate now the sensitivity limits of the FBG sensor. Assuming a linear behavior, this is also the resolution limit. The fundamental limits are set by the shot noise and the spontaneous emission induced frequency noise. The average photocurrent $0.5\cdot R_{max}\cdot R\cdot P_0$ is accompanied by shot noise, whose standard deviation is $i_s = \sqrt{e R_{\max} R P_0 B}$ where B is the detection bandwidth. Using Eq. (3), the minimum detectable strain imposed by shot noise is

$$\varepsilon_{\min,shot} = \sqrt{\frac{e\cdot B}{R_{\max}\cdot R\cdot P_0}}\cdot\frac{\Delta\nu}{0.79\cdot\nu} \quad (4).$$

As an example, assuming $R_{max} = 1$, $R = 1\ A/W$, $P_0 = 100\ \mu W$, $B = 1\ Hz$, $\Delta\nu = 35\ GHz$, and $\nu = 195\ THz$ ($\lambda = 1540\ nm$), the minimum detectable strain is $9\cdot10^{-12}/\sqrt{Hz}$. The laser intensity noise is often higher than the shot noise level. Limits imposed by laser intensity noise can be derived in a similar fashion by inserting the standard deviation of the current noise caused by laser intensity noise instead of ΔI_r in Eq. (3).

The second fundamental limitation is the spontaneous-emission-induced frequency noise. In an ideal laser, only the spontaneous emission process contributes to the laser frequency noise. In this case, the laser linewidth is Lorentzian with a linewidth $\Delta\nu_L$, and the frequency noise spectral density is $S_f = \sqrt{\Delta\nu_L/\pi}$ in units of $Hz/\sqrt{Hz}$. The frequency noise will be converted by the FBG frequency discriminator to intensity noise. The standard deviation of the induced change in the reflected photocurrent is therefore $R_{\max} R P_0 S_f \sqrt{B}/\Delta\nu$. By inserting this current noise in Eq. (3) instead of ΔI_r, the minimum detectable strain imposed by frequency noise is:

$$\varepsilon_{\min,freq.} = \frac{S_f\sqrt{B}}{0.79\nu} \quad (5).$$

Assuming $\Delta\nu = 1\ MHz$ leads to $S_f = 564\ Hz/\sqrt{Hz}$, hence the minimum detectable strain imposed by frequency noise is $3.6\cdot10^{-12}/\sqrt{Hz}$. In practice, the frequency noise spectral density is often higher than the level induced by spontaneous emission, owing to technical noises caused for example by acoustic and thermal disturbances. Depending on the frequency noise level, the sensitivity may be limited either by the frequency noise or the shot noise.

The width of the FBG slope $\Delta\nu$ also determines the maximum detectable strain. The highest peak to peak measurable dynamic strain is obtained when $\Delta\nu_s = \Delta\nu$. In this case the measured strain is $\varepsilon_{max} = \Delta\nu/0.79\nu$. To achieve a large ε_{max} one should increase $\Delta\nu$, which is equivalent to reducing the reflectivity vs. wavelength slope. It will also increase the shot noise contribution, but will have no effect on the frequency noise contribution. Hence, if the system is limited by frequency noise, it is worthwhile to increase $\Delta\nu$. This will increase the dynamic range without reducing the sensitivity. However, there is a critical $\Delta\nu$ at which the shot noise contribution

becomes equal to the frequency noise contribution and further increase of $\Delta\nu$ will not improve dynamic range but will reduce sensitivity. By comparing the sensitivity limits imposed by the frequency noise to that of the shot noise, using Eqs. (4) and (5), the critical $\Delta\nu$ is:

$$\Delta\nu = S_f \sqrt{\frac{R_{\max} R P_0}{e}} \qquad (6).$$

In this example the critical $\Delta\nu$ is *14 GHz* and ε_{max} is therefore *90* $\mu\varepsilon$.

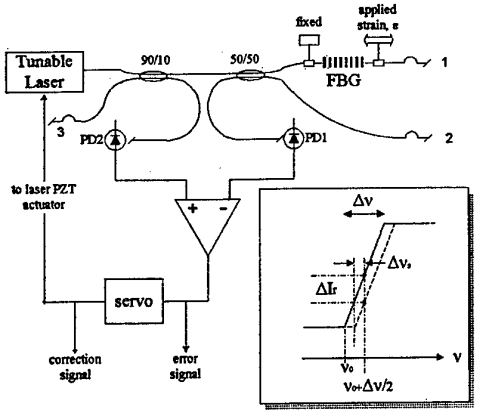

Fig. 1: Dynamic strain measurement setup. Inset shows the effect of applied strain on the FBG reflectivity curve.

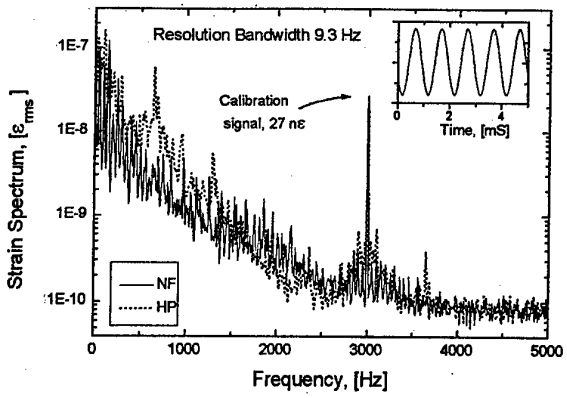

Fig. 2: Measured strain resolution spectrum using New Focus (NF) and HP laser sources. Inset shows the error signal for a *1.5* $\mu\varepsilon$ rms signal at *1 kHz*.

3. Experimental Set-up and Results

Our experimental setup is shown in Fig. 1. The light source is a tunable diode laser, New Focus model 6262. The laser frequency can be continuously tuned over *35 GHz* using a piezo-electric frequency actuator. Wider tuning range (*1491 - 1568 nm*) is achieved when using the laser picomotor. The laser light is coupled into the fiber after passing through an optical isolator. The FBG reflection, centered at $\approx$ *1540 nm* with a peak reflection of $\geq$ 96%, has FWHM of *1.5 nm* and a linear slop width of $\Delta\nu \approx$ *35 GHz*. The fiber is glued to a piezo-electric actuated mount in order generate dynamic strain calibration signals. To eliminate parasitic interference between the FBG and all fiber terminations we used both APC connectors and tightly bended all the un-used fiber ports. An error signal for locking to the mid-reflection point is obtained by subtracting the reflected signal (at PD1) from a reference signal (at PD2). The servo includes an integrator and a variable amplifier. Typical open loop gain of our system as a function of the electrical frequency f is $\approx$ *20/f*. The laser remains locked to the FBG for several hours without any further adjustments. Inset of Fig. 2 shows an oscilloscope trace of the error signal when a sinusoidal strain signal at *1 kHz* is applied by the PZT-actuated fiber holder.

To measure the sensitivity, a *27* $n\varepsilon$ rms calibration signal is applied by modulating this PZT at *3 kHz*. The power spectral density of the error signal is measured using an FFT spectrum analyzer, see Fig. 2. Since the signal to noise ratio is *46 dB* and the resolution bandwidth is *9.3 Hz*, the sensitivity at *3 kHz* is $\approx$ *45* $p\varepsilon/\sqrt{Hz}$ rms (*130* $p\varepsilon/\sqrt{Hz}$ peak to peak). Assuming a linear behavior of the sensor, this is also the sensor resolution. The intensity noise of the signal

transmitted through the FBG was considerably higher at the mid-reflection wavelength than outside the FBG reflection band. This indicates that the dominant noise is the laser frequency noise. The sensitivity deteriorates at lower frequencies, owing to higher frequency noise of the external cavity diode laser. For example, the sensitivity at *500 Hz* is $\approx$ *1* $n\varepsilon/\sqrt{Hz}$ rms. Our measurement enables to determine the frequency noise spectral density of the laser: At *500 Hz* for example, it is $\approx$ *150* $kHz/\sqrt{Hz}$.

We have tested another external cavity diode laser source - HP model 8168C. The wavelength of this laser cannot be continuously tuned, hence we cannot lock it to the FBG. However, since the relative drift between the laser and the FBG is slow, we simply tune the laser to the mid-reflection wavelength and immediately measure the intensity noise spectrum of the reflected signal, see Fig. 2. The sensitivity in this case is similar to that obtained with the New Focus laser.

Since the width of the linear range of the FBG is $\Delta\nu \approx 35$ *GHz*, the largest measurable peak to peak strain ε_{max} is *227* $\mu\varepsilon$ and the dynamic range is therefore *125 dB* in a *1 Hz* bandwidth. The highest calibration signal we have applied to the FBG using a PZT was *38.7* $\mu\varepsilon$ where the dynamic range in this case was *109 dB*. As mentioned above, the largest measurable strain and the dynamic range can be further increased using a different FBG with a moderate reflection slope. The high sensitivity and resolution can be maintained, since the dominant noise is the laser frequency noise.

Another option is to operate the sensor in a high gain mode, where the strain signal is applied at frequencies lower than the unity gain frequency of the servo. In this case, the strain information appears on the correction signal. This could potentially lead to a larger dynamic range, limited by the continuous tuning range of the laser and not by the FBG characteristics.

4. Discussion and Summary

We have demonstrated a novel narrowband interrogation method of FBG and obtained with it strain sensitivity and resolution of $\approx$ *45* $p\varepsilon/\sqrt{Hz}$ at *3 kHz* with a dynamic range of *109 dB*. The sensitivity and resolution are currently limited by the frequency noise of our source. Further improvement can be achieved using a source with lower frequency noise. The measured frequency noise spectral density is at the level of $\approx$ *150* $kHz/\sqrt{Hz}$ at *500 Hz*, whereas diode-pumped solid state lasers, for example, exhibit frequency noise spectral density of $\approx$ *50* $Hz/\sqrt{Hz}$. Another option that may be more practical for industrial applications is to use a DFB diode laser instead of an external cavity laser. It should be emphasized that the present strain resolution is already comparable to the best FBG strain sensing results of *0.6* $n\varepsilon/\sqrt{Hz}$ at *500 Hz*, obtained using unbalanced interferometric wavelength discriminator [2]. In addition to strain measurements, the current FBG sensor is sensitive enough to be used as a fiber-optic microphone. We are currently characterizing its acoustic sensitivity.

The experimental setup we use cannot measure static strain yet, since very slow ("static") variations of the locking point can be attributed either to strain variations of the FBG or to drift of the laser frequency. The laser frequency drift can be reduced to the sub-MHz level by locking the laser frequency to atomic [3] or molecular absorption lines. This should enable to measure static strain as well.

5. References

1. D. A. Jackson, R. G. Priest, A. Dandridge and A. B. Tveten, *Appl. Opt.* **19**, 2926 (1980); A. Dandridge and A. B. Tveten, *Opt. Lett.* **6**, 279-281 (1982).
2. A. D. Kersey, T. A. Berkoff and W. W. Morey, *Electron. Lett.* **28**, 236-238 (1992).
3. V. Mahal, A. Arie, M. A. Arbore and M. M. Fejer, *Opt. Lett.* **21**, 1217-1219 (1996); A. Bruner, A. Arie, M. A. Arbore and M. M. Fejer, *Appl. Opt.* **37**, 1049-1052 (1998).

SHORT IN-FIBRE BRAGG GRATINGS FOR MEASURING MHZ ULTRASONIC FIELDS

NE Fisher, DJ Webb, CN Pannell and DA Jackson
Applied Optics Group, The University, Canterbury, Kent, CT2 7NR, UK
Tel: (+44) 1227 764000, Fax: (+44) 1227 827558

LR Gavrilov and JW Hand
Radiological Sciences Unit, Hammersmith Hospital, Du Cane Road, London, W12 OHS, UK

L Zhang and I Bennion
Photonics Research Group, Department of Electronic Engineering, Aston University, Birmingham, B4 7ET, UK

1. INTRODUCTION

There is a need for the assessment of the safety of ultrasound for medical applications [1,2] due to the trend towards increasing output powers from diagnostic ultrasound equipment and the widening use of high intensity ultrasonic fields in a range of therapeutic applications. Often the assessment of such fields is based upon theoretical models of some complexity and so a direct determination of them *in vivo* is of importance. Conventional detection is most commonly achieved using piezoelectric devices but suffers from a susceptibility to electromagnetic interference and signal distortion. To overcome these "electrical" problems several approaches utilising optical fibres based on interferometric or polarimetric techniques have been described [e.g. 3,4]. In this paper we demonstrate that in-fibre Bragg gratings too may be used to detect high frequency (MHz) ultrasonic fields. These devices offer distinct advantages such as ease of multiplexing, simultaneous measurement of temperature, and a potentially low cost. We found however, that the acoustic coupling from the ultrasonic field to the grating leads to the formation of standing waves in the fibre. Because of these standing waves, the system response is complex and, as we show, the grating does not act as an effective probe. However, significant improvement in its performance may be gained with short gratings coupled with appropriate desensitisation of the fibre.

2. EXPERIMENT

The arrangement used to interrogate the grating is shown in figure 1. This utilised a ramped lithium niobate phase modulator (closely set to produce a 2π peak-to-peak phase excursion) to frequency shift the light in one arm of an unbalanced Mach-Zehnder interferometer (MZ) and thus allowed the use of heterodyne signal processing. Light from a pig-tailed superluminescent diode (*Superlum*, Moscow) giving an output power of 1mW centred at 824nm with a bandwidth of $\approx$42nm was launched into the unbalanced MZ; hence a channelled spectrum was created at the interferometer's outputs which was incident on the grating. Incorporated in one arm of the MZ was the phase modulator. The other arm contained a variable air gap which allowed the optical path difference (OPD) between the two arms to be adjusted.

Provided that the OPD between the MZ's arms is longer than the source coherence length and shorter than the effective coherence length of the back-reflected light from the grating, interference signals are observed at the detector which can be expressed as

$$I(\lambda_B) = A(1 + V\cos[\omega' t + \Phi + \delta\Phi \sin\omega t + \phi(t)]) \quad (1)$$

Here, λ_B is the wavelength of the reflected light from the modulated grating, ω' is the angular frequency of the ramp modulation, A is proportional to the grating reflectivity, V is the visibility of the signals (dependent on the grating bandwidth and the polarisation properties of the system), $\Phi = 2\pi.OPD/\lambda_B$ and $\phi(t)$ is a random phase drift term. A sinusoidally strain-induced change in λ_B from the grating - $(\delta\lambda_B)$ - induces a change in phase shift in equation 1, given by $\delta\Phi \sin\omega t = [2\pi.OPD/\lambda_B{}^2].[\delta\lambda_B] \sin\omega t$ where ω is the angular frequency of the ultrasound incident on the grating. Hence, from equation 1, strain induced changes in λ_B induce a corresponding phase modulation of the electrical carrier produced by the phase modulator, which we measured by determining the amplitudes of the upper and lower side-band frequency components observed on a radio frequency spectrum analyser. The phase modulator was ramped at and hence generated a carrier signal at 10MHz. The grating we used had a nominal Bragg wavelength of 820nm, a bandwidth of 0.2nm, a reflectivity of 80% and a length of 5mm. The transducer was driven at its resonant frequency of 1.911MHz in water, and generated a maximum acoustic pressure of $\approx$ 2Atm (measured using a calibrated PVDF hydrophone) in a focal spot of radius $\approx$ 1 - 2mm.

3. RESULTS AND DISCUSSION

3.1. *5mm GRATING*

In our preliminary experiments we observed two striking anomalies in the response of the system to the ultrasound. Consider figure 2 which shows a spectrum analyser trace recorded in a typical experiment. Firstly, note that the upper and lower side-band frequency components (the first order Bessel functions) are asymmetric, and secondly note the existance of a large homodyne signal at 1.911MHz, which was up to several dB's greater than the side-band magnitudes.

Now consider figure 3 in which we scanned the focal spot of the acoustical field longitudinally along the fibre/grating and recorded one of the side-band powers (normalised by its corresponding carrier signal power) with displacement. Note the multiple "peaks" and "troughs" in the system response which are observed over a distance that is much greater than the grating length. This too is another unexpected result since the radius of the focal spot is only about 1mm. However, consider the average distance between the peak responses which is 1.475mm. If we hypothesise that the acoustic coupling from the ultrasonic field to the optical fibre leads to the formation of stationary waves in the fibre, this value leads to an experimental acoustic wavelength of 2.95mm which is close to the predicted value of 3.087mm for compressional waves at 1.911MHz in fused quartz. We repeated these experiments but now driving the transducer at 1.6MHz and found an experimental value of 3.76mm which is again close to the predicted value of 3.68mm. Using the same system, we then modulated the grating with low frequency (10^2 Hz) sound waves in air and higher

frequency (76kHz) sound waves in water. In both these cases, the system response was as originally expected, with symmetric side-bands and no homodyne signal observed.

Hence we conclude the following. Compressional standing waves are set up by the ultrasound in the fibre (although the acrylic jackets which are on either side of the grating and which are, in the case of figure 3, spaced about 1cm apart, do tend to attenuate the acoustic modes). Since these waves must only partially modulate the grating (as their length is < the grating length), this means that the grating is subject to a *non-uniform* strain and so leads to regions of the grating acting as spectral filters for the back-reflected light from other regions of the grating. This gives rise to an amplitude modulation (the homodyne signal) and, as we show in [5], the amplitude modulation in turn gives rise to the asymmetric side-bands. We finally note that the wavelength of the lower frequency sound is greater than the length of the grating, hence in these cases the grating was subject to a more uniform strain and so none of the anomalies in the system response were observed.

3.2. *1mm GRATING*

Based on our hypothesis, it is apparent that for the grating to operate correctly in response to the MHz acoustic field, the grating length should be made smaller than the acoustic wavelength in fused quartz. In order to demonstrate this, we took a standard 5mm grating and gradually removed small pieces of it from one end until approximately only 1mm of grating was remaining. As each piece was removed, we recorded the system response to the ultrasonic field using the shortened grating, and noted a dramatic decrease in the homodyne signal along with more symmetric side-band magnitudes.

However because of the results of figure 3, it is apparent that this shortened grating on its own cannot be used as a high frequency probe since it will exhibit insufficient longitudinal resolution. In order to obtain an improved performance we must first desensitise nearly all the fibre to the acoustical field. This we did by jacketing the fibre with PVC sleeving (diameter < 1mm) such that only the 1mm grating at the end of the fibre was exposed to the field. The results of a longitudinal a scan of the acoustic focal spot is shown in figure 4 and, as may be seen, this data compares favourably with the diameter of the main diffraction maximum of the transducer.

We finally show in figure 5 the detected magnitude of one of the side-bands (normalised by its corresponding carrier signal) as a function of acoustical pressure incident on the grating. It is clear that the system response is linear and (for this probe) we determined a noise limited pressure resolution of $\approx 4.5 \times 10^{-3}$ Atm / $\sqrt{\text{Hz}}$.

4. CONCLUSIONS

Thus far we have shown that a Bragg grating may function effectively as an ultrasonic probe with mm resolution if: (a) the grating length is much less than the acoustic wavelength in fused quartz and (b) the grating/fibre is appropriately desensitised. One final point should however be noted. By shortening the grating we have dramatically reduced its reflectivity (as well as increased its bandwidth). In our case we found a reduction in the back-reflected light intensity of well over 100. Gratings of lengths less than 1mm but with 90% reflectivity can be manufactured and so we anticipate a greatly improved pressure resolution using such gratings.

5. REFERENCES

[1] Nyborg WL, *Ultrasound Med. Biol.* Vol. 11, pp.245-260, (1985)
[2] Hill CR, *Ultrasound Med. Biol.* Vol 20, pp.271-277, (1994)
[3] Knudsen S and Blotekjaer K, *J. Lightwave Techn.* Vol 12, pp.1696-1700, (1994)
[4] Beard PC and Mills TN, *Electronic Letts.* Vol. 33, pp801-803 (1997)
[5] Fisher NE et al, 12th Opt. Fiber Sensors Conf., OWC12, pp.190-193 (1997)

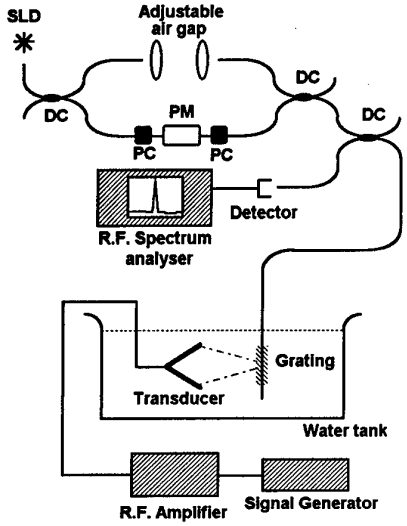

Figure 1. Experimental arrangement
PM = phase modulator
PC = polarisation controller
DC = directional coupler

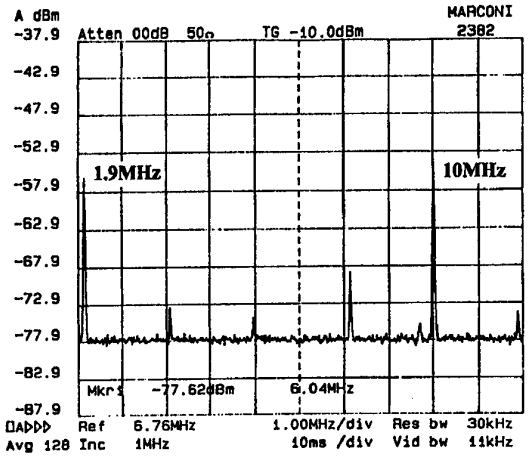

Figure 2. Spectrum analyser trace

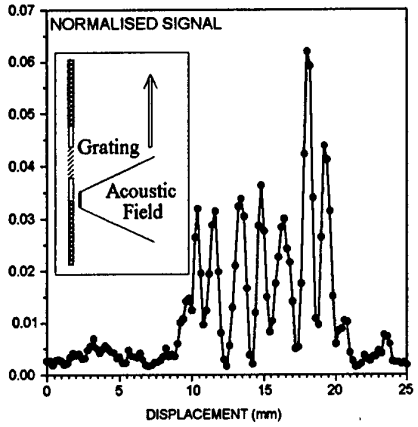

Figure 3.
Longitudinal scan for 5mm grating

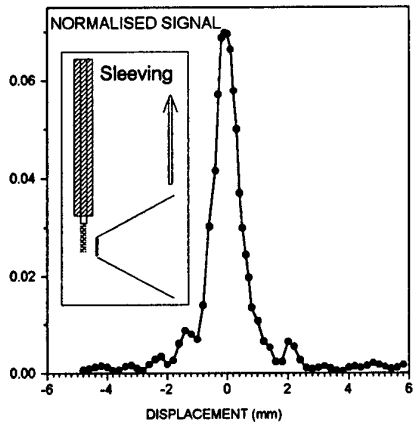

Figure 4.
Longitudinal scan for 1mm grating

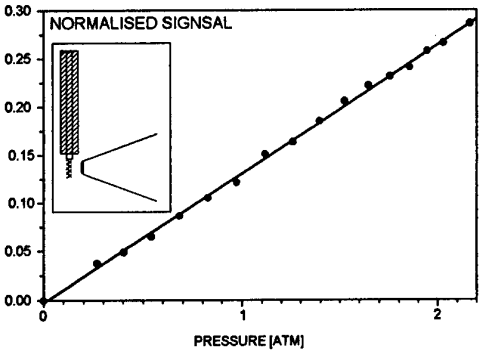

Figure 5.
Side-band amplitude (normalised by carrier amplitude) as a function of acoustical pressure incident on 1mm grating.

Quasi-Distributed Twin-Grating Sensor

M. G. Shlyagin, S. V. Miridonov, I. Márquez Borbón, and D. Tentori,
Departamento de Óptica, Centro de Investigación Cientifica y Educación Superior de Ensenada
Apdo. Postal #2732, 22860, Ensenada, B.C. Mexico
Phone:+52-(61)-75050, Fax: +52-(61)-750549, E-mail: mish@cicese.mx
D. S Starodubov, and J. Feinberg
Department of Physics, University of Southern California, Los Angeles, CA, 90089-0484, USA

Many different schemes of Bragg grating based quasi-distributed and multiplexed sensors have been reported.[1] Most of them utilize wavelength division multiplexing and detect the resonant wavelength for sensor interrogation. WDM can provide for limited number of sensors per single fiber, because a certain overlap-free wavelength range, or spectral channel, must be reserved for each grating within the entire working spectral range. Usually, this number is limited for a single fiber to a couple of dozens.[2,3] In order to increase the number of sensing points combined methods were devised: WDM was mixed with Time Division Multiplexing[4] and Spatial Division Multiplexing.[5] However, such a mixing of different techniques might complicate significantly an instrumentation increasing the cost of the sensing system.

Recently, we have demonstrated a new method[6,7] which, besides WDM, can employ frequency multiplexing/demultiplexing, FDM. The system utilizing this method uses twin-grating based local sensors, each built with a pair of low-reflective Bragg gratings. As result, a sinusoidal modulation, similar to the reflection spectrum of a low-finesse Fabry-Perot interferometer, appears in the reflection spectrum of each sensor. The frequency of this modulation (in units of $1/\lambda$, e.g. nm^{-1}) is proportional to the interferometer's OPD. Therefore, even if the local sensors occupy the same spectral channel but the distances between twin gratings are different, their signals still can be recognized on the basis of their modulation frequencies. Thus, using the same instrumentation we are able to combine WDM and FDM and, by this way, multiply the number of sensing elements in a single fiber. The principle of operation of such a sensor was first discussed in [6] and later, in [7], the experimental results with only one twin-grating sensor and a computer simulation model of a multi-component sensing network have been demonstrated.

In this paper, we present first, to our knowledge, experimental results on the twin-grating based quasi-distributed sensor utilizing wavelength- and frequency- multiplexing. We discuss also a demultiplexing technique, based on digital signal processing necessary to retrieve the information about measurand from each local sensor.

The operation of the sensor has been tested experimentally using the arrangement shown in Fig. 1. The Bragg gratings have been imprinted in the core of a photosensitive fiber by using a phase mask and near-UV light.[8] All gratings had approximately the same length of 1 mm and a typical reflectivity of 0.3%. Nominal resonant wavelengths and distances between gratings in pairs are shown in the figure. Reflection spectra were recorded with the help of an external cavity diode laser. The tunable laser had a linewidth of 500 MHz, tunable range of 1520 to 1570 nm, a minimum wavelength step of 0.001 nm and a wavelength repeatability of ±0.02 nm. We used a computer to control both wavelength sweeping of the laser and the data acquisition process. One of the local sensors together with a thermocouple were placed in a ceramic tube heater for temperature calibration. The thermocouple compact thermometer had a sensitivity of

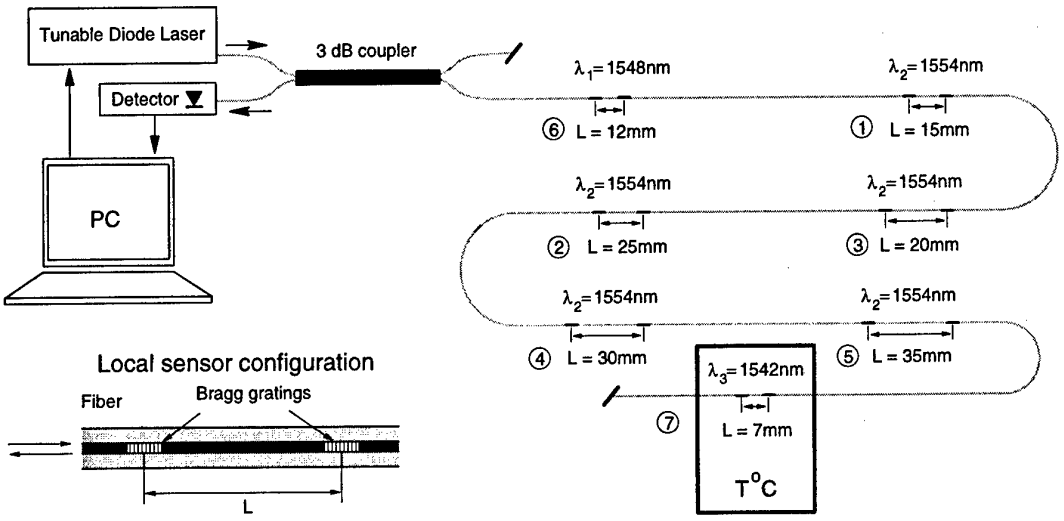

Fig.1 Experimental twin-grating quasi-distributed fiber-optic sensor

0.1C°. To keep a constant temperature during a few minutes for the sensor calibration a stabilized DC power supply was used.

As was shown earlier in [7], the composite reflection spectrum of multi-component twin-grating based fiber optic sensor is a superposition of reflection spectra of all local sensors. A typical example of this composite spectrum is shown in Fig. 2a. This spectrum was recorded using a wavelength step of 0.005 nm and a laser output intensity of 2.0 mW. To separate the signals coming from each sensor we process this composite spectrum using the fast Fourier transform (FFT) algorithm. The result of this operation is shown in Fig. 2b. The five peaks in the figure clearly indicate the presence of the signals from each local sensor. The signals can be demultiplexed using digital filters, whose central frequencies can be tuned to match the modulation frequency of each sensor. The separated signals are shown in Fig. 2c. The influence of the measurand leads to the shift of the reflection spectra. This shift can be evaluated both by analyzing the shift of the envelope function (rough estimation) and by calculation of the phase of the sinusoidal modulation (precise estimation). In practice, filtering is not necessary for measurand evaluation because all the information needed is already located in the frequency components of each signal which have been already separated by FFT. The volume of this summary does not allow us to present the complete analysis that lies in the basis of our processing scheme, so we outline only some basic principles here.

Considering only one local sensor, let's suppose that a change of the measurand leads to a shift of its reflection spectrum:

$$s_1(\lambda) = s_0(\lambda - \lambda_s), \tag{1}$$

where $s_0(\lambda)$ is the spectrum of an undisturbed local sensor, λ_s is the shift caused by the measurand. From Fourier transform theory it is well known that the Fourier transform of the shifted origin produces only phase changes in the resultant pattern. The transformation of the local sensor spectrum in this case is

$$S_1(\nu) = \int_{-\infty}^{\infty} s_1(\lambda) e^{-2\pi i \lambda \nu} d\lambda = S_0(\nu) e^{-2\pi i \lambda_s \nu}. \tag{2}$$

Here $S_0(\lambda)$ is the Fourier transform of the unshifted spectrum of a local sensor. Therefore, analyzing only the phase of the signal components already separated in the Fourier domain one can retrieve the information on the wavelength shift. The evaluation of the correspondent measurand is possible if proper calibration procedure was performed before actual measurements.

Since the phase $\phi(\nu) = -2\pi\lambda_s\nu$ is linearly dependent on the frequency ν, the above mentioned rough estimation of the shift λ_s can be found using a linear regression model for the experimentally obtained (after FFT) phase values of the correspondent Fourier components $S_1(\nu)$. At the next step, to obtain higher precision in the evaluation of the shift the phase can be calculated using only the most powerful (to reduce the influence of inevitable noise) component. Such a combination of almost independent computational procedures allows us to solve $2\pi n$ - related ambiguity problem which occurs when phase of only one component is used. Further precision improvements are also possible if the proposed sensor is used in an environment with slowly changing measurands and additional tracking capabilities are implemented in the processing software.

To test the proposed digital processing procedure and to estimate the precision of our experimental sensor, we performed simultaneously with the recording of the reflection spectra for the local sensor #7 temperature measurements using a thermocouple. After the sensor was calibrated at two different temperatures, the temperatures measured by the thermocouple and the temperatures calculated from the reflection spectra of sensor #7 were plotted. As it was expected, the position of the spectrum calculated by our program was linearly dependent on the temperature. The result is shown in (Fig. 3). The standard error of temperature measurements in this experiment

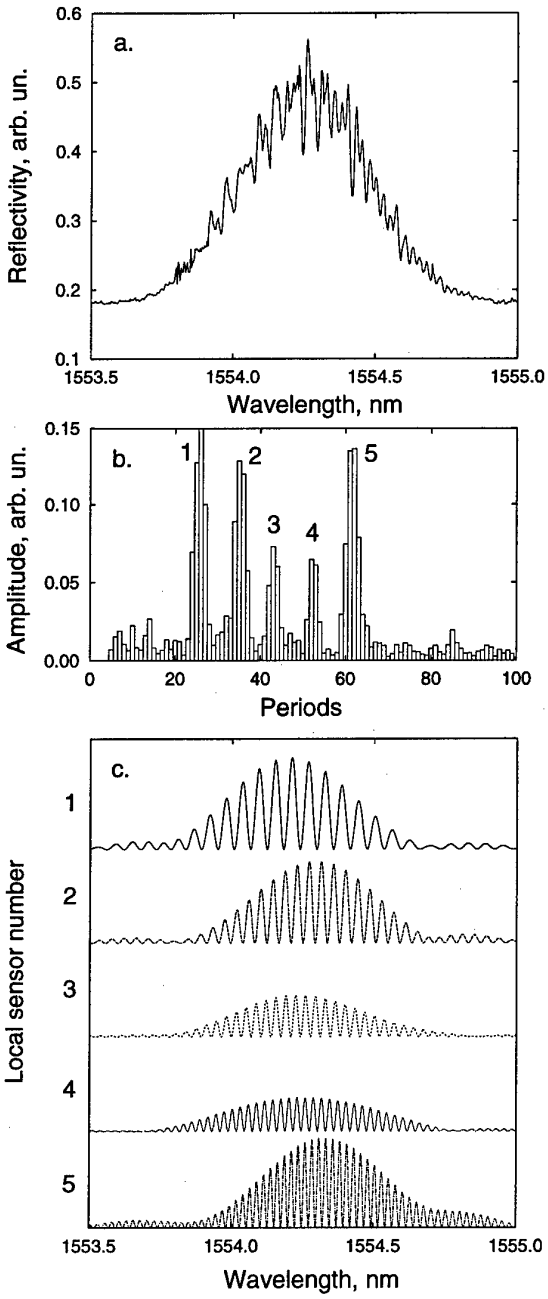

Fig. 2. Composite signal from twin-grating quasi-distributed fiber-optic sensor (a), its Fourier transform (b), and demultiplexed reflection spectra from local sensors 1-5 (c).

did not exceed 0.2C°. The wavelength repeatability of the laser diode was guaranteed by the manufacturer to be within ±0.02 nm. Since this value yields evaluated temperature random error within ±2C°, we can conclude that errors in temperature measurements using the twin-grating sensor do not exceed the expected values. Irregularities in wavelength steps of the laser result in an increased phase noise level thus reducing the accuracy of the sensor. This was predominant source of error in our experiments. We believe it can be significantly reduced by choosing a proper laser construction.

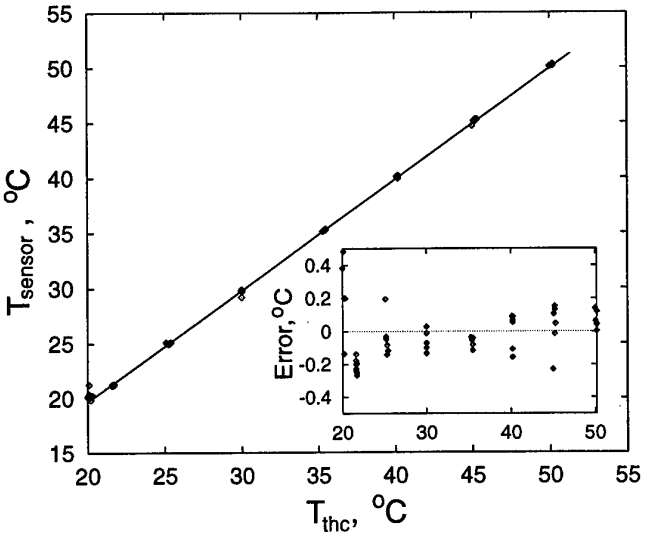

Fig. 3. Temperature measured by calibrated twin-grating sensor (sensor 7 in Fig. 1) vs temperature measured by thermocouple, and their difference.

In conclusion, we have demonstrated a novel quasi-distributed sensor based on a serial array of twin-grating interferometers. The sensor employs low reflective Bragg gratings and is easy to manufacture. The combination of wavelength- and frequency- division multiplexing together with the signal processing algorithm were discussed and tested experimentally.

References:

1. A. D. Kersey et al., "Fiber grating sensors," J. of Lightwave Technology Vol. 15, pp.1442-1462, (1997)
2. A. D. Kersey, M. A. Davis, and D. G. Bellemore, "Development of fiber sensors for structural monitoring," in Proc. SPIE vol. 2456, p. 262 (1995)
3. C. G. Askins, M. A. Putnam, E. J. Friebele, "Instrumentation for interrogating many-element fiber Bragg grating arrays," in Proc SPIE vol 2444, pp.257-266 (1995)
4. T. A. Berkoff, et al., "Hybrid time- and wavelength-division multiplexed fiber Bragg grating sensor array," in Proc. SPIE Vol. 2444, p. 288-294, (1995)
5. Y. J. Rao et al., "Simultaneously spatial-, time-, and wavelength-division multiplexed in-fiber Bragg grating sensor network," in Proc. SPIE Vol. 2838, pp.23-30 (1996)
6. M. G. Shlyagin, S. V. Miridonov, and D. Tentori, "Frequency multiplexing of in-fiber Bragg grating sensors using tunable laser," Proc. SPIE vol. 3099, pp.348-353, (1997).
7. M. G. Shlyagin, S. V. Miridonov, D.Tentori, and J. Castillo "Twin grating-based interferometric fiber optic sensor," in 12th Intern. Conf. on Optical Fiber Sensors, Vol. 16, OSA Technical Digest Series (Optical Society of America, Washington DC, 1997), pp. 472-474, (1997)
8. D. S. Starodubov, V. Grubsky, Jack Feinberg, et al. "Bragg grating fabrication in germanosilicate fibers by use of near-UV light: a new pathway for refractive-index changes," Optics Letters, vol. 22, pp.1086-1088, (1997)

Fiber Bragg Grating with Long Period Fiber Grating Superstructure for Simultaneous Strain and Temperature Measurement

Heather J. Patrick and Sandeep T. Vohra
U.S. Naval Research Laboratory
Washington, DC 20375
ph: 202-767-6337, fax: 202-404-8645
email: hpatrick@ccf.nrl.navy.mil

1. Introduction

Multiplexed FBG strain sensors are currently deployed for the monitoring and analysis of structural loading worldwide. One remaining issue is the separation of the strain-induced wavelength shift from that induced by temperature changes. In dual measurand techniques, strain and temperature are determined from measurements on a pair of sensors which are both sensitive to strain and temperature, but have different responses. Another very simple technique is to use unstrained reference gratings to measure the temperature. However, this precludes embedding the sensors, which is required for many applications.

Recently, we reported on a dual measurand technique which used a single, bare fiber LPG sensor in line with two FBG sensors to simultaneously measure strain and temperature.[1] The LPG and FBG are both in-fiber devices produced by writing a periodic, UV-induced index change into the core of a fiber, but while the period of the FBG is typically 500 nm, that of the LPG is 100-500 μm.[2] Additionally, the LPG acts not as a reflector but as an attenuator in the fiber, producing loss bands at specific wavelengths by coupling light into the fiber cladding. The LPG has a much larger temperature response than the FBG, and a smaller strain response, which enables accurate strain/temperature determination. It has also been shown that an FBG can be superimposed with a longer period superstructure.[3] In this work we show that an FBG can be superimposed with an LPG superstructure, giving a 20-mm long FBG/LPG sensor in which strain and temperature can be simultaneously determined by measuring the wavelength and reflected power from the FBG. The FBG/LPG sensor was also recoated with a low index Teflon coating to ease handling of the sensor.

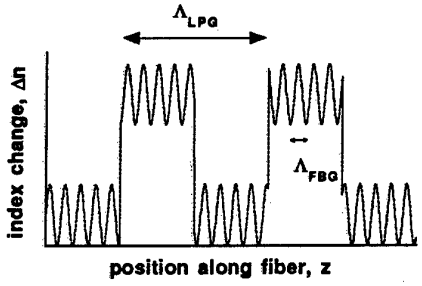

Figure 1: Profile of index of refraction along a section of the superimposed grating.

2. Sensor Fabrication

The FBG/LPG sensor was fabricated in a two-step process in boron-germanium codoped, H_2-loaded fiber by excimer laser exposure. First, the plastic jacket was removed from a short section of the fiber and the FBG was written using a phase mask. The phase mask was then replaced with a dielectric amplitude mask[4] and the exposure continued on the same section of fiber to produce the LPG superstructure. A schematic of the induced index modulation is shown in Fig. 1. The period Λ_{FBG} = 530 nm while Λ_{LPG} = 325 μm. The total length of the FBG/LPG pair was 20 mm. After exposure, the FBG/LPG was annealed at 75 °C 24 h to remove the remaining H_2 from the fiber.

The LPG spectrum displays large wavelength shifts during exposure and annealing[2,4] which were characterized and accounted for when fabricating a sensor. The sensor was then recoated with Dupont Teflon AF, which was applied and cured at 200 °C for few minutes using a recoater designed for application of polyimide coatings.[5] Since the refractive index of the coating is very low (n = 1.29) recoating the LPG with Teflon AF does not reduce the attenuation of the LPG resonance like a typical high-index UV-cured splice recoating material.[2] The only effect of the coating on the spectrum was a -4 nm shift of the LPG center wavelength.

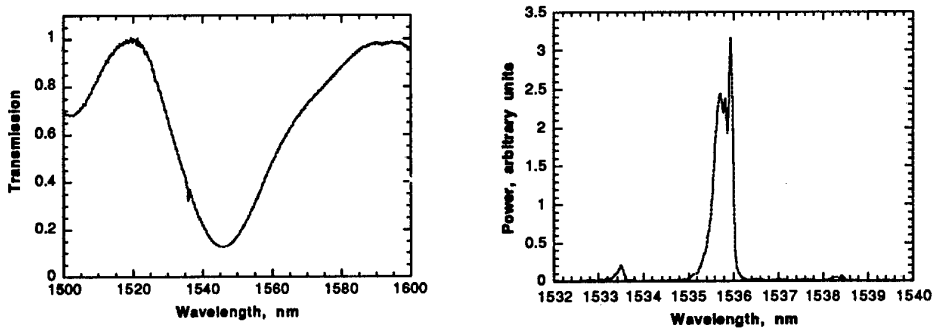

Figure 2: The FBG/LPG superstructure sensor in transmission (left) and reflection (right).

Figure 2 shows the spectrum of the FBG/LPG sensor in transmission and reflection. Both the broad attenuation band of the LPG and the narrow FBG at 1536 nm appear in transmission, while only the FBG appears in reflection. The FBG reflection displays two extra peaks at ± 2.5 nm from the center FBG reflection. These appear at the spatial beat frequencies of the two periodic index structures as described in Ref. 3. While the LPG does not have a reflection spectrum, its attenuation changes the amount of power reflected by the FBG depending on the difference between the FBG and LPG center wavelengths. The center wavelength of the LPG transmission (which is located at 1546 nm in Fig.2) was measured to have a large, negative temperature response (-0.06 nm/°C compared to the 0.01 nm/°C temperature response of the FBG) while the strain responses (0.0004 nm/°C for the LPG, and 0.001 nm/°C for the FBG) are similar. Thus the power reflected by the FBG will change with strain and temperature, and by monitoring both the reflected wavelength and reflected power, strain and temperature can be recovered.

3. Strain and Temperature Separation Experiment

A schematic of the experimental set-up is shown in Figure 3. The temperature of the sensor was controlled by passing it through a hole in an aluminum block which was mounted to a thermoelectric heater-cooler. One end of the fiber was fixed, and the other was attached to a computer-controlled translation stage to control the strain on the fiber. An erbium-doped superfluorescent fiber source (SFS) was used as a broad band light source, and the reflected spectrum (as shown in Fig. 2) was measured using an Ando optical spectrum analyzer (OSA).

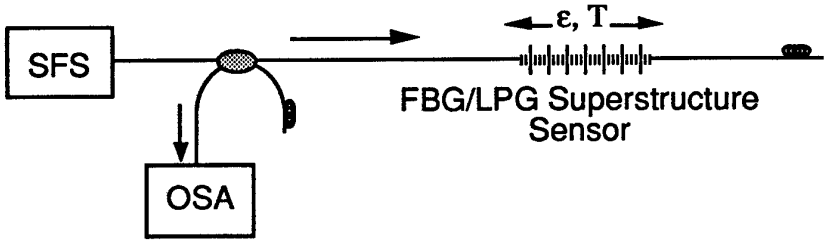

Figure 3: Configuration of the LPG/FBG superstructure sensor strain and temperature test system.

The sensor was calibrated by simultaneously measuring the wavelength of the main FBG reflection peak λ and the reflected power as known strains and temperatures were applied. In order to remove the effect of the SFS spectrum from the variation in reflected power, the reflected power was normalized by dividing it by a stored spectrum of the SFS. In this way the variations in reflected power should arise only from a change in the wavelength difference between the FBG and LPG.

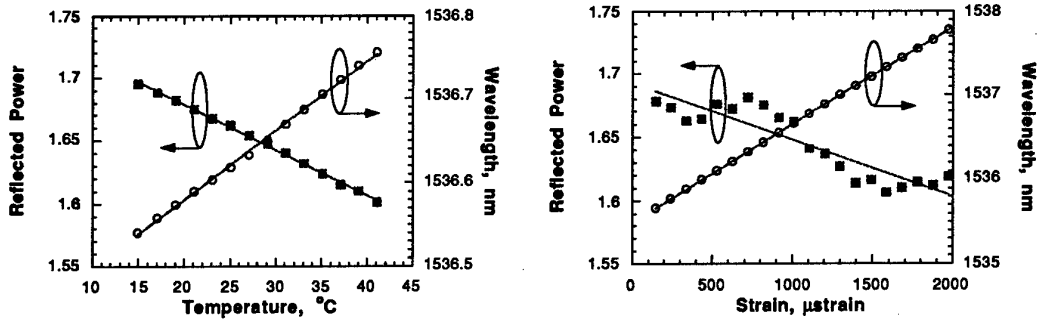

Figure 4: Reflected Power (normalized to SFS spectrum) and center wavelength of FBG reflection vs. temperature while strain held at 1011 μstrain (left) and vs. strain while temperature held at 30.1 °C (right), and linear fits to the data.

The results of the calibrations are shown in Figure 4. On the left is the normalized power and FBG wavelength vs. temperature, and on the right the normalized power and FBG wavelength vs. strain. From this set of measurements, we take the slopes and offsets of R and λ and can then write a matrix equation for the change in R and λ for any applied strain ε and temperature T which is given by:

$$\begin{pmatrix} R - 1.79808 \\ \lambda - 1535.2459 \end{pmatrix} = \begin{pmatrix} -4.4348x10^{-5} & -3.6038x10^{-3} \\ 1.1554x10^{-3} & 8.2321x10^{-3} \end{pmatrix} \begin{pmatrix} \varepsilon \\ T \end{pmatrix} \quad (1)$$

where T is in °C, ε is in μstrain, λ is in nm and R is the normalized integrated power received at the OSA. To determine strain and temperature given R and λ, we invert Eq. 1.

To test the sensor's ability to simultaneously determine strain and temperature from the calibration runs, a set of known strains and temperatures were applied to the sensor, R and λ were measured, and strain and temperature were then calculated from Eq. 1 and compared to the applied values. In the test shown in Fig. 5, the applied strain was increased from 150 μstrain to 2000 μstrain while the temperature was varied over a range of 15-40 °C. To show the quality of the strain measurement over this range, we plot calculated strain vs. applied strain. The applied temperature at each strain point is shown in the inset. The rms deviation of the calculated strain from the applied strain was ± 27 μstrain. Similarly, we compared the measured temperature to the applied temperature, and found that the rms deviation was ± 3.8 °C.

4. Discussion

Although the superstructure FBG/LPG described here is an advance over earlier work in that the sensor is a single, short gauge device, and is recoated for ease of handling, in its present configuration the sensor gives somewhat worse strain and temperature discrimination.[1] The greatest source of error can be seen from Fig. 4 to be the nonlinear variations in R with strain, which can be greater than 1% off the linear fit at some temperatures. The origin of this effect was

found to be a drift in the SFS spectrum as measured by the OSA on a nm scale over a period of minutes to hours. This gives variations in reflected power with wavelength which are unrelated to the strain and temperature of the sensor, and which are more pronounced in the strain calibration

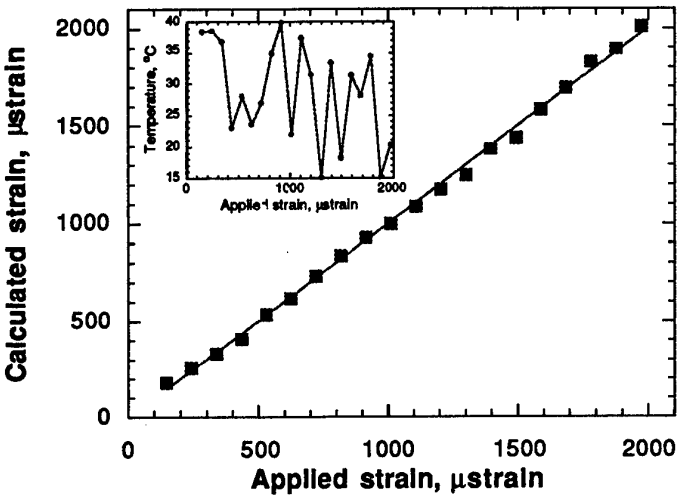

Figure 5: Strain calculated from Eq. 1 vs. applied strain, while temperature of sensor was varied randomly over a 15-40 °C range. Temperature applied at each strain point is shown in the inset.

curves because of the larger wavelength shift. If the drifts inherent in the readout system were reduced below the 0.3% level, it should be possible to measure strain and temperature to ± 10 µstrain and ± 1 °C with the FBG/LPG sensor. Alternatively, the length of the FBG/LPG pair could be increased, narrowing the LPG spectrum,[2] or a fiber which produces LPG's with a larger temperature response could be chosen, which would increase the change in R with temperature. Narrowing the LPG spectrum would also make it possible to multiplex the LPG/FBG sensors.

5. Conclusions

We have demonstrated simultaneous strain and temperature measurement using a short gauge length, recoated FBG/LPG superstructure sensor. The sensor has potential for use in embedded fiber sensor systems and should be compatible with existing reflection-based architectures.

Acknowledgments

We thank Wayne Varner of 3M Fiber Optics Laboratory for providing samples of boron-germanium codoped fiber, and Marty Putnam for assistance with recoating. This work was supported in part by the Office of Naval Research.

[1] H.J. Patrick, G.M. Williams, A.D. Kersey, J.R. Pedrazzani and A.M. Vengsarkar, IEEE Phot. Tech. Lett. **8**, p. 1223, 1996.
[2] A.M. Vengsarkar, P.J. Lemaire, J.B. Judkins, V. Bhatia, T. Erdogan, and J.E. Sipe, J. Lightwave Tech. **14**, p. 58, 1996.
[3] B.J. Eggleton, P.A. Krug, L. Poladian and F. Ouellette, Electron. Lett. **30**, p. 1620, 1994.
[4] H.J. Patrick, C.G. Askins, R.W. McElhanon and E.J. Friebele, Electron. Lett. **33**, p. 1167, 1997.
[5] M.A. Putnam, C.G. Askins, G. Smith, and E.J. Friebele, SPIE vol. 3044, p. 359, 1997.

Differential Mach-Zehnder Detection for Dynamic Fibre-Fabry-Perot Sensors

P.J.Henderson†, N.E.Fisher, D.A.Jackson
Applied Optics Group
School of Physical Sciences, University of Kent, Canterbury, Kent CT2 7NR, UK
Tel: +44 (0) 1227 764000 ext† 3771, Fax: +44 (0) 1227 827558
Email†: p.j.henderson@ukc.ac.uk

L.Zhang, I.Bennion
Photonics Research Group
Department of Electronic Engineering, Aston University, Birmingham B4 7ET, UK
Tel: +44 (0) 121 359 3611, Fax: +44 (0) 121 359 0156

1 Introduction

The all-fibre Mach-Zehnder interferometer (FMZI) is an optical instrument capable of high-resolution phase-analysis[1]. Constructed from a pair of 2×2 couplers spliced back-to-back, FMZIs dispense with the alignment problems of their bulk-optic counterparts, and offer the versatility of easily-implemented heterodyne phase-modulation and dual-output detection. While input intensity-modulation produces in-phase outputs, in the ideal case of lossless FMZI-coupling, input phase-modulation produces anti-phase outputs[2]. With the resulting benefits of efficient power-usage, two-fold heterodyne amplification and rejection of intensity-noise, differential FMZI-processing was first described as a means of suppressing amplitude-fluctuations in diode lasers[3]. Furthermore, pseudo-heterodyne processing using serrodyne phase-modulation within one FMZI-arm results in efficient phase-analysis without the need to maintain quadrature as in homodyne schemes[4]. With the input signal to the FMZI phase-modulated at frequency ω_1, spectral components then arise within the photodetector-outputs comprising a carrier at the serrodyne frequency ω_s and sidebands at frequencies $\omega_s \pm \omega_1$, $\omega_s \pm 2\omega_1$, ... $\omega_s \pm n\omega_1$, with respective amplitudes described by the arguments of the J_1, J_2, ... J_n Bessel functions. For signals with a small modulation index, the J_1 components vary linearly with the amplitude of the input phase-modulation. The advantage with this type of signal-recovery is that it provides immunity to signal-fading within the FMZI caused by random variations in the fibre-optic path-length.

In this paper we discuss dynamic all-fibre sensing utilising differential FMZI-processing of signals from fibre-Fabry-Perot interferometers (FFPIs) with mirrors defined by in-fibre Bragg-gratings (FBGs). Such sensors combine the manufacturing-ease, multiplexing-ability and arbitrary writing-locations of FBGs, with the enhanced sensitivity and selectable sensing-lengths of FFPIs. Phase-modulation, generated by changes in fibre-optic path-length between the FBG-mirrors, has been quantified thus-far by low-coherence heterodyne FMZI-processing using a single detector[5]. We extend the approach by applying balanced differential-detection using two detectors and examine the resulting ability to extract phase-information buried within large amounts of intensity-noise.

2 System

The system can be divided into sensing and local-instrumentation sections as shown in Fig.1.

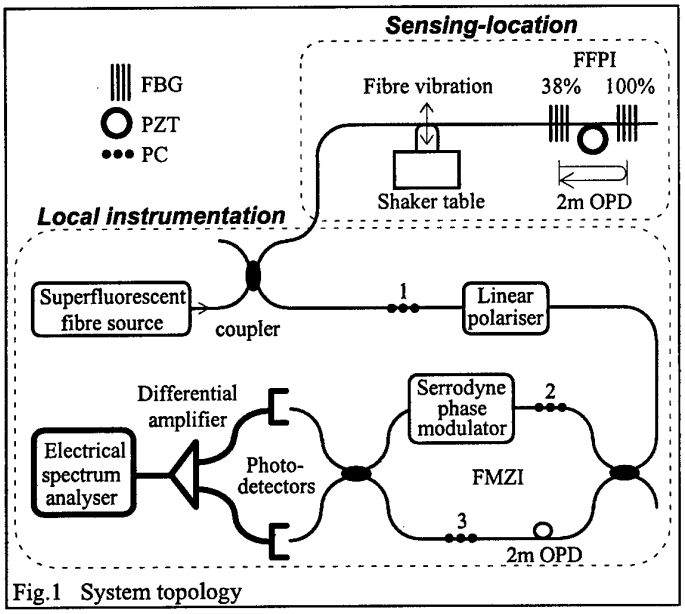

Fig.1 System topology

2.1 Sensing-location

The FFPI has an optical path-difference (OPD) of 2m and its FBG-mirrors have a central wavelength λ_0=1531nm and linewidth $\Delta\lambda$=0.2nm. The mirrors have reflectivities of about 38% and 100% to generate interferometric fringes of maximum contrast[6] - in this case a contrast of 30% is obtained, although 50% is theoretically possible. The FFPI is phase-modulated by tension-wrapping about 39cm of its length around a cylindrical piezoelectric transducer (PZT) and applying a variable-amplitude voltage at frequency ω=775Hz. Additional intensity-noise is induced by vibrating the fibre adjacent to the FFPI at about 3kHz with sufficient amplitude for fibre-bending losses.

2.2 Local instrumentation

Illumination is provided by a 10mW superfluorescent fibre-source of bandwidth $\Delta\lambda$=40nm and central wavelength λ_0=1545nm. Interferometric processing of the reflected FFPI-light requires the OPD between the arms of the FMZI to match that of the FFPI. Although the source has a short coherence-length ($L_c \gg \lambda_0^2/\Delta\lambda \approx 60\mu m$), the tolerance on OPD-matching is not severe since the reflected FFPI-light has a coherence-length of about 12mm defined by the $\Delta\lambda$=0.2nm FBG-linewidth. Thus OPDs of 2m matched to ±6mm are sufficient for interference to be observed.

A lithium-niobate modulator applies serrodyne phase-modulation to one arm of the FMZI at frequency ω_s=5kHz. As only one linear polarisation state is efficiently modulated, an in-fibre linear polariser on the input to the FMZI helps ensure efficient generation of the carrier frequency. Polarisation-controller (PC) 1 is adjusted for maximum transmitted signal in the absence of fibre vibration. PC2 and PC3 are then adjusted to generate >90% modulation contrast at the carrier frequency.

A photodetector is used on each of the FMZI-outputs. The detector-outputs are balanced, then differenced for optimal suppression of intensity-noise, and spectrum-analysed. The output from a single detector is spectrum-analysed for comparitive results without differential processing. Spectral plots are obtained within an electrical bandwidth of 47.742Hz. The sensor is characterised by determining the normalised ratio J_1/J_0 as a function of applied PZT-voltage.

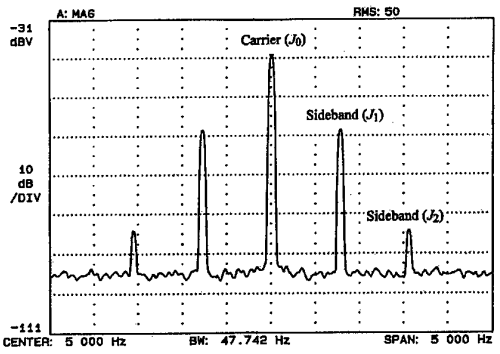

Fig.2 Carrier (J_0) and sensor-induced (J_1, J_2) components

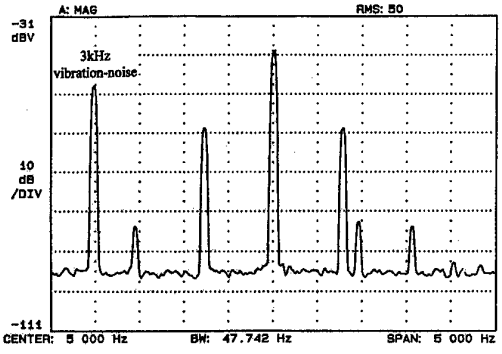

Fig.3 Additional 3kHz intensity-noise due to fibre-vibration

3 Results

3.1 Spectral analysis

With the PZT-voltage set at 4.2Vrms, Fig.2 shows the J_0 and J_1 components obtained using a single detector. (J_2 components are also observed, but are not used in this analysis.) The signal-to-noise ratio for the J_1 components is about 36dBV. Fig.3 shows the effect of applying the 3KHz fibre-vibration. A large homodyne noise-signal appears at 3kHz (together with a component at its first harmonic). Finally, Fig.4 shows the effect of differential detection. The 3kHz noise is suppressed by at least 40dBV. In addition, the signal-to-noise ratio has improved by 6dBV indicating that amplitude-fluctuations due to the source have been successfully rejected.

3.2 Sensor characterisation

A plot of J_1/J_0 (Fig.5) indicates a linear variation of J_1 amplitude with applied PZT-voltage, with a measurement resolution of $6mV/Hz^{-1/2}$. By comparison, a related voltage-measurement scheme utilising a single sensing-FBG and a single photodetector[7] had a resolution of $2V/Hz^{-1/2}$. Differential FFPI-sensing clearly offers the benefits of high dynamic resolution and tailorable sensitivity through choice of FFPI-length.

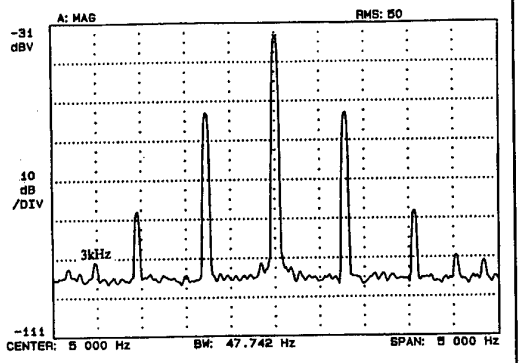

Fig.4 Suppression of 3kHz noise due to differential detection

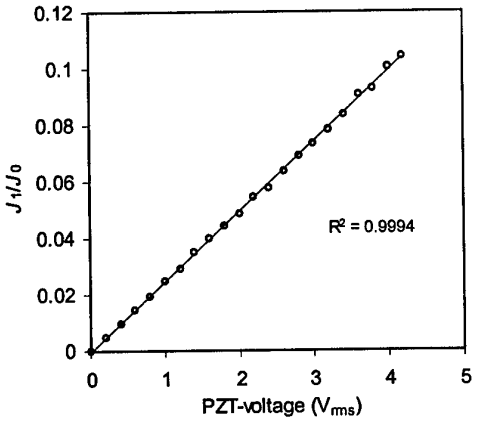

Fig.5 Variation of J_1/J_0 with applied PZT-voltage

4 Conclusions

The application of differential FMZI-detection to signals from a dynamic FFPI-sensor has been demonstrated to give a noise-rejection of better than 40dBV compared to similar systems using a single detector. With the additional benefits of high resolution and tailorable sensitivity, the scheme is particularly applicable to monitoring in noisy environments such as in the vicinity of overhead power-lines or electrical machinery.

Note, that to avoid cross-talk with other parameters (such as temperature), which also induce changes in FFPI-phase, the parameter to be measured must have a higher modulation-frequency. Also, polarisation changes within the FFPI may lead to a loss of signal, so that a practical FFPI-sensor may need a means to prevent excess bending and possibly the use of polarisation maintaining fibre. Finally, it is essential that the spectra of the FBG-mirrors always overlap. As differential temperatures and strains lead to relative changes in Bragg wavelength, practical applications may require strain-isolated FBGs of increased linewidth.

5 References

[1] D.A.Jackson, A.Dandridge, S.K.Sheem, Measurement of small phase shifts using a single-mode optical-fiber interferometer, Opt.Lett., vol.5, no.4, pp.139-141, (1980)

[2] T.Waite, A balanced mixer for optical heterodyning: the magic T optical mixer, Proc.IEEE, vol.54, pp.334-335, (1966)

[3] A.Dandridge, A.B.Tveten, Noise reduction in fiber-optic interferometer systems, App.Opt., vol.20, no.14, pp.2337-2339, (1981)

[4] D.A.Jackson, Monomode optical fibre interferometers for precision measurement, J.Phys.E: Sci.Instrum., vol.18, pp.981-1001, (1985)

[5] P.J.Henderson, Y.J.Rao, D.A.Jackson, Simultaneous dynamic-strain and temperature monitoring using a wavelength-multiplexed fibre-Fabry-Perot array with low-coherence interrogation, in 12th International Conference on Optical Fiber Sensors, Vol.16, OSA Technical Digest Series (Optical Society of America, Washington DC, 1997), pp.56-59, (1997)

[6] J.Meyer, S.J.Spammer and P.L.Swart, All fiber Fabry-Perot interferometer using coherence demultiplexing and fibre loop reflectors, Proc SPIE, Vol.2071, pp.169-179, (1993)

[7] N.E.Fisher, P.J.Henderson, D.A.Jackson, The interrogation of a conventional current transformer using an in-fibre Bragg grating, Meas.Sci.Technol., vol.8, pp.1080-1084, (1997)

A Genetic Algorithm for the Inverse Problem in Synthesis of Fiber Gratings

Johannes Skaar

Department of Physical Electronics

Johannes.Skaar@fysel.ntnu.no
Fax: +47 73 59 14 41
Phone: +47 73 59 14 32

Knut Magne Risvik

Algorithm Construction Group
Department of Computer and Information Science

kmr@idi.ntnu.no
Fax: +47 73 59 44 66
Phone: +47 73 59 44 89

The Norwegian University of Science and Technology (NTNU)
N-7034 Trondheim
NORWAY

Abstract

A new method for synthesis of fiber gratings with advanced characteristics is proposed. The method is based on an optimizing genetic algorithm, and facilitates the task of weighting the different requirements to the filter spectrum.

A classical problem in applied physics and engineering fields is the inverse problem. An example of such a problem is to determine a fiber grating index modulation profile corresponding to a given reflection spectrum. This is not a trivial problem, and a variety of synthesis algorithms has been proposed [1]-[3].

For weak gratings, the synthesis problem of fiber gratings reduces to an inverse Fourier transform of the reflection coefficient. This is known as the first-order Born approximation, and applies only for gratings for which the reflectivity is small. Another solution to this problem was found by Song and Shin [2], who solved the coupled Gel'fand-Levitan-Marchenko (GLM) integral equations that appear in the inverse scattering theory of quantum mechanics. Their method is exact, but is restricted to reflection coefficients that can be expressed as a rational function. An iterative solution to the GLM equations was found by Peral et. al. [3], yielding smoother coupling coefficients than the exact method. Their algorithm is converging relatively fast, and gives satisfying results even for high reflectivity gratings. However, when specifying ideal, unachievable filter responses, it is desirable to have a weighting mechanism, which makes it easier to weight the different requirements. For example, when synthesizing an optical bandpass filter, one may be interested in weighting linear phase more than sharp peaks, because the dispersion may be a more critical parameter. The iterative GLM method does not support such a mechanism in a satisfactory way.

SPIE Vol. 3483 • 0277-786X/98/$10.00

In this paper we present a new approach to the solution of inverse problems, in particular the problem of synthesizing waveguide gratings. The coupling coefficient is sampled, and the N samples are applied as inputs to a "black box". The "black box" calculates the reflection spectrum by using Runge-Kutta's method [2] and calculates the difference between this spectrum and the aimed reflection spectrum. This error value is the output of the "black box" to be minimized in order to achieve the aimed reflection spectrum. Thus, the synthesis problem is reduced to a minimization of a nonlinear function of N variables. This optimization problem is solved using a Genetic Algorithm (GA) [4], i.e. an algorithm that follows the same principle as the evolution process of nature.

Because the grating must have finite length, the aimed reflection spectrum is generally unachievable. Hence, the synthesized filter must be a compromise between different filter spectrum requirements. The form of the error function will decide how the grating will be optimized since the error value will be used as the individual fitness value for the GA. Two examples of error functions are given by

$$err\{r_{\text{calc}}, r_{\text{target}}\} = \sum_j \left(|r_{\text{target},j}|^p - |r_{\text{calc},j}|^p \right)^2 \tag{1}$$

$$err\{r_{\text{calc}}, r_{\text{target}}\} = \max_j \left\{ \left| |r_{\text{target},j}|^p - |r_{\text{calc},j}|^p \right| \right\} \tag{2}$$

where $r_{\text{calc},j}$ and $r_{\text{target},j}$ denote the jth complex value of the calculated spectrum and the target spectrum, respectively, and p is a parameter. For simplicity, we are only considering the amplitude spectrum, but the phase spectrum may also be taken into account, for example by choosing an error function weighting the phase and amplitude separately.

The process of optimizing the "black box" error value can be illustrated using the pipeline in Figure 1.

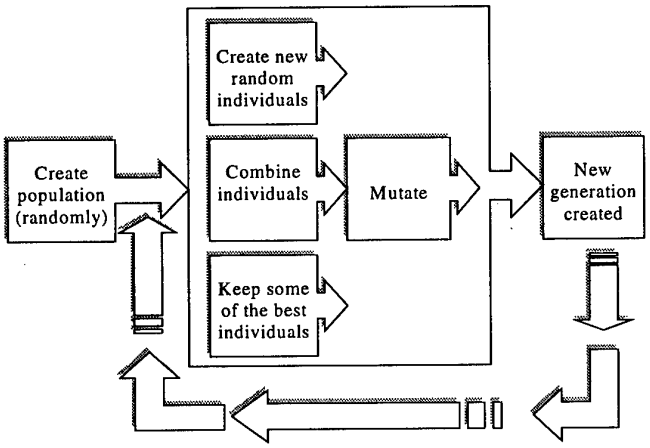

Figure 1 - GA pipeline

To create random solutions we create coupling coefficient vectors of size N of random values. However, since we have some domain knowledge of our problem, we can put a threshold on the random values. By investigating the coupled mode equations, we have found that by limiting the coupling coefficient to real values, we will get a symmetric reflectivity spectrum. Consequently, the random vector values should reside in a range $[-t, t]$, where t corresponds to the maximum achievable coupling coefficient.

When creating a new generation, we will always keep a certain percentage of the best individuals from the last generations unaltered. We also combine individuals from the last generation to create new offsprings, and create some new (random) individuals. When selecting the individuals for crossover, each individual has a probability to be used in a crossover that is related to the fitness of that individual. That is, a very fit individual is more likely to be used in a crossover than a poorly fit individual. After a crossover is performed, there is a slight possibility that the newly created offspring will be mutated. That is, for some of the newly created offsprings, we introduce a random value in the string of values.

An interesting application of the synthesis algorithm is to synthesize a fiber optic bandpass filter. The target bandpass filter is characterized by

$$\left|r_{\text{target}}(\delta)\right| = \begin{cases} 1, & |\delta| < a \\ 0, & |\delta| > a \end{cases} \tag{3}$$

where δ is a detuning parameter, and $2a$ refers to the width of the filter. We have applied (3) as input to our implemented algorithm using the error function (1) with p=1.5. The resulting coupling coefficient is shown in Figure 2, and is compared to the resulting coupling coefficient from the iterative GLM algorithm [3] using a non-linear minimum phase of $r(\delta)$ ("causal") and 12 iterations. The grating lengths are

3.1cm, and the corresponding reflection spectra are shown in Figure 3. The skirt steepness of the final genetic bandpass filter is somewhat higher than for the GLM filter, while the side lobes are slightly less for the GLM filter. In order to suppress the side lobes of the GLM filter, the resulting coupling coefficient is multiplied by a half Hamming window, i.e. a window function for which the top value matches the start position of the grating (z=0). Due to the truncation of the coupling coefficient, it is necessary to multiply this intermediate coupling coefficient by a constant to achieve the desired reflectivity of 99%.

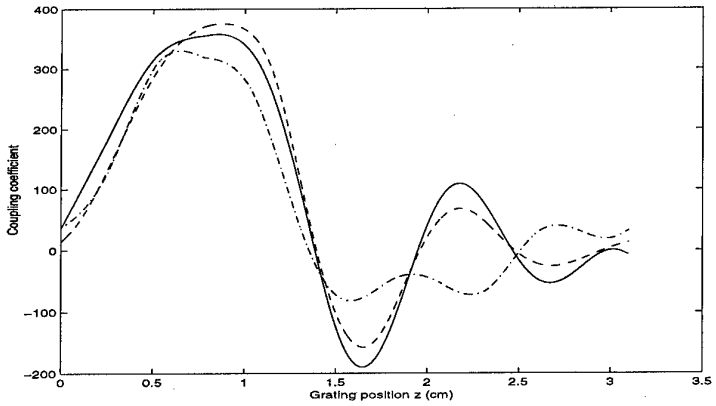

Figure 2: The coupling coefficient of the genetic bandpass filter after 5 minutes of " evolution", (dashdotted line), final result (solid line), and the causal GLM bandpass filter (dashed line).

By using our algorithm, it is not necessary to multiply the coupling coefficient by a window function or a final constant. However, the choice of an error function is very important, because it determines to what extent low side lobes or low pass band ripple is preferred. By choosing a different error function, other filter parameters may be optimized. This is not trivial when using the iterative GLM algorithm, because the optimization cannot be controlled.

The main drawback with our method is the running time. For the problem described above, an acceptable solution was found after 5 minutes, and the results given below were found after a couple of hours using a Pentium 150MHz PC. For comparison, the running time of the iterative GLM method is about a minute. However, GAs exploit a natural parallel form, which makes them ideal for parallel implementation. This has been verified by a supercomputer implementation, which showed that the speedup was approximately proportional to the number of processing units.

It is also worth mentioning that the resulting index modulation profiles from the synthesis algorithm can be written into fibers by using for example the method described by Asseh et al. [6].

In conclusion, a novel method for synthesizing fiber gratings is proposed. The algorithm is made by combining the Runge-Kutta analysis method and a genetic algorithm, which is analogous to the evolution process in nature. The numerical

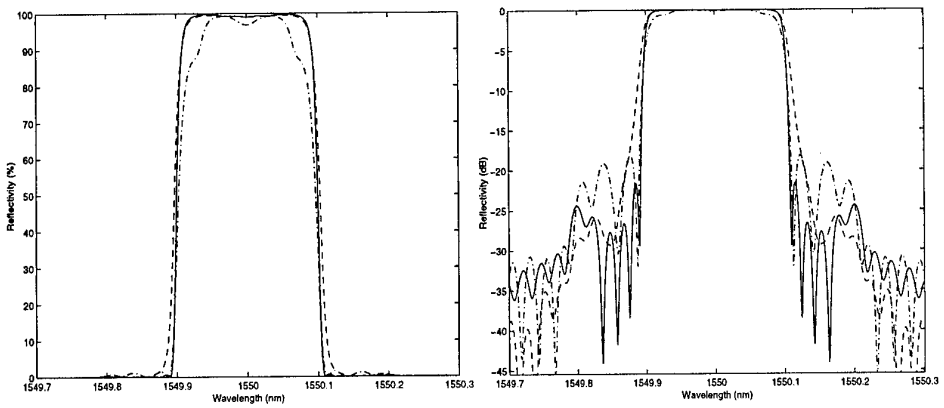

Figure 3: Calculated reflection spectrum for the intermediate genetic bandpass filter (dashdotted line), the final genetic filter (solid line) and the causal GLM bandpass filter (dashed line).

example presented shows that the method gives results that, for our case, are better than the results obtained by the iterative GLM synthesis algorithm. In addition, the proposed method greatly reduces the problem of weighting the different requirements to the filter response of a fiber grating.

Acknowledgements

This work has received support from The Research Council of Norway (Programme for Supercomputing) through a grant of computing time. The GP++ genetic programming library (Svingen, [5]) was used to do the genetic programming.

References

[1] K. A. Winick and J. E. Roman, "Design of corrugated waveguide filters by Fourier transform techniques," IEEE Journ. of Quantum Electronics, vol. 26, pp. 1918-1929, Nov. 1990.

[2] G. H. Song and S. Y. Shin, "Design of corrugated waveguide filters by the Gel'Fand-Levitan-Marchenko inverse-scattering method," J. Opt. Soc. Amer., vol. 2, no. 11, pp. 1905-1915, Nov. 1985

[3] Eva Peral, José Capmany, and Javier Marti, "Iterative solution to the Gel'Fand-Levitan-Marchenko coupled equations and application to synthesis of fiber gratings," IEEE Journ. of Quantum Electronics, vol.32, no. 12, pp. 2078-2084, Dec. 1996

[4] Z. Michalewicz. "Genetic Algorithms + Data Structures = Evolution Programs", Springer-Verlag, 1992.

[5] B. Svingen, "GP++ an introduction", Late breaking papers at the 1997 Genetic Programming Conference", pp. 231-239, Stanford University, CA, USA, 1997

[6] A. Asseh, H. Storøy, B.E. Sahlgren, S. Sandgren, and R. Stubbe, "A writing technique for long fiber Bragg gratings with complex reflectivity profiles, " Journal of Lightwave Technology, vol.15, no.8, August 1997.

Extended Range Interrogation Scheme for Fibre Bragg Grating Sensors Using a Multimode Laser Diode

P J Moreira[b,a], L A Ferreira[a], J L Santos[b,a] and F Farahi[c]

a Unidade de Optoelectrónica, INESC - Porto
b Departamento de Física da Faculdade de Ciências da Universidade do Porto
Rua do Campo Alegre, 687, 4150 Porto, Portugal.
Tel. +351 2 6082601, Fax. +351 2 6082799, email lferreir@goe.fc.up.pt

c Physics Department, University of North Carolina at Charlotte
Charlotte, NC 28223, U.S.A.
Tel. +1 704 5472818, Fax. +1 704 5473160, email ffarahi@uncc.edu

1. Introduction

Fibre Bragg grating has become the most attractive intrisic fibre sensor in recent years for various reasons [1-4]. One of the major advantage of this type of sensor is attributed to wavelength encoded information provided by the Bragg grating when affected by the mensurand. Since the wavelength is an absolute parameter, signal from a Bragg grating may be processed such that its information remain immune from power fluctuations along the optical path. Other advantages are the small size, rugged and intrinsic nature of these structures, as well as their multiplexing capability.

In order to fully utilise the advantages offered by this type of sensors, it is essencial to develop a demodulation scheme that translates the wavelength encoded signal from sensor into a correspondent signal more amenable to conventional electronic processing. This has been an active research field in the context of fibre Bragg sensing. Schemes have been proposed based on bulk filters [5], fibre edge filters [6,8], edge optical source spectrum [9], edge fibre grating spectrum [10], edge detector spectral response [11], tunable fibre filters [12], tunable acousto-optic filters [13], tunable single mode laser diodes [14], receiving fibre Bragg gratings [15-17], interferometric detection [18], fibre lasers [19] and Fourier techniques [20,21].

In a previous paper, the authors proposed a demodulation scheme for fibre Bragg grating sensors which is based on a receiving grating with its Bragg wavelength ramped by a strain induced sawtooth waveform [22]. The measurand information has been recovered by measuring the phase difference between the first harmonic (carrier) of the signal reflected by the receiving grating and the first harmonic of the sawtooth waveform. The main characteristic of the scheme was the fact that both the sensor status and the sensor sensitivity to the measurand action were found to be independent of the optical power level in the system (for power levels larger than the equivalent noise power level). However, the dynamic response of such a system is limited due to the practical constrain in generating a modulated wavelength via periodic application of strain to the reference grating. This problem was later resolved by using a ramped multimode laser diode and eliminating the reference grating [23]. As indicated by the authors in that work, the reasons for using a multimode laser diode are insensitivity of spectrum of such laser to back reflected light from the system (specially when lateral modes are considered), and the potencial to extend the measurand range by using more than one mode in the laser spectrum. In this paper, that possibility is demonstrated.

2. Experiment, results and discussion

The experimental set-up is shown in figure 1. A pigtailed multimode laser diode (FUJITSU FLD130C2LK/352) with spectrum centred at 1318 nm at 25 °C was used to illuminate the sensing fibre Bragg grating through a 3 dB coupler. With no strain applied to the grating (fabricated using the phase mask technique), its characteristics were λ_B=1304.4 nm and $\delta\lambda \approx 0.2$ nm. By tuning the laser temperature, the laser spectrum was shifted to ensure that lateral modes were always present in the Bragg wavelength interval defined by the strain measurement range. This procedure also eliminates system sensitivity to back reflected light coupling into the laser cavity.

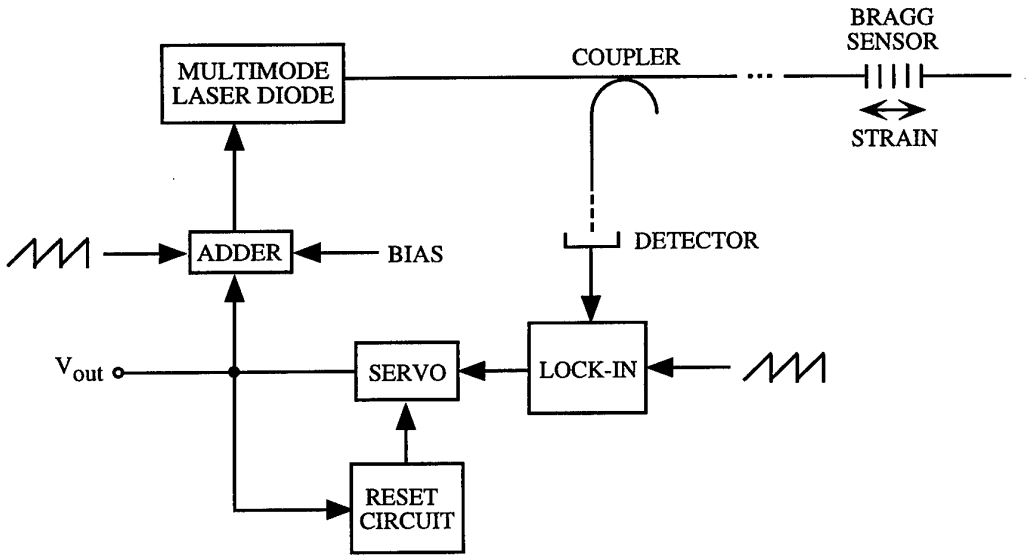

Fig.1 Experimental set-up.

The laser spectrum was ramped at 518 Hz by applying a sawtooth waveform to its injection current. The light reflected by the grating was detected and after amplification the phase of the voltage signal was compared with the phase of the sawtooth waveform using a lock-in. Its voltage output, proportional to the measured phase difference, acted as an error signal to the servo. This produces a change in the laser injection current and keeps the relative position of the laser spectrum and grating wavelength unchanged. To utilise more than one mode of the laser, the servo output (also system output, V_{out}) was allowed to change only in the interval [-0.57, 0.57] V, corresponding to a laser diode injection current variation of ≈70 mA (which induces a spectrum shift of ≈0.8 nm, slightly larger than the laser mode separation, 0.75 nm). When V_{out} reaches one of the limits of the above interval, a reset circuit sets V_{out} to the symmetric limit and the system moves to lock from that position, that is, system is locked to an adjacent mode. The bandwidth of the tracking system is ≈1 Hz, essentially defined by the time constants of the integration circuit and lock-in amplifier.

Figure 2 shows the system output when strain is applied to the sensing grating in a range large enough to sweep four laser modes. When the discontinuities associated to the laser mode jumps are eliminated, results in a linear behaviour evident in figure 3, where the lines for increasing and decreasing strain are shown. The histeresis observed was attributed to the

mechanical system utilised to apply strain to the grating. The maximum strain level that was possible to apply to the grating was 4800 με, a point at which the fibre broke (seven laser modes were swept). Figure 4 shows the correspondent results. It is clear the linear behaviour of the measurement system up to these large strain values, with a slope of 1.41 V/mε. The static strain sensitivity was found to be $0.08\ \mu\varepsilon/\sqrt{\text{Hz}}$. Therefore, the system dynamic range was evaluated as 95 dB.

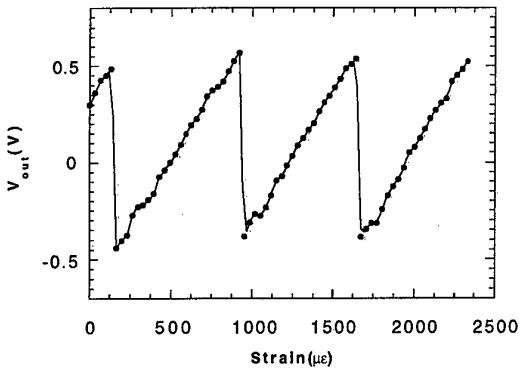

Fig.2 System output versus strain applied to the sensing grating.

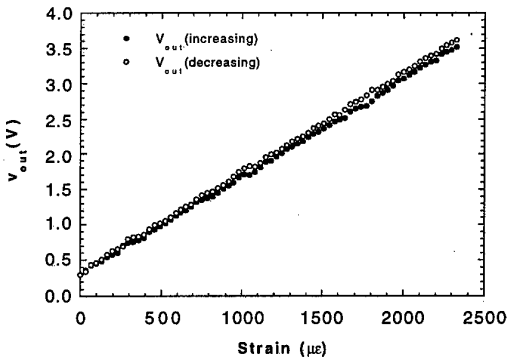

Fig.3 System output versus strain applied to the sensing grating (increasing and decreasing).

It has been shown that when sensing gratings are illuminated by optical sources emitting polarised light, aleatory measurement errors can occur [24]. This is so because, in general, the grating fabrication process generates structures which are anisotropic. Therefore, the characteristics of light reflected by these devices will depend on the polarisation of light incident on them, which changes randomly under the effect of perturbations coupled to the lead fibre. Naturally, it is highly desirable to have a fibre Bragg grating demodulation scheme which is immune to this phenomena. Since the multimode laser diode utilised in the described experiment is a polarised optical source, the performance of the proposed demodulation scheme to the effect described above was tested. For this purpose, during a strain measurement process the polarisation state of light that illuminates the grating was changed by modifying the lead fibre. The result is illustrated in Figure 5, which indicates that the measurement is not affected by the polarisation change. It was observed that the shape of the waveform returned by the grating is indeed dependent on the input polarisation state. However, the phase of the first harmonic of this waveform is remarkably insensitive to variations of that state, which explains the effectiveness of the proposed demodulation scheme on these conditions.

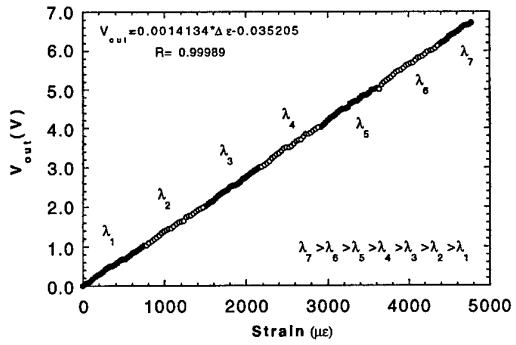

Fig.4 System output versus applied increasing strain up to its maximum value.

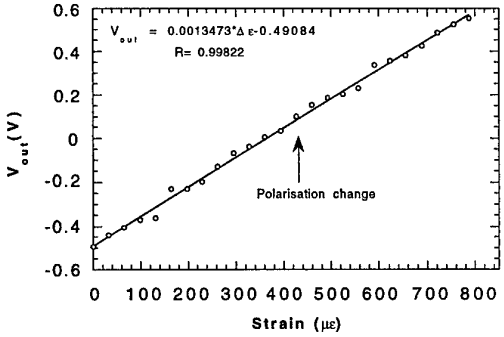

Fig.5 Strain measurement when the light polarisation state changes.

A mechanical device is under development which will allow to apply compressive and extensive strain to the sensing fibre grating. With that, we expect to demonstrate that the proposed interrogation technique is able to recover a measurement range larger than the one reported in this work.

3. Conclusion

An extended range interrogation scheme for fibre Bragg grating based sensors using a multimode laser diode was demonstrated. A dynamic range of 95 dB was achieved. It was also verified that a fibre Bragg sensor using this demodulation scheme is insensitive to variations in the state of polarisation of input light.

Acknowledgements. P J Moreira and L A Ferreira acknowledge financial support from "Programa PRAXIS XXI". F Farahi acknowledge support from NSF grant DMI-9413966.

References

[1] K. O. Hill, G. Meltz, J. Lightwave Technol., 15(1997), 1263.
[2] A. D. Kersey, M. A. Davis, H. J. Patrick, M. LeBlanc, K. P. Koo, C. G. Askins, M. A. Putnam, E. J. Friebele, J. Lightwave Tecnol., 15(1997), 1442.
[3] A. Othonos, Rev. Sci. Instruments, 68(1997), 4309.
[4] Y. J. Rao, Meas. Sci. Tecnology, 8(1997), 355.
5] S. M. Melle, K. Liu, R. M. Measures, Appl. Opt., 32(1993), 3601.
[6] M. A. Davies, A. D. Kersey, Electron. Lett., 30(1994), 75.
[7] Q. Zhang, D. A, Brown, H. Kung, J. E. Townsend, M. Chen, L. J. Reinhart, T. F. Morse, Electron. Lett. 31(1995), 480.
[8] A. B. Lobo Ribeiro, L. A. Ferreira, M. Tsvetkov, J. L. Santos, Electron. Lett., 32(1996), 382.
[9] L. A. Ferreira, J. L. Santos, Pure Appl. Opt., 5(1996), 257.
[10] A. D. Kersey, M. A. Davies, T. Tsai, OFS 11(1996), 634.
[11] T. Coroy, R. M. Measures, Electron. Lett., 32(1996), 1811.
[12] A. D. Kersey, T. A. Berkoff, W. W. Morey, Opt. Lett., 18(1993), 1370.
[13] M. G. Xu, H. Geiger, J. L. Archambault, L. Reekie, J. P. Dakin, Electron. Lett, 29(1993), 1510.
[14] J. D.R. Hjelme, L. Bjerkan, S. Neegard, J. S. Rambech, J. V. Aarsnes, Appl. Opt., 36(1997), 328.

[15] D. A. Jackson, A. B. Lobo Ribeiro, L. Reekie, J. L. Archambault, Opt. Lett., 18(1993), 1192.
[16] M. A. Davis, A. D. Kersey, Electron. Lett., 31(1995), 822.
[17] R. W. Fallon, L. Zhang, A. Gloag, I. Bennion, Electron. Lett.,33(1997), 705.
[18] A. D. Kersey, T. A. Berkoff, W.W. Morey, Electron. Lett., 28(1992), 236.
[19] S. M. Melle, A. T. Alavie, S. Karr, T. Coroy, K. Liu, R. M. Measures, IEEE Photon. Technol. Lett., 10(1992), 516.
[20] M. A. Davis, A. D. Kersey, J. Lightwave Technol., 13(1995), 1289.
[21] D. A. Flavin, R. McBride, J.D.C. Jones, Electron. Lett.,33(1997), 319.
[22] L. A. Ferreira, J. L. Santos, F. Farahi, IEEE Photon. Technol. Lett., 9(1997), 487.
[23] L. A. Ferreira, J. L. Santos, E. V. Diatzikis, F. Farahi, OFS 12(1997), 150.
[24] W. Ecke, J. Schauer, K. Usbeck, R. Willsch, OFS 12(1997), 484.

METAL-COATED OPTICAL FIBRE BRAGG GRATING FOR ELECTRIC CURRENT SENSING

P. M. Cavaleiro, F. M. Araújo and A. B. Lobo Ribeiro [1]

Unidade de Optoelectrónica, INESC - Porto, R. Campo Alegre 687, 4150 Porto, PORTUGAL.
Phone: +351-2-6082601, Fax: +351-2-6082799, email: pmcaval@goe.fc.up.pt

[1] Also with: Dept. Ciência e Tecnologia, Univ. Fernando Pessoa, Praça 9 Abril 349, 4200 Porto, Portugal.

The use of optical fibres as sensing elements for electric current measurement has been developed by several methods such as those utilising magnetic field to generate the Faraday effect [1], magnetomotive force to make fibres bend [2], magnetostrictive material bonded on a fibre to constrict or lengthen the fibre [3], and heating effect to change the fibre's length and refractive index [3]. In all of the above methods, perturbations (e.g., magnetic field, pressure, strain and temperature) are induced by the measurand, i.e., the electric current, accordingly resulting in change of the optical fibre characteristics and then modulation of the light within the fibre. Recently, it has been shown that a system employing a fibre Bragg grating bonded to a piezoelectric transducer (PZT) in conjunction with an optical fibre Mach-Zehnder interferometer [4] can be constructed to measure alternating currents. There are, however, several disadvantages to the PZT scheme: 1) comparatively high voltages must be applied to the PZT; 2) the PZT's are fairly bulky and their frequency response is limited by circumferential resonance; 3) as an hybrid current sensor, in real applications they need a calibrated shunt resistor ('*burner*') which will increase considerably the cost of the system.

The sensitivity of optical fibres to minute changes in temperature suggests their potential use to measure electric current. The electric current measurement using the thermal characteristics of optical fibres was already implemented many years ago by detecting the heat generated by the electric current flowing through metallic coating on the fibre using a fibre Mach-Zehnder interferometer [3]. The strains and refractive index changes resulting from thermally induced stresses in the fibre alter the phase of the light propagating through it. However, unwanted changes in the amplitude of the detected signal, caused by differential drift in the arms of the interferometer, need to be eliminated through the use of an electronic compensation scheme.

This paper describes a current sensor device which utilises this temperature sensitivity to modulate the wavelength of the light reflected by an optical fibre Bragg grating (FBG). In the present work, the temperature change and, consequently, the wavelength change, is accomplished by passing electric current through a thin conductive coating on the surface of a short length of fibre where the fibre grating is located. The measurement of the Bragg wavelength shift produced by the heating effect is obtained using a passive all-fibre demodulation scheme previously described by one of the authors [5]. The aim of the scheme is to combine the resolution of a conventional current transformer (CT) with the electrical insulation achievable with a fibre optic system.

The configuration of the optical fibre current sensor system is shown in Fig. 1. A pigtailed superluminescent diode (Superlum SLD 361), emitting at 830 nm with ≈2mW optical power and ≈20 nm linewidth, was used to illuminate the metal-coated FBG via one port of a standard

3 dB fibre coupler (C_1). The FBG was written using the phase mask method in a hydrogen loaded standard singlemode fibre, and demonstrated a Bragg wavelength of ≈836 nm at room temperature, with a reflectivity ≈85% and bandwidth of ≈0.3 nm. The inset box of Fig. 1 depicts the FBG coated with a ≈1.4 mm layer of low ion conductive pure silver epoxy. Electrical contacts were made at both ends of the coated region (typically 2 cm long and having a ≈1.2 Ω total resistance). The electrical current to be measured (I_P) is converted by the CT (a Rogowski' coil with a current conversion of 4000:1) to a secondary current (I_s), which is passed directly through the metallic coating of the FBG. Since the FBG period and hence the reflected Bragg wavelength are dependent on the temperature or strain of the fibre, the $I_s^2 R$ heating produced by the secondary current (ranging form 0 to 1 A) in the FBG metal coating will shift the Bragg wavelength, and thus by monitoring this shift the value of the electrical current was recovered.

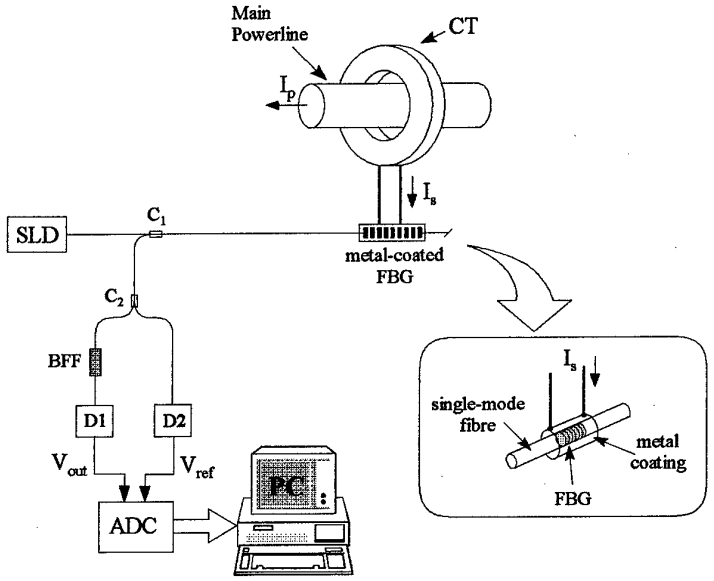

Fig. 1 Schematic design of the fibre-optic current sensor (inset box: the metal-coated FBG sensor head).

The returned wavelength component from the FBG was split by a second 3dB fibre coupler (C_2) into two paths: in one path the intensity was directly measured while in the other is passed through a biconical fibre filter (BFF) before reaching the detector. The BFF was fabricated with an oscillation period of ≈3.5 nm and an extinction ratio of ≈8.1 dB. Over the working range of the FBG (835.9 - 836.8 nm) the BFF had near linear response of ≈7 dB/nm, as shown in Fig. 2(a). The Bragg wavelength variation of the FBG as a function of the squared applied secondary DC current is shown in Fig. 2(b). To measure the wavelength shift of the FBG, and consequently the secondary electrical current, the ratio of the two detected intensities was implemented by software using the LabView™ program. In this way, compensation is performed for time-varying intensity fluctuations and spectral intensity variations of the broadband source, and also for any coupling loss and microbend fluctuations up to coupler C_2.

The response of the current sensor to an alternating current is composed of two components, i.e., an AC component at twice the driving frequency (this terms predominates at low frequencies), and DC term which predominates at high frequencies. Both terms are proportional to the square of the electrical current. Fig. 3 shows the sensor output response to a sinusoidal secondary current with frequency 50 Hz and driving RMS current ranging from 0.07 A up to 0.4 A. It should be pointed out that these results were obtained without the CT and were simulated using a laboratory variable current source with capability to change the shape, frequency and amplitude of the test current signal applied to the metal-coated FBG.

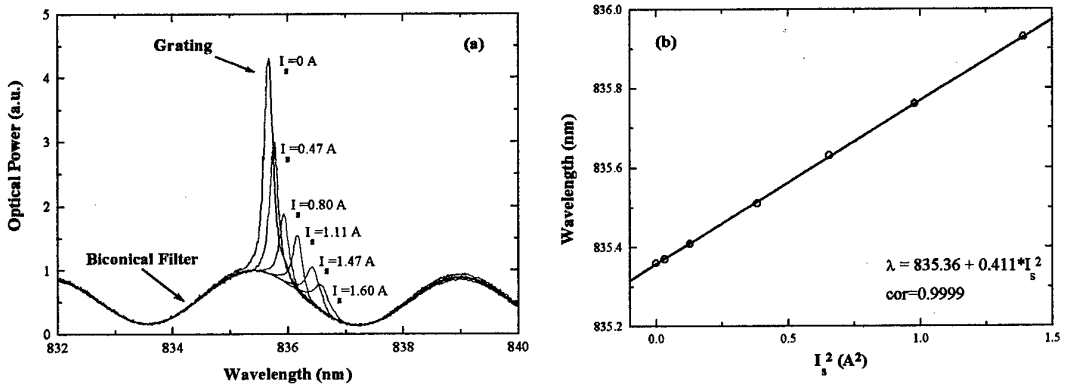

Fig. 2 (a) Biconical fibre filter transfer function superimposed with the FBG spectra for different values of the secondary current. (b) Bragg wavelength shift as a function of the squared secondary current.

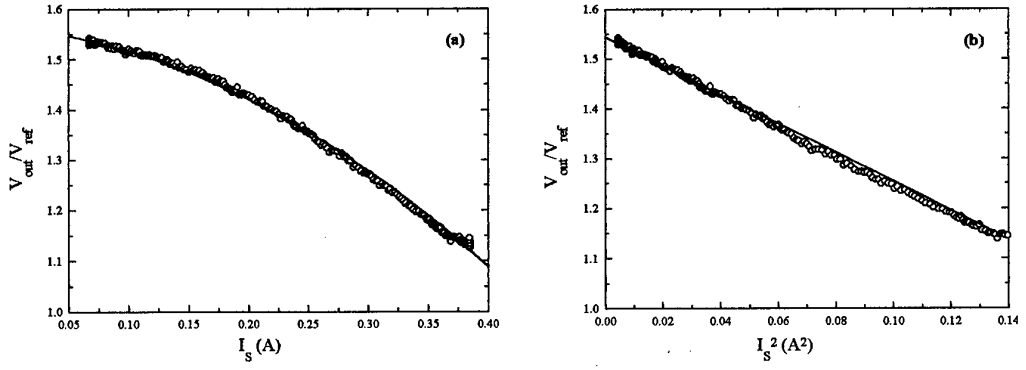

Fig. 3 Output of the sensor to an applied alternating secondary current with frequency 50 Hz as a function of (a) the driving RMS current, and (b) the square of the same RMS current (the solid lines represents curve fitting).

From the results of Fig. 3b, linearity can be observed throughout the measured region and the obtained data indicates a RMS current resolution of 2 mA. The bandwidth (at -3dB point) of the sensor system for a constant RMS current was found to be 2.2 Hz. For frequencies higher than this one, the sensor output produce the RMS average of the secondary current waveform, but the DC term cannot be easily distinguished from the low frequency drift due to environment

temperature. Fig. 4 shows the response of the sensor to a secondary current step from 175 mA to 250 mA. The time constants for heating and cooling regimes are (0.46±0.01) s and (0.47±0.01) s, respectively (obtained from Fig. 4(b)). These AC results give a dynamic sensitivity of ≈1mA/√Hz. This response behaviour is characteristic from this type of temperature devices [6,7]. Nevertheless, it should be possible to increase the frequency response up to tens of kilohertz using a sputtering technique to produce a thinner layer of metal along the FBG.

Because CTs are both used for metering (frequency of interest is 50 or 60 Hz) and relaying purposes (overload conditions and current spikes), it is also necessary that the frequency response of the sensor system be much higher than the line frequency. Improvements in the design and response of the described sensor system are presently being investigated in order to overcome these issues. Another drawback for this application is the sensitivity of the FBG both to the temperature and to the strain, which means that some kind of compensation scheme to de-coupling the two effects will be necessary.

The use of an hybrid scheme offers several advantages over more 'conventional' optical schemes, such as the ones based on the Faraday effect. The inherent wavelength encoded output information of these devices make them independent on light levels and good candidates for incorporation into wavelength-division multiplexing schemes. Also, this sensor configuration has the advantage of presenting a purely resistive impedance to the current source.

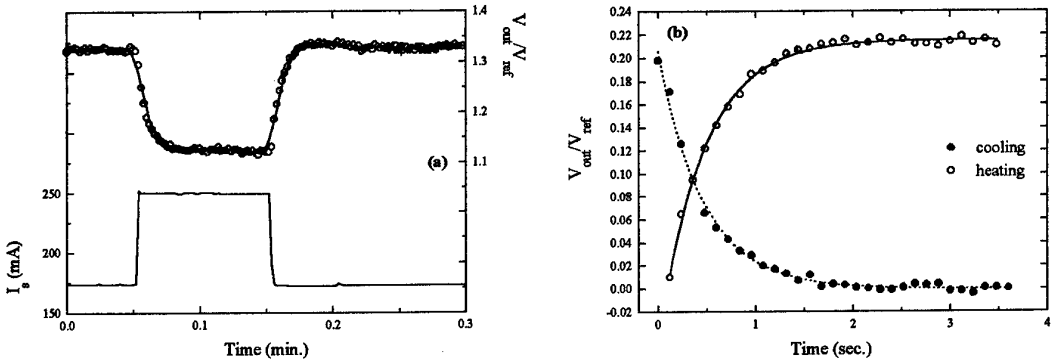

Fig. 4 (a) Response of the sensor (on top) to a step change of the secondary current (on bottom). (b) Detailed response of the sensor to the heating and cooling time intervals from fig. 4(a).

In summary, a metal-coated fibre Bragg grating sensor for measuring the RMS current of power lines at 50 Hz was constructed, providing a resolution of ±2 mA and a dynamic sensitivity of ≈1mA/√Hz at 2 Hz.

Acknowledgements: P. M. Cavaleiro and A. B. Lobo Ribeiro acknowledge the financial support from "Agência de Inovação" under the project HIPOWER. F. M. Araújo acknowledge the support from "Programa PRAXIS XXI".

References

[1] S.C. Rashleigh and R. Ulrich, *Appl. Phys. Lett.* **34**, 768-770 (1979).
[2] G.L. Tangonan, D.I. Persechini, R.J. Morrison and J.A. Wysocki, *Electron. Lett.* **16**, 958-959 (1980).
[3] A. Dandridge, A.B. Tveten and T.G. Giallorenzi, *Electron. Lett.* **17**, 523-524 (1981).
[4] N.E. Fisher, P.J. Henderson and D. A. Jackson, *Meas. Sci. Technol.* **8**, 1080-1084 (1997).
[5] A.B. Lobo Ribeiro, L.A. Ferreira, M. Tsevtkov and J.L. Santos, *Electron. Lett.* **32**, 382-383 (1996).
[6] B.J. White, J.P. Davis, L.C. Bobb, H.D. Krumboltz and D.C. Larson, *J. Lightwave Technol.* **5**, 1169-1174 (1987).
[7] C. Shyu and L. Wang, *J. Lightwave Technol.* **12**, 2040-2048 (1994).

IMPROVEMENTS ON THE MULTIPLEXING SYSTEM USING A 2D SPECTROGRAPH FOR FBG BASED SENSOR ARRAYS

Y. Hu, B. Bridge
School of Electronic, Electrical and Information Engineering
South Bank University, 103 Borough Road, London SE1 0AA, UK
Tel: 0044 171 815 7543, Fax 0044 171 815 7599
Email huya@sbu.ac.uk

L. Zhang, I. Bennion
Photonics Research Group, Aston University, Birmingham B4 7ET, UK

S. Chen
Smart Materials and Structures Research Center
Mechanical Engineering, University of Maryland, College Park, MD 20742, USA

INTRODUCTION

FBGs are especially useful for structure monitoring applications because their small physical cross-section and the mechanical strength of the optical fiber. However, the monitoring of large and complex structures often requires a very large number of sensors and high sampling rate.

Several methods have been reported to multiplex FBGs along a single length of optical fiber [1, 2]. Although a maximum sample rate of 1kHz was reported [1], the total number of FBGs in the array was below 20 due to the limited bandwidth of optical sources available. It is possible to improve this sample rate by simply employing separate detectors and processing electronics for FBGs along different fiber channels as demonstrated by Rao et. al. [3]. However, the weight, size, cost and complexity of the interrogation instrument inevitably rises in proportion to the number of sensors in the network.

The authors have developed a technique, i.e. a combination of wavelength and spatial division multiplexing. It can integrate a large number of FBGs by using a 2D spectrograph [4, 5]. However, the sampling speed is limited by the frame rate of the CCD camera and the frame grabber available. The improved multiplexing technique described here has the potential to achieve a significant performance enhancement over existing ones in terms of sensor numbers and sample rate. In addition, every sensor in the array can be randomly addressed with different measurement ranges and sample rate. This feature is very useful when FBGs in the array are adapted to detect different physical parameters. A maximum sample rate of more than 10kHz can be reached. Furthermore, the interrogation instrument is compact, light, low cost and has no mechanical moving parts. The last feature ensures the operational precision and reliability in rough environments.

SYSTEM CONFIGURATION

A schematic diagram of the envisaged sensing network is shown in Figure 1, where a light from a broad band source is split into M optical fiber sensing channels in the network. There are up to N FBGs distributed along each channel, each with pre-determined, different Bragg wavelengths. Light reflected from the FBGs in each fiber channel is coupled into a down-lead fiber via a 1x2 coupler and sent to the interrogation instrument. The instrument is basically a compact, 2D optical fiber spectrograph. The 2D CCD is placed at the output port of the spectrograph while the end-faces of all the down-lead fibers are arranged to form a line positioned at the input slit. The digital output of the imager is sent to a computer for processing.

The imaging system of the spectrograph separates light from different fibers and distributes them along pixel columns of the 2D image sensor (Y-axis). Because of the effect of the diffraction grating, the light at different wavelengths will be diffracted to different positions along X-axis, hence form bright spots at different positions along pixel rows of the image sensor. Therefore, since the system has M fiber channels and N FBGs of different wavelengths along each fiber, there will be a $M \times N$ matrix of discrete spots on the image sensor array. The spatial position of its fiber channel is encoded into the position along Y-axis of the imager while its wavelength is encoded along X-axis. The precise central wavelength of a FBG sensor can therefore be detected by locating the exact

position of the associated spot along X-axis of the imager pixel array. This position can be interpolated to the sub-pixel level precision by calculating the centroid of the relevant spot.

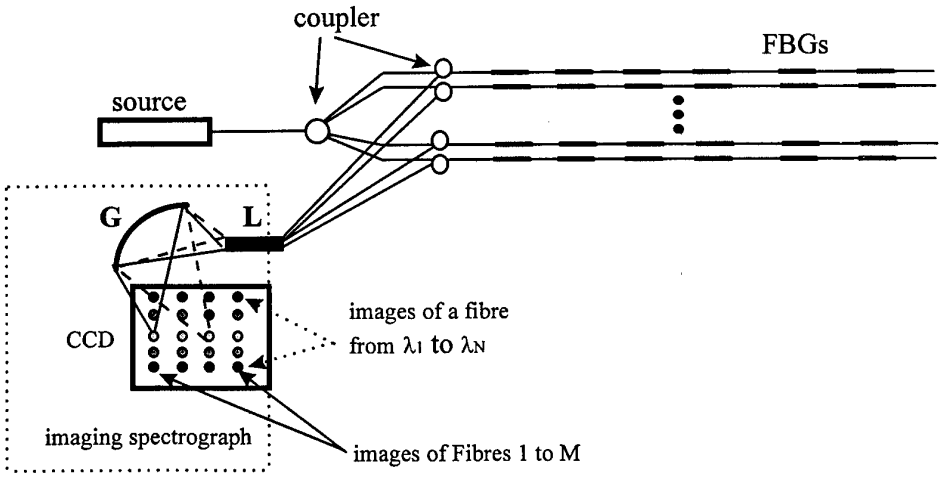

Figure 1 Schematic of the proposed optical fibre sensing network

In a preliminary experiment, an Anritsu pigtailed SLD module with the central wavelength at 840nm and a FWHM of 23nm was used. Total 23 FBG sensors in four fibre channels have been interrogated with the system successfully as shown in Figure 2. Figure 3 shows the dynamic strain signal obtained from one of the gratings.

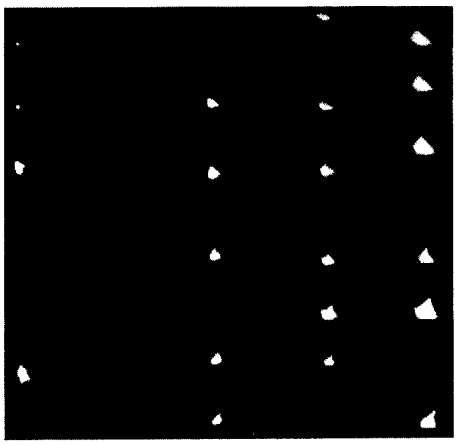

Figure 2 Photograph of the intensity distribution of 23 FBGs integrated in the system

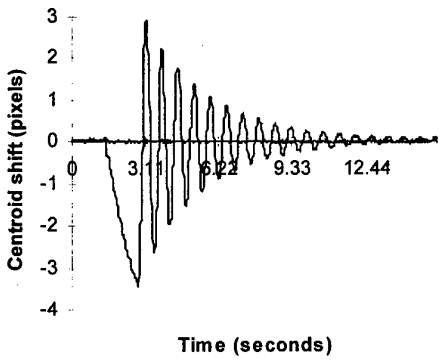

Figure 3 Output signal of a FBG in the array under dynamic s train

MULTIPLEXING CAPACITY

The multiplexing capacity of a system based on a 2D spectrograph depends on many factors, e.g. the dynamic range of starin, the effective pixel number of the image sensor and the image spot size of the fibre endfaces. We have demonstrated that the maximum multiplexing capacity of our preliminary system was 175 FBGs by using an industrial standard CCD camera with 512 by 512 pixels and the maximum measurable range $\pm 3500\mu\varepsilon$[5]. This capacity was limited by the large image spot with astigmatism, say 20 by 20 pixels. If the spot size reduces, the capacity can be incerased.

However, the spot size cannot be too small, otherwise the measurement resolution and accuracy will be severely affected. Let us assume that the intensity profile of the image spot is ideally Gaussian. The spot size can then be described by a specific radius $r = \sigma$ at which the intensity reduces to 1/e of the peak intensity at the centre of the image spot. In the area where $r > 3\sigma$, the optical energy is less than 5% of the total of the spot image. Therefore, 3σ represents the effective radius of the spot. Figure 2 shows the results of computer simulation about the RMS errors of the centroid algorithm versus the spot size without noise. When $\sigma < 1$ pixel, the smaller the spot, the larger the RMS error. When $\sigma \geq 1$ pixels, or the effective spot size $\geq$ 7 by 7 pixels an acceptable accuracy can be achieved. On the other hand, any further larger size of the spot cannot improve the measurement precision significantly. Obviously, the multiplexing capacity can be increased to more than 500 FBGs using the imaging system described in [5] with the optimized image spot size which was obtained using our newly developed transmitting version spectrograph.

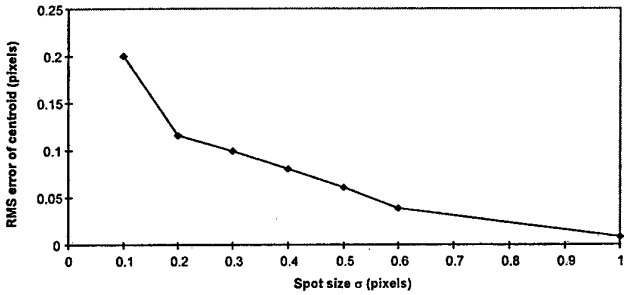

Figure 4 Measurement accuracy of centroid versus the spot size

PROCESSING SPEED

The processing speed of the 2D spectrograph FBGs multiplexing system is limited by the computer speed, the sampling speed of the CCD array and the frame grabber. As mentioned previously, the spot size is reduced to 7 by 7 pixels. In a recent experiment, we have measured that the time to calculate the centroid of a 7 × 7 cluster using centroid algorithm and a high level language program took approximately 10μs to run on a Pentium 200MHz PC without MMX power available. We are confident that computation time can be easily brought down to a level well below the FBG access time.

Obviously, the bottleneck of the system speed currently is the frame rate of the CCD camera used. The frame rate for a standard industrial CCD is 25 fps. Although 2D cameras of 100 fps speed are available in the market, they are still not fast enough to satisfy the requirement in sensing area.

A special two-dimensional (2D) complementary metal-oxide semiconductor (CMOS) image sensor will be used in the interrogation instrument of the sensor system. CMOS image sensors enjoy many advantages over CCDs, including lower cost, miniaturization, lower power consumption and enhanced functionality.

Because of the random accessibility of the CMOS imager used, any FBG in the network can be addressed in a truly random fashion by simply reading out only the relevant pixels and calculating its centroid. This unique feature not only adds great flexibility in application but also enables the system to utilize its resources efficiently resulting in quantum performance enhancement.

The maximum sample rate to any FBG in the array is limited by the photoreceptor time constant of the imager which is inverse proportional to the light density on the pixel. From the data provided by the manufacturer of the Fuga15 CMOS imager, the maximum sample rate can be expressed as $f_{mx} = 12.5\ d$ (kHz), where d is the average light density within a bright spot on the imager in W/m^2. As calculated in [6], the maximum sample rate limited by the time constant of the pixels is 2.1kHz at the maximum scale (nearly 2000 FBGs).

On the other hand, the maximum read out rate for the CMOS camera is 6MHz horizontally, 1MHz vertically. The time to read a single sensor can be expressed as

$$T_a = \frac{49}{6MHz} + \frac{7}{1MHz} = \frac{91}{6MHz} \qquad (1)$$

Or the maximum read out rate for a single sensor is 6.6×10^4 Hz. However, in practice this rate for any FBG element should not be larger than f_{mx}. Therefore, taking all the factors into account, the actual sample rate achievable due to limits in pixel read out rate for a 500 sensor array will be 132 Hz.

From the above discussion we can see that the addressing rate for every FBG can be arranged at will from 0 to 10KHz for different sensors using software control. For the sensors which detect faster dynamic measurands can be assigned a higher addressing rate. This makes the sensing system more flexible.

CONCLUSION

We have presented a novel digital spatial and wavelength division multiplexing technique, which utilizes a 2D spectrogragh with a special 2D random addressable CMOS imager to interrogate FBG based sensors in multiple fiber channels. The technique is capable of multiplexing a very large number of FBGs and providing absolute measurements at a high spectral resolution. Each FBG in the array can be addressed in a random fashion with different sample rates ranging from 0 to 10kHz. The interrogation instrument is simple, low cost, compact and robust with no moving parts. We are currently working with a spectrometer manufacturer to further improve the design and implementation of the interrogation instrument, and to incorporate the random addressable CMOS imager into the system.

The authors acknowledge the support of The Engineering and Physical Science Research Council in the U. K. for this project.

REFERENCES

1. Askins, C.G., Putnam, M.A., Friebele, E.J., "Instrumentation for interrogating many-element fiber Bragg grating arrays", SPIE Vol. 2444, pp.257-266, 1995.
2. Kersey A D, Berkoff T A, and Morey W W, "Multiplexed fiber Bragg grating strain sensor system with a fiber Fabry-Perot filter", Opt. Lett., Vol.18, no.16, pp.1370-1372, 1993.
3. Rao, Y. J., Ribeiro, A. B. L., Jackson, D. A., Zhang, L., and Bennion, I. :' Simultaneous spatial, time and wavelength division multiplexed in-fiber grating sensing network', Opt.Commun., 1995, **125**, pp. 53-58.
4. S. Chen, Y. Hu, L., Zhang, I. Bennion, "Digital wavelength and spatial domain multiplexing of Bragg grating optical fiber sensors", Proc. of OFS12, ISBN1-55752-514-5, pp.448-451, Williamsburg, USA, October, 1997.
5. Y. Hu, S. Chen, "Multiplexing Bragg gratings using combined wavelength and spatial division techniques with digital resolution enhancement", Electronic Letters, Vol.33, pp.1973-1975 (1997).
6. S. Chen, Y. Hu, L., Zhang, I. Bennion: "Multiplexing of large scale FBG arrays using a two-dimensional spectrometer", SPIE's 5th Annual International Symposium on Smart Structures and Materials, San Diego, California, USA, March 1998.

Enhanced Temperature Sensitivity using Coated Fiber Bragg Grating

Sacharia Albin
Photonics Research Laboratory
Department of Electrical & Computer Engineering
Old Dominion University, Norfolk, VA 23529, USA
Phone: (757) 683-4967
Email: albin@ece.odu.edu

Jianli Zheng, Arnel C. Lavarias and Jessy Albin
Science & Engineering Applications Company (SEACOM)
PO Box 5168, Virginia Beach, VA 23471-0168, USA
Phone: (757) 363-7833
Email: aclavarias@worldnet.att.net

Introduction

Fiber optic sensors are being used in many biomedical applications. In particular, their dielectric nature makes them more suitable than thermocouples for temperature measurement in an environment of high electromagnetic field such as that used for hyperthermia treatment [1]. Fiber Bragg grating (FBG) temperature sensors have been developed which have the characteristic advantages of wavelength encoding, distributed sensing, and low cost [2,3]. The normalized temperature sensitivity at room temperature is given by:

$$\frac{1}{\lambda_B}\frac{\Delta\lambda_B}{\Delta T} = \alpha + \xi \qquad (1),$$

where α is the thermal expansion coefficient of the fiber, equal to $0.55\text{x}10^{-6}$ for silica, and ξ is the thermo-optic coefficient, equal to $8.3\text{x}10^{-6}$ for germania doped fiber. Therefore, the temperature sensitivity of an FBG depends mainly on the thermo-optic coefficient. For 1.55 μm FBG, the wavelength shift is about 13.7 pm/° C which is experimentally verified [4]. Hence, a major drawback of the FBG sensor is that a temperature resolution better than 0.1° C, which is required for some medical applications, cannot be obtained even with a detection scheme capable of 1 pm resolution. One approach to alleviate this problem is to enhance its temperature sensitivity by thermally induced strain on the fiber. The FBG can be attached to a substrate of higher thermal expansion than the fiber [5]. Such a scheme has been reported for cryogenic temperature sensing by epoxy bonding an FBG on polymethyl methacrylate (PMMA) substrate [6]. However, this method of bonding is not compatible with temperature measurement for biomedical applications. Moreover, the thermally induced strain depends on the property of the epoxy between the substrate and the FBG.

We have attempted coating the FBG with PMMA by direct polymerization on the fiber. In this paper, we present results of temperature measurement using uncoated and PMMA-coated FBG's to elucidate enhanced temperature sensitivity of the PMMA-coated FBG. The normalized strain sensitivity is given by:

$$\frac{1}{\lambda_B}\frac{\Delta\lambda_B}{\Delta\varepsilon} = 1 - p_e, \qquad (2)$$

where p_e is the photo-elastic constant of silica at room temperature. The thermal expansion coefficient of PMMA, α_{PMMA}, is approximately two orders of magnitude higher than that of silica (α in equ.1 above). Therefore, one can safely assume that the induced strain is solely due to PMMA and is proportional to its thermal expansion for a limited temperature range, i.e.,

$$\Delta\varepsilon = \alpha_{PMMA}\Delta T. \qquad (3)$$

Assuming the thermo-optic coefficient to be linearly dependent on temperature for a limited range, and the photo-elastic constant independent of temperature, the temperature sensitivity of a PMMA coated FBG can be written as:

$$\frac{1}{\lambda_B}\frac{\Delta\lambda_B}{\Delta T} = (1 - p_e)\alpha_{PMMA} + \xi. \qquad (4)$$

At room temperature, $p_e = 0.22$ and $\alpha_{PMMA}=6.1\times10^{-5}$[7]. Using equation (4), we expect the temperature sensitivity of the coated FBG to be higher than that of the uncoated FBG by a factor of six.

Experiments

FBG's written on Corning SMF-28 fiber with center wavelength approximately 1550 nm have been used for the experiments. The FBG's have a full-width-half-maximum around 0.2 nm and reflectivities between 80-85%. Methyl methacrylate monomer and Vazo-64 initiator were used to polymerize on the FBG region. The coated FBG's were then mounted in a temperature-controlled thermostat to vary the temperature between –40° and +50° C with an accuracy of ±0.01° C. A 1550 nm LED source with ±100 nm spectral width is connected to one port of a 3dB coupler. The FBG is connected to one of the output ports of coupler. The other input port of the coupler is connected to an HP 71450 optical spectrum analyzer capable of 1 pm resolution (See Figure 1). The experiment was repeated with an uncoated FBG.

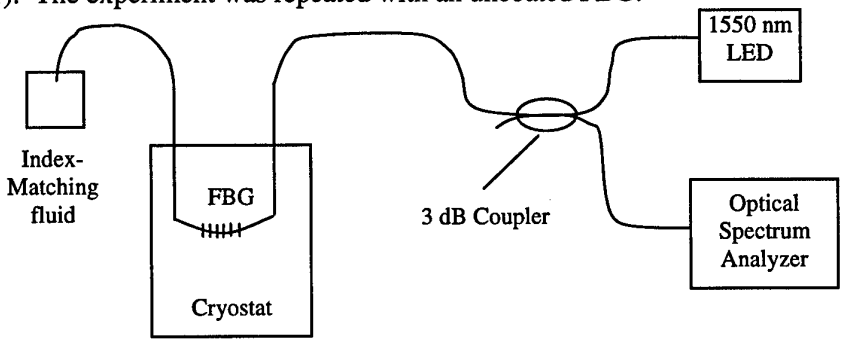

Figure 1: Schematic of the experimental setup.

Results

Before polymerization, the center wavelengths of the two FBG's were 1550.104 nm and 1550.464 nm at room temperature. The latter FBG was coated with PMMA, and its center wavelength shifted to 1544.728 nm. This is due to built-in strain caused by volume contraction of the coating during the polymerization process. Figure 2 shows the variation of the Bragg wavelength peak with temperature for PMMA-coated and uncoated FBG's. Clearly, the PMMA-coated FBG has higher sensitivity. Table 1 shows a comparison of sensitivity for various temperatures. The experimentally-determined sensitivity of the PMMA-coated FBG is an order of magnitude higher than that of the uncoated FBG for the entire temperature range 230 to 320 K. This result is better than that predicted by Equation 4. One possible explanation for this enhancement is that the polymerization process produced higher strain. At 300 K, the temperature resolution is 6 mK if the detection system is capable of 1 pm wavelength resolution. The response time of the sensor will depend on the thickness of the coating due to the low thermal conductivity of PMMA. This needs to be optimized for specific applications. The optimum thickness of the coating is currently being modeled using finite element analysis.

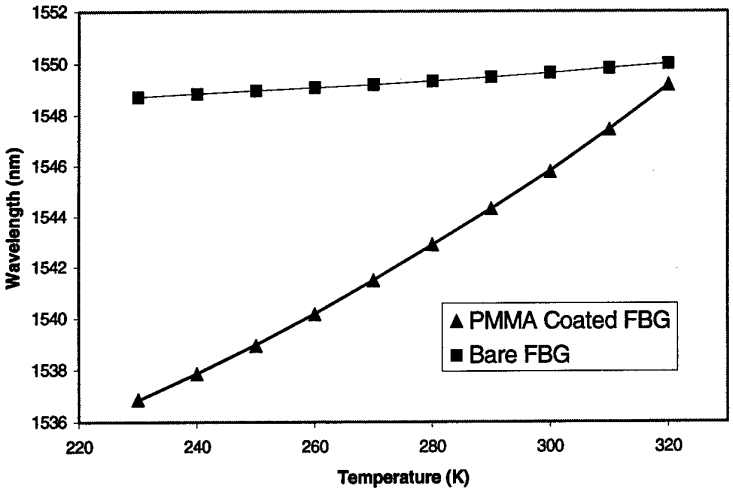

Figure 2: Variation of Bragg wavelength peak with temperature.

In conclusion, an order of magnitude enhancement of temperature sensitivity is demonstrated using a PMMA-coated FBG compared to a bare FBG. Experimental result shows a temperature resolution of 6 mK using a detection system with a wavelength resolution of 1 pm.

Table 1: Temperature sensitivity.

Temperature(K)	Sensitivity of PMMA-coated FBG (nm/K)	Sensitivity of uncoated FBG (nm/K)
230	0.103	0.012
240	0.107	0.012
250	0.115	0.012
260	0.126	0.012
270	0.135	0.013
280	0.140	0.014
290	0.147	0.016
300	0.157	0.017
310	0.168	0.018
320	0.173	0.018

References

[1] A. G. Mignani and F. Baldini, J. Lightwave Technol., Vol. 13, p. 1396, 1995.
[2] Y. Rao et al., J. Lightwave Technol., Vol. 15, p. 779, 1997.
[3] S. Tsao and J. Wu, IEEE J. Select. Topic in Quant. Electron., Vol. 2, p. 894, 1996.
[4] A. B. L. Ribeiro et al., Appl. Opt., Vol. 35, p. 2267, 1996.
[5] W. W. Morey, G. Meltz, and W. H. Glenn, Proc. SPIE, Vol. 1169, p. 98, 1989.
[6] S. Gupta et al., Applied Optics, Vol. 35, p. 5202, 1996.
[7] Y. S. Touloukian et al., Thermophysical Properties of Matter: Thermal Expansion-Nonmetallic Solids, Vol. 13, IFI/Plenum, New York, p. 1470, 1977.

A TEMPERATURE SENSOR BASED ON A SINGLE BRAGG GRATING

G A Cranch (Defence Evaluation and Research Agency UK)
DERA-Winfrith, Winfrith Technology Centre, Winfrith Newburgh,Dorchester,Dorset
Email : gacranch@dera.gov.uk

Introduction : The use of Bragg gratings for measurement of pressure, strain and temperature has been the subject of considerable research over the last decade. Techniques for temperature/strain discrimination are summarised in Reference 1 and often involve either a specialised interrogation system or a dual grating approach. Presented here are techniques to manipulate the components of strain induced in a Bragg grating under pressure such that their total contribution to the Bragg resonance shift equates to zero. It will also be shown that the temperature sensitivity of the grating is either unchanged or in some instances enhanced.

Theory : The pressure and temperature sensitivity of optical fibre has been studied extensively in Reference 2,3 by Hocker and Hughes and from this it can be shown that the pressure and temperature sensitivity of a Bragg grating are given by Equation (1) and (2),

$$\left.\frac{\Delta\lambda_B}{\Delta P}\right|_T = 2n\Lambda\left[\varepsilon_{z0} - \frac{n^2}{2}\left(p_{12}\varepsilon_{z0} + (p_{11}+p_{12})\varepsilon_{r0}\right)\right] \quad (1)$$

$$\left.\frac{\Delta\lambda_B}{\Delta T}\right|_P = 2n\Lambda\left[\frac{1}{n}\left(\frac{\partial n}{\partial T}\right)_\rho + \frac{1}{\Delta T}\left(\varepsilon_{z0} - \frac{n^2}{2}\left[p_{12}\varepsilon_{z0} + (p_{11}+p_{12})\varepsilon_{r0}\right]\right)\right] \quad (2)$$

where n=refractive index, Λ is the grating pitch, ε_* is the strain component, and p_{**} are the Pockels coefficient. The first term in Equation 1 is the contribution from the length change due to the axial strain and the second and third terms are due to the refractive index change from the axial and radial strains respectively. The first term in Equation 2 is the refractive index change due to the temperature change for constant density and the second, third and forth terms refer to the length change due to axial strain, the refractive index change due to axial strain and the refractive index change due to radial strain respectively. For a bare grating the first term dominates over the others.

The sensitivities to temperature and pressure of bare gratings @ 1550 nm have been measured in Ref. 5 as $\frac{\Delta\lambda_B}{\Delta P} = -3.1*10^{-9}\,nm/Pa$ and $\frac{\Delta\lambda_B}{\Delta T} = 0.011nm/K$.

Modelling of the pressure sensitivity of a Bragg grating : The approach taken here to model the pressure sensitivity of a grating is similar to that taken by Hocker and Jarzynski. It is based on 2D plain strain elastic theory for a grating with a single layer (the core and cladding are assumed to have identical mechanical properties). The model, therefore, assumes that there is no z-dependance of axial strain and that it is the same in each layer. The different axial strains in each layer are replaced by an average axial strain across the layers calculated by equating the axial stresses in each layer to the end condition on the fibre. For an unsupported fibre the end condition can either be taken as a radial boundary condition [RBC]

where the effective pressure on the end of the cylinder is zero, or as a hydrostatic boundary condition [HBC] where the effective end pressure is taken to be equal to ambient pressure. It has been shown in Ref. 4 and 5, that the hydrostatic boundary condition gives the most accurate results. Hughes has also shown that this 2D plain strain approximation produces results that are within 1.5% of the results given by an exact 3D model.
If the mechanical properties of the glass are taken as $E_{glass} = 72GPa$, $\nu_{glass} = 0.23$, $p_{11} = 0.121$, $p_{12} = 0.270$ then the predicted sensitivities at 1550 nm are $\frac{\Delta\lambda_B}{\Delta P} = -3.6*10^{-9} nm/Pa$ for HBC which is in reasonable agreement with the measured values. The discrepancy between the two values is believed to be due partly to the uncertainty in the mechanical properties of the fibre and partly to the uncertainty in Pockels coefficients. These have been shown in Reference 6 to differ for glass containing a Bragg grating.

Modelling of the temperature sensitivity of a Bragg grating : Modelling of the temperature sensitivity of optical fibres has been carried out by Lagakos in Reference 7 using a similar approach to that described above for the pressure sensitivity. This model is used to determine the temperature sensitivity of Bragg gratings. If the coefficient of thermal expansion of the core and cladding are taken as $\alpha_{glass\_core} = 5*10^{-7}/K$ and $\alpha_{glass\_clad} = 10*10^{-7}/K$ respectively, $\frac{1}{n}\left(\frac{\partial n}{\partial T}\right)_p = 0.68*10^{-5}/K$ for fused silica and the mechanical parameters given above are used then the temperature sensitivity of a grating is $\frac{\Delta\lambda_B}{\Delta T} = 0.01 nm/K$. As mentioned above, this is primarily determined by the value of the first term in Equation 2 and is in close agreement with the measured sensitivity.

Analysis : It can be seen that a low Bulk modulus layer applied to the grating can increase the sensitivity to pressure by amplifying the induced strains in the glass core. Figure 1 shows this for a layer with properties of $E_{layer} = 1$ GPa, $\nu_{layer} = 0.3$ and R is the ratio of the layer radius to the fibre radius (HBC). If however the Poisson ratio of the layer is increased towards 0.5, the sensitivity can be shown to change sign, Figure 2. Although this indicates a novel way to insensitise the fibre to pressure, it is felt that the precise value of the Poissons ratio required (to achieve zero sensitivity) will be difficult to achieve in practice. It is also known that the Poisson ratio of rubber is both temperature and frequency dependant and can change over time when submersed in water. For this reason a slightly different approach has been sought. As well as applying a coating to give a zero pressure sensitivity it may also be possible to manipulate the axial strain component using an external clamping, such as a rigid bar, on a tensioned fibre which would add an extra control over the sensitivity required. This structure has been modelled by assuming the bar to be much larger cross sectional area than the fibre and the bonding at each end of the grating is assumed to be perfect. The axial strain in the bar under HBC is given by Equation (3) and this determines the axial strain in the fibre.

$$\varepsilon_{z\_bar} = \frac{p}{E_{bar}}(2\nu_{bar} - 1) \qquad (3)$$

p is the external pressure. Since the fibre is assumed to be unshielded from the external pressure, the effect of this modified axial strain on the radial strain in the fibre is accounted for modifying the boundary conditions at the ends of the grating. The grating is now taken as being fixed in position but can exhibit an axial strain equal to that in the support bar. Figure 3 shows the contributions from each term in Equation 1 to the pressure sensitivity for a supported grating with mechanical parameters, E_{bar}=49.9GPa, ν_{bar}=0.357 (characteristics of tin), E_{layer}=1GPa, ν_{layer}=0.3. L is the length change contribution, IA and IR are the refractive index change due to the axial and radial strains respectively and M is the grating sensitivity. It can be seen that the pressure sensitivity goes to zero for R=1.8.

It should be emphasised that the grating sensitivity is strongly dependent on both the Young's modulus and Poisson's ratio of the support bar. The effect of uncertainty in the mechanical properties of the bar can be counteracted by carefully controlling the layer thickness on the fibre. Alternatively the mechanical properties of the bar can be chosen (giving a much reduced pressure sensitivity) so that a large error in coating thickness has little effect on the sensitivity. It has also been shown that the mechanical properties of polymers are both temperature and frequency dependent, however, sufficient data is available to make a suitable choice of coating material for the required temperature range of operation.

It is shown in Figure 4 that applying a coating with a high coefficient of thermal expansion (relative to the glass), to an unsupported grating can increase the temperature sensitivity. For example, with a coating of R = 10 and α=1000*10^{-7}/K, typical for polyurethane, an amplification of 19 dB can be achieved. Figure 5 shows the contributions from each term in Equation 2 to the temperature sensitivity for the same layer material used above. L is the length change contribution and IA and IR are the refractive index change due to the axial and radial strains respectively. M is the grating sensitivity. The contribution from the first term in Equation 2 is also shown. If a bare grating is now clamped, under tension, the magnitude of the first term in Equation 2 is unlikely to be effected. Hence the temperature sensitivity of a grating clamped by a material with the same coefficient of thermal expansion as the fibre will be unchanged from that of the unsupported grating. If, however, the grating is clamped with a bar made from tin with α_{tin}=210 * 10^{-7}/K the increased temperature induced axial strain in the grating increases its temperature sensitivity by 6 dB.

Discussion : It has been shown that, in theory, the pressure sensitivity of a Bragg grating can be made to go to zero if the contributions between the axial and radial strains in the fibre can be appropriately balanced. Exact balancing between these effects will probably be difficult to achieve, however, a large reduction in pressure sensitivity with little effect on the temperature sensitivity is an attractive option for some applications. It should also be noted that the level of sensitivity reduction using a rigid support bar will depend strongly on the quality of the bond between the fibre and the bar. The modelling assumes a perfect bond with no slippage, but experimental measurements will indicate how well this assumption can be realised. Techniques to achieve this are currently being considered. A similar technique to pressure desensitise fibre has been reported in Reference 8 which involves applying a metal coating to the fibre. This would achieve the same effect of balancing the terms in Equation 2. It is felt, however, that the technique suggested here may be a more repeatable and cost-effective way to achieve this effect.

The model is currently being improved to handle up to 3 layers, so that the differences in mechanical properties of the core and cladding can be taken into account as well as an extra coating layer. A programme of experiments is also being conducted to measure the pressure and temperature sensitivity of these Bragg grating based sensors, the results of which will be presented at the conference.

Acknowledgements : The author would like to acknowledge the support and advice from P Nash and R Crickmore.

Figure 1: Pressure sensitivity of a Bragg grating

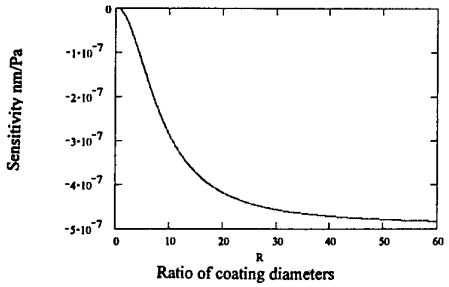

Figure 2: Grating pressure sensitivity as function of Poisson ratio of coating

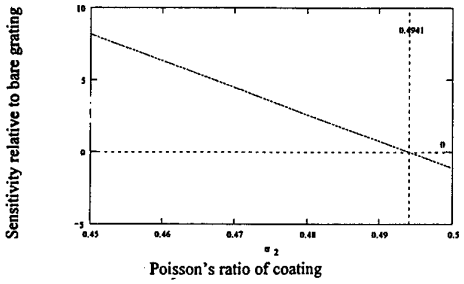

Figure 3: Contributions to grating sensitivity from Equ 1 for a clamped, coated grating.

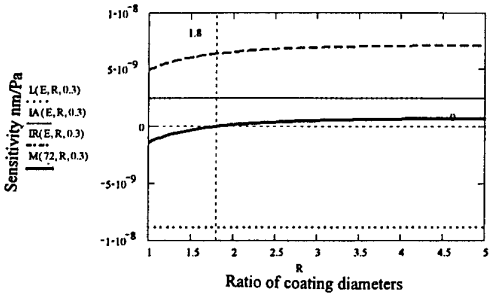

Figure 4:Temperature sensitivity of Bragg grating vs R

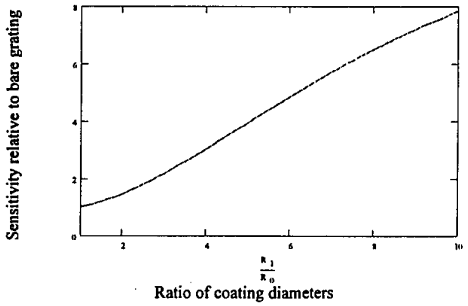

Figure 5: Contributions from each term in Equation 2 to the temperature sensitivity

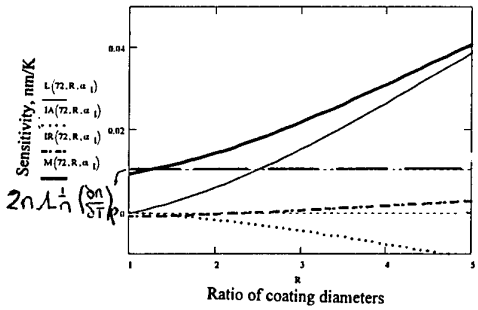

References

1. Jones J, "Review of Fibre Sensor Techniques for Temperature-Strain Discrimination", OFS 12, 1997, p36-39
2. Hocker GB, "Fiber optic acoustic sensors with composite structure : an analysis", Applied Optics, vol 18, no. 21, 1979
3. Hughes R, Jarzynski J, "Static pressure sensitivity amplification in interferometric fiber-optic hydrophones", Applied Optics, vol 19,no. 1, 1980
4. Hocker GB, "Fiber-optic sensing of pressure and temperature", Applied Optics, v18,no.9
5. Xu MG et al, "Optical in-fibre grating high pressure sensor", Electronics Letters, vol 29, no. 4, 1993
6. Bertholds A, Dändliker, "Determination of the individual Strain-Optic Coefficients for single-Mode Optical Fibers", IEEE J. Lightwave Tech., LT-6,1988
7. Lagakos N et al, "Temperature-induced optical phase shifts in fibers", Applied Optics, vol. 20, no. 13, 1981
8. Lagakos N et al, "Acoustic desensitisation of single-mode fibers utilising nickel coatings", Optics Letters, vol 7 ,1982

Progress toward an Ultra Thin Optical Hydrophone Array

D.J. Hill, P.J. Nash, DERA (Sensors and Processing Sector), Underwater Sensors and Oceanography Department, Winfrith Technology Centre, Dorchester, Dorset. DT2 8XJ. UK. Tel.: +44 (0)1305 212121

S. D. Hawker, I. Bennion, Photonics Research Group, Department of Electrical Engineering, Aston University, Birmingham. B4 7ET. UK. Tel.: +44 (0)121 3593611

Introduction

Fibre optic hydrophones have been under development for twenty years, and have attained similar performance to the more conventional piezoelectric based transducer. However, the recent development of fibre Bragg grating (FBG) sensors makes possible an alternative approach to optical hydrophones, which offers the advantages of small sensor size and very simple manufacture. The Defence Evaluation and Research Agency (DERA) has initiated a project with the Universities of Aston and Kent to investigate the use of FBG sensors in an acoustic array. To compete with existing technology the specification required is very demanding with each sensor having to be capable of detecting an applied radial pressure of 10^{-4} Pa. In bare fibre, this corresponds to an axial strain of 0.5×10^{-15} (or 0.5 femto-strain). In addition, the system must handle signals with a wide acoustic bandwidth and must include a high degree of multiplexing. Although technically challenging, this programme will lead to the possibility of ultra-thin hydrophone arrays containing large numbers of sensors which can be manufactured very cheaply.

General approach

To achieve the required sensitivity both the sensor and interrogation system must be optimised. This sensitivity can only be achieved with the use of interferometric interrogation techniques [1[1]]. The effective phase gain in an interferometer configuration, such as a Mach-Zender, is given by the length of the path imbalance within the interferometer. If such an interferometer is used to interrogate the reflected signal from a FBG, this path imbalance is limited by the coherence length of that signal. It is therefore essential that the signal have the highest possible coherence length, which implies a very narrow linewidth. The linewidths required cannot be obtained using simple FBGs, and so a resonant FBG structure is likely to be required. Initial investigations focused upon the use of highly resonant passive grating structures such as Moiré, and short as well as $\pi/2$ shifted Fabry-Perot cavity arrangements. Modelling of these configurations showed that very narrow structures were attainable (10^{-4}nm FWHM) although multiplexing raises problems. An alternative line of research has focused upon active structures using in-fibre Bragg grating lasers (FBGL) as the sensing element. These devices, each operating at a unique wavelength, have been shown to have a very narrow linewidth of laser emission (10-50kHz). Studies by Koo *et al* [2] at NRL have shown that using a FBGL in conjunction with an unbalanced Mach-Zender interferometer, it is possible to measure strains down to as low as ~10 femto-strain.

Such lasers are formed by fabricating individual Fabry-Perot resonator cavities in erbium-doped fibre, using in-fibre Bragg gratings written directly into the fibre to act

as the cavity reflectors. These lasers can be used for either single or multi-mode operation, although single mode has a number of advantages for this application.
Single mode operation relies upon two factors:

(i) ensuring a sufficiently large spacing of the longitudinal cavity modes; this necessitates the use of short cavities, of the order of a few cm.
(ii) introducing wavelength discrimination so that only one of the possible longitudinal modes is allowed to lase; this requires Bragg gratings with a narrow reflection spectrum.

Narrowband gratings can be fabricated using a phase-mask exposure; which allows the generation of gratings that are physically longer and therefore have a narrower reflection spectrum compared to holographically generated gratings.

FBGL Design

A software package was used to model the optical transmission spectra obtained from a variety of passive Fabry-Perot cavity structures. The Fabry-Perot cavity is formed by a pair of spaced gratings, using 5cm long gratings with bandwidths less than 0.1nm and various reflective strengths Fig. 1 illustrates the modelled transmission profiles for pairs of 99% reflectivity gratings with increasing spacing; note that for clarity the transmission "T" values are offset for each profile. These profiles clearly show how the number of Fabry Perot longitudinal cavity modes increases with the spacing of the gratings.

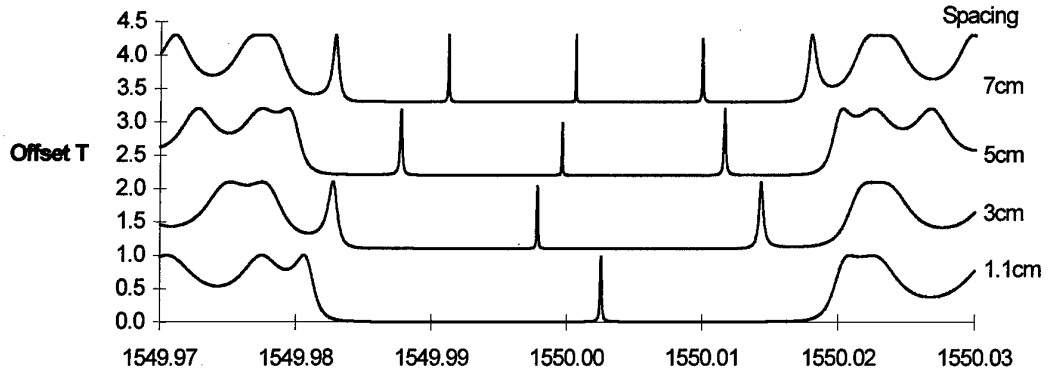

Figure 1 - Number of longitudinal modes for cavity lengths = 1.1, 3, 5 and 7cm

Single mode operation could be obtained with a grating spacing of 1.1cm, but such a short length of even highly-doped Erbium fibre will not provide sufficient optical gain. Longer cavities will offer greater gain, but at the risk of lasing occurring at more than one of the possible longitudinal cavity modes. Which of these modes are liable to support lasing depends upon the differential loss mechanisms within the cavity.

As a first approximation, a cavity length of 5cm was selected as offering a compromise between obtaining sufficient gain whilst minimising the number of laser modes. It was also shown that a passive cavity continues to support three modes for length of 4, 5 and 6cm; the exact grating spacing is therefore not an overly critical parameter in the fabrication process.

It was also found that as the grating reflectivity increases the cavity modes become sharper and the sides of the stop band envelope become squarer. Narrowing the width of the passive cavity modes should correspondingly narrow the laser linewidth, as required for this sensor application. The FBGL design therefore consisted of a pair of 5cm gratings, with reflectivities of 90% or greater, spaced by 5cm.

FBGL Fabrication and Characterisation

The grating cavities were fabricated in highly-doped Erbium fibre which had been hydrogenated to obtain the necessary degree of photosensitivity. They were then introduced into the system illustrated in Fig. 2 to permit optical pumping of the cavity and observation of the lasing signal.

The erbium fibre is pumped at 980nm, and the 1550nm laser signal is taken from either of the two ports shown. The EDFA (erbium-doped fibre amplifier), tuneable filter and polariser are optional elements; the EDFA can be used to amplify the laser signal with the filter then removing the broadband amplified spontaneous emission. The in-line polariser and polarisation controller can be added to assist in the characterisation process.

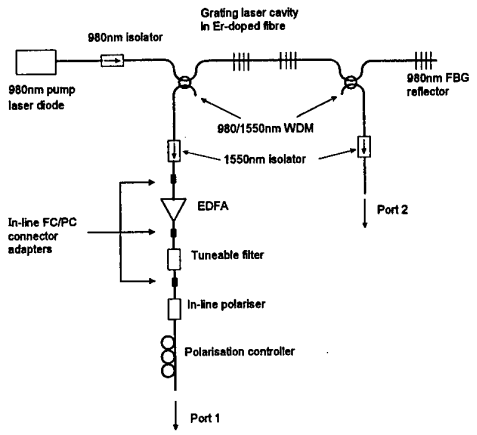

Figure 2: FBGL pump system

The modal structure of the FBGL was examined using a scanning Fabry-Perot interferometer, which confirmed that the FBGL operated in a single laser mode. Higher resolution measurements of the laser linewidth were made using the ring resonator. An example output spectrum is illustrated in Fig. 3 with the PZT being used to modulate the optical path length of the ring. This was from a resonator with a total ring length of 15m and a free spectral range of 14MHz. The spectrum shows three free spectral ranges obtained from single mode FBGL input.

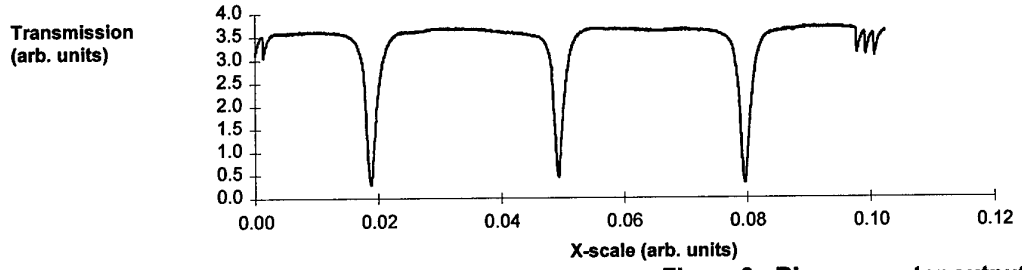

Figure 3 - Ring resonator output

Initial evaluation of the FBGL sensors were performed using a standard unbalanced Mach-Zender interferometer.

Coating the sensor

Although a single FBGL sensor has predicted strain sensitivity close to our requirement, additional amplification is still needed. Since the inception of fibre optic hydrophone design in the late 70's, coatings have been shown [3] to enhance the pressure sensitivity of a fibre. We have therefore extended this research by initially modelling and then experimentally evaluating the effectiveness of coating a FBGL structure to enhance its sensitivity to pressure. Fig. 4 shows the results from the modelling and suggests that under hydrostatic conditions up to 30dB of gain is attainable by applying a Teflon coating to the sensor of at least twenty times the bare fibre radius.

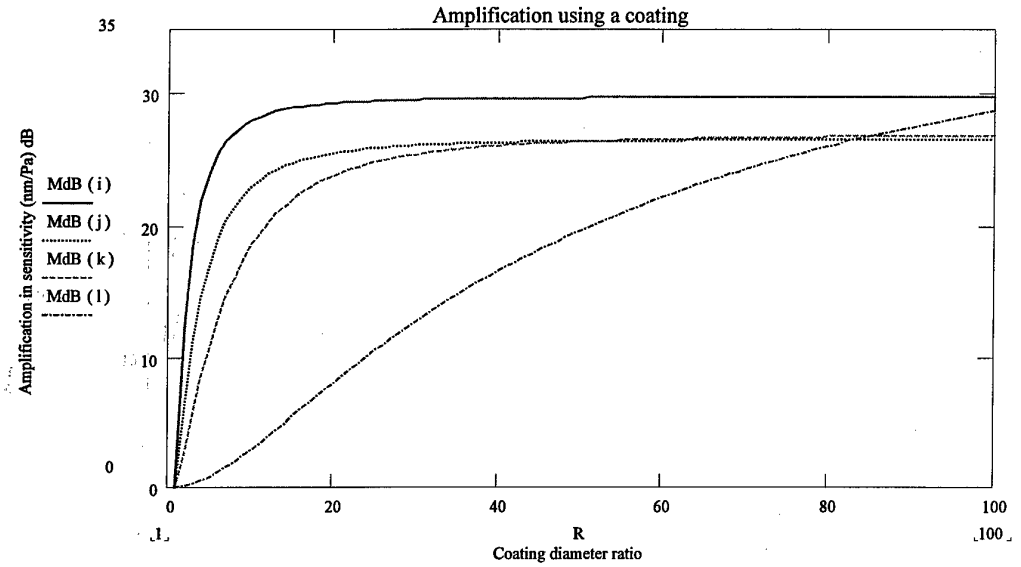

Figure 4 – Amplification in wavelength shift of a FBGL sensor with different coatings. R is the ratio of bare fibre radius to coating radius. I, j, k, and l correspond to coating materials Teflon, Polyethylene, Polyester, and Silicon.

This amplification in addition to the performance of our FBGL sensors and the gain in the Mach-Zender interferometer are expected to result in a measurable sensitivity down to the target pressure level.

Future work

A number of FBGLs have been constructed and their sensitivity to acoustic signals will be tested. The effects of coatings on the grating acoustic sensitivity will also be measured. In parallel with this work, multiplexing issues will be addressed and a design produced for a small multiplexed array. Results of these investigations will be described at the workshop.

1. A.D. Kersey, T.A. Berkoff and W.W. Morey, Electron. Lett., 28, p.236 (1992)
2. K. P. Koo and A. D. Kersey, *J. Lightwave Technol.*, **13**, p.1243 (1995)
3. R. Hughes and J. Jarzynski, *Applied Optics*, **19**, p.98 (1980)

Integrated Regenerative Multicellular Optical Fiber Grating Control System

Gareth Knowles*
Bruce Bower

EMF Technologies, Inc.
So. Williamsport, PA 17701

Robert Rogowski
Leland Melvin
Brookes Childers
Sid Allison

Non-Destructive Evaluation Branch
NASA Langley Research Center
Langley, VA

L Eric Cross
Ruibin Lui

Materials Research laboratory
Penn State University
University Park, PA

ABSTRACT

A new technique is presented for active distributed fiber sensing for interrogating structural integrity and environmental monitoring using an innovation in low power integrated compact tunable fiber optic laser capability.

* Point of Contact

Dr. Gareth Knowles
EMF Technologies, Inc.
1700 Riverside Drive
Phillips Business Park
So. Williamsport, PA 17701
e-mail: gareth@ptdprolog.net
tel: (717) 320-1788
fax: (717) 326-9339

SPIE Vol. 3483 • 0277-786X/98/$10.00

SUMMARY

Introduction

The schematic of Figure 1 shows an integrated VME/VXI low profile designs is developed that incorporates both the drive electronics and precision actuation mechanisms within standard VME or VXI specifications for use on standard military or commercial rack equipment.

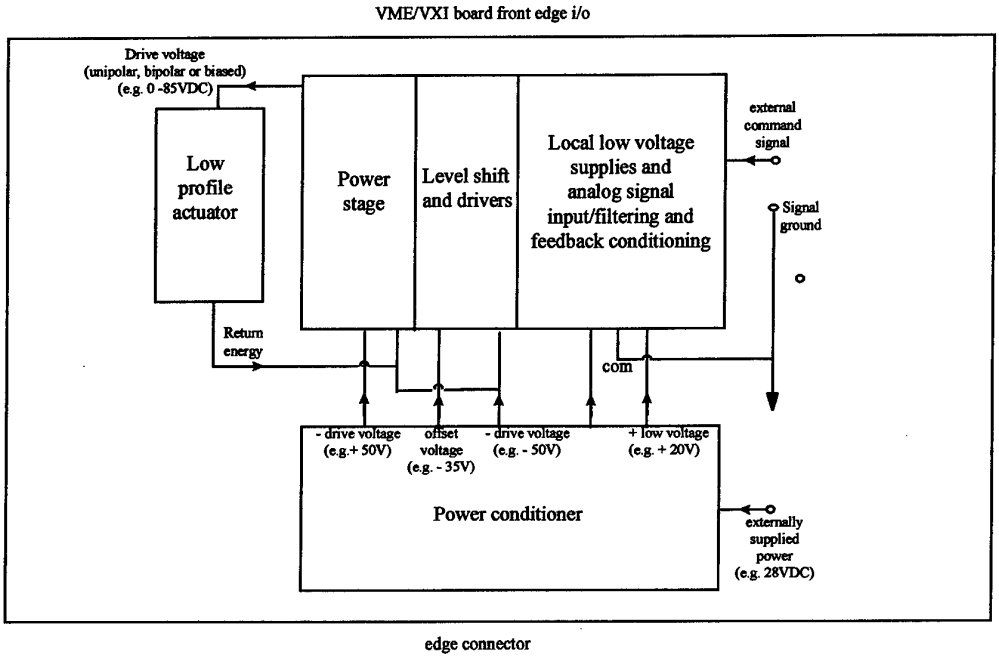

Figure 1: Integrated VME/VXI Board Incorporating Low Profile Multicellular Actuator

This capability that is introduced relies upon the integration of regenerative switchmode electronics that can operate at 92% efficiency or better to allow for integrated board mounted upconversion and drive electronics as to achieve a single board low profile implementation, Some of the most immediate needs for this integration technology include structural and/or environmental health monitoring such as NASA's Bragg grating Integrated Vehicle Health Monitoring (IVHM) systems, multiplexed fiber optic discriminators such as those being developed by the communications industry and oil and gas exploration that relies upon integrated fiber optic (Bragg) sensor systems to interrogate controlled seismic responses. The technical portion of this paper will focus on the requirements, design issues and solution to developing integrated regenerative multicellular optical fiber grating control systems utilizing this new technology.

TECHNICAL DESCRIPTION

For applications using Bragg gratings, the central idea behind the fiber optic laser is to change the optical wavelength corresponding to the grating in the fiber. The central idea is to place Bragg sensors along a silicon fiber. Each Bragg sensor becomes a sensitive temperature and strain sensor at its location which is EMI and RF insensitive (see Figure 2).

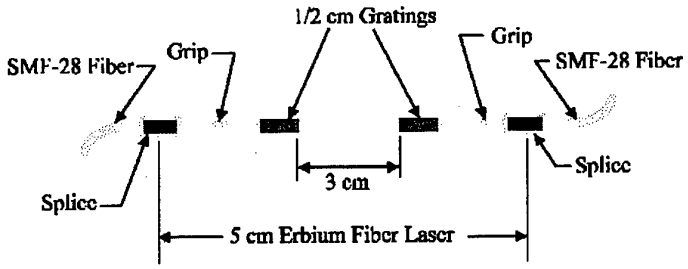

Figure 2: NASA Langley NESB Branch Fiber Laser

Tunable fiber lasers have an advantage due to the use of OTDR/FFT methods to interrogate each (Bragg) sensor individually with an ability to determine which sensor is being evaluated without having to make each one operate at a different wavelength. This advantage allows far more Bragg grating sensor readings, since numerous Bragg sensors can be (laser) inscribed at exactly the same wavelength along a single single-mode fiber. However, the force necessary to meet the displacement needs of a tunable fiber laser system are significant. Further, the "reset" time constant induces a large bandwidth requirement for the device. For example, for the NESB fiber of gauge length of 3 cm as shown in Figure 2, a required strain of 6,400μ-in corresponds to an extension of 180μ in length. It requires a force of $2Kg_f$ over 3.2cm. This cannot be directly implemented by induced strain materials (at least in a reasonable size design) to meet the bandwidth requirement. The solution must therefore use a different approach.

Figure 2, shows the top-level integration of high bandwidth integrated fiber optic strain (frequency varying) system that resides completely on a standard VME/VXI board configuration. The ability to integrate a low profile actuator mechanism with compact high bandwidth electronics within the x-y planform provided by standard VME or VXI can be used for fiber optical systems in general and fiber optic lasers in particular. The design shown in Figure 2, incorporates a method for designing a high bandwidth integrated fiber optic strain (frequency varying) system that is furthermore capable of residing completely on a standard VME/VXI board configuration. The ability to integrate a low profile actuator mechanism with compact high bandwidth electronics within the x-y planform provided by standard VME or VXI can be used for fiber optical systems in general and fiber optic lasers in particular.

The new integrated design enables the following features:

A. Integration of the fiber "pull" into the actuator,
B. Mounting of the integrated fiber "pull" actuator onto a (VME) board,
C. Surface mount or hybrid driver electronics and power regulation electronics integrated on the same board as the fiber "pull" actuator,
D. Use of high efficiency switching electronics to drive the integrated device,
E. The compact, high bandwidth design of the actuation mechanisms,

F. *The introduction of redundant operation through integrating primary and secondary electronics drivers on same (VME) board,*
G. *Low voltage operation through use of thin layer d_{33} piezo-(or PMN) stack actuators as electromechanically coupled drive elements and*
H. *Higher work rate for same power range (i.e. mechanical "pull" per milliwatt) through incorporation of d_{33} piezo-stack actuators.*

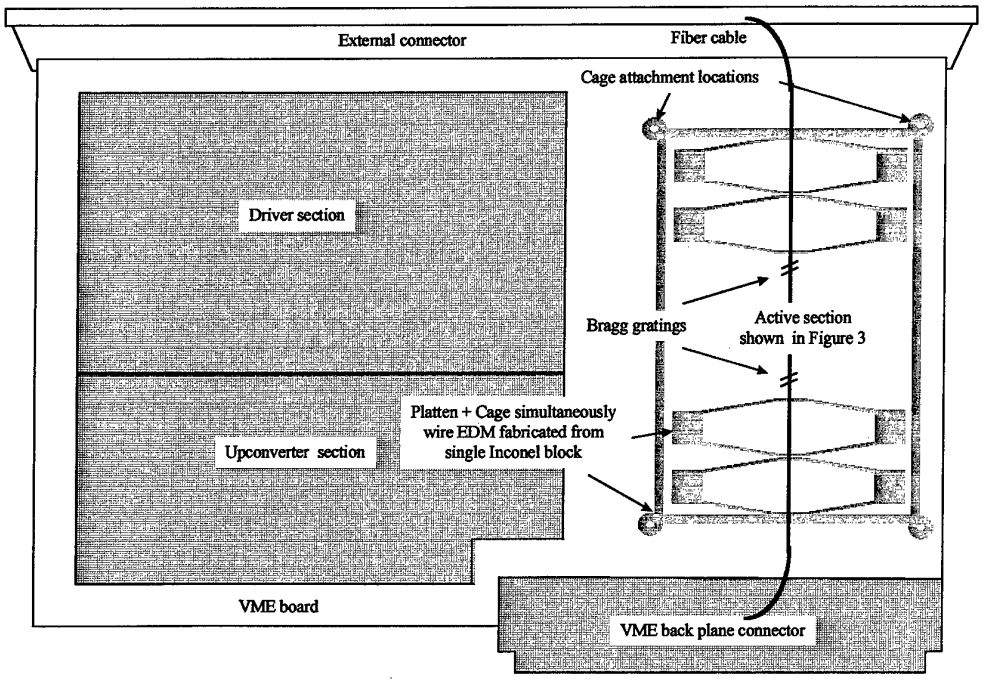

Figure 3: VME Board Mounted Multicellular Actuator/Driver (Actual Size)

This design consists of a split opposing system with a detachable fiber replacement and detachable single multilayer-multistack implementation. The single unit design enables the option of integrating a detach mechanism so that the precision actuation device can be used on a board mounted system or an integrated system. Figure 4 presents a more detailed schematic of the actuation section:

As illustrated in Figure 4, a 2+2 cell split opposing actuator design provides a high bandwidth-low voltage configuration capable of substantial force/displacement. The center block is placed between the two ceramic halves and a thin axial hole is made (e.g. drill or laser) through the platens and center blocks of each cell. The fiber is then threaded through this axial hole. The fiber can be attached by adhesive bonding, electromagnetic capture or EMF's new shape memory capture technique for ferrules at either interior end of the split actuator assembly. The further advantage to this invention is its ability to incorporate a fiber damping mechanism. The design implements can incorporate axial flexural motion damping of any center traversed rod or fiber, such as the tunable fiber optic laser system to improve signal to noise characteristics.

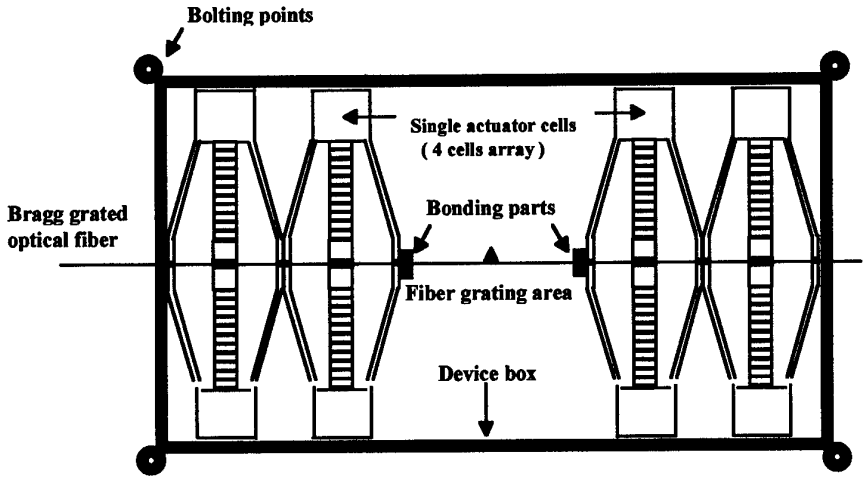

Figure 4: Optical Fiber Grating Control System Based on the Multicellular EMF Actuator - "Duo Configuration"

The multicellular EMF Actuator in an opposing symmetric geometry has some distinct advantages including always active in tension but with relaxed state when no charge is applied, center "pass-through" and fiber "capture", very low profile, provision for internalized axial fiber damping mechanism

A. Internalized fiber damping mechanism
B. Cage design isolation mount system,
C. Opposing actuation mechanism,
D. Center "pass-through" and fiber "capture",
E. Electromagnetic ferrule capture,
F. Shape memory ferrule capture,
G. On-board electronics drive mechanism,
H. Built-in redundancy design,
I. VME/VXI board mounting system and

CONCLUSION

The recent development of regenerative switchmode electronics has very significant impact to the design, geometry and systems integration of a variety of (Bragg) grating fiber optic based devices. As the ability to produce such high power-high efficiency designs improves with availability of hybridization it will increasingly play a significant role in the development of such sensor systems.

Author Index